Surface ocean circulation and organic carbon export across the mid-Pleistocene climate transition

Erin Louise McClymont

McClymont, Erin Louise (2004) Surface ocean circulation and organic carbon export across the mid-Pleistocene climate transition. Doctoral thesis, Durham University.

SURFACE OCEAN CIRCULATION AND ORGANIC CARBON EXPORT ACROSS THE MID-PLEISTOCENE CLIMATE TRANSITION

Erin Louise McClymont

University of Durham

A thesis submitted to the University of Durham in
accordance with the requirements of the degree of Doctor of
Philosophy in the Faculty of Science

Department of Geography

May 2004

53500 words

ABSTRACT

The mid-Pleistocene climate transition (MPT) marks a change in the nature of the climate system response to external forcing by insolation. This is represented first by the expansion of the northern hemisphere ice-sheets ca. 920 ka, and the emergence and dominance of glacial-interglacial oscillations with a 100-kyr period by 640 ka. The principal aim of this thesis is to understand the role of surface ocean circulation systems in the Atlantic and tropical Pacific and the strength of the biological carbon pump as drivers of the MPT. These two systems are examined as they exert important influences over global climate change through their impacts on heat and moisture transports, and carbon cycling and atmospheric CO_2 concentrations.

The robustness of the alkenone-derived U^{K}_{37}' index for reconstructing past sea-surface temperatures (SSTs) during the mid-Pleistocene is confirmed. It is shown that the index is insensitive to changes in the alkenone source organisms, the Prymnesiophytes, has minimal impact on the relationship between U^{K}_{37}' and SST. Reconstructions of SSTs from the mid-high latitudes of the Atlantic Ocean and the tropical Pacific Ocean between 1500-500 ka reveal that a synchronous and global drop in surface ocean temperatures of more than 1°C occurred ca.1145 ka (from Marine Isotope Stage, MIS, 34). The global cooling is coincidental with a shift toward a 'La Niña'-state of atmospheric circulation within the tropical Pacific. By analogy with the modern climate system, this intensification of atmospheric circulation in the tropical Pacific would have reduced the flux of heat to the high northern latitudes. It is proposed that this development of a cooler global climate system eventually drove the mid-Pleistocene expansion of the northern hemisphere ice-sheets. However, the global cooling was accompanied by a synchronous expansion of sea-ice cover in the North Atlantic and North Pacific that reached its maximum extent ca. 990 ka. It is proposed that this initially limited the supply of moisture to the ice-sheet source regions. Thus, ice-sheet response lags the onset of the global cooling by nearly 300-kyr, occurring between 920 and 880 ka (MIS 22). The driving mechanism for the global cooling remains unclear, but may be related to a long-term decline in deep-water temperatures. It is accompanied by an increase in the export of organic carbon to the ocean floor at a global scale. This is interpreted to reflect a strengthening of the biological carbon pump, which may have maintained or even driven the cooling trend by drawing down atmospheric CO_2 concentrations.

TABLE OF CONTENTS

LIST OF TABLES

LIST OF FIGURES

DECLARATION

I hereby certify that the work described in this thesis is my own, except where otherwise acknowledged, and has not been submitted previously for a degree at this or any other University.

The copyright of this thesis rests with the author. No quotation from it should be published without their prior consent and information derived from it should be acknowledged.

ACKNOWLEDGEMENTS

I would like to thank my supervisors, Prof. Antoni Rosell-Melé and Dr. Jerry Lloyd, for their guidance, support and seemingly endless enthusiasm throughout this PhD project. Many thanks are also offered to Dr. Marie Russell (now at FRS Marine Laboratory), who acted as a 'surrogate supervisor' and whose advice was invaluable in the laboratory analyses. The discussions, support and general good company of my fellow lab workers Dr. James Bendle and Oksana Kornilova were also greatly appreciated during the many hours spent in the laboratory.

I thank Dr. Jacques Giraudeau (DGO, University of Bordeaux I) for his hospitality and expertise during the working visit to his laboratories to perform the coccolith analyses. The advice of Dr. Heather Stoll (Williams College) and Barbara Balestre (University of Firenze) in coccolith preparation techniques is also gratefully acknowledged. A working visit to the laboratories of Prof. Richard Evershed (OGU, University of Bristol) made possible the GC-CI-MS analyses. Dr. Ian Bull is thanked for his supervision during the visit and the subsequent analyses.

I thank the Ocean Drilling Program for the provision of the samples analysed in this thesis. This thesis has also benefited from the provision of supporting data from a number of individuals, including the age model data provided by Dr.Kikki Kleiven (University of Bergen), Prof. Maureen Raymo (Brown University), Dr. Catherine Pierre (Université Pierre et Marie Curie, Paris), Prof. Alan Mix (Oregon State University) and Prof. Wolfgang Berger (Scripps Institute of Oceanography). The advice of Dr Nicklas Pisias (Oregon State University) regarding evolutive spectral analysis is also gratefully acknowledged. James Smith (University of Durham) is also thanked for his analysis of diatoms from the sediments of ODP 1087.

The technical and administrative staff in the Department of Geography at Durham are thanked for their support, particularly Derek, Frank, Brian, Neil and Ed in the labs, and Freda for the decoding of the laboratory orders.

The University of Durham is thanked for funding the studentship that made this PhD possible. I thank the Quaternary Research Association, the Royal Scottish Geographical Society, and the Challenger Society for providing further support to attend and present at the XVI INQUA Congress in Reno, Nevada, 2003. The European Geophysical Society/Union is thanked for a Young Scientists Travel Award to attend and present at the EGS-AGU-EUG Joint Assembly, Nice, France 2003.

Finally, I would like to express my gratitude to my family and friends, whose continued support never ceased to be a source of encouragement during the course of this thesis. A special thank you is also owed to Stewart, for his enthusiasm and continued support throughout.

1. Introduction

1.1 Introduction

The mid-Pleistocene climate transition (MPT) marks a change in the nature of the climate system response to the external forcing of insolation variations. This is most clearly represented by the emergence and subsequent dominance of glacial-interglacial oscillations with a period of ca. 100-kyr, which occurs despite negligible changes to insolation forcing. The MPT must therefore have been driven by processes within the climate system itself. In this thesis, two components that are important within the modern global climate system are reconstructed: surface ocean circulation, and the export of organic carbon from the surface ocean by the biological carbon pump. These two systems are important for the transport of heat and moisture and to carbon cycling and concentrations of atmospheric carbon dioxide (CO_2). However, the roles that they played in the MPT are unclear, due to a limited number of detailed reconstructions of their behaviour for this time. The approach followed in this thesis in order to address these issues is outlined in this Chapter. This includes site selection and sampling strategies, and an introduction to the analytical techniques to be employed. First, the issues surrounding the MPT and its implications for understanding global climate change are discussed.

1.2 Quaternary climate change

During the most recent geological period, the Quaternary, the climate system has oscillated between two extreme states, *glacials* and *interglacials*. The build-up of major continental ice sheets and expansion of mountain glaciation during cold glacial stages are interspersed with interglacials, where temperatures of the mid- to high-latitude regions were as warm as (or warmer than) the present day (Lowe and Walker, 1994). Glacial-interglacial oscillations also affected sea-level, ocean and atmosphere circulation patterns, weathering rates, and vegetation and animal distributions on a global scale (Lowe and Walker, 1994). The Quaternary period began between ca. 1.6 and 2.5 million years ago (Ma), and is often sub-divided into two systems or epochs, the Pleistocene and the Holocene. The latter defines the present interglacial, which developed after the last glacial maximum (LGM) ended ca. 10 thousand years ago (ka).

The global climate system is driven by the energy input of solar radiation (Beer et al., 2000), which is greatest at the tropics and lowest at high latitudes. This uneven heating of the Earth's surface drives circulation systems in the ocean and atmosphere that act to redistribute heat, and result in the development of regional climates. Biogeochemical cycling is also important, through determining atmospheric concentrations of a number of gases including water vapour, carbon dioxide (CO_2), methane (CH_4), and nitrous oxides (N_yO_x). These gases influence the absorption of radiation by the atmosphere and therefore play a role in determining atmospheric temperatures. Climate at a regional or global scale is the product of the interactions between these and other internal processes and the external forcing by solar radiation. These interactions have also determined climate changes during the Quaternary.

1.2.1 Solar radiation

The seasonal and spatial distribution of radiation, and the total amount received, varies on time-scales of thousands of years due to variations in the Earth's orbital and axial parameters (Figure 1.1). The Astronomical Theory of climate change was developed by Milutin Milankovitch (1930) from Croll (1875) and others, based on the assumption that the surface temperature of the Earth responds directly to the changing solar radiation patterns that result from these orbital variations. The theory emphasises the role of insolation at high northern latitudes, due to its impact on the balance between cool summer temperatures for ice sheet growth, or warm summers encouraging ice-sheet ablation (Milankovitch, 1930; Imbrie et al., 1992).

Support for the Astronomical Theory is found in the glacial-interglacial oscillations that correspond in time and phase to obliquity (ca. 41-kyr) and precession (ca. 19- and 23-kyr; Figure 1.2). This reveals an apparent direct, or *linear* response of the climate system to orbital variations (e.g. Hays *et al.*, 1976; Imbrie et al., 1992). During the last 640 ka, glacial-interglacial oscillations with a frequency close to eccentricity (ca. 96-kyr) have also been identified (Figure 1.2). This evidence led Hays *et al.* (1976) to propose that orbital variations were the 'pacemaker of the Ice Ages'.

1.2.2 Atmospheric gas composition

The impact of orbital variations is anti-phased between the two hemispheres (Figure 1.1). The synchronous ice-sheet growth between Antarctica and the Northern Hemisphere ice sheets on glacial-interglacial timescales suggests that additional

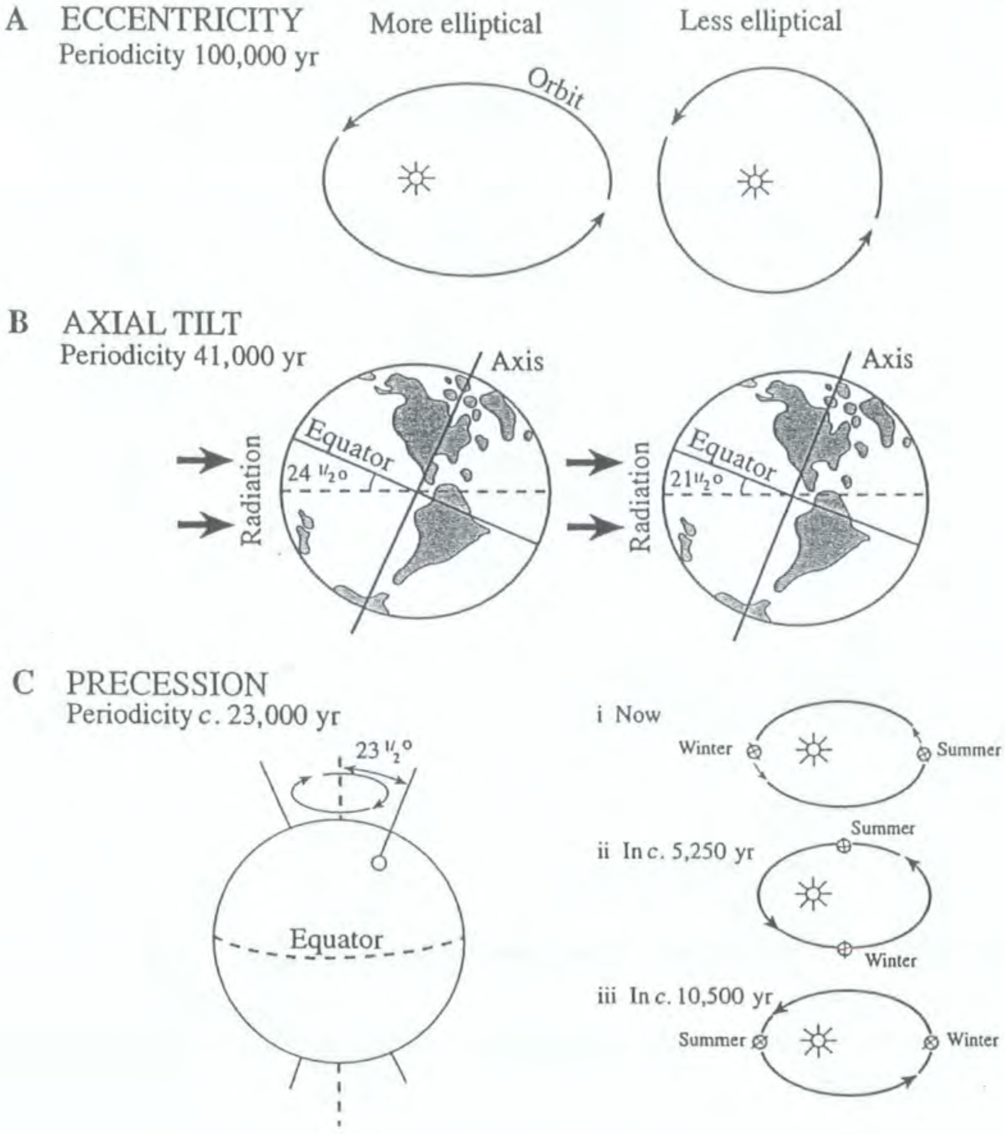

Figure 1-1 Milankovitch variations in the Earth's orbit. Modified by Benn and Evans (1998) from Lowe and Walker (1994).

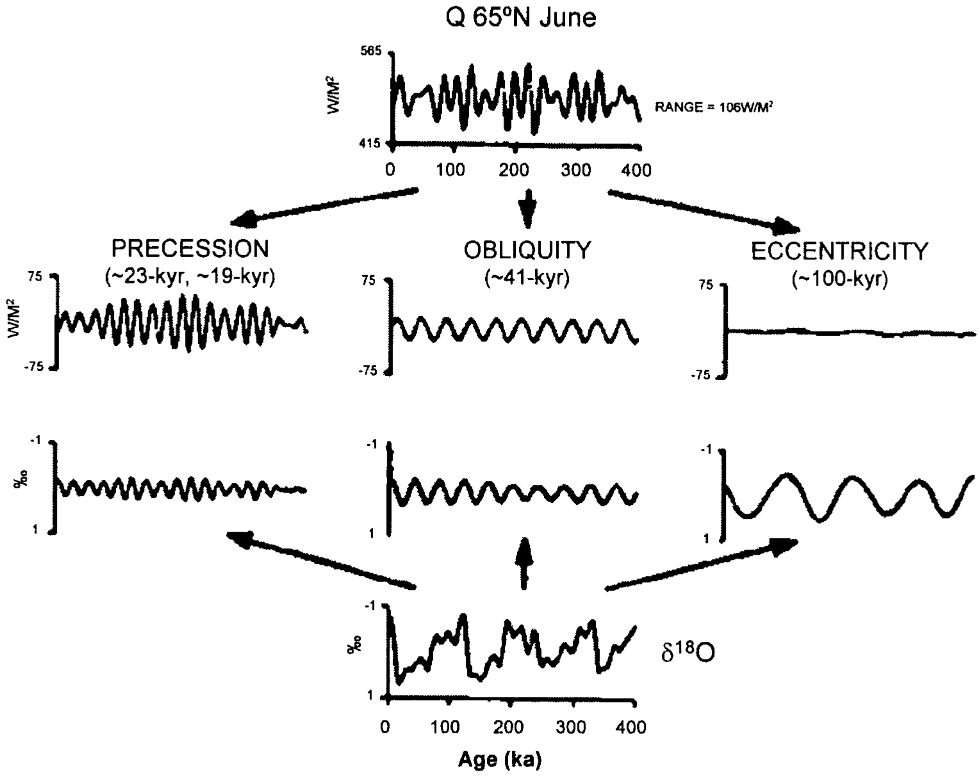

Figure 1-2 Comparison of orbital variations in solar radiation to global ice volume oscillations over the last 400 ka. Top: Solar radiation input (Q) at 65°N, broken down into variation in the three orbital bands: precession, obliquity and eccentricity. Bottom: Global ice volume variations ($\delta^{18}O$) and the variance displayed by global ice volume in the three orbital bands. Source: Imbrie et al. (1993).

processes must be operating within the climate system to modify the insolation signal (Hays et al., 1976; Broecker and Denton, 1990). Global temperature change may result from variations in atmospheric gas composition. Absorption of radiation by the atmosphere is increased with high levels of the 'greenhouse gases' of water vapour, CO_2, CH_4, and nitrous oxides (e.g. N_2O). These gases act to warm the climate by absorbing shorter wavelength energy and re-radiating it back to Earth as longer wavelength radiation. Variations to atmospheric concentrations of CO_2, CH_4 and N_2O have been detected in ice-core records that extend back to ca. 420 ka (e.g. Stauffer et al., 1998; Flückiger et al., 1999; Petit et al., 1999). These records show low greenhouse gas concentrations during glacials and stadials (cool stages within a glacial cycle) relative to interglacials. As a result, a key role for the atmospheric partial pressure of CO_2 (pCO_2) in Quaternary climate change has been proposed. Shackleton (2000) demonstrated a close relationship between eccentricity and pCO_2 variations during the late Pleistocene. He proposed that a sensitive response of the carbon cycle to eccentricity resulted in variations to pCO_2, which in turn influenced atmosphere and ocean temperatures and ultimately became translated into ice volume variations. This feedback mechanism may account for the large glacial-interglacial oscillations in comparison to the minimal eccentricity variation (Figure 1.2). This relationship has been questioned by Mudelsee (2001), who identified CO_2 variations lagging Southern Hemisphere temperature variations over the same interval, although CO_2 variations still led those of ice volume. Ruddiman (2003) argued that pCO_2 could play a role in driving the climate system into deep glacial states, when a combination of low obliquity, precession and eccentricity during ice-sheet growth resulted in draw-down of atmospheric CO_2 by a series of insolation-driven feedbacks. He proposed that this lowering of pCO_2 would drive further cooling, and 'tip' the climate system toward intense glaciation and ice-sheet expansion.

Variations to pCO_2 and other greenhouse gas concentrations may result from a variety of processes. Over timescales of millions of years, plateau uplift and weathering of continental landmasses have been proposed to result in CO_2 draw-down (e.g. Raymo, 1994). Variations in the size of the continental biosphere may also influence the amount of CO_2 utilisation by photosynthesis. The extents of tropical soils, as sources of N_2O and CH_4, are proposed to account for the millennial-scale variations in atmospheric gas composition (e.g. Flückiger et al., 1999; Stott et al., 2002). The biosphere may also respond to pCO_2 changes however, as demonstrated by the competition between C_3 and

C_4 plants (trees and cold-season grasses versus warm-season grasses) which use different photosynthetic pathways and have different CO_2 demands (e.g. Ehleringer et al., 1997).

As the largest carbon reservoir in the modern climate system, the global ocean is an important component of the carbon cycle (Siegenthaler, 1993; Levin and Hesshaimer, 2000). A reduction in the degassing of CO_2 by upwelling waters in the Antarctic region due to more extensive sea-ice cover has been proposed to account for some of the glacial fall in pCO_2 (Stephens and Keeling, 2000). Millennial-scale variations in atmospheric gas composition have been attributed to variations in tropical upwelling, which releases CO_2 and N_2O to the atmosphere, in combination with the changes in tropical soil extent (Flückiger et al., 1999; Stott et al., 2002). Absorption of atmospheric CO_2 by the surface ocean is promoted by the 'biological carbon pump' (Figure 1.3). This pump exports to the deep-ocean the organic carbon produced during photosynthesis by phytoplankton, the latter process utilising surface ocean CO_2 and defined as *primary productivity* (Shaffer, 1993; Falkowski et al., 2000). The transport pathway is not simple or linear however, as degradation processes including microbial decay, grazing by zooplankton, and remineralisation and oxidation in subsurface layers act to limit the downward flux of organic material (e.g. Shaffer, 1993; Grice et al., 1998). As a result, more than 99% of organic carbon produced in surface waters may be lost before reaching the sediment (e.g. Prahl et al., 2001). A strong biological carbon pump has the potential to reduce pCO_2 through increasing primary production and/or preservation potential (Figure 1.3). High abundances of organic carbon within sediments therefore indicate high *export production* and a strong biological carbon pump, rather than simply high *primary production*.

Increased biological carbon pump strength due to higher ocean productivity has been proposed to account for some of the glacial reductions in pCO_2 during the late Pleistocene (e.g. Sarnthein et al., 1988). This process may have been particularly important in regions where primary production is presently nutrient-limited, predominantly in areas with a relatively low supply of iron from continental sources, including the eastern equatorial Pacific and the Southern Ocean (Chavez et al., 1991; Martin et al., 1991). It has been proposed that enhanced aeolian dust flux to these regions due to glacial aridity and more intense atmospheric circulation may have

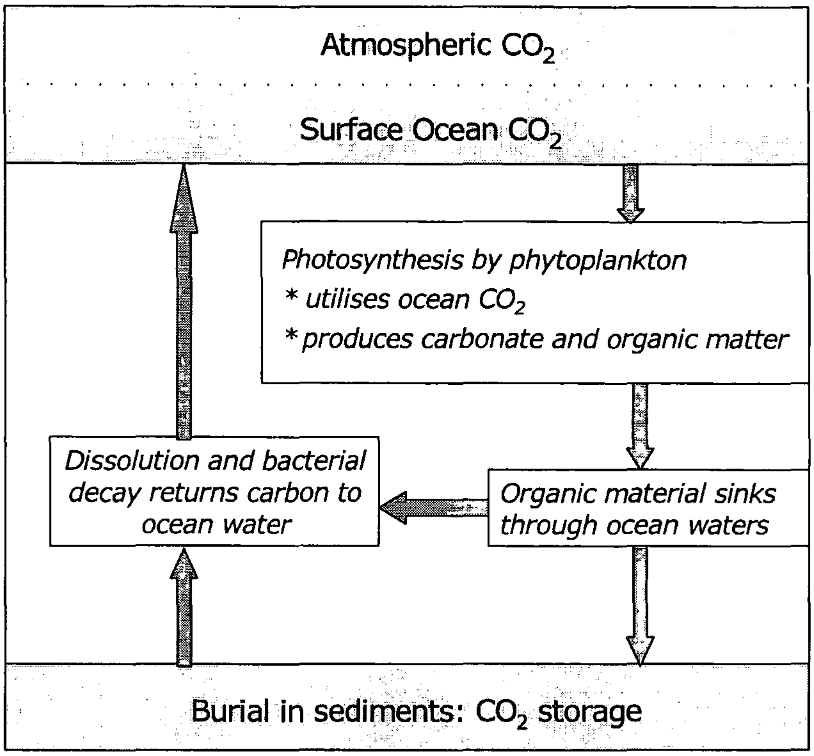

Figure 1-3 A simplified illustration of the marine organic carbon cycle, the 'biological carbon pump'. A strong biological pump is determined by a strong right-hand limb, which results in high organic carbon burial in marine sediments and a draw-down of surface ocean and atmospheric CO_2. Note that the surface ocean and atmospheric CO_2 levels are closely related (shown by the dashed line): the exchange between the two is primarily controlled by sea-surface temperature variations under equilibrium conditions.

triggered an increase in primary production and a consequent draw-down of pCO_2 (e.g. Martin, 1990; Watson et al., 2000; Ridgwell and Watson, 2002; Bopp et al., 2003; Ruddiman, 2003).

1.2.3 Ocean and atmosphere circulation

Driven by variations in solar radiation input and global temperature change, ocean and atmosphere circulation systems have also changed in association with the Quaternary glacial-interglacial oscillations. The expansion of continental ice sheets and sea-ice during glacials increases the thermal gradient between the equator and poles, encouraging intensification and/or migration of atmospheric circulation systems (e.g. Bassinot et al., 1997; Villanueva et al., 1998; Zhao et al., 2000; Smith et al., 2003). Coastal and equatorial upwelling systems vary in intensity in response to changes in the position or strength of the equatorward Trade Winds (Hay and Brock, 1992; Summerhayes et al., 1995; Little et al., 1997). The monsoons that influence precipitation patterns across Asia, Australasia, India and Africa, have also varied in strength with glacial-interglacial oscillations (e.g. Prell and Kutzbach, 1987; Clemens et al., 1996; Xiao and An, 1999; Kissel et al., 2003). Circulation systems in the ocean and atmosphere are closely linked to the development of regional climates, as they drive the transfer of heat and energy from the tropical regions towards the high latitudes. Ocean and atmosphere circulation systems therefore play two important roles in global climate change: first, through translation of solar radiation variations into regional climate change, and second, as feedback systems, amplifying or modulating forcing signals.

A key part of ocean circulation is the operation of the *thermohaline circulation system* (THC) which has components in both the surface and deep-ocean (Figure 1.4). In the northern North Atlantic and the Nordic Seas, deep convection results from the cooling of warm and saline Atlantic waters carried from the south in the North Atlantic Current (NAC; Figure 1.4). This sinking cold and saline water forms the North Atlantic Deep Water (NADW). As NADW flows southward at depth, it entrains intermediate Labrador Sea Water formed by convection in the Labrador Sea (Figure 1.4), and encounters northward flowing Antarctic Bottom Water (AABW) formed by convection in the Weddell Sea (see review by Weaver et al., 1999a). In response, northward circulation develops in the surface ocean of the Atlantic incorporating not only the NAC but also the Benguela Current from the South-east Atlantic (Figure 1.4). The operation of the

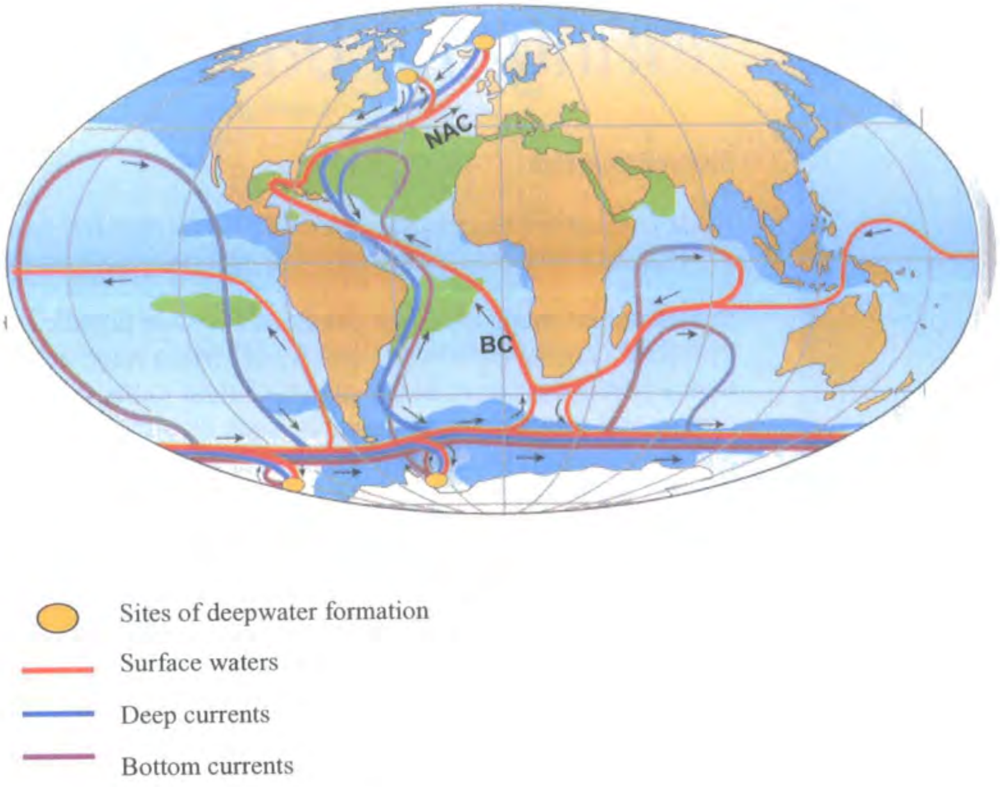

Figure 1-4 The thermohaline circulation system. Major surface, deep and bottom water currents are marked by the red, blue and purple lines. Green shading represents surface salinity >36 PSU, blue shading represents surface salinity <34 PSU. The northward flow of heat in the Atlantic Ocean by the North Atlantic Current ('NAC') and Benguela Current ('BC') are marked. *Source*: Rahmstorf (2002).

THC plays a key role in the climate of the North Atlantic. The heat release through convection in the North Atlantic is equivalent to c.25% of solar heat reaching the Atlantic Ocean surface north of 35°N, and causes warming in Europe (Broecker and Denton, 1990). The northward flow of the NAC may also be key to the supply of moisture to the northern hemisphere ice sheets during glacial inceptions (e.g. Ruddiman and McIntyre, 1979; Ruddiman et al., 1980; Sarnthein et al., 1995; McManus et al., 2002).

The operation of the THC is sensitive to the temperature and salinity of surface waters in the North Atlantic and Nordic Seas (Broecker and Denton, 1990). Periods of THC 'shut-down' on sub-orbital timescales (e.g. Boyle and Keigwin, 1987; Oppo and Lehmann, 1995; Curry et al., 1999) are associated with massive and episodic iceberg and meltwater discharges from the circum-Atlantic ice-sheets ('Heinrich events'). Coupled with a reduced input of NAC to the North Atlantic due to more extensive sea-ice, these freshwater perturbations may account for the glacial reductions in NADW formation (e.g. Venz et al., 1999). Weaker convection may also have acted as a positive feedback to high-latitude cooling, by reducing the associated heat release to the atmosphere from the flow of the warm North Atlantic Current to the North-east Atlantic (Broecker and Denton, 1990).

An ongoing debate in the climate research community is the role played by tropical circulation systems in global climate change. Section 1.1.2 introduced their potential for influencing atmospheric gas composition. The tropics are also major sources of heat and moisture to the atmosphere in the modern climate system. Although early analyses suggested that glacial cycles had minimal tropical impact, with sea-surface temperatures (SSTs) falling by only 1°C±1°C during the LGM (CLIMAP Project Members, 1976), it has more recently been shown that glacial cooling in the tropics was more intense. A comparison of reconstructed SSTs using two methods, the alkenone palaeothermometer and general circulation model results, demonstrated that tropical SSTs during the LGM fell by up to 4°C, with an average of approximately 2°C (Rosell-Melé et al., 2004). A similar magnitude of SST decline in the tropical Pacific has also been reconstructed using the Mg/Ca ratios of planktonic foraminifera (Lea et al., 2000; Koutavas et al., 2002; Stott et al., 2002; Visser et al., 2003), while coral records have revealed cooling of up to 5°C (Guilderson et al., 1994; Gagan et al., 2000). Variations in the strength of the closely coupled atmosphere-ocean circulation system in the tropical Pacific have been identified on both glacial-interglacial and millennial time-scales (McCulloch et al., 1999; Lea et al., 2000; Tudhope et al., 2001; Koutavas et al., 2002; Stott et al., 2002). As this system presently plays a key role in the supply of heat and moisture to the extra-tropics, including the ice-sheet source areas of the high-latitudes (e.g. Cane, 1998), the tropical Pacific has emerged as a potential key player in global climate change. A sensitive response of the Laurentide ice-sheet region to tropical warming (Rodgers et al., 2003), and rising SSTs in the tropical Pacific prior to a decline in global ice volume (Lea et al., 2000; Visser et al., 2003) has led to proposals that the region may be particularly important in driving late Pleistocene deglaciations.

1.3 The mid-Pleistocene climate transition

The late Pleistocene climate system (post-640 ka) is dominated by glacial-interglacial oscillations with a frequency of ca. 100-kyr (Mudelsee and Schulz, 1997). The 100-kyr cycles have a distinctive asymmetric ‘saw-tooth’ geometry, highlighting a gradual cooling toward maximum glacial conditions accompanied by rapid deglaciations (Figure 1.5B). This contrasts with the sinusoidal glacial-interglacial oscillations with lower amplitude and a frequency of 41-kyr that characterise global ice volume records for the preceding ca. 2.5 Myr (Figure 1.5B, and discussed in Raymo and Niscancioglu, 2003). This transition from 41-kyr to 100-kyr glacial-interglacial oscillations is defined as the ‘mid-Pleistocene climate transition’ ('MPT', Mudelsee and Schulz, 1997), also referred to as the ‘mid-Pleistocene Revolution’ ('MPR', Clark and Pollard, 1998). The MPT is shown schematically in Figure 1.5A.

The MPT is problematic for the Astronomical Theory for two reasons. First, although the 100-kyr cycles correlate with the ca. 96-kyr frequency of eccentricity, the latter is the weakest orbital parameter during the late Pleistocene, driving variations of <0.5% in solar radiation (Figure 1.2, Hays et al., 1976; Imbrie et al., 1993). Second, as Figures 1.5C and D demonstrate, no significant changes to orbital forcing are detected during the mid-Pleistocene that could account for the emergence of 100-kyr cycles in global ice volume (Berger and Loutre, 1991). Both issues highlight the operation and development of *non-linear* climate system behaviour at the ca. 100-kyr period, where climate change is controlled by internal processes (Imbrie et al., 1993). The MPT therefore represents

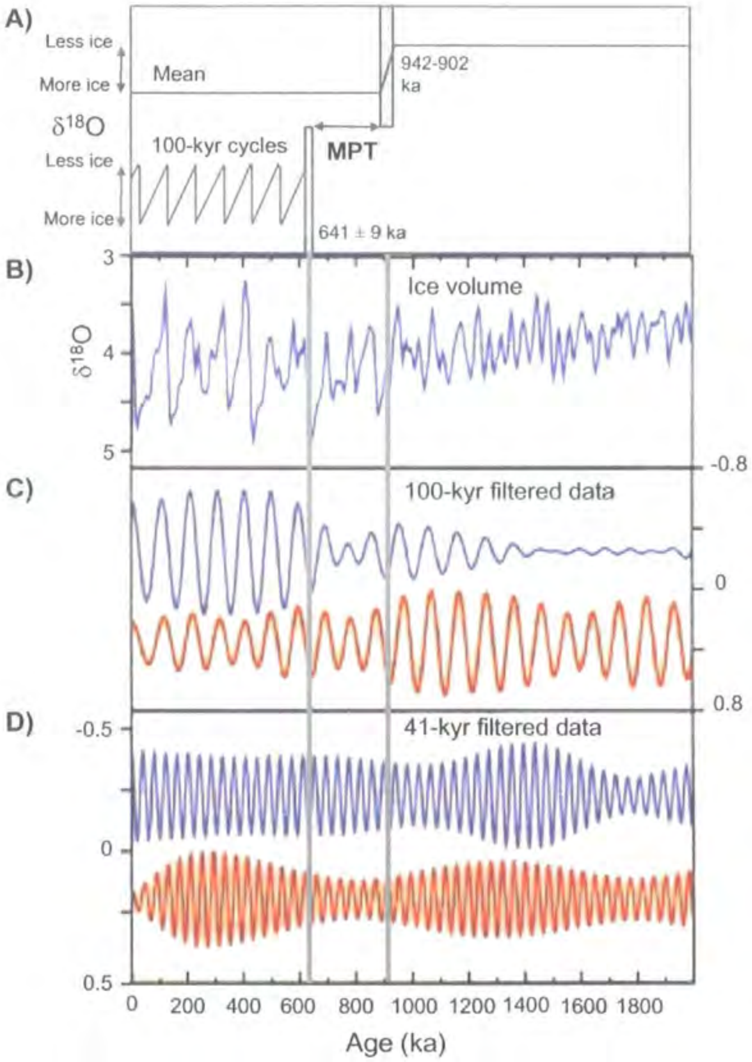

Figure 1-5 The mid-Pleistocene climate transition (MPT). (A) Schematic view of the MPT from time and frequency analysis of the $\delta^{18}O$ record of global ice volume, adapted from Mudelsee and Schulz (1997). The onset of the MPT is marked by a shift in mean global ice volume centred on 920 ka, followed ca.280-kyr later by the onset of the first dominant 100-kyr cycle. (B) $\delta^{18}O$ proxy record of global ice volume from 2000-0 ka at ODP Site 849 from Mix et al. (1995). High $\delta^{18}O$ values show high global ice volume. (C) The strength of variance at 100-kyr in ice volume (blue) and eccentricity (red). (D) The strength of variance at 41-kyr in ice volume (blue) and obliquity (red). Note the declining strength of the eccentricity signal as 100-kyr cycles emerge in ice volume. Note also the continued influence of obliquity over ice volume.Figures B-D from Clark et al. (1999).

either a change in the sensitivity of the climate system to eccentricity forcing, or the development of an internal regulation mechanism that operates with a frequency of ca. 100-kyr. Both possibilities imply that significant changes to the behaviour of the climate system took place during the mid-Pleistocene. The development of an internal regulatory mechanism is suggested by the absence of a climate system response to the stronger eccentricity cycle that operates at ca. 400-kyr (Imbrie *et al.*, 1993).

1.3.1 Mid-Pleistocene climate change

Prior to the onset of the first dominant 100-kyr cycle at ca. 640 ka a number of climate changes occurred that may highlight precursory modifications to climate system behaviour taking place. At ca. 920 ka, the mean state of the climate system moved toward apparently cooler conditions as marked by an increase in mean global ice volume (Figure 1.5A,B). As this shift represents an increase in glacial ice volume, with little change to interglacial ice volume, it also marks the development of higher amplitude glacial-interglacial oscillations. This is accompanied by an increase in the duration of the glacial-interglacial oscillations, first to ca. 77-kyr, then the development of the first 100-kyr cycle at 640 ka (Mudelsee and Schulz, 1997). This transition between global ice volume increase and the onset of the first dominant 100-kyr cycle has been used to delineate the 'MPT' as ca. 920-640 ka (Figure 1.5A; Mudelsee and Schulz, 1997).

This time interval is also marked by a number of other climate changes (Figure 1.6). The East Asian winter monsoon underwent an episode of strong circulation at 900 ka (Jian et al., 2003) followed by a sustained weakening until ca. 650 ka (Heslop et al., 2002). More vigorous atmospheric circulation then developed with the onset of the 100-kyr cycles in the monsoons and the Trade Wind systems (de Menocal, 1995; Bassinot et al., 1997; Xiao and An, 1999; Heslop et al., 2002; Wang et al., 2003b). A sustained period of reduced NADW formation between ca. 920-640 ka (Schmieder et al., 2000) also marks the development/intensification of glacial reductions in NADW formation (e.g. Raymo et al., 1990b; Bickert et al., 1997; Gröger et al., 2003; Kleiven et al., 2003). A synchronous perturbation to mean ocean $\delta^{13}C$ in the Atlantic and Pacific basins near 1 Ma is proposed to represent a one-time addition of ^{13}C-depleted carbon to the ocean, perhaps in response to increased continental aridity and reduced biosphere size (Raymo et al., 1997). Increased tropical aridity at this time has been identified in dust and palaeo-vegetation records (de Menocal, 1995; Schefuß et al., 2003). After ca. 600 ka, a shift to warm humid interglacials and cold dry glacials has been identified in tropical Africa (Dupont et al., 2001). The 920-640 ka period also marks a number of significant evolutionary events occurring onshore, including hominid evolutions and migrations in Africa and Europe (e.g. Azzaroli, 1995; Vrba et al., 1995; Bromage and Schrenk, 1999). Despite its significance for understanding global climate changes, the driving mechanism(s) of the MPT remain unclear.

1.3.2 Potential mechanisms for the mid-Pleistocene climate transition

Muller and MacDonald (1995; 1997) proposed that a fourth orbital parameter, the inclination of the Earth's orbital plane, may account for the 100-kyr climate cycles. They proposed that this hypothesis could be tested by analysing the flux of extraterrestrial dust reaching the Earth, which is also controlled by inclination. Although initial support was found in the 100-kyr cyclicity of interplanetary dust particles in Atlantic and Pacific sediments (Farley and Patterson, 1995; Patterson and Farley, 1998), subsequent analyses have demonstrated that these may be attributed to sediment focussing by deep-sea currents (Marcantonio et al., 1996; Higgins, 2001; Marcantonio et al., 2001; Higgins et al., 2002).

Figure 1-6 (Overleaf) Mid-Pleistocene climate change. The onset or termination of long term trends are marked by arrows. Periods of distinct climate change are delineated by the vertical grey bars. G: glacial, IG: interglacial, ACC: Antarctic Circumpolar Current, IRD: ice-rafted detritus. In brackets the reference sources are indicted.

Sources:

Becq: Becquey and Gersonde (2002); Berg: Berger et al. (1993a); Bick: Bickert et al. (1997); Bloe: Bloemendal et al. (1995); Can: Cannariato and Ravelo (1997); Clem: Clemens et al. (1996); deM: de Menocal (1995); Diek: Diekmann and Kuhn (2002); Dup: Dupont et al. (2001); Dur: Durham et al. (2001); Fro: Fronval and Jansen (1996); Groger: Gröger et al. (2003); Hel-1: Helmke et al.(2003b); Hel-2: Helmke et al. (2003a); Hen-1: Henrich and Baumann (1994); Hen-2: Henrich et al. (2002); Hes: Heslop et al. (2002); Jian: Jian et al. (2000); Marlow: Marlow (2001) and Marlow et al. (2000); Mud-1: Mudelsee and Schulz (1997); Mud-2: Mudelsee and Stattegger (1997); Oppo: Oppo et al. (1995); Ray-1: Raymo et al. (1990); Ray-2: Raymo et al. (1997); Sch: Schefuß et al. (2003); Schm: Schmieder et al. (2000); Sej: Sejrup et al. (2000); St-J: St John and Krissek (2002); Tian: Tian et al. (2002); Wang: Wang and Zhao (2000); Xiao: Xiao and An (1999).

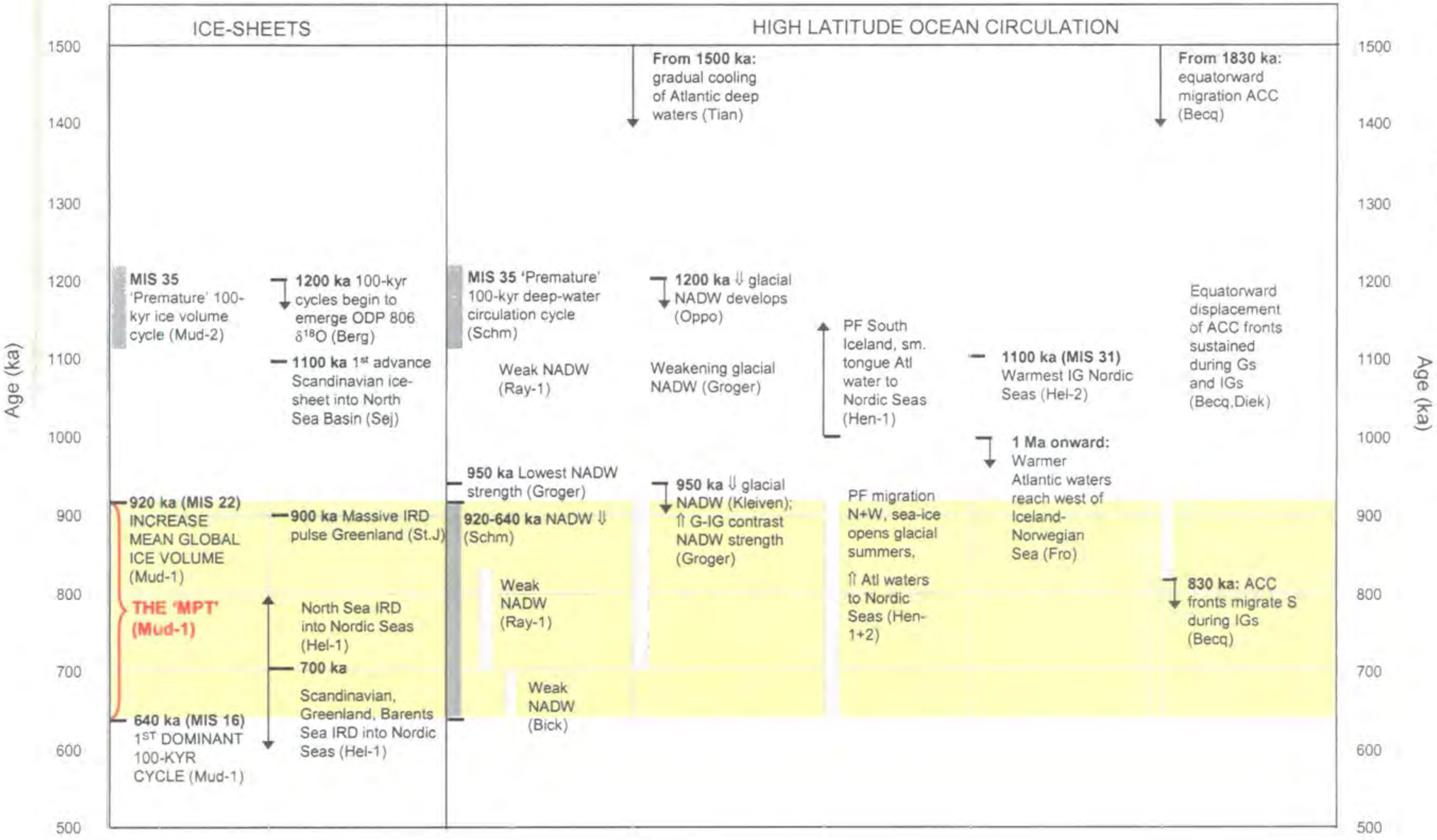

Figure 1-6: Mid-Pleistocene climate changes. For explanation see the caption on the previous page. Figure continues overleaf.

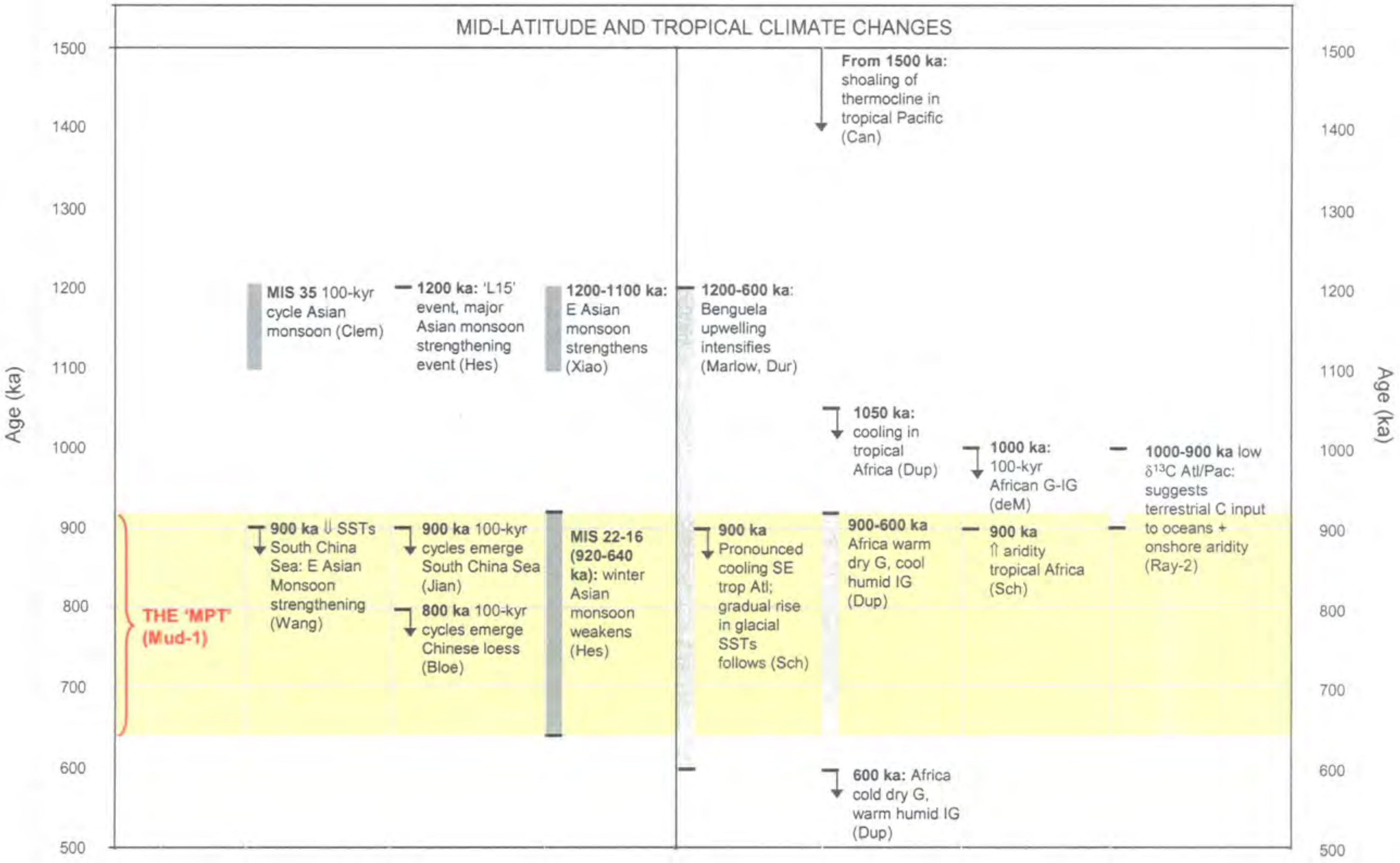

Figure 1-6 (continued): Mid-Pleistocene climate changes.

The development of larger northern hemisphere ice sheets after ca. 920 ka has been proposed to account for the shift toward 100-kyr cycles, due to their greater inertia with respect to external forcing (e.g. Imbrie et al., 1993; Berger and Jansen, 1994; Raymo, 1997; Clark and Pollard, 1998; Paillard, 1998; Ruddiman, 2003). This mechanism gains support from the immediate increase in duration of the glacial-interglacial oscillations after the ice volume expansion, initially to a 77-kyr frequency between 920-640 ka, before finally developing 100-kyr cycles (Mudelsee and Schulz, 1997). The ice-sheets are proposed to continue to steadily grow until they reach a critical size, whereby non-linear and rapid deglaciation occurs due to the development of calving margins (e.g. Imbrie et al., 1993; Berger and Jansen, 1994; Clark and Pollard, 1998). Although larger by ice volume, the 100-kyr northern hemisphere ice sheets are less spatially extensive than their pre-MPT 41-kyr counterparts (Clark and Pollard, 1998). Clark and Pollard (1998) attributed this to the impact of progressive erosion of the underlying regolith with each successive glaciation causing the basal substrate of the ice sheets to shift from soft, unconsolidated sediments to bedrock-dominated. They argued that the consequent increase in stability then encouraged development of thicker ice sheets that could survive warming episodes, but also increased crustal depression and the sensitivity of the ice sheets to rapid deglaciation by calving. Changes in the nature of glacially-deposited sediments from the Laurentide (North American) ice-sheet support this mechanism (Clark and Pollard, 1998; Balco et al., 2003; Roy et al., 2004).

The expansion of the northern hemisphere ice-sheets may alternatively have been driven by other climate system components. A long-term reduction in $p\mathrm{CO}_2$, and the consequent global cooling, has been proposed as the driving mechanism for the mid-Pleistocene increase in global ice volume (e.g. Berger and Jansen, 1994; Raymo, 1997; Paillard, 1998; Berger et al., 1999). A scarcity of detailed early- to mid-Pleistocene $p\mathrm{CO}_2$ reconstructions limits evaluation of the CO_2-cooling hypothesis, which relies instead upon theoretical relationships between the tectonic uplift rates and their impact through weathering on atmospheric CO_2 draw-down (e.g. Raymo, 1994). Pearson and Palmer (2000) generated only three data points for the Pleistocene, which appear to show a rise rather than fall in $p\mathrm{CO}_2$ values. Evidence for global cooling is also limited. Cooling in the surface waters of the coastal upwelling zones in the Benguela and eastern equatorial Pacific regions has been identified after ca. 1150 ka (Emeis et al., 1995; Marlow et al., 2000). However, these records may reflect intensification of upwelling rather than global cooling, as little change in tropical Atlantic SSTs occurred until the onset of the ice volume increase at ca. 920 ka (Bassinot et al., 1997; Schefuß et al., 2003). Significantly, the upwelling records demonstrate that climate change was occurring prior to the expansion of the northern hemisphere ice sheets. These cannot be accounted for by the Clark and Pollard (1998) mechanism.

The presence of large northern hemisphere ice sheets may not be a prerequisite for the development of 100-kyr climate cycles, as they can be identified during other geological periods when global ice volume was lower than the late Pleistocene (e.g. Beaufort and Aubry, 1990; Crowley et al., 1992; Beaufort, 1994). For the mid-Pleistocene, Berger et al. (1993a) identified strengthening at the 100-kyr frequency in global ice volume from ca. 1200 ka, prior to the ice-sheet expansion, a trend which is also visible in Figure 1.5C. The mid-Pleistocene increase in global ice volume and the onset of 100-kyr cycles may therefore be controlled by alternative climate system components. The potential role of $p\mathrm{CO}_2$ in translating and amplifying eccentricity variations into ice-sheet cycles, as proposed by Shackleton (2000), has been outlined above in Section 1.2.2. A mechanism to drive the development of this relationship during the mid-Pleistocene is not clear, particularly whether it occurred due to a change in the behaviour of the carbon cycle (e.g. with falling $p\mathrm{CO}_2$) or as a response to changes within other climate system components.

Gildor and Tziperman (2000; 2001) argue that the 100-kyr cycles are regulated by a ‘sea-ice switch’ mechanism. They propose that the ‘sea-ice switch’ is driven by the development of extensive sea-ice during cooling and growth of the continental ice sheets. This ultimately reduces the supply of moisture to the ice-sheets, driving rapid deglaciation and the development of asymmetric 100-kyr cycles (Gildor and Tziperman, 2000; Gildor and Tziperman, 2001). Tziperman and Gildor (2003) argue that the sea-ice switch developed during the mid-Pleistocene in response to a long-term decline in deep-water temperatures, which they propose was driven by a global cooling. They propose that cooler deep-waters resulted in a stronger vertical temperature gradient in the water column. In turn, they argue that this promoted stratification and resulted in a surface water mass that was more sensitive to atmospheric cooling and thus sea-ice development. Cooling of deep-waters has been identified during the mid-Pleistocene (Tian et al., 2002), and may also account for the SST decline in the upwelling records outlined above. However, after ca. 1 Ma in the North Atlantic and the Nordic Seas, a northward migration of the Polar Fronts, delimiting the extent of at least seasonal sea-ice cover, has also been detected (Henrich and Baumann, 1994; Wright and Flower, 2002), which tends to suggest a reduction in high-latitude sea-ice extent at this time.

Ocean and atmosphere circulation in the tropics has also been proposed as a potential driving mechanism for the MPT and the 100-kyr cycles. Rutherford and D'Hondt (2000) argued that 100-kyr cycles were dependent upon the propagation of tropical semi-precessional cycles (ca. 11.5-kyr) from the tropics to the high latitudes. They demonstrated that after ca. 1500 ka the semi-precessional cycles emerged in NADW circulation records, suggesting an increased influence of tropical processes in high-latitude climates. The mechanism to account for this propagation was not outlined by Rutherford and D'Hondt (2000), although they suggest that increased heat flow either across or along the equator may have enhanced the modern teleconnections between the tropics and high-latitudes. The intensity of tropical circulation during the mid-Pleistocene is uncertain, however. Evidence for shoaling of the thermocline in the eastern Pacific after 1500 ka suggests that tropical Pacific circulation may have intensified at this time (Cannariato and Ravelo, 1997), in support of Rutherford and D'Hondt (2000). In the Atlantic, significant changes to SSTs occur later, in association with the intensification of glacial ice volume after ca. 920 ka (Bassinot et al., 1997; Schefuß et al., 2003). More intense circulation in the tropical Pacific has been proposed to account for the Pliocene onset of Northern Hemisphere glaciation after 3 Ma, due to its influence over the supply of heat and moisture to the high latitudes (Molnar and Cane, 2002; Philander and Fedorov, 2003). Stronger circulation in the tropical Pacific therefore also shows potential for encouraging the mid-Pleistocene expansion of the northern hemisphere ice-sheets.

1.3.3 Unresolved issues

It has been demonstrated that evaluation of several proposed driving mechanisms for the MPT is restricted by a limited set of proxy data for a number of climate variables. Although there is extensive literature discussing changes in deep-water circulation during this time, reconstructions of surface ocean circulation systems are limited. Yet the latter (coupled with atmospheric circulation) has been shown to play a key role in the generation of regional climate systems, and have the potential to influence ice-sheet growth and decay through a number of feedbacks (Section 1.2.3). The transitional (rather than abrupt) nature of the MPT may potentially represent the gradual propagation of climate change between regional climate systems, rather than a globally synchronous and potentially more rapid event.

Assessing the global or regional signal of temperature change can be undertaken through comparison of sea-surface temperature data from a variety of regions (e.g. CLIMAP Project Members, 1976; Rosell-Melé et al., 1998a; Pflaumann et al., 2003; Rosell-Melé et al., 2004). Such a data set is currently unavailable for the mid-Pleistocene. There is also scarce evidence for the $p\mathrm{CO}_2$ changes proposed to drive global cooling, which instead relies upon theoretical relationships between uplift, weathering and CO_2 (e.g. Raymo, 1994). Despite the proposed importance of the biological carbon pump in influencing late Pleistocene climate change and $p\mathrm{CO}_2$, detailed reconstructions of its behaviour during the mid-Pleistocene are also limited.

Identification of the key driving mechanism(s) for the MPT is also hampered by issues surrounding the timing of the MPT itself. Although major climate changes occur during the transition defined by Mudelsee and Schulz (1997), a number of other changes can be identified prior to ca. 920 ka (Figure 1.6). Changes in upwelling intensity (Emeis et al., 1995; Marlow et al., 2000; Durham et al., 2001), deep-water circulation (Raymo et al., 1990; Oppo et al., 1995; Gröger et al., 2003) and tropical circulation (Cannariato and Ravelo, 1997; Xiao and An, 1999; Heslop et al., 2002) and even the frequency of the δ^{18}O glacial-interglacial oscillations (Berger et al., 1993a) may have begun as early as 1200 ka. Furthermore, a 'premature' 100-kyr cycle is also evident within global ice volume and deep-water circulation records from ca. 1200 ka (Mudelsee and Stattegger, 1997; Schmieder et al., 2000). This cycle suggests that the climate system may have been changing towards its late Pleistocene, 100-kyr state earlier than defined by the MPT of Mudelsee and Schulz (1997). The latter trend also suggests that the MPT may be evidence of a 'threshold response' within the climate system to longer term climate change, whereby progressive climate change suddenly triggers a shift towards a new or modified climate state. That the post-MPT climate system persists to the present day has implications for our understanding of the behaviour and potential sensitivities of our modern climate system.

1.4 Aims and objectives

The MPT represents a change in the climate system response to the external forcing of insolation variations. The principal aim of this thesis is to assess the roles of surface ocean circulation and the biological carbon pump in the MPT. In turn, this thesis aims to use this information to address the uncertainties surrounding the timing and definition of the MPT. These aims will be achieved through the reconstruction of changes to surface ocean circulation and the strength of the biological carbon pump in the Atlantic and tropical Pacific circulation systems. Despite these two systems playing an important part in global climate change, due to their influence over heat and moisture transfers and carbon cycling, their role in driving the climate changes associated with the MPT is unclear. This is largely as a result of limited information for their behaviour at this time.

The main objectives of this thesis are:

1. to reconstruct sea-surface temperature (SST) records and thus surface ocean circulation patterns in the Atlantic and the tropical Pacific;
2. to use these SST records to determine a global signature of mid-Pleistocene temperature change;
3. to reconstruct the strength of the biological carbon pump at these sites, to determine the potential for the biological carbon pump to drive mid-Pleistocene climate change through its impact on pCO_2.

The remainder of this chapter describes the approach followed to meet these objectives. First, the selection of the Atlantic and tropical Pacific circulation systems, and the sites to be analysed within them, is outlined. This is followed by an introduction to the sampling strategy employed, and the selection and application of age models for the sediments analysed. Finally, the analytical techniques to be employed are discussed.

1.5 Site selection

The key roles played by the Atlantic and equatorial Pacific circulation systems in global climate change have already been introduced (Sections 1.1.3 and 1.2.2). Both oceans are dominated by strong surface ocean circulation patterns, which transport heat northward in the Atlantic, and westward in the Pacific (Figure 1.7). To monitor the behaviour of these two systems during the mid-Pleistocene, sites were chosen to represent end-members of each surface ocean circulation system. Four Ocean Drilling Program (ODP) sites were selected (Figure 1.7): ODP 983 (Northern North Atlantic), ODP 1087 (South-east Atlantic), ODP 849 (East equatorial Pacific) and ODP 806 (West equatorial Pacific).

By analysing SSTs from two different oceanic circulation systems, and with cores located at a variety of longitudes and latitudes, we interpret any common trends between sites to be 'global-scale' imprints of mid-Pleistocene climate change, although the absence of data from the Indian Ocean is acknowledged. Analysis of two circulation systems will also allow an investigation of the relative sensitivity of different regions of the climate system to forcing mechanisms. The behaviour of the biological carbon pump at each site is also affected by regional processes. Comparison of the four sites may therefore also highlight any global-scale changes in the biological carbon pump strength.

1.5.1 The Atlantic Ocean

As a result of the net transport of heat northward at the equator, surface circulation in the Atlantic Ocean exports heat from the South to the North Atlantic (Figure 1.7). In the southern Benguela region of the South-east Atlantic, the relatively shallow (<80m) Benguela Current flows equatorward with the eastern limb of the subtropical gyre (Hay and Brock, 1992; Dowsett and Willard, 1996). After c.20°S the Benguela Current is deflected to the northwest toward the western tropical Atlantic (Figure 1.7). Here, c.13 Sv of South Atlantic water combines with waters from the eastern North Atlantic gyre (c.17 Sv), and flows northward as the relatively warm and saline North Atlantic Current, NAC (Schmitz and McCartney, 1993; Hansen and Østerhus, 2000). Cooling of the NAC in the Nordic Seas of the North Atlantic, and of a branch of NAC in the Labrador Seas, leads to sinking and formation of NADW (see Figure 1.4, Broecker and Denton, 1990; Hansen and Østerhus, 2000).

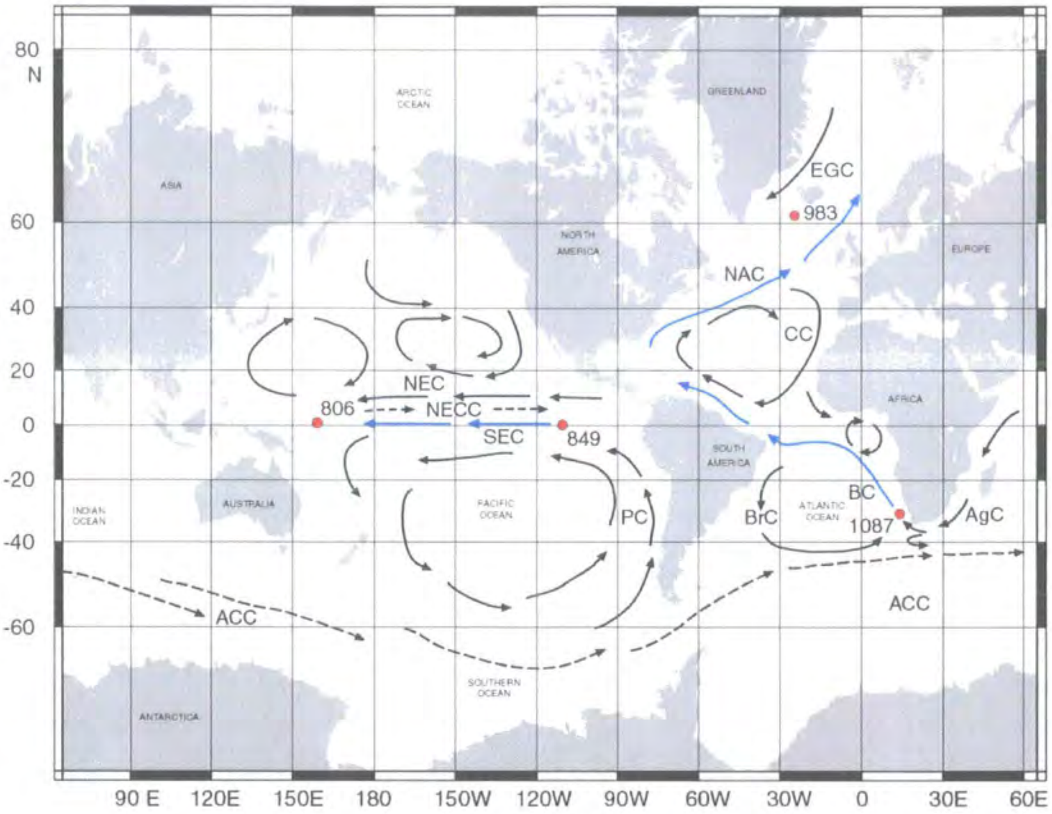

Figure 1-7 Major surface ocean circulation systems and the locations of the four cores analysed in this thesis. The heat transport pathways that link the Atlantic and Pacific cores are highlighted in blue. Base map source: www.odp-tamu.edu. Currents based on Open University (1989).

Current notation:

AgC: Agulhas Current; BC: Benguela Current; BrC: Brazil Current; CC: Canaries Current; EGC: East Greenland Current; NAC: North Atlantic Current; NEC: North Equatorial Current; NECC: North Equatorial Counter-current; PC: Peru Current; SEC: South Equatorial Current.

The high northern latitudes are considered to be particularly sensitive to orbital forcing, due to the strong influence of insolation variations over ice-sheet accumulation and ablation (Milankovitch, 1930; Imbrie et al., 1992). Near contemporaneous increases in SSTs, sea-ice extent and summer insolation at 65°N also highlights a sensitive response of the surface ocean of the Nordic Seas to orbital forcing (Koç and Jansen, 1994). If orbital variations played a role in driving mid-Pleistocene climate change, this may be evident through analysis of the SST record at ODP 983 (Figure 1.7).

The sensitivity of NADW formation to freshwater forcing in the North Atlantic has been outlined (Section 1.1.3). On millennial timescales, it has been proposed that diminished NADW formation during cool periods reduces the northward flow of heat from the South to the North Atlantic, resulting in warming either in the tropical and/or South Atlantic (Broecker and Denton, 1990; Rühlemann et al., 1999). The operation of this 'bipolar seesaw' (Broecker, 1998; Stocker, 1998; Stocker, 2000), where temperature changes in the North and South Atlantic act in opposing directions, has been proposed to account for millennial-scale asynchronous climate change between Antarctica and Greenland (Blunier et al., 1998; Rühlemann et al., 1999; Blunier and Brook, 2001; Kim et al., 2002).

The properties of the surface ocean of the South-east Atlantic also change in response to processes beyond the North Atlantic, and may in turn influence the formation of NADW. The temperature and salinity of the Benguela Current (BC), and the surface waters at ODP 1087, are determined by the relative inputs of a number of water masses to the region (Figure 1.7). The BC is fed by a combination of Atlantic waters from the South Atlantic gyre, and variable inputs of warm and saline Indian Ocean waters via the Agulhas retroflection (Gordon et al., 1992; Lutjeharms, 1996), and cool Southern Ocean waters from the subtropical convergence zone of the Antarctic Circumpolar Current (ACC) system to the south (Morley and Hays, 1979; Shannon et al., 1989; Giraudeau et al., 2001). Variations to the relative inputs of Indian and Southern Ocean waters may therefore alter the SST and salinity balance of the South Atlantic. As these waters flow northward to the NAC, changes to the properties of the BC may have implications for the temperature and salinity driven NADW formation (Gordon et al., 1992; Lutjeharms, 1996; Richardson et al., 2003). Northward migration of the ACC has been proposed to have restricted the inputs of Agulhas waters to the South-east Atlantic during glaciations, resulting in cooling of SSTs in the region and in the Benguela Current (McIntyre, 1970; Wefer et al., 1996; Kuhn and Diekmann, 2002; Gersonde et al., 2003; Pflaumann et al., 2003).

An additional influence over the heat and moisture transport from the South Atlantic to the north may be the intensity of upwelling within the Benguela system. The Benguela upwelling system runs along the western coastline of southern Africa, driven by the combination of longshore winds generated by the low pressure system that develops over the Kalahari desert, and by offshore divergence as the Benguela Current and eastern limb of the south Atlantic gyre flow equatorward (Hay and Brock, 1992; Dowsett and Willard, 1996). An increase in the strength of the trade winds that drive upwelling in the Benguela region may also increase heat and moisture transport across the equator and into the North Atlantic. By increasing moisture supplies to the northern hemisphere and enhancing ice sheet accumulation, ice-sheet instability may be encouraged as the ice-sheets advance into the marine realm and consequently develop less stable calving margins (Ruddiman and McIntyre, 1981; Imbrie et al., 1989; Little et al., 1997). This mechanism has been proposed to account for the early cooling signal identified in the South Atlantic prior to the onset of Heinrich events (Little et al., 1997).

The importance of Atlantic circulation (both at the surface and at depth) for northern hemisphere ice-sheet growth and European climates was outlined in Section 1.1.3. The surface oceanography of the South-east Atlantic also influences regional climates, particularly the aridity onshore. It is the presence of the relatively cool waters of the Benguela system that contribute to the arid conditions found in southern Africa, particularly evident by the presence of the Namib Desert, by reducing evaporation offshore and precipitation onshore (Dowsett and Willard, 1996).

1.5.1.1 ODP Site 983 (Northern North Atlantic)

ODP Site 983C (60°24'N, 23°38'W) was drilled at a water depth of 1985 m on the Bjorn-Gardar Drift in the northern North Atlantic as part of ODP Leg 162 (Figure 1.8). Surface waters at the site are presently influenced by an extension of the NAC, the Irminger Current, which flows westward toward East Greenland (Hansen and Østerhus, 2000). Seasonal SSTs range between 8-11°C, around an annual mean value of c.9°C (Figure 1.8, data from Conkright et al., 2002). The site presently lies to the south of the

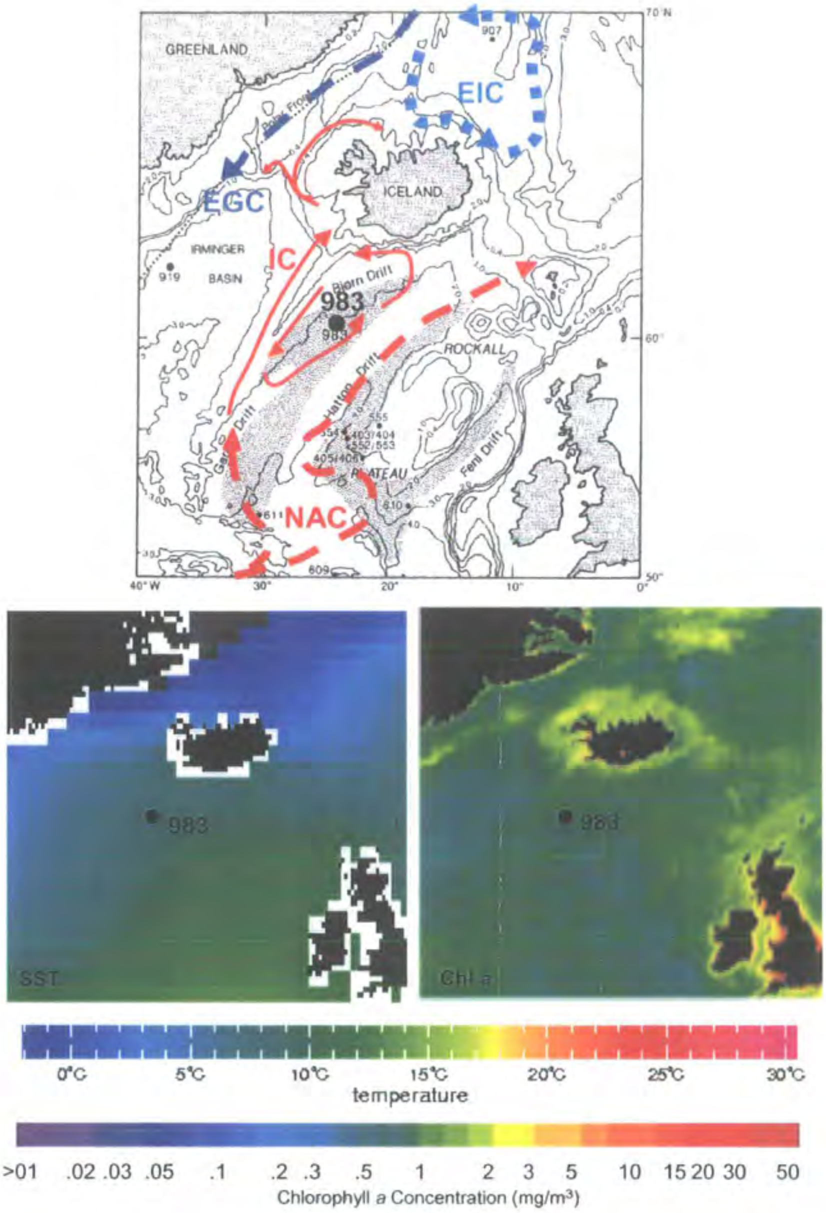

Figure 1-8 ODP 983. Top: Surface ocean currents in the northern North Atlantic and Nordic Seas. NAC: North Atlantic Current, IC: Irminger Current, EIC: East Icelandic Current, EGC: East Greenland Current. Waters enclosed by the EIC correlate with the Arctic Water domain, those of the EGC and to the west with Polar Water domain (see text for discussion). Base map: Koç et al. (1999). Currents: Hansen and Østerhus (2000). Bottom left: Modern annual SST values. Source: Conkright et al. (2001). Bottom right: Modern annual chlorophyll a concentrations in surface waters. *Source:* SeaWIFS data set: http://seawifs.gsfc.nasa.gov/SEAWIFS/IMAGES/IMAGES.html

Arctic and Polar Fronts, that delineate the southern extent of at least seasonal sea-ice cover (Swift, 1986). Modern phytoplankton productivity is high during spring blooms, in response to stabilisation of the water column after moderate winter mixing (Longhurst, 1998). Glacial migrations of these fronts to the south of the British Isles have been identified during the late Pleistocene (e.g. Ruddiman and McIntyre, 1981; Bard et al., 1987; Koç et al., 1993; Bond et al., 1997; Rosell-Melé et al., 1998b; Calvo et al., 2001). At the LGM, summer and winter SSTs at the location of ODP 983 fell to c.6°C and <2°C respectively, and winter sea-ice may also have developed at the site (e.g. de Vernal and Hillaire-Marcel, 2000; Pflaumann et al., 2003). At present, production in the polar waters to the north is more closely constrained by light and temperature rather than by nutrient levels, due to the longer presence of seasonal sea-ice cover (Longhurst, 1998).

The sediments of ODP 983 are derived from a number of sources (Jansen et al., 1996). Relatively low organic carbon (<0.48%) and carbonate contents (<40%) are found throughout. Calcareous nannofossils dominate the biogenic sediments, accompanied by abundant and generally well-preserved planktic foraminifera and diatoms (Jansen et al., 1996). ODP 983 sediments are dominated by fine-grained terrigenous particles, largely due to deposition associated with the overflow of Norwegian Sea Overflow Water (NSOW). NSOW, a component of NADW, advects fine-grained particles across the Greenland-Scotland Ridge, resulting in unusually high sedimentation rates (>16 cm kyr-1) and the development of the Gardar and Bjorn Drifts (Figure 1.8). Minor contributions from iceberg rafting are also evident (Jansen et al., 1996).

Both NSOW flow and iceberg rafting may have influenced the proxy records to be analysed here. Wang and McCave (1990) identified mid-Pleistocene variations to NSOW flow speed by analysing particle size variations. In addition to transporting terrigenous particles, NSOW advects coccoliths and organic carbon from the Nordic Seas to the Gardar Drift, with variable coccolith accumulation rates identified in response to changing NSOW flow speed during the Holocene (Giraudeau et al., 2000). This influence will be assessed during interpretation of the results from ODP 983. An additional allochthonous sediment source is through iceberg-rafting. Reworked pre-Quaternary nannofossils can be identified in association with iceberg rafted detritus at ODP 983 (Jansen et al., 1996). This may be accompanied by iceberg-rafting of terrigenous and/or pre-Quaternary organic carbon (Rosell-Melé and Koç, 1997; Rosell-

Melé et al., 1997; Calvo et al., 2001). Methods for detecting these inputs at ODP 983 are presented in Section 1.5.3.3.

1.5.1.2 ODP Site 1087 (Eastern South Atlantic)

ODP Site 1087A (31°28'S, 15°19'E) was drilled in a water depth of 1383 m, in the Southern Benguela Region (SBR) of the South-east Atlantic (Wefer et al., 1998). ODP 1087 is located near the southernmost tip of the extensive Benguela upwelling system that extends along the coastline of southern Africa (Figure 1.9). This system brings to the surface ocean relatively cool and nutrient-rich waters of South Atlantic Central Water (SACW) and the upper layer of Antarctic Intermediate Water (AAIW), and can be identified by high levels of primary productivity (Figure 1.9) and organic rich surface sediments (e.g. Wefer et al., 2001).

The relatively high carbonate and low organic carbon contents of the sediments in the SBR reflects the seasonal upwelling and lower nutrient contents in the upwelling waters, which contrasts with the perennial upwelling experienced further north (Rogers and Bremner, 1991). At ODP 1087 carbonate and organic carbon contents are c.80% and 2% respectively (Giraudeau et al., 2002). This north-south contrast in upwelling evolved by ca. 2 Ma (Giraudeau et al., 2002). Consequently, upwelling has had a limited influence at ODP 1087. Despite the seaward expansion of the coastal upwelling cells in response to lower glacial sea-levels (Mollenhauer et al., 2002) or upwelling intensification due to more favourable winds during warm intervals (Summerhayes et al., 1995), only a few samples from ODP 1087 for the late Pleistocene contained foraminifer species indicative of 'new' upwelled waters (Giraudeau et al., 2001).

SSTs at ODP 1087 reflect the balance between the relative inputs of Indian Ocean (via the Agulhas retroflection) and Southern Ocean waters (as described above). Modern annual SSTs average c.17°C (Conkright et al., 2002). To the south lies the subtropical convergence zone of the ACC (Figure 1.9), whose northward migration and consequent restriction of the Agulhas retroflection are proposed to have reduced glacial SSTs in the region (McIntyre et al., 1989; Wefer et al., 1996; Kuhn and Diekmann, 2002; Gersonde et al., 2003; Pflaumann et al., 2003). Winter SSTs at ODP 1087 fell during the LGM to

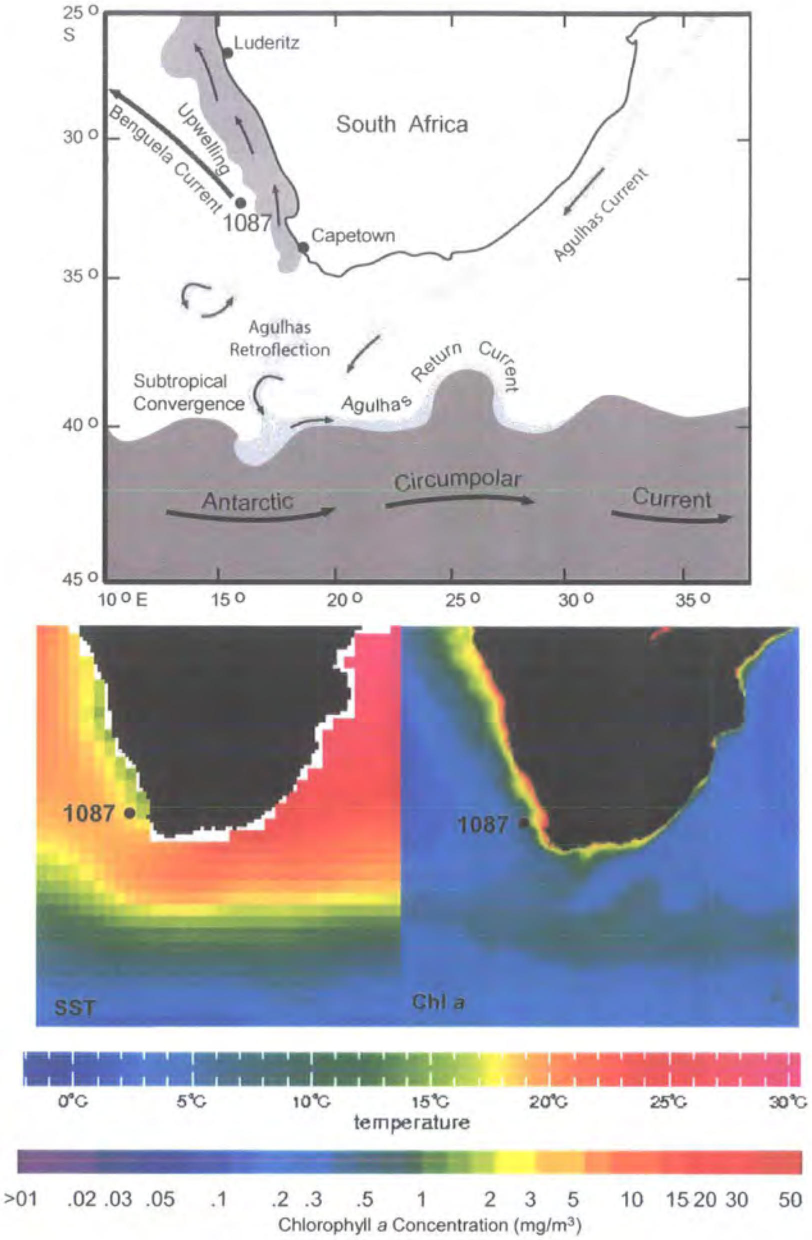

Figure 1-9 ODP 1087. Top: Surface ocean currents in the South-east Atlantic, showing location of modern Benguela upwelling cells, the Agulhas retroflection, and the position of the Antarctic Circumpolar Current (ACC) system. Adapted from Richardson et al. (2003). Bottom left: Modern annual SST values. Source: Conkright et al. (2001). Bottom right: Modern annual chlorophyll a concentrations in surface waters. Source: SeaWIFS data set: http://seawifs.gsfc.nasa.gov/SEAWIFS/IMAGES/IMAGES.html. Note the clear delineation of the Benguela upwelling system and the subtropical convergence zone of the ACC in SST and chlorophyll distributions.

c.11-12°C, although summer SSTs were maintained at c.18°C (Gersonde et al., 2003; Pflaumann et al., 2003). Two regions of relatively high productivity lie close to ODP 1087 and show a strong correlation with surface water conditions: in the Benguela and ACC systems (Figure 1.9). It is expected that changes in the spatial extents of these systems, in addition to affecting SSTs at ODP 1087, will also determine productivity in the surface ocean. The interaction between Atlantic, ACC and Agulhas waters has been shown to influence dinoflagellate production close to the site during the late Pleistocene at both orbital and sub-orbital scales (Esper et al., 2004). High levels of organic-walled dinoflagellate production occurred with enhanced influx of nutrient-rich subantarctic waters or upwelled waters, which contrasted with high production by calcareous dinocysts with inputs of warmer, stratified waters from the Agulhas retroflection (Esper et al., 2004).

The sediments of ODP 1087A are predominantly nannofossil ooze (Wefer et al., 1998). Foraminiferal abundance varies from abundant to few, with trace amounts of siliceous spicules, dinoflagellate cysts, and radiolarian tests identified. Sandy nannofossil layers suggest intervals of potential winnowing or turbidite activity (Wefer et al., 1998).

1.5.2 The equatorial Pacific Ocean

Surface ocean circulation in the equatorial Pacific Ocean is strongly coupled to the overlying atmospheric circulation (the Walker Circulation). The surface ocean is marked by an east-west SST gradient that is closely coupled to the overlying Trade winds and surface ocean transport of heat from east to west (Figure 1.10). Coastal and equatorial upwelling in response to this transport can be identified in the formation of the productive east Pacific cold tongue (Figure 1.10). In the west, the West Pacific Warm Pool (WPWP) is identified by the warmest SSTs of the global ocean (>28°C, Yan et al., 1992). The east-west SST gradient is accompanied by a progressive increase in the depth of the thermocline from east to west.

The tropical Pacific circulation system undergoes an annual cycle, described by Wyrtki (1965), that is closely related to the position of the Inter-tropical Convergence Zone (ITCZ). The ITCZ marks the position of convergence of the South-east and North-east Trade Winds. These wind systems drive two westward flowing surface ocean current

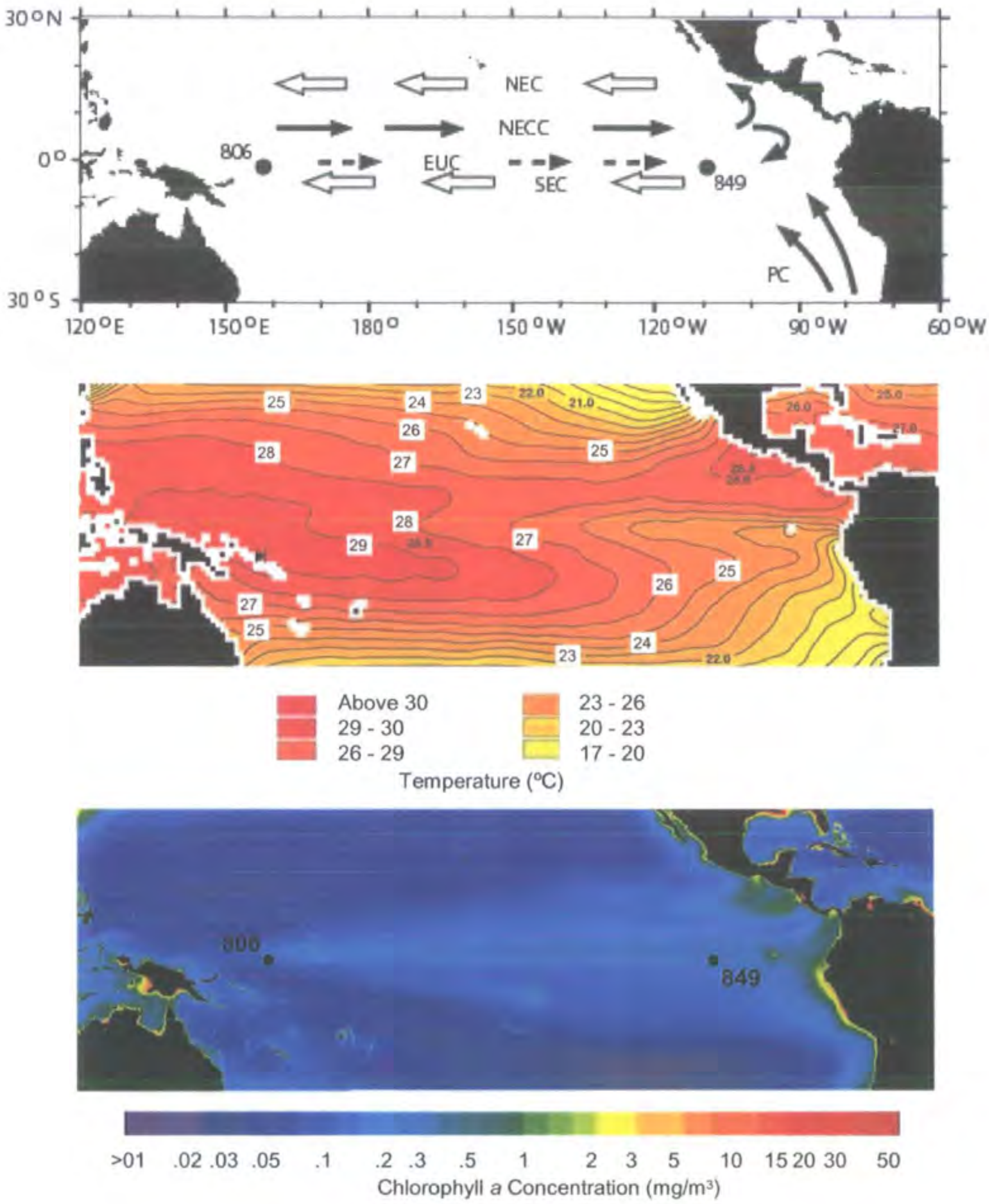

Figure 1-10 The tropical Pacific circulation system, and the locations of ODP cores 849 and 806. Top: Surface and subsurface ocean currents. SEC: South-east Current, NECC: North-east Counter Current, NEC: North Equatorial Current, PC: Peru Current. The eastward flow of the Equatorial Undercurrent (EUC) also marked. The positions of the SEC and NEC systems are closely related to the position and strength of the South-east and North-east Trade Winds. Based on Pisias et al. (1995a) and Open University (1989). Middle: Modern annual SST values. Source: Conkright et al. (2001). Bottom: Modern annual chlorophyll a concentrations in surface waters. Source: SeaWIFS data set: http://seawifs.gsfc.nasa.gov/SEAWIFS/IMAGES/IMAGES.html. Note clear delineation of the east equatorial Pacific cold-tongue and productive equatorial upwelling system at the northern margin of the SEC in the SST and chlorophyll distributions.

systems, the South Equatorial Current (SEC) and the North Equatorial Current (NEC; Figure 1.10), between which flows the North Equatorial Counter Current (NECC). Between August and December, the ITCZ is at its most northerly position, and the South-east Trades, the SEC and the NECC are at their strongest. This also corresponds with greater upwelling of waters from the Equatorial Undercurrent (EUC), which flows eastward below the northern margin of the SEC. Upwelling occurs in response to the equatorial divergence caused by the action of the Coriolis force on the westward flowing current systems, encouraging high levels of primary production (Figure 1.10). From February to April, the ITCZ is at its most southerly position, with weakened South-east Trades and stronger North-east Trades.

The equatorial Pacific circulation system is an important component in the modern global climate system due to its influence over global heat and water vapour moisture transports (Cane, 1998; Pierrehumbert, 2000). Its global significance is demonstrated by the impact of its inter-annual variability on both tropical and extra-tropical climates. This variability is defined as the El Niño-Southern Oscillation (ENSO; Figure 1.11), which may also be sustained on decadal timescales as persistent 'warm' El Niño or 'cool' La Niña states (e.g. Diaz and Markgraf, 2000). Weakening or collapse of the east to west circulation during an 'El Niño' event results in dramatic changes to trade wind strength and SST and precipitation patterns (Figure 1.11). The South-east Trade Winds weaken, and the cold tongue of the eastern Pacific becomes greatly reduced in size as upwelling declines. The WPWP and its associated low pressure zone migrate eastward, reducing precipitation in the western Pacific and impacting upon monsoon circulation (Figure 1.11).

Despite the modern significance of the ENSO system in extra-tropical climate change, its long-term evolution and stability is still not well understood (Bradley, 2000). ENSO-like variations have been identified on millennial timescales (e.g. Clement et al., 1999; Haug et al., 2001; Koutavas et al., 2002; Stott et al., 2002; Turney et al., 2004), between glacial-interglacial oscillations (e.g. Andreasen and Ravelo, 1997; Lea et al., 2000), and in association with the Pliocene onset of Northern Hemisphere glaciation (Molnar and Cane, 2002; Philander and Fedorov, 2003). Due to the extra-tropical impacts of the modern ENSO system, the potential for the tropical Pacific to play a role in driving or modulating global climate change has also been realised. A reduction in the size of the

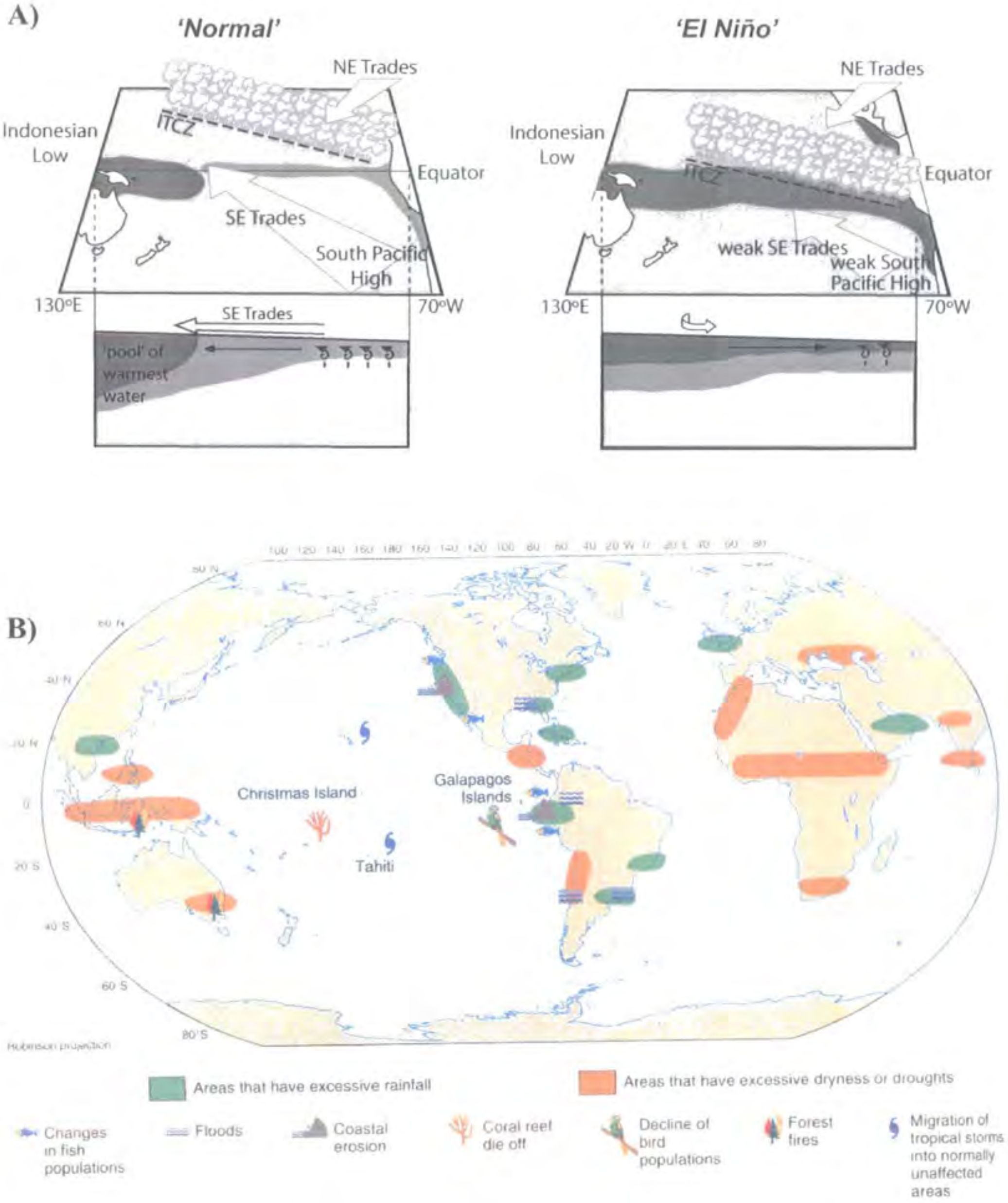

Figure 1-11 The El Niño / Southern Oscillation (ENSO) and its impacts. (A) Comparison of 'normal' ocean-atmosphere circulation in the tropical Pacific (left) to circulation exhibited during an El Niño year. Warm surface waters indicated by dark grey shading. The eastern Pacific cold tongue is visible with the grey shading along the equator and coastline of the Americas in the left figure. An El Niño event is marked by weaker South-east Trades and collapse of the east-west gradients in SST and thermocline depth. *Source:* Wilson et al. (2000, p.34). (B) The impacts of El Niño events. *Source:* Segar (1998).

WPWP at the LGM, due to lower SSTs and sea-levels in the West Pacific, may have limited cloud convection and reduced the moisture supply to the atmosphere (De Dekker et al., 2002). The influence of the tropical Pacific circulation system over convection strength may also be important for driving variations in monsoon intensity (e.g. Morley and Heusser, 1997; De Dekker et al., 2002; Kissel et al., 2003; Wang et al., 2003a). A stronger circulation system (a 'La Niña'-like state) has been proposed to have played a key role in the onset of Northern Hemisphere glaciation during the Pliocene, due to its influence over the supply of heat and moisture to the high-latitude ice-sheet source regions (Molnar and Cane, 2002; Philander and Fedorov, 2003). Increased primary production in the eastern equatorial region, in response to more vigorous aeolian activity and/or or increased dust supply due to continental aridity, has been proposed to account for at least part of glacial reductions in pCO_2 (e.g. Martin, 1990; Watson et al., 2000; Bopp et al., 2003; Ruddiman, 2003). By influencing tropical soil extents and the intensity of upwelling along the equator and in the eastern region, circulation change in the tropical Pacific may also determine the flux of the greenhouse gases N_2O and CH_4 to the atmosphere (Flückiger et al., 1999; Stott et al., 2002). The notion that the tropical Pacific may play a key role in global climate change is further supported by ocean-atmosphere modelling results, which suggests that long term ENSO variability is particularly sensitive to precessional forcing (Clement et al., 1999). This sensitivity is proposed to be the product of the control exerted by the precessional cycle over seasonal variations in solar radiation distribution across the equator (Clement et al., 1999). Rutherford and D'Hondt (2000) suggest that stronger circulation along the equator during the mid-Pleistocene would strengthen the teleconnections between low and high latitudes, driving the propagation of semi-precessional cycles to the high-latitudes. Support is found in the emergence of semi-precessional cycles in high-latitude deep-water circulation records after 1.5 Ma, and which Rutherford and D'Hondt (2000) suggest may be key to the development of the 100-kyr glacial-interglacial oscillations.

Reconstructing the strength of the ENSO system has previously been undertaken by comparing proxies for SSTs and thermocline depth from sites in the western and eastern equatorial Pacific (e.g. Chaisson, 1995; Chaisson and Ravelo, 2000; Lea et al., 2000). This strategy is employed here, through analysis of SSTs at ODP 849 in the east, and ODP 806 in the west (Figure 1.10). Although the resolution of the analyses here (5-kyr) may not be sufficient to identify the precessional forcing (23-kyr) that has previously been identified as a strong control over ENSO behaviour at glacial-interglacial timescales (Clement et al., 1999), the resolution will enable identification of longer term 'ENSO-like' trends. ODP 849 is located within the SEC, which is controlled by the South-east Trade Winds, and which weakens during El Niño events. The strength of the biological carbon pump at these two sites may also be linked to changes in thermocline depth, through its impacts over nutrient supplies and SSTs, and thus surface productivity. The sites are therefore ideally located for monitoring ENSO-like climate changes during the mid-Pleistocene.

1.5.2.1 ODP Site 849 (Eastern equatorial Pacific)

ODP Site 849D (0°11' N, 110°31' W) was drilled in a water depth of 3839 m in the eastern equatorial Pacific (EEP). The site lies near the northern boundary of the SEC system, but within the high-productivity equatorial divergence zone where upwelling of the EUC occurs (Figure 1.10). Mean annual SSTs at the site are c.25°C, with a range of c.23-26°C (Conkright et al., 2002). Biological production in the EEP is controlled by the rate of upwelling, which brings nutrient-rich waters to the surface ocean. Nutrient contents in the upwelled waters along the equatorial divergence are also strongly influenced by the properties of the EUC (Pisias and Mix, 1997; Loubere, 1999). The EUC supplies nutrients to the EEP via two processes: re-circulation of upper EUC waters into equatorial upwelling waters as it flows eastward, and advection via the Peru Current of deep EUC waters upwelled along the coastal margin of Peru (Wyrtki, 1981; Toggweiler et al., 1991). The input of iron from aeolian dust sources also influences productivity in the EEP, as discussed above.

The dominant primary producers of the EEP are blue-green algae, picoplankton, dinoflagellates and diatoms (Chavez et al., 1990). Coccolithophores are also important taxa (Chavez et al., 1990). The sediments of ODP 849 reflect the modern producers, being composed primarily of a diatom nannofossil ooze (Mayer et al., 1992). Diatoms, radiolaria and calcareous nannofossils are abundant, with common but generally poorly-preserved foraminifera. High-frequency variability in carbonate contents are proposed to relate primarily to productivity variations (Mayer et al., 1992).

1.5.2.2 ODP Site 806 (Western equatorial Pacific)

ODP Site 806B (0°19'N 159°21'E) was drilled in a water depth of 2520 m on the Ontong Java Plateau (Kroenke et al., 1991). The site lies within the West Pacific Warm Pool (WPWP; Figure 1.10). Mean annual SSTs exceed 29°C, with a small range of c.29-29.5°C (Figure 1.10, data from Conkright et al., 2002). Although frequently reported as an oligotrophic region comparable to the subtropical gyres (e.g. Chavez and Barber, 1991), the west equatorial Pacific is also affected by typical tropical circulation features, including the presence of the SEC, EUC, NECC and NEC (Mackey et al., 1995).

The thermocline is considerably deeper than that of the eastern Pacific, although its depth may vary in association with ENSO (Figure 1.11). The surface waters are currently capped by a low-salinity layer that isolates surface waters from the nutrient-rich thermocline below, resulting in relatively low surface productivity (Mackey et al., 1997; Longhurst, 1998). During the LGM, increased surface salinity in response to lower sea-level and reduced precipitation resulted in an increase in surface salinity in the region (Martinez et al., 1997). This may encourage the thermocline to shallow and thus increase the nutrient supply to the surface waters of the region. Modern production is concentrated in two zones, c.2°N and 2°S, with lower rates than those reported from the central and eastern Pacific (Mackey et al., 1995; Longhurst, 1998). Modern surface plankton communities are composed of abundant Prymnesiophytes (a class of phytoplankton that includes coccolithophores), with minor and localised inputs of green algae and cyanobacteria (Everitt et al., 1990). Diatoms are not abundant in the region (Everitt et al., 1990).

These characteristics are strongly reflected in the sediments of ODP 806B, which are dominated by calcareous nannofossils (generally >70%), with abundant foraminifera (generally 15-30%) and rare to minor contributions from radiolarians and diatoms (Kroenke et al., 1991). Pleistocene carbonate contents are generally 85-90%, as observed in sediments across this region, resulting in sediment accumulation rates that primarily reflect changes in surface productivity (Kroenke et al., 1991). Due to a coring gap at c.16 metres depth, a selection of samples from ODP 805C (located to the north and down slope of ODP 806B) were used to bridge the record, following the age model generated by Berger *et al.* (1993a).

1.6 Approach

1.6.1 Sampling strategy

Figure 1.6 demonstrates that in addition to the climate changes associated with the MPT as defined by Mudelsee and Schulz (1997), a number of other climate changes could be identified prior to 1.0 Ma. To evaluate the role played by these longer-term climate trends in the development of the MPT, all cores were analysed for the time interval 1500-500 ka. All four sediment cores were analysed at a resolution of ca. 5-kyr. This resolution was selected to allow identification of variance with orbital frequencies (from the 19-kyr precession band to the 413-kyr eccentricity band).

1.6.2 Age models

The age models for each core were generated in two stages (Table 1.1). First, the preliminary age models generated by Shipboard analyses in each ODP Leg were applied. These were refined by application of higher-resolution oxygen isotope stratigraphies tuned to the astronomical timescale.

The shipboard preliminary age models for ODP cores are constructed by identification of a number of magnetic polarity reversals and biostratigraphy events (species extinctions or emergences) with known ages (for example, the preliminary age model

Table 1-1 Age models for the four sediment cores analysed in this thesis. Average sedimentation rates for the interval 1500-500 ka are also shown, calculated using the oxygen isotope stratigraphies. Note the relatively high sedimentation rates at ODP 983C. A coring gap in ODP 806B was bridged using samples from ODP 805C following the oxygen isotope stratigraphies.

ODP Hole (Drilling Leg)	**Preliminary Shipboard Age Model**	**Oxygen Isotope Age Model**	**Average linear sedimentation rates (cm/kyr)**
983C (Leg 138)	(Jansen et al., 1996)	M.E. Raymo (*pers.comm.*, Dec. 2002)	16.01
1087A (Leg 175)	(Wefer et al., 1998)	CA. Pierre (*pers.comm.*, May 2003)	3.86
849C,D (Leg 138)	(Mayer et al., 1992)	(Mix et al., 1995)	2.64
806B, plus 805C (Leg 130)	(Kroenke et al., 1991)	(Berger et al., 1993a; Berger et al., 1993b)	2.09

generated for ODP 983C is shown in Table 1.2). The age model is completed by calculating the linear sedimentation rates between these events. This procedure assumes that constant sedimentation rates are maintained between each stratigraphic event. When examining climate change on glacial-interglacial timescales (or at sub-orbital timescales), it is necessary to construct a higher-resolution age model to account for climate driven variability in sedimentation rates due to changes in the fluxes of biogenic or terrigenous particles (e.g. through higher primary production, or deposition of iceberg-rafted detritus). This was achieved at the four cores analysed here using oxygen isotope stratigraphies (Table 1.1).

Table 1-2 An example of an ODP shipboard preliminary age model: Pleistocene and late Pliocene age-control points for ODP 983C. (N): nannofossil (coccolith) biostratigraphy datums (FO: first occurrence, LO: last occurrence). Other dates refer to magnetic polarity events. *Source*: (Jansen et al., 1996).

Event	**Age (Ma)**	**Metres composite depth (mcd)**	**Sedimentation Rate (mcd/m.y.)**
Core top	0.00	0.00	
			118.04
FO *E.huxleyi* (N)	0.26	30.69	
			99.45
LO *P.Lacunosa* (N)	0.46	50.58	
			125.25
Brunhes/Matuyama	0.78	90.66	
			126.57
Jaramillo top	0.99	117.24	
			182.42
Jaramillo bottom	1.07	131.83	
			155.73
LO *Gephyrocapsa* spp. A/B (N)	1.23	156.75	
			167.11
Olduvai top	1.77	246.99	
			193.39
Olduvai bottom	1.95	281.80	

1.6.2.1 Oxygen isotope stratigraphy

Oxygen exists in three isotopic forms, ^{16}O, ^{17}O and ^{18}O. The relative abundance of the ^{16}O and ^{18}O isotopes in a sample is described by the notation '$\delta^{18}O$' where:

$$\boldsymbol{\delta^{18}O = 1000 \times (^{18}O/^{16}O \text{ sample} - {}^{18}O/^{16}O \text{ standard}) / (^{18}O/^{16}O \text{ standard})} \qquad \textbf{(1-1)}$$

The $^{18}O/^{16}O$ standard is the PDB standard. $\delta^{18}O$ is described as *isotopically light* if it is deficient in ^{18}O, and $\delta^{18}O$ becomes more negative (Lowe and Walker, 1994).

$\delta^{18}O$ values in marine carbonates reflect the interaction of a number of processes. Evaporation from the surface ocean preferentially removes the lighter ^{16}O isotope (in $H_2{}^{16}O$). The temperature-dependent nature of the fractionation process means that greater fractionation occurs between the surface ocean and the atmosphere at high latitudes, where clouds contain less ^{18}O (Lowe and Walker, 1994). Precipitation at high latitudes (and ice-sheet accumulation) therefore contains greater concentrations of ^{16}O. This fractionation process became more pronounced during glaciations, when ^{16}O became trapped in the high latitude ice sheets, resulting in enrichment of the oceans in ^{18}O and enrichment of the ice-sheets in ^{16}O. This is recorded in the $\delta^{18}O$ values of foraminiferal carbonates (Figure 1.12). Benthic foraminifera are usually analysed to generate the proxy record of global ice volume variations, as surface ocean $\delta^{18}O$ values may also be affected by non-ice volume environmental signals, principally SST and salinity (e.g. Duplessy et al., 1992; Maslin et al., 1995). Changes to water temperatures may also complicate the benthic $\delta^{18}O$ ice volume signal however, as the precipitation of carbonate (and the formation of the $\delta^{18}O$ signal) is at least partly temperature dependent (Lowe and Walker, 1994). Variations to deep-water temperatures over glacial-interglacial timescales have been reconstructed using other proxy methods, including Mg/Ca ratios in benthic carbonates (Dwyer et al., 1995). A recent study presented a comparison of benthic $\delta^{18}O$ values between the Atlantic and Pacific Oceans, and demonstrated that deep-water temperatures in the Atlantic had been falling gradually since 1500 ka (Tian et al., 2002).

Recognition that benthic foraminifera record global ice volumes by their oxygen isotope ratio ($\delta^{18}O$; see discussion in Section 1.5.3.6), coupled with the apparently linear response of global ice volume to obliquity and precession (e.g. Imbrie et al. 1993; Section 1.1.1), led to the development of an *oxygen isotope stratigraphy* for deep-sea sediments. This method assigns an *isotopic stage* to glacials and interglacials, denoted by even and odd numbers respectively (Emiliani, 1955; Shackleton and Opdyke, 1976; Ruddiman et al., 1986; Shackleton et al., 1990). Figure 1.12 illustrates the $\delta^{18}O$ time-series for the four cores analysed in this thesis, and shows a selection of isotope stage names. The MPT as defined by Mudelsee and Schulz (1997) corresponds to the interval between Isotope Stages 22 and 16 (ca. 920-640 ka). Absolute ages for the isotope stages are generated by 'orbital tuning', where the oscillations in global ice volume are

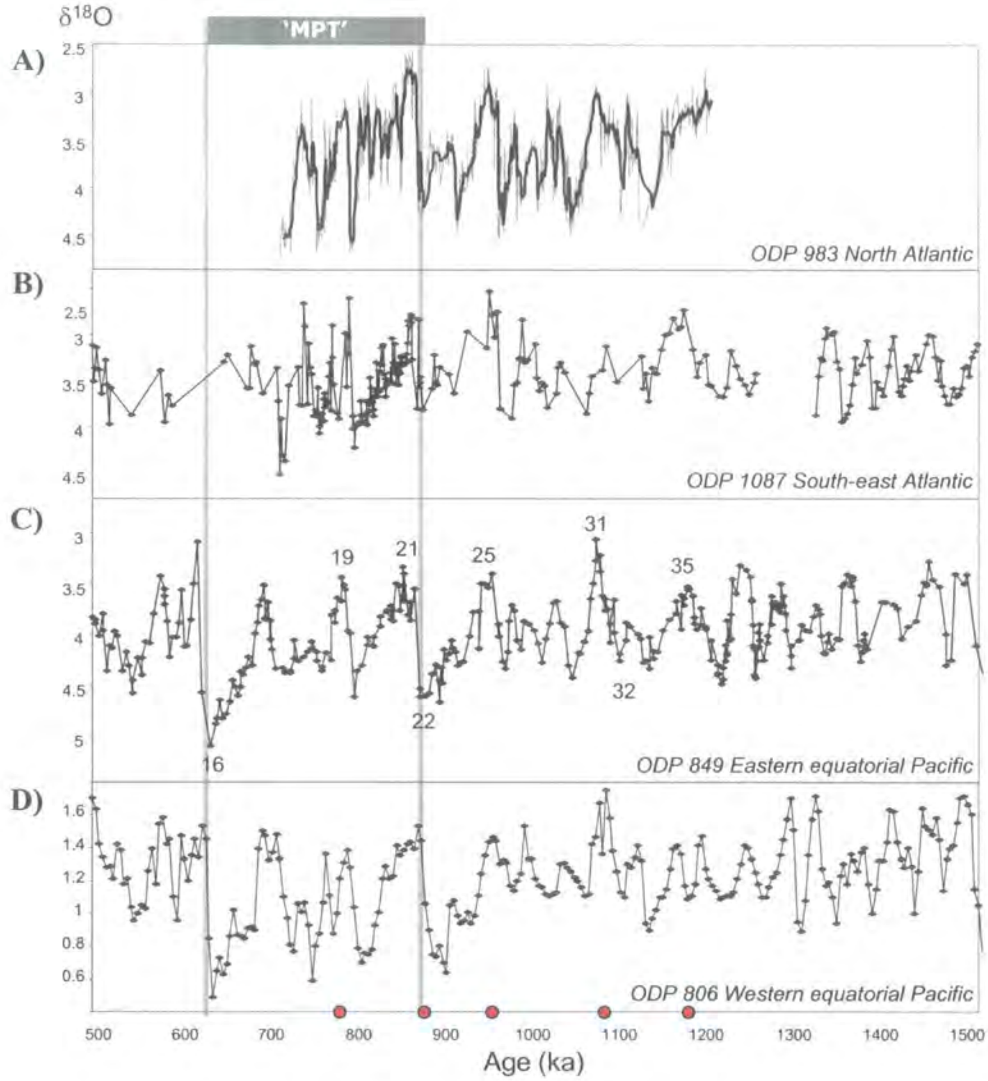

Figure 1-12 Mid-Pleistocene oxygen isotope records from all four cores analysed in this thesis. Selected oxygen isotope stages marked in record C. Events used to test the precision of the age models are marked by red dots on the x-axis, as described in Table 1-3. The mid-Pleistocene climate transition as defined by Mudelsee and Schulz (1997) marked as 'MPT'. (A) ODP 983C (Data from H.F.Kleiven, 2000); (B) ODP 1087A (Data from C. Pierre, pers.comm.); (C) ODP 849D (Data from Mix et al., 1995); (D) Composite $\delta^{18}O$ record from ODP 806B and 805C (Data from Berger et al., 1993a,b). A coring gap in ODP 806B between 755-785 ka inclusive is bridged using samples from ODP 805C following the age model of Berger et al. (1993a,b).

correlated with calculated insolation variations, usually summer insolation at 65°N (e.g. Imbrie et al., 1984; Martinson et al., 1987; Shackleton et al., 1990). This timescale can be applied globally, due to the geographically consistent recording of global ice volume by benthic foraminifer $\delta^{18}O$ (Lowe and Walker, 1994).

The $\delta^{18}O$ records used to generate the age models applied here analysed benthic foraminifera *Cibicidoides wuellerstorfi* at ODP 983C (Channell and Kleiven, 2000), ODP 1087A (C.Pierre, pers.comm.) and ODP 849C (Mix et al., 1995). At ODP 806B however, the stratigraphy was developed using planktic foraminifera $\delta^{18}O$ (*Globigerinoides sacculifer* and *Pulleniatina obliquiloculata*; Berger *et al.* 1993a,b). However, the minimal seasonality (in SST and salinity) experienced by the West Pacific Warm Pool led Berger et al. (1993a,b) to propose that over 75% of the planktic $\delta^{18}O$ variation at this site could be attributed to global ice volume variations.

Figure 1.12 shows that a good correlation exists between the benthic $\delta^{18}O$ records for the four cores analysed here. This can be tested further by comparing the dates of globally synchronous palaeomagnetic reversals using the stratigraphies for each core, for example using the Brunhes-Matuyama palaeomagnetic reversal event, conventionally dated at around 780 ka BP (Shackleton et al., 1990). Table 1-3 reveals excellent correlation between the dating of the Brunhes-Matuyama event between ODP 983C and ODP 806B. Problems encountered in detecting palaeomagnetic reversals at ODP 849 (Mayer et al., 1991) prevents a comparison of the timing of this event between all four cores. Interpretation of the palaeomagnetic record at ODP 1087A was also problematic during Shipboard analyses (Wefer et al., 1998). The Brunhes-Matuyama event was

Table 1-3 Comparison of a selection of marine isotope stages (MIS) and the Brunhes-Matuyama palaeomagnetic reversal event assigned using the $\delta^{18}O$ age models shown in Figure 1.12 to test the relative precision of the age models between cores. Palaeomagnetic ages as published by Channell and Kleiven (2000) for ODP 983C, and Berger et al. (1994) for ODP 806B.

Event	ODP 983C	ODP 1087A	ODP 849D	ODP 806B	Range of ages obtained (kyr)
Brunhes/Matuyama	775		N/A	780	
MIS 22	868.06	867.18	869.88	884	15.94
MIS 25	956.25	956.83	954	952	4.25
MIS 31	1069.8	1079.41	1068.5	1080	11.5
MIS 35	1176.6	1167.81	1170.95	1160	16.6

placed between 27 and 39 mbsf (Wefer et al., 1998), which results in an age range based on the $\delta^{18}O$ stratigraphy (C.Pierre, pers.comm.) of 900-1380 ka. The lower depth conflicts with the biostratigraphy, which places 39 mbsf as older than 1250 ka (Wefer et al., 1998), however the upper age of 900 ka for the Brunhes-Matuyama boundary is still some 120 ka greater than that of the two Pacific sites. Comparison of palaeomagnetic reversals between the four sites analysed here has therefore proved to be challenging. An alternative test of the precision of the age assignments is to select and date a series of climate events using the oxygen-isotope stratigraphies for each core. Interglacial and glacial maxima, as recorded by benthic $\delta^{18}O$ were chosen, which are defined by short intervals of high or low ice volume (shown in Figure 1.12). The results in Table 1.3 demonstrate that at some intervals errors in the age assignment were up to 16-kyr, although this may be due to an erroneous value in only one core (e.g. the age for MIS 22 at ODP 806B is ca. 15-kyr greater than the other three). These errors may result from variable sampling resolution and sedimentation rates between cores, and to possible differences in the tuning method between each age model formation. Identification of potential leads and lags between the palaeoclimate records here should therefore be undertaken bearing in mind the correlations between the benthic $\delta^{18}O$ records. Where an event in one core leads or lags another, the time offset must exceed the potential error in age assignment for that interval to be considered significant.

Attenuation of palaeoclimate signals may occur due to the action of bioturbation, which mixes the uppermost layers of sediments and results in a 'blurring' of time-horizons. Bioturbation typically affects sediments to a depth of c.5-20 cm (Patience and Kroon, 1991; Mix et al., 1995). This smoothing effect is greatest in fine sediments, which experience deeper bioturbation (Bard, 2001b). Moderate bioturbation was identified in all four cores analysed here (Kroenke et al., 1991; Mayer et al., 1992; Jansen et al., 1996; Wefer et al., 1998). Assuming that bioturbation affected surface sediments to a depth of 10 cm, the sedimentation rates (Table 1.1) at each site suggest that bioturbation will have smoothed the palaeoclimate signals over a period of up to 5-kyr for ODP 806, 849 and 1087 and <1-kyr for ODP 983.

1.6.3 Proxies

The longest direct measurement of any climate variable is the ice-core record of pCO_2 and pCH_4 variations from the Vostok ice core in Antarctica, which extends back to ca.

420 ka (Petit et al., 1999). Reconstruction of past environmental and climatic change therefore requires the analysis of indirect, or *proxy* records. A series of proxies are analysed in this thesis to achieve the objectives outlined above, including a number of *biomarker* proxy records. Biological marker compounds ('biomarkers') are organic compounds synthesised by specific source organisms (Rosell-Melé, 2000). Their presence within sedimentary sequences provide powerful tools in reconstructing past biological activity and its environmental controls. The biomarkers analysed here are the alkenones, chlorins and porphyrins. These results are supported by analysis of coccoliths, sediment particle size, and oxygen isotope ratios in benthic foraminifera carbonate ($\delta^{18}O$).

1.6.3.1 Sea surface temperature

The modern surface ocean circulation patterns of the Atlantic and equatorial Pacific systems can be identified in SST distributions (Figures 1.8-1.10). SSTs at ODP 983C record changes in the strength of the North Atlantic Current, and at ODP 1087A SSTs record the relative influence of Agulhas waters to the South-east Atlantic. In the equatorial Pacific, SSTs from ODP 849C and ODP 806B represent changes in the eastern cold-tongue and western warm pool respectively. SSTs at each core have been reconstructed here through application of the alkenone palaeothermometers, the U^K_{37} and U^K_{37}' indices. This analysis was performed using Gas Chromatography (GC) on the organic carbon contained within the marine sediments (Chapter 2).

Long-chain C_{37} to C_{39} ketones, or alkenones, are biomarkers synthesized by some members of the *Prymnesiophyceae* class of algae, including the coccolithophores (Volkman et al., 1980; Marlowe, 1984). The temperature dependent property of the alkenones is the relative number of unsaturations (the number of carbon-carbon double bonds) within the molecules. This property could be expressed in a variety of ways, although these mathematical expressions are empirical and have no biological or theoretical basis. The U^K_{37} and U^K_{37}' indices have been chosen to express the degree of <u>u</u>nsaturation within long-chain <u>k</u>etones (alkenones) with <u>37</u> carbon atoms:

$$\mathbf{U^K_{37} = [C_{37:2}] - [C_{37:4}] \,/\, [C_{37:2} + C_{37:3} + C_{37:4}]} \qquad \mathbf{(1\text{-}1)}$$

Where $[C_{x:y}]$ represents the abundance of an alkenone with x carbon atoms (C) in the chain, and y carbon double bonds within that chain (Brassell et al., 1986). Unlike its counterparts, the $C_{37:4}$ component is not ubiquitous in sediments. As a result, the simplified index U^K_{37}' is often reported, which contains no $C_{37:4}$ (Brassell et al., 1986; Prahl and Wakeham, 1987):

$$\mathbf{U^K_{37}' = [C_{37:2}] / [C_{37:2} + C_{37:3}] \qquad (1\text{-}2)}$$

Initial cultures of the most abundant coccolithophore in the modern ocean, *Emiliania huxleyi* (Okada and Honjo, 1973; Okada and McIntyre, 1977) in combination with field data, highlighted the strong correlation between the relative abundances of the C_{37} alkenones, usually expressed as the U^K_{37} or U^K_{37}' indices, and growth temperatures (Marlowe, 1984; Prahl and Wakeham, 1987; Prahl et al., 1988). This relationship was confirmed by the comparison of surface sediment U^K_{37}' values covering the global ocean between 60°N and 60°S to overlying annual mean SSTs undertaken by Müller *et al.* (1998):

$$\mathbf{U^K_{37}' = 0.033T + 0.044 \qquad (r^2 = 0.958) \qquad (1\text{-}3)}$$

The U^K_{37}' index is therefore considered to provide an estimation of annual mean SSTs at the ocean surface. The close correlation of U^K_{37}' to mean annual SSTs demonstrated in regression equation 1-3 may be due to the 'averaging' of seasonal variability in alkenone production in surface sediments, thus producing an average annual SST signal within sediments. The regression equation 1-3 covers all major biogeographical zones in the global ocean, thus demonstrating that the U^K_{37}'-SST relationship is not dependent upon *E.huxleyi*, the dominant species in many modern marine environments (Okada and Honjo, 1973; Okada and McIntyre, 1977). A similar response to temperature change by other Prymnesiophytes is particularly important for sites where *E.huxleyi* is not the dominant species, and for those sedimentary archives that pre-date the emergence of *E.huxleyi* ca. 260 ka (McIntyre, 1970). As it accounts for seasonal and species-related variations in alkenone production, the application of the global core-top calibration therefore avoids a number of the issues that may account for the variance in the calibrations derived from coccolithophore cultures (e.g. Prahl and Wakeham, 1987; Prahl et al., 1988; Volkman et al., 1995; Sawada et al., 1996; Conte et al., 1998), or water column particulates (e.g. Sikes et al., 1997; Conte et al., 2001). It should be noted that there is some scatter within the Müller *et al.* (1998) calibration of equation 1-3 (r^2 = 0.958). Comparable deviations in U^K_{37}'-SST correlations were observed when culture experiments of *E.huxleyi* were subjected to nutrient and light stress (Prahl et al., 2004). Further research is required to determine the impact that these physiological controls may exert upon the estimation of SSTs using the U^{K}_{37}' proxy, which may differ between different oceanographic regimes and their corresponding environmental controls over alkenone synthesis (Prahl et al., 2004).

U^{K}_{37}' has been used to reconstruct palaeo-SSTs at a variety of temporal and spatial scales (see reviews by Eglinton et al., 2001 and; Schneider, 2001). The global application of the proxy was demonstrated by the summary of LGM SSTs across the surface ocean by the TEMPUS project (Rosell-Melé et al., 1998a and references therein) and later by Rosell-Melé *et al.* (2004). The potential for U^{K}_{37}' to reconstruct SSTs beyond the Quaternary has also been demonstrated with records extending into the Pliocene (Haug, 1996; Herbert and Schuffer, 1998; Marlow et al., 2000). Reasonable agreement is generally reported between SSTs based on U^{K}_{37}' values, and other proxies including faunal SST estimates and reconstructions based on Mg/Ca ratios in planktic foraminifera (see review by Bard, 2001a). Where differences have been reported, these have been attributed to different ecological factors influencing the temperature signal, including seasonality and depth of production in the water column.

Application of U^{K}_{37}' to the mid-Pleistocene sediments of the four cores analysed here raises a number of issues for SST reconstructions:

1) the robustness of the U^{K}_{37}'-SST relationship through the mid-Pleistocene;
2) application of alkenone palaeothermometry to high latitude sites;
3) SST calibrations for U^{K}_{37}' in tropical waters.

Application of the U^{K}_{37}' index to mid-Pleistocene climate change

The U^{K}_{37}' index has been shown to be robust to degradation processes. These include passage through the food chain and the water column, and during early sedimentary diagenesis, which may account for a loss of >99% of the organic carbon synthesised in the surface ocean before deposition in surface sediments (e.g. Prahl et al., 1989; Conte et al., 1992; Prahl et al., 1993; Grice et al., 1998; Prahl et al., 2001; Prahl et al., 2003). Concern has been expressed that selective degradation of the $C_{37:3}$ alkenone relative to the $C_{37:2}$ alkenone, due to the former's additional unsaturation (double bond) and thus point of weakness to processes including oxidation, may post-depositionally bias U^{K}_{37}' records over millions of years toward warmer SSTs. Through simulated chemical degradation experiments, Marlow (2001) showed that post-depositional diagenesis of organic carbon exerted minimal influence over the U^{K}_{37}' value over the last 5 Ma. In Miocene sediments, Prahl et al. (2003) predicted U^{K}_{37}' values due to oxidation of organic carbon in Miocene sediments, but found that the observed values were not consistent with the predictions. This apparent long-term stability demonstrates the potential of the U^{K}_{37}' index in reconstructing long time-series of climate change, given the identification of alkenones in sediments back to 45 Ma (Farrimond et al., 1986), and more recently to ca. 120 Ma (Brassell et al., 2004).

Reconstructing SSTs using U^{K}_{37}' prior to the emergence of *E.huxleyi* near 260 ka (Thierstein et al., 1977) relies upon the assumption that fossil alkenone-synthesisers respond to changes in growth temperatures in a similar manner to those of the present day. Combined analyses of coccolithophore assemblages and alkenones from sediments in the south-east and north-east Atlantic suggest that this assumption is correct for the last 400 kyr (Müller et al., 1997; Weaver et al., 1999b; Villanueva et al., 2002). Changes to the coccolithophore assemblages occurred with no detectable impact on U^{K}_{37}' values, and vice versa. The assemblages also tended to be dominated by species of *Gephyrocapsa*, which are abundant in the modern ocean. By comparing the relative abundances of the C_{37} and C_{38} alkenones, Müller *et al.* (1997) showed that the alkenones had similar biogeochemical properties to those showing strong SST sensitivity at the present day. These results support the application of the modern U^{K}_{37}'-SST calibration to late Pleistocene sediments.

The U^{K}_{37}'-SST relationship has not been tested during the early- and mid-Pleistocene, despite this interval being characterised by a series of zones dominated by a single species of coccolithophore ('acme zones', Weaver, 1993), and a number of coccolithophore extinction events marking the development of the modern coccolithophore assemblage (Table 1.2). To test this issue, the combined coccolith-alkenone approaches of methods of Müller *et al.* (1997), Weaver *et al.* (1999b) and Villanueva *et al.* (2002) were applied to the sediments of ODP 1087. The results are presented in Chapter 3.

Application of alkenone palaeothermometry in the high latitudes

The absence or low abundance of the $C_{37:4}$ alkenone in many sediments has encouraged application of the U^{K}_{37}' index for SST reconstructions. $C_{37:4}$ can be found in high abundances in the high latitudes of both hemispheres (e.g. Sikes et al., 1997; Rosell-Melé et al., 1998b; Sicre et al., 2002; Sikes and Sicre, 2002; Bendle, 2003). In the northern North Atlantic and the Nordic Seas, high abundances of $C_{37:4}$ (>5% of total C_{37} alkenones) are associated with an increase in the scatter between U^{K}_{37}' and surface sediments and overlying SSTs (Rosell-Melé, 1998; Bendle, 2003). This reduction in the temperature dependence of U^{K}_{37}' occurs despite the absence of $C_{37:4}$ from the U^{K}_{37}' equation. Under these circumstances U^{K}_{37} provides a more reliable SST estimation (Rosell-Melé, 1998; Bendle, 2003). This is demonstrated by the calibration of U^{K}_{37} to summer SSTs from North Atlantic core-tops (Rosell-Melé et al., 1995b):

$$\mathbf{SST = (U^{K}_{37} - 0.093) / 0.030 \qquad r^2 = 0.979 \qquad (1\text{-}4)}$$

In response to this issue, all SSTs from ODP 983C were estimated using U^{K}_{37} values and the calibration in equation 1-4.

In the Southern Ocean, $C_{37:4}$ shows poor relationships to temperature and salinity (Sikes et al., 1997). High abundances (up to 40%) occur at a wide range of SSTs (up to 18°C). In contrast to the North Atlantic where U^{K}_{37}' values scatter with high $C_{37:4}$ abundance, great scatter to the U^{K}_{37}-SST relationship at low SSTs is introduced with increasing values of $\%C_{37:4}$ (Sikes et al., 1997). As a result, the U^{K}_{37}' index provides a more reliable SST estimation in the southern high latitudes than U^{K}_{37} (Sikes et al., 1997). SSTs were estimated from ODP 1087 sediments using U^{K}_{37}' and the calibration of Müller *et al.* (1998).

SST values from U^{K}_{37}' in the tropics

The highest SST that can be estimated using the Müller *et al.* (1998) calibration is 29.0°C ($U^{K}_{37}' = 1$). Slight variations to this calibration in surface sediments (Sonzogni et al., 1997) and water samples (Bentaleb et al., 2002) with high U^{K}_{37}' values highlights two concerns: the analytical precision of determining U^{K}_{37}' at high SSTs, and potential non-linearity in the calibration of these values to SSTs. As U^{K}_{37}' approaches unity, the accurate determination of very low $C_{37:3}$ abundances in the presence of very high concentrations of $C_{37:2}$ becomes increasingly difficult (Pelejero and Calvo, 2003). However, U^{K}_{37}' values close to 1 have been attained from surface sediments, water column particulates, and in palaeotemperature reconstructions (e.g. Prahl and Wakeham, 1987; Sonzogni et al., 1997; Pelejero et al., 1999; Rühlemann et al., 1999; Pelejero and Calvo, 2003 and references therein). The absence of $C_{37:3}$ has often been reported as $U^K_{37}' = 1$, but Pelejero and Calvo (2003) argue that these samples should instead be presented as '$C_{37:3}$ undetected', with no U^K_{37}' value assigned. They demonstrate that by excluding U^K_{37}' values of 1 from the data set of Bentaleb *et al.* (2002), the latter SST calibration no longer deviates from the Müller *et al.* (1998) calibration above 26.4°C.

Slight variations to the slopes of published U^K_{37}'-SST calibrations results in variation to the calculated SST maxima that can be generated by U^K_{37}', although 29.0°C appears the most feasible upper limit (Pelejero and Calvo, 2003). This SST corresponds to the modern annual SSTs experienced in the WPWP at the location of ODP 806B (Conkright et al., 2002). SSTs exceeding 29°C in the region during the late Pleistocene have been reconstructed using Mg/Ca and Sr/Ca analyses of carbonates (McCulloch et al., 1999; e.g. Lea et al., 2000; Stott et al., 2002; Visser et al., 2003). As a result, the U^K_{37}' SST record from ODP 806 is not expected to record interglacial SSTs, but should instead produce a record of SST trends during cooler intervals. To increase the precision of U^K_{37}' estimates at ODP 806, a selection of samples was analysed by Gas Chromatography-Chemical Ionisation Mass Spectrometry (GC-CI-MS), which has been shown to be more sensitive to low concentrations of alkenones than the Gas Chromatography-Flame Ionisation Detection (GC-FID) method used for the bulk of alkenone analyses in this thesis (Rosell-Melé et al., 1995a).

1.6.3.2 Water Mass Domains

The $C_{37:4}$ alkenone represents the 'cold' end-member of the C_{37} alkenones, increasing in abundance at low SSTs. In the previous section, issues surrounding application of U^K_{37} or U^K_{37}' in the presence of high abundances (>5%) of $C_{37:4}$ in the North Atlantic were introduced. High abundances of the $C_{37:4}$ alkenone in the North Atlantic generally correlates to cold and low salinity waters (Rosell-Melé, 1998; Rosell-Melé et al., 2002; Bendle, 2003). However, scatter in the relationship between the abundance of $C_{37:4}$ relative to the other C_{37} alkenones ($\%C_{37:4}$) and sea-surface salinity prevents the application of $\%C_{37:4}$ as a palaeo-salinity proxy (Bendle, 2003). A better correlation has been achieved when relating $C_{37:4}$ abundance to the distinct surface water domains that characterise the Nordic Seas, shown on Figure 1.8 and described in detail by Swift

(1986) and Hansen and Østerhus (2000). $C_{37:4}$ abundances exceeding 5% have been correlated to the presence of Arctic or Polar Waters, i.e. those with at least seasonal sea-ice cover (Rosell-Melé et al., 1998b; Bendle, 2003). This interpretation is applied to the sediments of ODP 983, where high $\%C_{37:4}$ values are used as a proxy for the presence of Arctic Waters over the site due to an equatorward migration of the Arctic Front.

1.6.3.3 Export productivity

The strength of the biological carbon pump can be determined through analysis of the abundance of organic carbon within marine sediments. High abundances represent high levels of export primary productivity or good preservation during transport through the water column, or both: i.e. the operation of a strong biological carbon pump (Section 1.1.2). The strength of the biological carbon pump during the mid-Pleistocene will be determined through analysis of two organic compounds: the chlorins and alkenones. These compounds are biomarkers found in marine sediments that can be traced to production in the surface ocean by marine phytoplankton.

The concentration of the photosynthetic pigment chlorophyll in surface waters reflects levels of primary productivity (e.g. Figures 1.8-1.10), because chlorophyll is necessary for photosynthesis to take place (Harris and Maxwell, 1995). Chlorophyll is rapidly degraded after production (e.g. Louda *et al.*, 1998). As a result, its diagenetic transformation products, chlorins, are analysed in sediments instead (Harris et al., 1996). Good correlations have been demonstrated between chlorin abundances in modern sediments and productivity patterns in overlying surface waters (e.g. Higginson, 1999; Shankle et al., 2002), and between abundances down-core and other palaeo-productivity proxies (Summerhayes et al., 1995; e.g. Harris et al., 1996).

Chlorins are biomarkers produced by all phytoplankton. In contrast, alkenones are synthesised by a restricted group of phytoplankton, the *Prymnesiophyceae*, which includes the coccolithophores. Coccolithophores produce calcium carbonate plates (coccoliths) that surround the alkenone-synthesising algal cell. They have been proposed as the main producers of calcium carbonate in the open ocean (e.g. Archer et al., 2000). Coccolithophore productivity may therefore play an important role in the cycling of both carbonate and organic carbon, which may both impact upon pCO_2 (e.g. Archer et al., 2000; Stoll et al., 2002).

The abundance of chlorins and alkenones in marine sediments, as with all organic carbon, does not simply represent variations in their production within surface waters. These biomarkers also degrade in the water column and sediments (e.g. Conte et al., 1992; Prahl et al., 2001; Shankle et al., 2002). This prevents use of their sedimentary abundance to quantitatively reconstruct palaeo-productivity. However, as their abundance reflects the balance between productivity and preservation, chlorins and alkenones can be used to assess changes in the relative strength of the biological carbon pump. Significantly, it is this system (rather than biological productivity alone) that acts to draw down atmospheric CO_2.

Alkenone abundances are generated as part of the GC determination of U^{K}_{37}' and $\%C_{37:4}$. The relative abundance of chlorins is calculated in this thesis using ultraviolet-visible (UV-Vis) spectrophotometry (Rosell-Melé, 1994), which records the absorbance of each solvent extract in the range 350-850 nm. Comparison of the relative absorbance in the Soret (S) band, between 360-420 nm, to the Satellite (I) band, close to 665 nm, also allows an assessment of the relative contribution of chlorins produced by marine phytoplankton to the allochthonous inputs of older or terrigenous-derived photosynthetic pigments. By dividing the magnitude of absorbance at 410 nm by that at 665 nm, the 'S/I' ratio can be generated for each sediment sample. In the North Atlantic, Rosell-Melé and Koç (1997) and Rosell-Melé et al. (1997) revealed that sediment horizons dominated by iceberg-rafted detritus (the 'Heinrich layers') had S/I ratios >10. This contrasted with S/I values <5 in the intervening sediments, which were associated with the presence of chlorins. High S/I values were attributed to the presence of the longer-term diagenetic products of chlorins, termed *porphyrins*. Porphyrins have not been found *in situ* in sediments younger than the Pliocene (Keely et al., 1994). Their appearance in marine sediments in the North Atlantic was attributed to the transport of terrigenous sediments by iceberg rafting of glacially eroded sediments from the circum-Atlantic ice masses (Rosell-Melé and Koç, 1997; Rosell-Melé et al., 1997). In the Northern Benguela region, Durham *et al.* (2001) found high S/I values during interglacial intervals. These correlated with magnetic susceptibility values indicative of terrestrial inputs, and were attributed to interglacial increases in fluvial transport of porphyrins by the Congo River (Durham et al., 2001).

To account for the influence of variations in sedimentation rates or sediment properties over organic carbon accumulation in sedimentary sequences, all biomarker abundances are corrected for the sediment *mass accumulation rates* (MARs). Biomarker accumulation rate (AR) is the product of the biomarker abundance and the bulk MAR of the sediment (Emeis et al., 1995). Bulk sediment MARs are calculated using linear sedimentation rates and the dry bulk density of the sediment (Emeis et al., 1995). The calculations that were undertaken to generate biomarker accumulation rates for each of the sediment cores analysed in this thesis are described in Chapter 2.

A complicating factor in examining sediment accumulation rates is the potential influence of erosion and redistribution of surface sediments after deposition. Organic carbon tends to be found in fine-grained sediments (e.g. Mayer, 1994), and is therefore sensitive to the erosive power of high-energy bottom-water currents. Redistribution of organic-rich sediments by undercurrents flowing along the outer continental shelf has been identified under the Benguela upwelling system (Mollenhauer et al., 2002; Sachs and Anderson, 2003), and may account for the complete absence of a Pleistocene organic carbon record from ODP 1086 drilled in the region (Berger et al., 2002). Resuspension of interglacial organic carbon from exposed continental shelves during the sea-level fall of the last glacial maximum was proposed to account for a significant fraction of increased glacial organic carbon contents on the Benguela shelf (Summerhayes et al., 1995). Redistribution of organic carbon has also been proposed to account for the difference in the ages of foraminifers and alkenones within the same sediment horizons in these high-energy environments (Ohkouchi et al., 2002; Mollenhauer et al., 2003). The impacts of sediment redistribution on mass accumulation rates can be accounted for by application of the ^{230}Th normalisation method (see review by Francois et al., 2004). This procedure is based on the principle that the flux to sediments of ^{230}Th scavenged from seawater is constant, and can be calculated from known rates of production of ^{230}Th. Variations to the ^{230}Th content of sediments can therefore be used to normalise mass accumulation rates to take into account any sediment redistribution that may have affected the core site (see review by Francois et al., 2004). The absence of ^{230}Th data for the four cores analysed here prevented this normalisation procedure from being applied. However, the potential impacts of sediment redistribution processes on the biomarker accumulation rates for each core are examined in Chapter 3.

1.6.3.4 Coccolith stratigraphy

Coccoliths are well-preserved in marine sediments found above the carbonate compensation depth (CCD) throughout the ocean. They constitute a significant fraction of biogenic sediments in all four cores studied here (Kroenke et al., 1991; Mayer et al., 1992; Jansen et al., 1996; Wefer et al., 1998). Although small in size (found in the <32 μm sediment fraction), the geometry of coccoliths can be used for identification to species level.

Analysis of coccolith abundances and species assemblages performs two functions in this thesis. First, the species assemblage is used to assess changes to the type of alkenone-synthesising species during the mid-Pleistocene. This allows evaluation of the potential role played by changes to the coccolithophore assemblage in distorting U^{K}_{37}' values and the subsequent SST reconstructions. This analysis was performed following the approach outlined above (following the methods of Müller et al., 1997; Weaver et al., 1999b; Villanueva et al., 2002). Second, it has been shown that coccolith abundance in marine sediments may parallel alkenone abundance (e.g. Weaver et al., 1999b). Under these circumstances, production rather than preservation may account for relative changes in alkenone abundance. Coccolith abundance may therefore aid interpretation of the controls over variations to biomarker accumulation rates.

1.6.3.5 Aeolian inputs

The particle size distributions of non-biogenic marine sediments can provide insight into variations in the flux of wind-transported material to open-ocean settings. The amount of aeolian detritus within marine sediments is determined by two inter-related factors: the intensity of the wind (controlled by temperature and pressure gradients in the atmosphere), and the availability of sediment in the hinterland (determined by aridity, Wefer et al., 1999). Coarsening of sediment grain size, in the absence of fluvial and iceberg rafting influences, correlates with intensification of aeolian inputs (Janecek and Rea, 1985; Hovan, 1995; Zhao et al., 2000). By analysing the fine fraction (<30 μm) of sediments in a latitudinal transect, including ODP 849C, Hovan (1995) was able to detect shifts in the position of the ITCZ in the eastern Pacific since 8 Ma. The zone of low wind-strength associated with the ITCZ could be identified by small grain sizes, between the more intense circulation (and higher grain-sizes) of the South-east and North-east Trade Winds (Hovan, 1995). This approach was applied to a selection of samples from two cores, ODP 1087A and ODP 849D. The strength of upwelling at ODP 849D is closely linked to the strength and position of the South-east Trade Winds (Section 1.4.2.1). Upwelling in the Benguela region is also determined by the strength and position of the same Trade Wind system (Section 1.4.1.2). However, the major upwelling cells lie to the north of ODP 1087A, and thus unless there is a southward migration of the South-east Trade Winds and therefore upwelling to the site of ODP 1087A the particle size data will not record Trade Wind strength. Rather, the intensity of the westerlies which are associated with the ACC, during the mid-Pleistocene may be recorded by changing aeolian flux to the site to ODP 1087A. Samples in both cores were selected during glacial minima in U^{K}_{37}'-SSTs, to determine whether the mid-Pleistocene ice volume increase impacted upon atmospheric circulation, and to evaluate the role that this may have played in any ocean circulation changes observed in these two cores.

1.7 Summary

The MPT marks a change in the response of the climate system to the external forcing of insolation variations. This is most clearly represented by the emergence and subsequent dominance of glacial-interglacial oscillations with a period of ca. 100-kyr. The roles played by surface ocean circulation and the export of organic carbon from the surface ocean by the biological carbon pump in the mid-Pleistocene climate changes are unclear, despite their importance for the transport of heat and moisture within the climate system and to carbon cycling and concentrations of atmospheric carbon dioxide (CO_2).

These issues are addressed in the following chapters by the reconstruction of a series proxy records for SST and organic carbon export during the early- and mid-Pleistocene, from the Atlantic and equatorial Pacific Oceans. The analytical methods employed to achieve these objectives are outlined first (Chapter 2) followed by a presentation of the results gained from each core (Chapter 3) and an evaluation of the validity of the U^{K}_{37}' index for reconstructing SSTs in sediments pre-dating the late Pleistocene (Chapter 4). By comparing the SST and biomarker accumulation rate records between all four cores, the roles played by changes to surface ocean circulation and global temperatures (Chapter 5), the biological carbon pump (Chapter 6), and the tropical Pacific circulation system (Chapter 7) in mid-Pleistocene climate change are discussed. Finally, the implications of the results presented in this thesis, and outstanding issues for further work, are discussed in Chapter 8.

2. Laboratory and Analytical Methods

2.1 Introduction

This chapter describes the laboratory methods employed in this thesis. These may be divided into two principal groups of analyses: biomarkers (organic geochemistry) and coccoliths (carbonates). The same procedures were applied to each sediment core, except where stated. The procedures for the analysis of sediment particle size, the development of age models for each site, and the time-series analysis performed are also described.

2.2 Biomarker analysis

2.2.1 Preparation of materials and chemicals

2.2.1.1 Glassware

Reusable glassware was manually cleaned by rinsing with tap water to remove any residues, then soaked for 24 hours in 1% nitric acid solution. After rinsing with tap water, the glassware was soaked for 24 hours in 2% Decon 90® soap solution (Decon Laboratories Ltd., Hove, UK), rinsed in distilled water, dried in a heating cabinet, and then fired at 450°C for 12 hours. The latter stage was not undertaken for volumetric flasks and measuring cylinders, which were allowed to dry gently at room temperature. Disposable glassware (e.g. pasteur pipettes and vials) was fired at 450°C prior to use and discarded afterwards. All glassware was rinsed in dichloromethane (DCM) and allowed to dry immediately prior to use.

2.2.1.2 Reagents and solvents

The solvents and reagents used in the laboratory procedures described here are shown in Table 2-1. Reagent solutions were prepared using deionised water. Prior to use, non-absorbent cotton wool, and anhydrous sodium sulphate (Fisher Chemicals, certified for analysis) were cleaned overnight by soxhlet extraction using a 2:1 mixture of DCM and MeOH. Cotton wool was dried by gentle heating. The anhydrous sodium sulphate was heated to 120°C for 24 hours, then stored in a dessiccator.

Table 2-1 Solvents and reagents employed in this thesis, with their abbreviated notations and analytical grade. All supplied by Fisher Chemicals, U.K.

Notation	Name	Grade
Solvents:		
DCM	Dichloromethane (Methylene chloride)	Residue analysis
MeOH	Methanol	Residue analysis
	Hexane	Residue analysis
	Acetone	Residue analysis
iso-octane	2,2,4-trimethylpentane	Residue analysis
Reagents:		
BSTFA	Bis(trimethylsilyl)trifluoracetamide	98%
	Anhydrous sodium sulphate	Certified® (87.99%)
	Nitric Acid	AnalaR® 69- 70.5%

2.2.1.3 Standards

Table 2-2 shows the synthetic standards used in this thesis and their abbreviations. All were dissolved in known quantities of *iso*-octane in glass volumetric flasks, and transferred to vials for storage. Parent solutions of the most commonly used standards (nC_{36}, nC_{32}, $nC_{19}O$) were initially prepared, with aliquots removed to make the weaker daughter solutions (those added to the sample) on an *ad hoc* basis. Synthetic standards of the $C_{37:3}$ and $C_{37:2}$ alkenones were also used. These standards were those synthesised by Rechka and Maxwell (1988).

Table 2-2 Standards used in the procedures described here, their notations and purities. All standards from Sigma-Aldrich (Gillingham, U.K.), except 2-nonadecanone (Fluka).

Notation	Name	Purity
$nC_{19}O$	2-nonadecanone	97%
nC_{32}	Dotriacontane	97%
nC_{36}	Hexatriacontane	98%
nC_{27}	Cholestane	98%
$nC_{27}O$	5α-cholestan-3one (Cholestanone)	98%
$nC_{27}OH$	Cholesterol	98%
$nC_{22}OH$	1-Docosanol	98%

A sediment standard was also produced to aid the development of instrumental procedures (spectrophotometry, and chromatography), and for assessing the degree of error associated with the alkenone analysis. This was generated using a mixture of marine sediments from the various core sites analysed in this thesis. Over 100 g of dry sediment was obtained. An aliquot of approximately 50 g was soxhlet-extracted overnight in DCM:MeOH (3:1). The extract was taken to dryness and frozen. This "sediment-standard" contained abundant alkenones and was rich in photosynthetic pigments. The remaining 50 g of sediment was used to test the repeatability of the extraction and clean-up procedures. This was accomplished by analysing a 1 g aliquot of this mixed sediment in each extraction batch. Finally, some of the extracted "sediment-standard" was fired at 850°C for 24 hours, to remove all traces of organic material. This was used as a "blank" of the analyses. Approximately 1 g of this extracted/fired sediment was analysed in each extraction batch. These "blanks" allowed the identification of any problems that may have occurred during the extraction and instrumental stages of the analysis.

2.2.1.4 Sample storage & preparation

The Ocean Drilling Program (ODP) undertook the sub-sampling of all cores in their core repositories, and posted them in cool boxes with ice packs to the laboratory. On arrival, samples were kept at <4°C and away from light.

Prior to biomarker analysis and extraction with organic solvents, water was eliminated from the sediment. Analytical tests were performed to assess the advantages of freeze-drying in comparison to drying sediment by heating in an oven. These two techniques are radically different. With freeze-drying, the sample is under vacuum and the drying occurs by sublimation. In contrast, using an oven the sample is in contact with air, and water is removed by evaporation.

Approximately 10 g of wet sediment was divided into 12 aliquots. Three were freeze-dried, and the remaining aliquots dried in batches of three at 30°C, 60°C and 90°C. Figure 2.1A shows that water removal by heating caused a loss of up to 26% of photosynthetic pigments from the mixed sediment standard when compared to freeze-drying. Increasing the oven temperature had a minimal impact on the losses of pigments from the sediment. For the C_{37} alkenones, moderate heating gave comparable results to freeze-drying (Figure 2.1A). At higher oven temperatures, the losses of alkenone increased, initially by a relatively small amount (~11% at 60°C), but increasing to almost 80% at 90°C. This is accompanied by an increase in the alkenone saturation index, U^{K}_{37}', so that as oven temperature increases so does the values of the index (Figure 2.1B). These results demonstrate that oxidation, which degrades organic carbon within the water column and sediments , may also reduce biomarker abundances when marine samples are air-dried. The faster removal of the pigments (Figure 2.1A) can be attributed to their more labile nature in comparison to the alkenones. The higher degree of unsaturation of the $C_{37:3}$ alkenone relative to $C_{37:2}$ makes it more sensitive to the

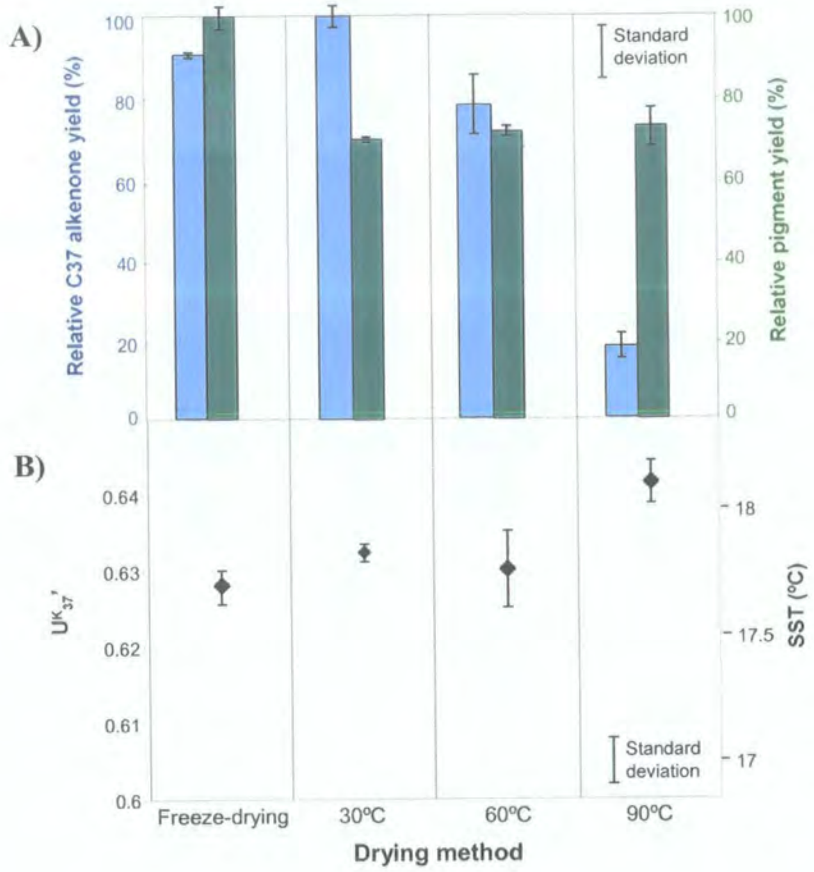

Figure 2-1 The impact of two methods of drying sediments, freeze-drying and oven heating, on biomarker abundances in marine sediments. X-axis indicates the drying method. (A) Impact on C37 alkenone abundance (blue) and photosynthetic pigment abundance (green). Abundances expressed as percentage of the maximum abundance for each data set; (B) Impact on U^K_{37}'.

oxidation process, which attacks the double bonds (Prahl et al., 1988; Hoefs et al., 1998). The increase in U^{K}_{37}' values may therefore also reflect oxidation. A number of analyses from cultured coccolithophore populations and within marine sediments have shown that U^{K}_{37}' remains relatively unaffected by oxidation however (e.g. Prahl et al., 1989; Prahl et al., 1993; Teece et al., 1998). The increase in U^{K}_{37}' at high oven temperatures may therefore also represent preferential removal of the $C_{37:3}$ alkenone due to its lower boiling point in comparison to $C_{37:2}$. The results in Figure 2.1 show that biomarker analyses should not be undertaken on sediment samples which have been air-dried for analysis by other proxy techniques (e.g. coccolith analyses, foraminiferal analyses).

Water was removed from all samples analysed in this thesis by freeze-drying using a cold-trap (Labconco Centrivap®) and vacuum system. The final step of preparation, homogenisation, was then undertaken using an agate pestle and mortar, which was rinsed in a DCM:MeOH mixture (3:1) and dried prior to manually grinding each sample.

2.2.2 Biomarker extraction

This thesis involved the analysis of large numbers of sediment samples which were relatively small in size (approximately 1-3 g). Sediments were solvent extracted following the microwave-assisted extraction (MAE) method of Kornilova and Rosell-Melé (2003). As MAE reduces the solvent volumes used and the overall extraction time in comparison to the more commonly employed sonication method (Kornilova and Rosell-Melé, 2003), it offered a more efficient extraction procedure. Appraisal of the MAE method for the analysis of pigments and alkenones was undertaken by comparing the results of multiple extractions of the mixed sediment standard described in Section 2.2.1.3 using MAE and sonication. The results support those of Kornilova and Rosell-Melé (2003)(2003), who found that MAE was more efficient in extracting alkenones and photosynthetic pigments with little impact on U^{K}_{37}' values (Figure 2-2).

Extractions were undertaken in batches containing 10 samples, 1 mixed sediment standard, and 1 'blank' (Section 2.2.1.3). Prior to the analysis of a new core, sediment from different sections were combined to form an homogenous mixture of 3-5 g of sediment. Aliquots of this mixed sediment of approximately 1 g were extracted and

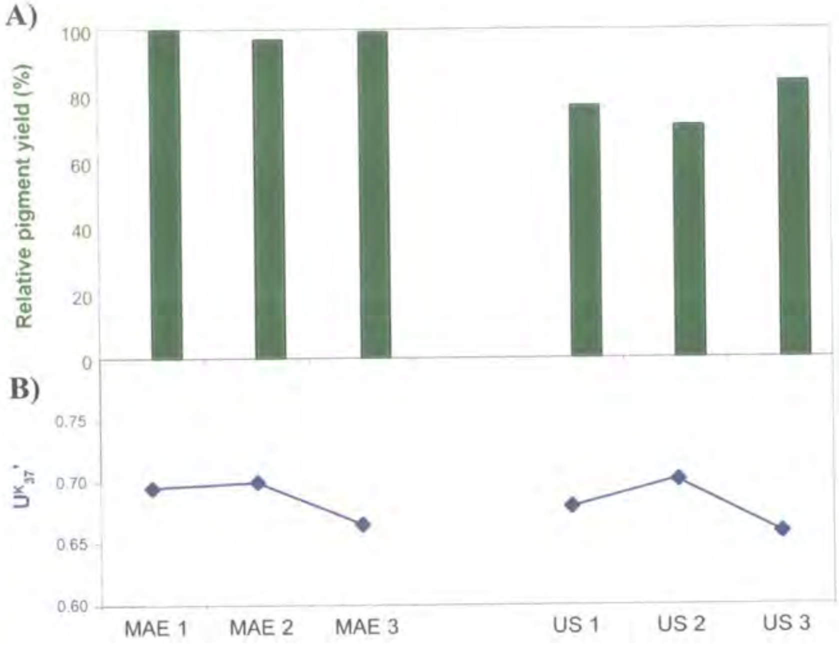

Figure 2-2 Comparison of two methods to extract biomarkers from sediments, using sonication and microwave-assisted extraction (MAE). Each experiment was repeated three times using aliquots of the same sediment. (A) Pigment recovery; (B) U^K_{37}'.

analysed to determine the approximate average alkenone concentration within the core. This data was used to optimise the required sediment volume to be extracted for a given core to maximise the accuracy of the U^{K}_{37} and U^{K}_{37}' measurements (Section 2.2.5.2). For the two Atlantic sites, approximately 1 g dry sediment was extracted. Lower alkenone abundances at the two Pacific sites required extraction of 2-3 g of sediment. However, for a number of Pacific core sections it was not possible to obtain more than 1 g of sediment from ODP as the required core intervals were devoid of sediment.

2.2.2.1 Microwave-assisted Extraction (MAE)

Aliquots of freeze-dried and homogenised sediment were weighed into 100 ml Teflon liners, with a known quantity of internal standard (C_{32} and/or $C_{19}O$), 10 ml DCM:MeOH (3:1), and magnetic stirrers. The liners were loaded into Greenchem pressure vessels, heated from room temperature to 70°C over 1.5 mins, held at 70°C for 5 mins, then allowed to cool. The cooling step took around 20-30 mins, with sample removal only after solvent temperature had fallen below 30°C (DCM b.p. 39-40°C, MeOH b.p. 64.7°C). The sediment-solvent mixture was rinsed into 12 ml Pyrex test tubes, centrifuged at 2500 rpm for 5 mins, and the supernatant decanted. The extract was then taken to dryness using the CentriVap Vacuum Concentrator® (Labconco).

Dried extracts were filtered through Pasteur pipettes plugged with extracted cotton wool and transferred into vials using DCM. The vials were taken to dryness under a flow of nitrogen, and stored in the freezer until further analysis.

2.2.3 Pigment analysis

Dry extracts were re-dissolved in acetone and an aliquot was injected into a Photodiode Array Detector or PDA (Dionex PDA-100) attached to a Dionex P580 Quaternary pump. The absorbance spectra were compared to those of standard pigments (Jeffrey et al., 1997) for the identification of major photosynthetic pigment classes (Figure 2.3). Quantification of absorbance at the 410 nm and 665 nm wavelengths was used as a proxy to measure total abundance of tetrapyrrolic pigments (i.e. chlorophylls and porphyrins; Chapter 1). Relative pigment abundances down-core were generated according to the following equation:

$$\mathbf{P\lambda = (A\lambda \times DF) / M} \qquad \textbf{(2-1)}$$

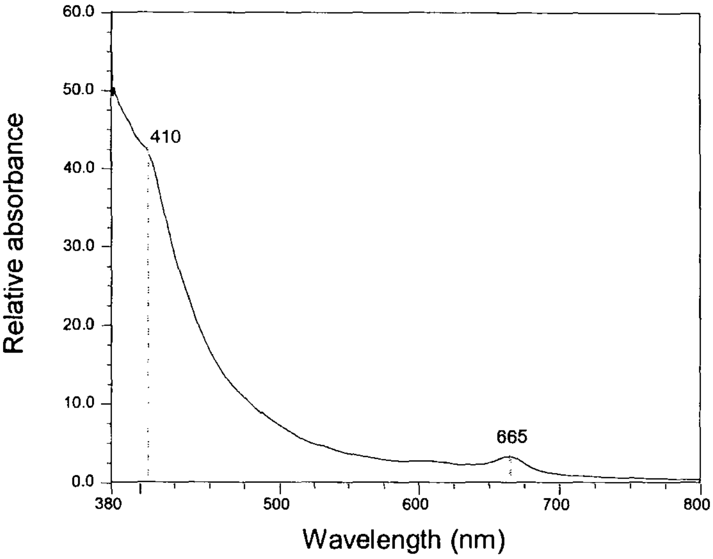

Figure 2-3 Representative UV-Vis absorbance spectrum, showing peak absorbance at 410 nm and 665 nm. Sample: ODP 983C-11H-3W, 135-137cm (ca. 902.5 ka).

Where Pλ = relative magnitude of absorbance for a given wavelength (λ), as 'area units'/g dry sediment; Aλ = integrated area for that wavelength; DF = dilution factor, defined as the volume of acetone used to dissolve the sample divided by the aliquot size injected; and M = mass (g) of dry sediment extracted.

Triplicate analysis was undertaken for each sample (including extraction standards and blanks). The stability of the PDA detector during and between sample batches was also monitored by multiple injections of the mixed sediment extract described in Section 2.2.1.3. Average reproducibility was determined to be around 11%. No significant drift was observed between periods of analysis.

Once samples had passed through the PDA, they were collected in Pyrex test-tubes by the Foxy™ Junior Fraction Collector. These were taken to dryness using the Centrivap rotary concentrator, and recombined with the total extract in the vials. Total extracts were dried under a stream of nitrogen and then stored in the freezer until further analysis.

2.2.4 Clean-up of lipid extracts: compound class fractionation

Total lipid extracts were cleaned to remove mineral particulates e.g. clays that may have been transferred into the supernatant during the decanting steps of extraction, compounds not amenable to GC analysis, and any potential co-elutants that may interfere with analysis of the alkenones e.g. alkyl alkenoates which are found in North Atlantic sites with the $C_{37:3}$ and $C_{37:2}$ alkenones (Rosell-Melé, 2000). Total lipid extracts were eluted with DCM through a Pasteur pipette plugged with cotton wool and anhydrous sodium sulphate to remove residual water. Filtered extracts were then taken to dryness under a stream of nitrogen, and stored in the freezer until fractionation into separate compound classes. This procedure was not undertaken for the two Pacific cores (ODP 806B and 849C,D), due to their overall low organic carbon contents. The fractionation method was adapted from Schulz et al. (2000). Fractionation was achieved using a High Performance Liquid Chromatograph or HPLC (Dionex P580 HPLC system), attached to a Foxy™ Junior Fraction Collector. Filtered extracts were dissolved in 120 µl hexane, drawn into a syringe and injected into a 100 µl sample loop. The sample loop was rinsed with hexane between each sample.

Each extract was fractionated using a Thermo Hypersil® column (50 × 4.6 mm) packed with Lichospher® Si100 5 µm silica, and a Thermo Hypersil® guard column. Solvent flow was maintained at 1 ml min^{-1}. The elution times (Table 2-3) were calculated by a series of tests using the mixed sediment standard described in Section 2.2.1.3., and a mixed solution of synthetic standards (dotriacontane, hexatriacontane, 2-nonadecanone, the $C_{37:2}$ and $C_{37:3}$ alkenones, 5α-cholestan-3-one, cholesterol and 1-docosanol; all with a concentration of c.100 ng/µl). The *n*-alkanes were collected in fraction 1, alkenones in fraction 2, and more polar compounds in fractions 3 and 4. The reproducibility of the

Table 2-3 Solvent volumes used for HPLC fractionation (flow rate: 1 ml min^{-1}). The standards eluted in each fraction from the mixed standard solution are also shown.

Fraction number: solvent used	**Solvent volume (elution time)**	**Standards eluted**
Fraction 1: 100% hexane	4.875 ml (4.875 min)	Dotriacontane Hexatriacontane
Fraction 2: hexane : DCM (85 % :15 %)	2.25 ml (2.25 min)	2-nonadecanone $C_{37:3}$ and $C_{37:2}$ alkenones
Fraction 3: 100% DCM	2.25 ml (2.25 min)	Cholestanone
Fraction 4: 100% Acetone	2.625 ml (2.625 min)	Cholesterol Docosanol
Total sample time	**12.000 min**	

HPLC procedure was determined through repeated fractionations of the mixed sediment standard and the mixed synthetic standard used in the method development. Sample recoveries generally exceeded 90%. Fractions were concentrated using the Centrivap rotary evaporator, and transferred to vials. Dry samples were stored in the freezer until further analysis by gas chromatography.

2.2.5 Gas Chromatographic analysis with Flame Ionisation Detector

2.2.5.1 Derivatisation

Immediately prior to analysis by gas chromatography (GC), polar compounds were derivatised using bis(trimethylsilyl)trifluoracetamide ('BSTFA'). To each dry extract 40 µl of BSTFA, 40 µl DCM, and a known concentration of standard used for monitoring GC performance (the 'GC standard', here $n\mathrm{C}_{36}$ hexatriacontane) were added. Samples were derivatised overnight at room temperature in a desiccator, then taken to dryness using a gentle stream of nitrogen.

2.2.5.2 Instrumental conditions

Total extracts and compound fractions of all samples were analysed using a Fisons 8000 series Gas Chromatograph (GC), fitted with a flame-ionisation detector (FID), and a split/split-less injector. The split opened 30 seconds after injection. The carrier gas was hydrogen (18 psi, 3 ml min^{-1}), generated using a Peak Scientific CFH200 Hydrogen Generator. The injector was held at 300°C, the detector at 320°C. Chromatographic separation of the analytes was achieved using a 30m SGE BP-1 capillary column (30 m length, 0.25 mm internal diameter, 0.25 µm film thickness). Following injection, the column was held at 60°C for 1 min, then increased at 20°C min^{-1} to 200°C. The temperature then continued to rise at 6°C min^{-1} until 295°C, where it was held for 30 mins. To ensure removal of all elutants from the column, oven temperature was then increased to 310°C, held for 2 mins, then allowed to cool back to 60°C.

All sample extracts were dissolved in *iso*-octane, and 1 µl aliquots injected either manually or by autosampler (AS800 autosampler). To minimise loss of sample from the Pacific cores during autosampler injections (the autosampler was programmed to discard the first 0.5 µl of sample to ensure the needle contained 100% sample), the Pacific extracts were dissolved in 40 µl *iso*-octane, with 2 µl aliquots injected.

2.2.5.3 Biomarker identification and quantification

Compound identification using GC-FID was achieved through comparison of the chromatographic relative retention times of target compounds with those of known standards. The principal compound groups analysed in this thesis, the long-chain alkenones and their related alkyl alkenoates (Tables 2-4 and 2-5) have distinctive patterns in the GC chromatograms (Figure 2-4). The identity of the alkenones was further confirmed by mass spectrometry (Section 2.2.6).

Compound quantification was achieved by integrating peak areas using the software system Chromeleon v6.20. Unsaturation indices were generated through comparison of integrated peak areas between different alkenones, for example:

$$U^{K}_{37} = [C_{37:2}] - [C_{37:4}] / [C_{37:2} + C_{37:3} + C_{37:4}] \qquad \textbf{(2-2)}$$

Where $[C_{x:y}]$ represents the abundance of an alkenone with x carbon atoms (C) in the chain, and y carbon double bonds within that chain (Brassell et al., 1986). A full list of the indices generated is shown in Table 2-4 below.

Table 2-4 Alkenone indices analysed in this thesis.

Index	**Formula**	**Reference**
K37	$[C_{37:2}Me] + [C_{37:3}Me] + [C_{37:4}Me]$	1
K38	$[C_{38:2}Me] + [C_{38:2}Et] + [C_{38:3}Me] + [C_{38:3}Et]$	1
U^{K}_{37}	$[C_{37:2}Me] - [C_{37:4}Me] / [C_{37:4}Me] + [C_{37:3}Me] + [C_{37:2}Me]$	2
$U^{K}_{37}{}'$	$[C_{37:2}Me] / [C_{37:3}Me] + [C_{37:2}Me]$	3
U^{K}_{38}	$[C_{38:2}Me] + [C_{38:2}Et] / [C_{38:2}Me] + [C_{38:2}Et] + [C_{38:3}Me] + [C_{38:3}Et]$	4
$U^{K}_{38}Et$	$[C_{38:2}Et] / [C_{38:2}Et] + [C_{38:3}Et]$	5
$U^{K}_{38}Me$	$[C_{38:2}Me] / [C_{38:2}Me] + [C_{38:3}Me]$	5
$\%C_{37:4}$	$[C_{37:4}Me] / K37$	6

References: 1 (Prahl et al., 1988); 2 (Brassell et al., 1986); 3 (Prahl and Wakeham, 1987); 4 (Rosell-Melé et al., 1994); 5 (Conte et al., 1998); 6 (Rosell-Melé, 1998).

Absolute biomarker concentrations were generated by comparison of integrated peak areas between the target compound(s) and the internal standard, using the formula:

$$\mathbf{BM = \frac{(IS / \{IS\}) \times \{BM\}}{M}} \qquad \textbf{(2-3)}$$

Where BM = abundance of the relevant biomarker per gram of dry sediment; IS = mass of internal standard added to sample; {IS} = integrated area of internal standard; {BM} = integrated area of the biomarker in question; M = dry weight of sediment extracted.

Table 2-5 Long chain alkenones and alkyl alkenoates in marine sediments found and monitored (✓) in this thesis. Me and Et refer to methyl or ethyl groups on the ketone chain respectively.

Designation	**IUPAC nomenclature**	**Shorthand notation**	**Ammonia-CI-MS pseudo-molecular ions m/z $[M + NH_4]^+$**	**Monitored**
Alkenones				
a	Heptatriaconta-8E,15E,22E,29E-tetraen-2-one	$C_{37:4}$Me	544	✓
b	heptatriaconta-8^{E},15E,22E-trien-2-one	$C_{37:3}$Me	546	✓
c	heptatriaconta-15E,22E-dien-2-one	$C_{37:2}$Me	548	✓
d	Octatriaconta-9E,16E,23E,30E-tetraen-3-one	$C_{38:4}$Et	558	✓
e	Octatriaconta-9E,16E,23E,30E-tetraen-2-one	$C_{38:4}$Me	558	✓
f	octatriaconta-9^{E},16E,23E-trien-3-one	$C_{38:3}$Et	560	✓
g	octatriaconta-9E,16E,23E-trien-2-one	$C_{38:3}$Me	560	✓
h	octatriaconta-16E,23E-dien-3-one	$C_{38:2}$Et	562	✓
i	octatriaconta-16E,23E-dien-2-one	$C_{38:2}$Me	562	✓
j	Nonatriaconta-10E,17E,24E,31E-tetraen-one	$C_{39:4}$	572	
k	nonatriaconta-10E,17E,24E-trien-one	$C_{39:3}$	574	
l	nonatriaconta-17E,24E-trien-one	$C_{39:2}$	576	
Alkyl alkenoates				
m	methyl heptatriaconta-7E,14E,21E-trienoate	$C_{36:3}$OMe	562	✓
n	methyl heptatriaconta-14E,21E-dienoate	$C_{36:2}$OMe	564	✓
o	ethyl heptatriaconta-14E,21E-dienoate	$C_{36:2}$OEt	578	✓

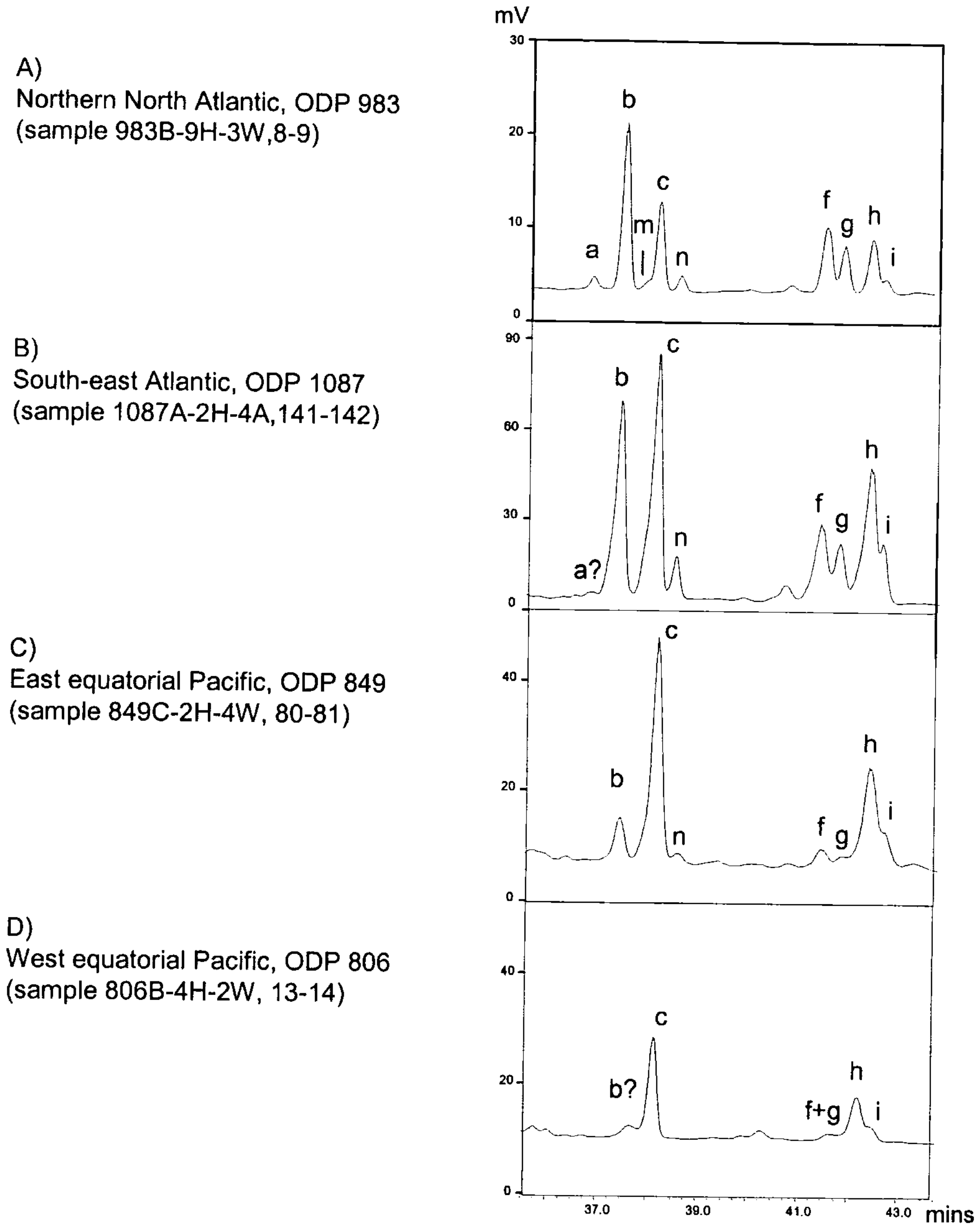

Figure 2-4 Representative GC traces of the eluting region of the long-chain alkenones and alkyl alkenoates for each of the four cores analysed in this thesis. Peak designations shown in Table 2.5.

Biomarker accumulation rates were calculated following the approach described by Emeis et al. (1995):

Component AR (component abundance/cm^{2}kyr^{-1}) =
Bulk MAR (g/cm^{2}kyr^{-1}) x Component abundance **(2-4)**

e.g. Pigment AR (AU/cm^{2}kyr^{-1}) = Bulk MAR (g/cm^{2}kyr^{-1}) x Pigment abundance (area units/g)

Bulk MARs are the product of linear sedimentation rates and the dry bulk density of the sediment (Emeis et al., 1995):

Bulk MAR (g/cm^{2}kyr^{-1}) =
Linear sedimentation rate (cm/kyr) x Dry Bulk Density (g/cm^3) **(2-5)**

Linear sedimentation rates are calculated using the oxygen isotope stratigraphies for each core (discussed in Section 2.5). Dry bulk density data were obtained from the *ODP Initial Reports* volume for each core (Kroenke et al., 1991; Mayer et al., 1992; Jansen et al., 1996; Wefer et al., 1998).

2.2.5.4 Reproducibility and Repeatability of the $U^K{}_{37}'$ analysis

The temperature program of the GC was optimised for separation of alkenones and the alkyl alkenoates, which may co-elute with the alkenones and introduce errors in SST estimation. Ongoing appraisal of the reproducibility of GC-FID analysis was determined by repeated injections of a mixed alkenone standard with sequences of samples. The average standard deviation for this standard was $U^K{}_{37}'$ = 0.0105, which gives an error range of 0.31°C using the Müller *et al.* (1998) calibration. The error associated with the whole procedure (from dry sediment) was determined using the mixed sediment standard aliquots extracted with each batch of samples (Section 2.2.1.3). The standard variation of $U^K{}_{37}'$ in these standards was 0.016, which gives an error range for the extraction method of 0.48°C using the Müller *et al.* (1998) calibration.

Low concentrations of C_{37} alkenones can introduce errors into $U^K{}_{37}'$ generation that may result in palaeotemperature estimation errors greater than ±0.5°C (e.g. Rosell-Melé, 1994; Rosell-Melé et al., 1995; Villanueva and Grimalt, 1996; Rosell-Melé et al., 2000; Grimalt et al., 2001). The errors are attributed to the irreversible adsorption of $C_{37:3}$ to the chromatographic column becoming more significant when concentrations are low.

Appraisal of the analytical accuracy of the GC-FID system used here was undertaken by comparing U^{K}_{37}' values from solutions of $C_{37:3}$ and $C_{37:2}$ which were progressively diluted and analysed by GC-FID (Figure 2.5). Two solutions were generated: one with a 'cold' signal comparable to the Atlantic samples, and one with a 'warm' signal for comparison with the Pacific sediments. Scatter was identified at low concentrations (Figure 2.5). This may reflect irreversible adsorption of the $C_{37:3}$ alkenone at low concentrations, but may also be the result of a reduced signal to noise ratio restricting the accuracy of the integrations and thus introducing scatter. Threshold values of alkenone abundances were c.10 ng per injection ('cold' standard) and 5 ng per injection ('warm' standard). A stronger indication of errors was identified when U^{K}_{37}' values were compared to integrated peak areas. Scatter was introduced when peak areas fell below c.2 area units for both standards (Figure 2.5). Samples below these thresholds were either re-concentrated and re-injected, or analysed by mass spectrometry (Section 2.2.6). This 'area unit' threshold will be specific to laboratories and GC systems. Continuous monitoring of GC-FID sensitivity was undertaken to determine any long-term increases in errors of U^{K}_{37}' estimation, and is recommended for further laboratory analyses.

The error introduced by low alkenone concentrations was minimised in samples from ODP 806B and 849D by extraction of several grams of sediment where available. As a result, alkenone concentrations within each GC trace generally exceeded the lower threshold. U^{K}_{37}' generation from ODP 806B in the West Pacific Warm Pool was complicated by minor or absent $C_{37:3}$ in comparison to $C_{37:2}$ (Pelejero and Calvo, 2003, also evident in Figure 2.4). A selection of samples with a variety of U^{K}_{37}' values from ODP 806B was subsequently analysed by mass spectrometry.

2.2.6 Gas Chromatography - Mass spectrometry analysis

A selection of samples from ODP sites 983C and 806B were analysed by GC coupled to Chemical Ionisation Mass Spectrometry (GC-CI-MS) at the NERC-Organic Mass Spectrometry Facility (School of Chemistry, University of Bristol). GC-CI-MS analysis is an effective method for analysis of those samples where low alkenone concentrations and/or potential co-elutants make U^{K}_{37}' estimation by GC-FID unfeasible (Rosell-Melé et al., 1995). The combination of selected ion monitoring (SIM) mass spectrometry and the specific reaction of ammonia with the targeted compounds in the sample results in high sensitivity and selectivity in GC-CI-MS analyses (Rosell-Melé et al., 1995).

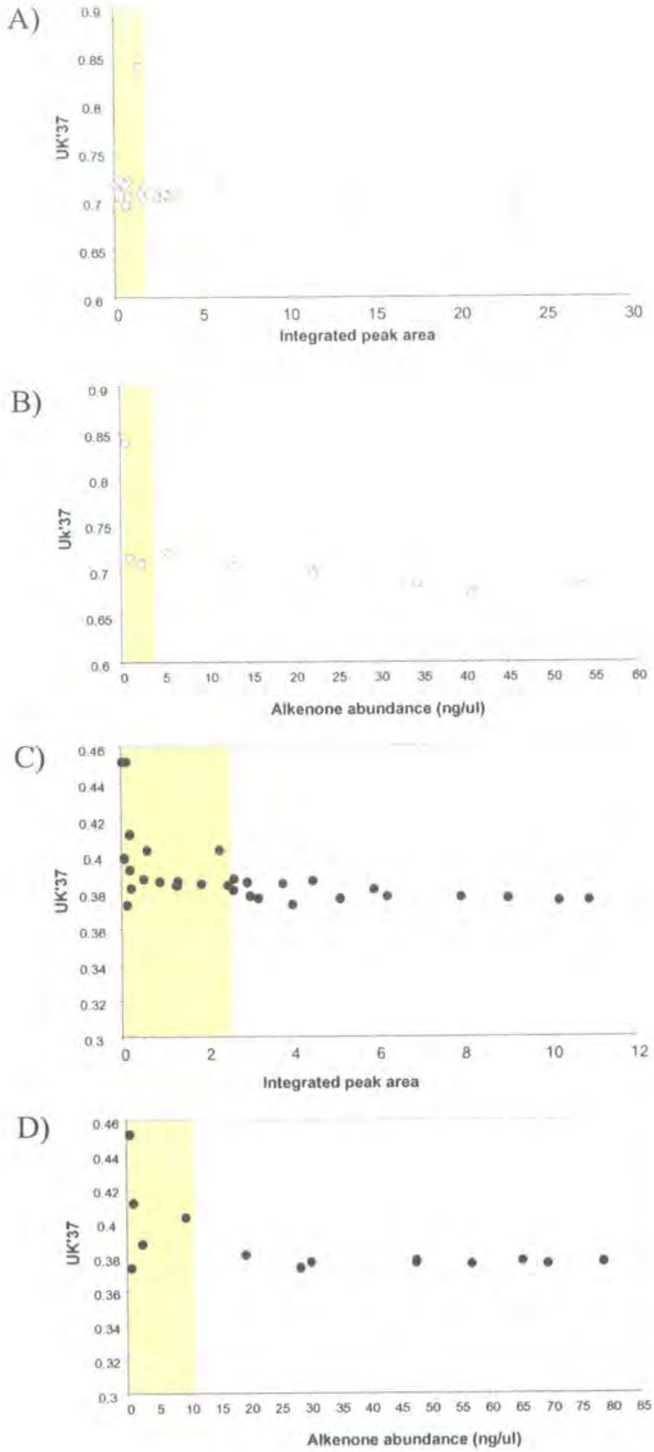

Figure 2-5 Assessment of the influence of integrated peak areas and alkenone concentrations over U^{K}_{37}' values. Yellow shading indicates onset of significant scatter in U^{K}_{37}' generation. A and B) 'warm' U^{K}_{37}' standard solution; C and D) 'cold' U^{K}_{37}'' standard solution. The impact of integrated peak area is shown in A and C, and of alkenone abundance in B and D.

Dilution tests suggested that the optimum range of alkenone concentrations was between 3-30 ng/component (Rosell-Melé et al., 1995), demonstrating the higher sensitivity of the method to GC-FID.

The instrumental set-up was based upon the methods of Rosell-Melé (1994). A Varian 3400 gas chromatograph fitted with a septum equipped programmable injector (SPI) was directly coupled to a Finnigan MAT TSQ 700 triple stage quadrupole mass spectrometer. Aliquots of 1 µl were injected by a CTC A200S autosampler. The SPI was operated in "high performance" non-vaporizing mode, whereby the injector was held at 80°C during injection then rapidly temperature programmed from 80-300°C at 200°C min^{-1}. GC separation of the analytes was achieved using a 50 m, 0.32 mm i.d. fused silica column, with 0.12 µm CPSIL5-CB film thickness (Chrompack). The oven temperature program was: 200-300°C at 6°C min^{-1} with no initial hold time, and a final isothermal period of 10 minutes. Hydrogen was employed as a carrier gas with a head pressure of 8psi.

Operating conditions for the mass spectrometer were optimised for sensitivity with respect to the C_{37} methyl alkenones. The conditions used were: ion source temperature 160°C, electron energy 70eV, electron current 400 µA, and electron multiplier voltage at 1500V with an electrometer gain of 10^8. Chemical ionisation was achieved using high purity ammonia (BOC micrographic grade) introduced to the ion source through the conventional CI gas inlet. The pressure inside the ion source was regulated to *ca.* 0.85 Torr, giving rise to a pressure of 4.5×10^{-6} Torr in the vacuum manifold. Ten ions, corresponding to the $[M+NH_4]^+$ species of the analytes (Table 2-4) were monitored by scanning the third quadrupole with a scan rate of 0.1 sec per Dalton. The overall analysis was governed from the TSQ 700 using an Instrument Control Language (ICL) procedure, which controlled the autosampler, the GC and the MS.

Generation of U^K_{37} and U^K_{37}' was achieved by integration of the pseudo-molecular ions (Figure 2-6). Data processing was undertaken using the Xcalibur software. Reproducibility of the analysis was determined by repeated injections of an mixed alkenone standard used in the previous method tests described here. The average standard deviation was U^K_{37}' =0.029, a SST deviation of 0.86°C using the Müller et al. (1998) calibration. Figure 2.7 shows that the enhanced sensitivity of the GC-CI-MS system reduces the number of samples which give a U^K_{37}' value of unity for the West

A)
West equatorial Pacific:
ODP 806B-4H-3W, 4-5cm (ca.1410 ka)

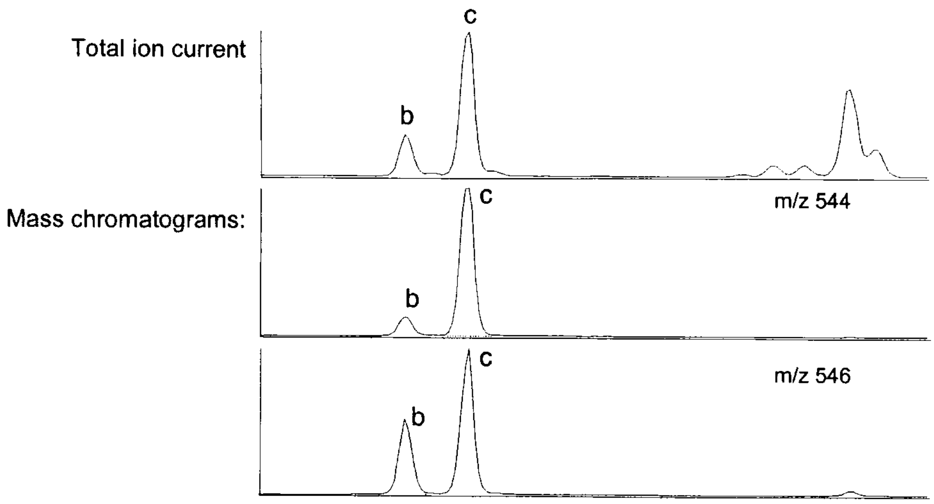

B)
Northern North Atlantic:
ODP 983C-11H-5W, 144-145 cm (ca.932 ka)

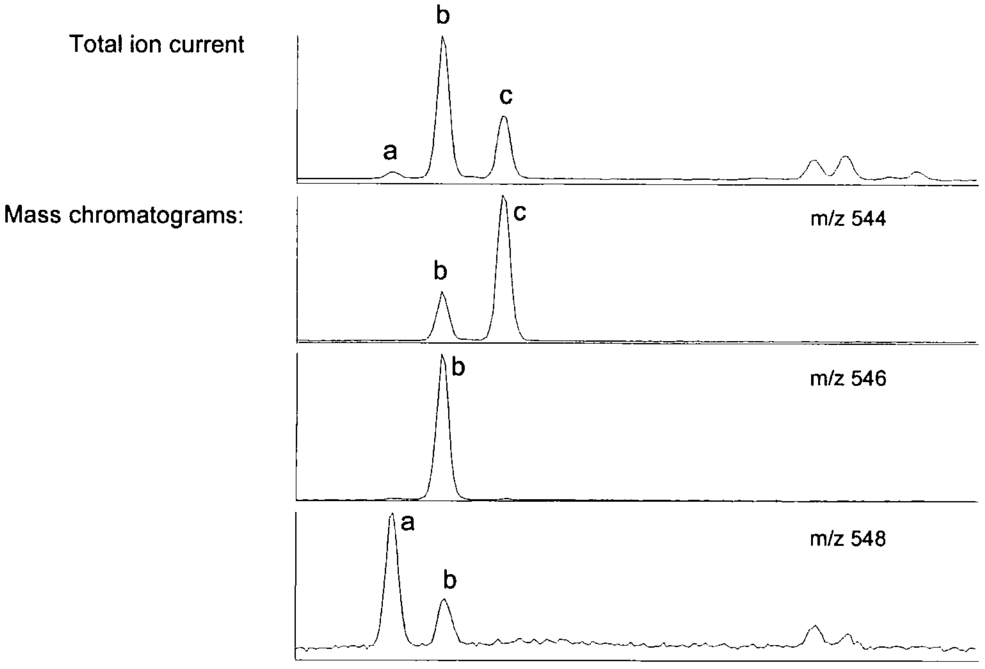

Figure 2-6 Ammonia chemical ionisation mass chromatograms of the total ion current and pseudo-molecular ions of the C_{37} alkenones from cores ODP 806B and 983C. Compound identities from Figure 2.4 and Table 2.4. A) ODP 806B, in the western equatorial Pacific. C37:2 ('c') dominates, but C37:3 ('b') can also be quantified. B) ODP 983C, in the northern North Atlantic. C37:4 ('a'), C37:3 ('b') and C37:2 ('c') can all be identified.

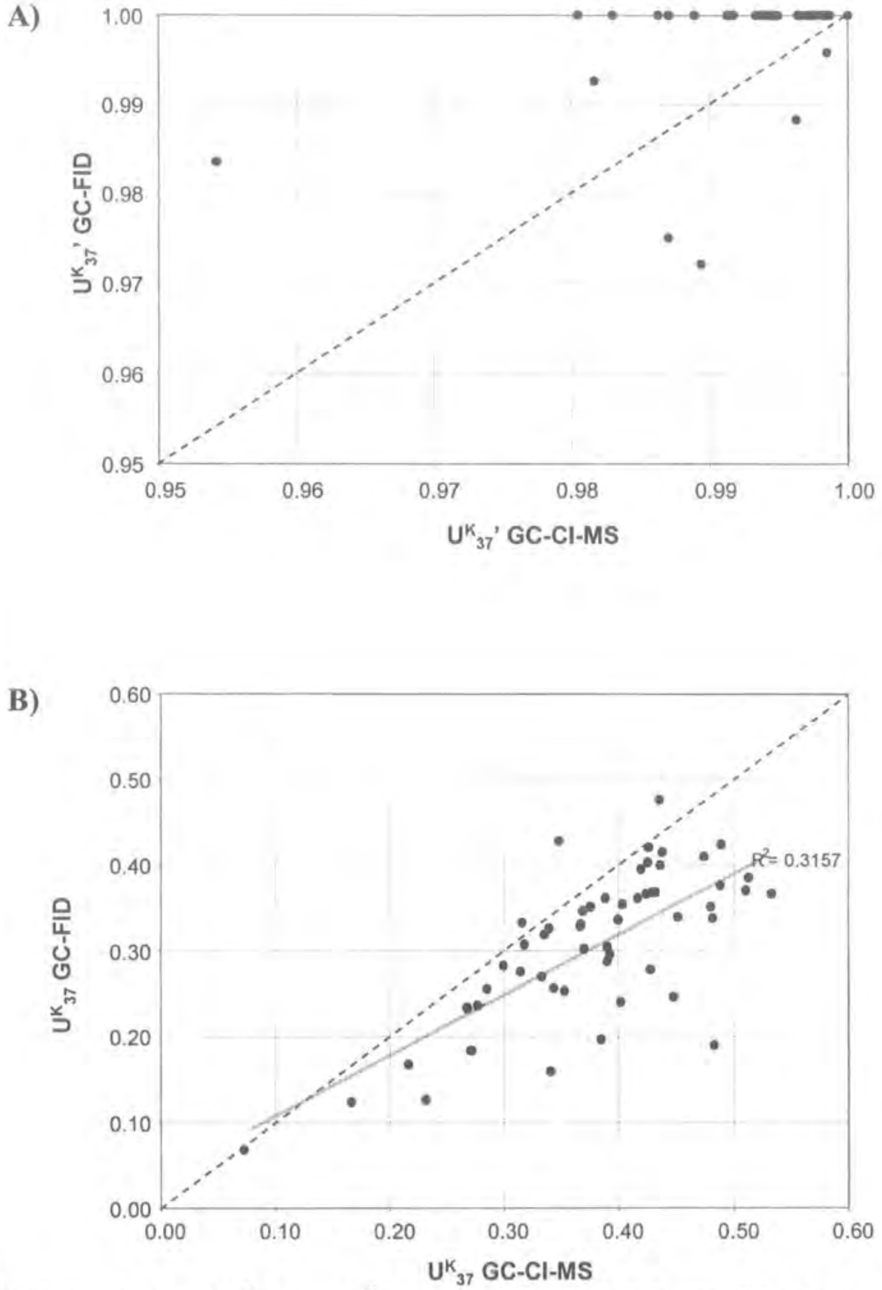

Figure 2-7 Comparison of U^K_{37}' and U^K_{37} values using GC-FID and GC-CI-MS for cores ODP 806B and 983C. Diagonal line indicates FID = CI-MIS. A) ODP 806B. The increased sensitivity of GC-CI-MS reduced the number of samples where U^K_{37}' = 1; B) ODP 983C. Scatter in UK37 values between the two methods reflects the more sensitive GC-CI-MS detection of the $C_{37:4}$ alkenone where alkenone abundance is low. Linear correlation is shown by the solid grey line.

equatorial Pacific core, ODP 806B. The scatter for ODP 983C U^{K}_{37} values is largely due to the more sensitive response of GC-CI-MS in detecting $C_{37:4}$ when alkenones are in low abundance. GC-FID overestimates the abundance of $C_{37:4}$ under these circumstances, resulting in generation of cooler U^{K}_{37} values in comparison to the GC-CI-MS (Figure 2.7). The scatter may also be due to the reduced reproducibility of the GC-CI-MS system, a property also identified by Rosell-Melé *et al.* (1995).

2.3 Coccolith analyses

Coccolith accumulation rates and the assemblage of coccolith species were reconstructed using two preparatory methods: using smear slides and a filtration method developed by Andruleit (1996). The preparation of smear slides was undertaken to provide initial exploratory data on the relative abundances and dominant species of coccolith within the sediments. The filtration method was employed for the quantitative assessment of coccolith accumulation rates and the coccolith species assemblages. A polarising light microscope with a magnification of x1250 was used to analyse both sets of samples on slides.

2.3.1 Smear slide preparation

A small amount of dry sediment was placed on a slide, then spread thinly across the slide surface using a drop of water and a spatula. The slide was then dried on a heated plate, before the addition of Canada balsam and the cover slide. Once all air bubbles were removed from the slide, it was left to set before analysis.

2.3.2 Filtration method

Following the method of Andruleit (1996), approximately 40 mg of dried sediment was weighed and diluted in c.10 ml tap water, and left overnight. The next day, after 15 seconds sonication each sample was diluted to 500 ml in tap water. A 15 ml aliquot was immediately removed and vacuum filtered through cellulose acetate filters (pore size ≤0.8 µm). After gentle drying in an oven, a 1 cm^3 area was cut from each filter, and mounted in Canada balsam on a slide.

2.3.3 Coccolith accumulation rates

Three coccolith counts were performed (3 fields of view), using a light polarising microscope at x1250 magnification. Coccolith concentrations per gram of dry sediment were calculated following the method described in Müller *et al.* (1997):

$$\textbf{Coccoliths (no.g}^{-1}\textbf{) = (A * Nc) / (a * M * D)} \qquad \textbf{(2-6)}$$

Where A = effective filter area (mm^2), Nc = number of counted coccoliths (average of three fields of view), a = examined filter area, M = mass of dry sediment (g), and D = dilution factor (aliquot volume / total volume of solution). Coccolith Accumulation Rates (AR) were generated following the method described in Emeis *et al.* (1995):

$$\textbf{Coccolith AR (number of coccoliths/cm}^2\textbf{kyr}^{-1}\textbf{) =}$$
$$\textbf{Bulk MAR/100 x Coccolith abundance g}^{-1} \qquad \textbf{(2-7)}$$

Where bulk MAR was generated following the methods outlined in Section 2.2.5.3.

2.3.4 Coccolith assemblage reconstruction

Species diversity counts were generated by grouping coccolith species according to the method of Okada (2000), and calculating their percentage abundance within the total assemblage. The coccolith groups analysed are shown in Table 2.6 and Figure 2.8. These species groups allow identification of the early- and mid-Pleistocene nannofossil (coccolith) acme zones (Gartner, 1977; Weaver, 1993). These are used in conjunction with nannofossil extinction events for biostratigraphy generation (Chapter 1), as shown in Figure 2-8. These groups account for at least 95% of the coccolith assemblages analysed here.

Table 2-6 Coccolith groups analysed in this thesis, based on the method of Okada (2000).

Category	Size	Principal species
Small placoliths / small Reticulofenestra	< 0.2 µm	(not determined)
Small *Gephyrocapsa*	2.0 - 3.0 µm	(not determined)
Medium *Gephyrocapsa* (open)	3.0 - 5.0 µm	Predominantly *Gephyrocapsa oceanica.*
Medium *Gephyrocapsa* (closed)	3.0 - 5.0 µm	Predominantly *Gephyrocapsa carribbeanica*
Medium *Reticulofenestra*	3.0 - 5.0 µm	
Pseudoemiliania lacunose		
'Others'		*Calcidiscus leptoporas* *Coccolithus pelagicus* (cold-water) *Helicosphaera carteri* *Pontosphaera species* (warm water) *Helicosphaera sellii* *Calcidscus macintyrei*

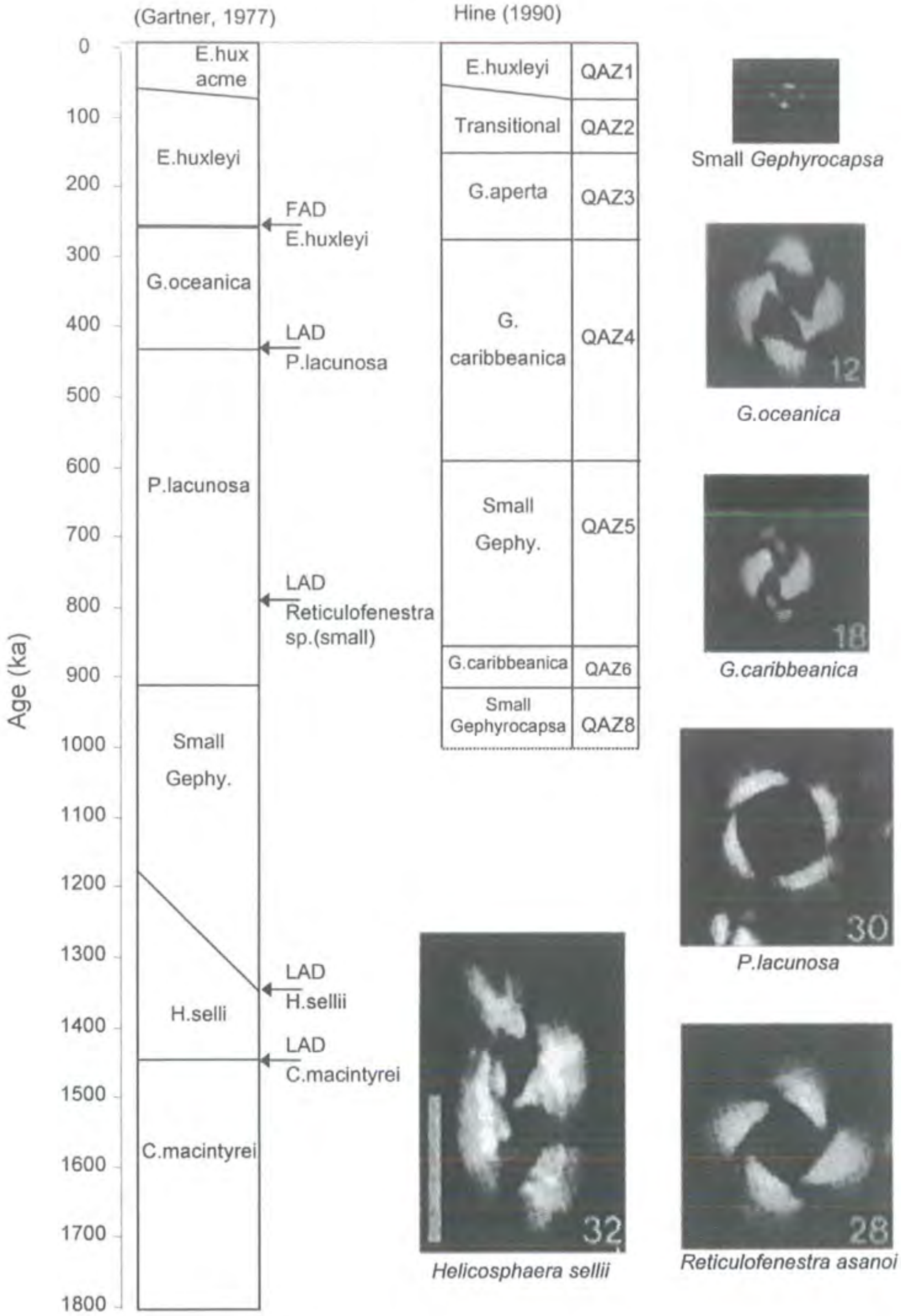

Figure 2-8 Nannofossil acme zones and biostratigraphic datums 0-1800 ka. Tables: adapted from Weaver (1993) and Hine and Weaver (1998). Photographs of light microscope views of coccolith species from Matsuoka and Oksada (1989).

Medium *Gephyrocapsa* (3.0-5.0 μm) were divided into two categories, depending on the size of the central opening (Okada, 2000). *G.caribbeanica* coccoliths were identified as forms with a very small or closed opening, in contrast to the relatively large opening in those from *G.oceanica* (Figure 2.8). Smaller coccoliths were not subdivided by species, due to difficulties in identification at this scale. They were grouped according to their size, into 'small' (2.0-3.0 μm) *Gephyrocapsa* species and the smaller (<2 μm) 'placoliths'. It is likely that some small *Reticulofenestra* species may have been included in this grouping, as below 3 μm it becomes difficult to separate *Gephyrocapsa* that have lost or failed to develop a bridge from *Reticulofenestra* (Okada, 2000). A relatively large form (6.0–8.0 μm) of *Reticulofenestra* was identified as *R.asanoi*, which became extinct near 830 ka BP (Sato and Takayama, 1992). The relatively abundant biostratigraphic marker *Pseudoemiliania lacunosa*, which became extinct ca.458 ka BP (Thierstein et al., 1977), was also counted. The presence of additional biostratigraphic marker species was also noted: *Pseudoemiliania lacunosa*, *Reticulofenestra asanoi*, *Helicosphaera sellii,* and *Calcidscus macintyrei* (Table 2-6, Figure 2.8).

2.4 Particle size analysis

A selection of samples from ODP sites 1087A and 849C and D were analysed for particle size analysis. To determine the particle size distribution of the non-biogenic component of the sediments, organic material and carbonate were first removed. Hydrogen peroxide was added to wet sediment to remove organics. After rinsing with distilled water, carbonate was removed using hydrochloric acid. A further rinse with distilled water was undertaken. Analysis was performed using a Coulter LS230 Particle Size Machine (PSM), with samples dissolved in a solution of sodium hexametaphosphate. Following the method of Hovan (1995) and Krissek and Janecek (1993), variations in the grain-size of aeolian detritus were determined by calculating the mean grain size of the fine fraction (1-30 μm).

2.5 Age Models

Sample selection for site ODP 806B was undertaken using the $\delta^{18}O$ stratigraphy of (Berger et al., 1993a). The age model bridged a coring gap in ODP 806B using samples from the nearby ODP 805C (Berger et al., 1993a). The same method was followed here, with the 745-790 ka interval comprising 5 samples from ODP 805C. For sites ODP 849C and D, samples were selected using the $\delta^{18}O$ stratigraphy of Mix *et al.* (1995). Wherever possible, samples were requested that had also been analysed for $\delta^{18}O$. Where this prevented maintaining a resolution of c.5 kyr, linear interpolation was applied between adjacent age control points, assuming a constant sedimentation rate between the two dated points.

At site ODP 983C, the $\delta^{18}O$ stratigraphy was initially only available for the interval 700-1200 ka (Kleiven, 2000). Samples for this interval were requested using this age model, following the procedure described for the two Pacific cores. The preliminary ODP age model (Jansen et al., 1996) was used to request samples that did not fall within this range, assuming linear sedimentation rates between tie-points. Following the later availability of the complete $\delta^{18}O$ stratigraphy for ODP 983C (M.E. Raymo, personal communication, December 2002), revised ages for all samples were assigned.

All samples from site ODP 1087A were selected following the preliminary ODP age model (Wefer et al., 1998). The oxygen isotope stratigraphy for the interval 0-500 ka (Pierre et al., 2001) was used to identify the youngest samples, from which the preliminary age model sedimentation rates were used to extrapolate down-core. The later development of the oxygen isotope stratigraphy to 1500 ka (C. Pierre, personal communication, May 2003) was used to assign revised ages to all samples. A break of 2.58 m occurred between Cores 4H and 5H (Wefer et al., 1998). This had not been bridged using other cores in the age model generation, and was not bridged here. This resulted in a ca.65-kyr interruption in the data record between isotope stages 39 and 40.

2.6 Time-series analysis

Two methods of time-series analysis were performed here. First, harmonic analysis was performed using the SPECTRUM programme (Schulz and Stattegger, 1997) to determine the dominant periodicities of the U^{K}_{37}' and biomarker accumulation rate time-series. This procedure identifies the presence of periodic components within a data series that exceed background noise (Schulz and Stattegger, 1997). As the programme does not require evenly spaced data sets, the data series generated in this thesis could be analysed without any interpolation. Following the procedures described by Schefuß (2003), the significance level was set to 0.05, oversampling factor to 4, and high-frequency factor to

1. The oversampling and high-frequency factors determine the number of frequencies that are investigated and highest frequency to be analysed (Schulz and Stattegger, 1997). To balance computing time with the smoothness of the spectra that result, the parameters used here are recommended by Schulz and Stattegger (1997).

The identification of changes in the dominant periodicities through time in the analysed time-series was limited using SPECTRUM. This was due to the division of the complete time-series (c.200 data points) into discrete sections inevitably resulting in time-series which had fewer than 100 data points, the minimum level for significant periodicities to be detected (Schulz and Stattegger, 1997). This was addressed by performing evolutive spectral analysis on all of the data sets, using a Matlab based code developed by Dr. Nicklas Pisias (e.g. Pisias et al., 1995b). Spectra were calculated over a 500-kyr interval, with a sampling interval of 5 kyr, and a significance level of 0.1. The evolutionary spectral matrix was generated by offsetting each 500-kyr interval by 10% i.e. interval 1 covered 500-1000 ka, interval 2 550-1150 ka, interval 3 600-1200 ka etc. (Pisias et al., 1995b). This generates a 3-dimensional representation of the analysis, with time and frequency displayed on the x- and y-axes, and the significance of any periodicity displayed in a topographic surface. The procedure requires data points to be evenly spaced. In the Atlantic cores, where dating had been performed after the analysis, the uneven distribution of the data may have reduced the amplitude of some of the U^{K}_{37}' and biomarker accumulation variations. This may account for the generally poor evolutive spectra from these cores when results are compared to the harmonic spectra (see Chapter 3). Due to the resolution of all of the data sets, c.5 kyr, both the harmonic and evolutive analyses struggled to identify the high-frequency variations related to precession (c.19-23 kyr) above the background noise. This issue has also been identified in other studies employing these analyses (e.g. Pisias et al., 1995b; Liu and Herbert, 2004).

3. Results

3.1 Introduction

In this chapter, the results generated for each core are presented. This does not include the coccolith species assemblage data, which is discussed in Chapter 4. All raw data are available in the Appendices. The principal aim of this Chapter is to identify the major trends within each core record, and the relationships between changes in surface ocean conditions and in the accumulation rates of biomarkers at each site and between sites.

The benthic $\delta^{18}O$ record of global ice volume from ODP 849 (Mix et al., 1995) is shown as a reference curve for each site, with selected marine isotope stages (MIS) marked. This record is used as the common reference of global ice volume for every site, as the $\delta^{18}O$ values are proposed to record values of average deep Pacific Ocean water, which has properties identical to the most abundant water mass in the world ocean, known as 'Common Water' (Mix et al., 1995). This $\delta^{18}O$ time-series is thus considered indicative of global changes to $\delta^{18}O$ driven by changes in global ice volume. Furthermore, at the time of writing, a complete benthic $\delta^{18}O$ time-series was unavailable for ODP 983C (e.g. Figure 1.12), coring gaps and variable resolution at ODP 1087A provide an incomplete record (Figure 1.12), and ODP 806B may contain additional influences of salinity and temperature within the $\delta^{18}O$ signal as it is a planktic rather than benthic record.

3.2 ODP 983C (Northern North Atlantic)

All results from ODP 983C are shown in Figure 3.1. For reference, the $\delta^{18}O$ record of global ice volume from ODP 849D (Mix et al., 1995) is also shown. In Chapter 1, the uncertainties of estimating SSTs using alkenones in polar and subpolar environments were discussed. Consequently, the U^{K}_{37} index is used as a SST proxy here. Both U^{K}_{37} and U^{K}_{37}' indices are shown in Figure 3.1b. SSTs calculated using the U^{K}_{37} calibration of Rosell-Melé *et al.* (1995b) generally range from between 3°C to 12°C (Figure 3.1B). These values are consistent with reconstructed winter and summer SSTs at the last glacial maximum (around 1-4°C; Pflaumann et al., 2003) and with the modern annual SST range at the site (8-11°C; Conkright et al., 2002). $\%C_{37:4}$ values above 5% are interpreted as indicative of the presence of Arctic Waters at the site, where at least seasonal sea-ice cover is present (Swift, 1986; Rosell-Melé et al., 1998; Bendle, 2003).

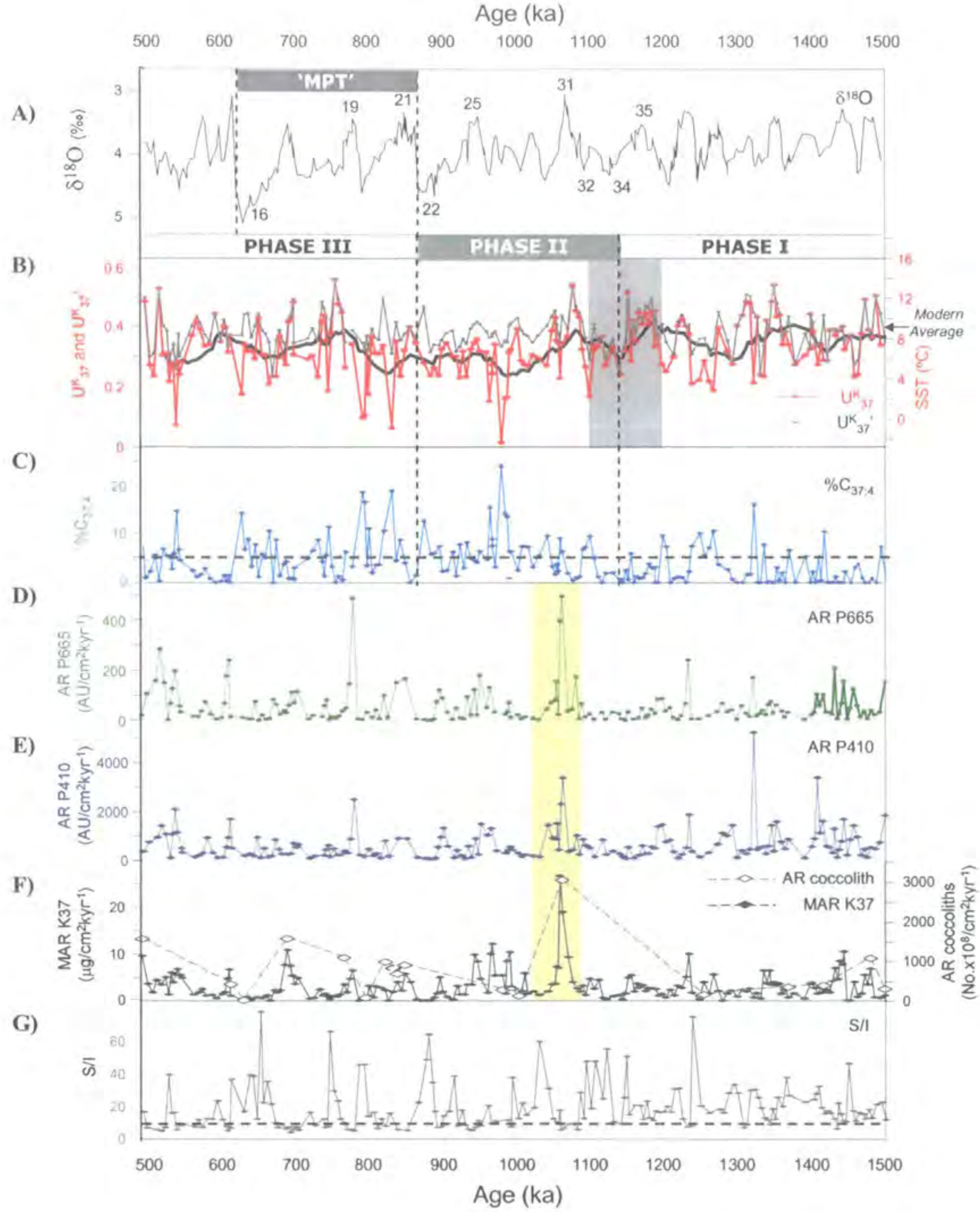

Figure 3-1 Results from ODP 983C. The Mid-Pleistocene Transition as defined by Mudelsee and Schulz (1997) marked as 'MPT'. The three phases of surface circulation discussed in the text are marked. Periods of significant increased organic carbon export in all three organic carbon export proxies are indicated by vertical yellow bars. (A) Benthic oxygen isotope curve from ODP 849 (Mix et al. 1995). Selected isotope stages marked; (B) U^{K}_{37} (red) and U^{K}_{37}' (grey). SST values are shown on the right-hand scale. A 10-pt running mean (i.e. a 50-kyr filter) is shown in black. The 'premature' 100-kyr cycle at the onset of Phase II is highlighted by grey shading; (C) Abundance of the $C_{37:4}$ alkenone. The horizontal dashed line marks $C_{37:4} = 5\%$; (D) Relative accumulation rate of the photosynthetic pigments with absorbance at 665 nm ('P665', as defined in Section 2.2.3, page 63); (E) Relative accumulation rate of the photosynthetic pigments with absorbance at 410 nm ('P410'); (F) Mass accumulation rates of C37 alkenones ('K37', solid line) and accumulation rate of coccoliths (open diamonds, dashed line). (G) S/I values, S/I = 10 marked by horizontal dashed line.

Periods of high ice volume are generally associated with low U^{K}_{37} (Figure 3.1B) high %$C_{37:4}$ (Figure 3.1C) and S/I values (the ratio P410/P665, see discussion in Chapter 1) exceeding 10 (Figure 3.1G). By analogy with late Pleistocene records (Rosell-Melé and Koç, 1997; Rosell-Melé et al., 1997), high glacial S/I values are interpreted as evidence for iceberg-rafting of terrigenous-derived organic carbon (specifically the porphyrins) to the site. Porphyrins raise S/I values by increasing absorbance at the Soret band (410 nm) relative to the absorbance band I at 665nm. Absorbance in the latter wavelength is therefore used to calculate accumulation rates of chlorin pigments (AR P665), which are interpreted here as a proxy for export production by phytoplankton. Throughout the interval of study, high accumulation rates of P665 and the C_{37} alkenones (K37) occur during interglacials, when the total organic carbon contents of ODP 983C sediments are also high (Hyun et al., 1999).

The accumulation rates of the biomarkers and coccoliths and the U^{K}_{37} time-series from ODP 983C may be affected by the advection of fine-grained particles (including organic carbon and coccoliths) to the site by the action of Norwegian Sea Overflow Water (NSOW). During the Holocene, accumulation rates of organic carbon and coccoliths on the Gardar Drift fell during periods of stronger NSOW flow (Giraudeau et al., 2000). Coccolith and biomarker accumulation rates at ODP 983C during the mid-Pleistocene are highest during interglacials (Figures D-F), despite the coarsening of Gardar Drift sediments indicating stronger NSOW flow during these intervals (Wang and McCave, 1990). This suggests that the variations in biomarker and coccolith accumulation rates shown in Figure 3.1 were not driven by variations in NSOW strength, and supports their application as proxies for export production at the ODP 983 site during the mid-Pleistocene.

A combination of long-term trends in the U^{K}_{37} and %$C_{37:4}$ time series at ODP 983C allows the 1500-500 ka interval to be sub-divided into three phases (Figure 3.1). The 50-kyr running mean from U^{K}_{37} shows a shift toward cooler average SSTs after ca. 1050 ka (MIS 30), coupled with a reduction in the amplitude of SST variations until ca. 850 ka (MIS 21) and an increase in the abundance of $C_{37:4}$. This cooling trend is preceded by an anomalous glacial-interglacial cycle identified in both the U^{K}_{37} and $\delta^{18}O$ time-series between 1200-1100 ka (MIS 35-32; Figure 3.1). The ca. 100-kyr duration of this cycle contrasts with the ca. 41-kyr cycles that precede and follow it (Figure 3.1). This cycle is thus used here to define the transition from Phase I to II, although the cooling trend that characterises Phase II begins some time later. The shift toward higher amplitude SST variations with the onset of MIS 21 (ca. 875 ka) is used to define the transition between Phases II and III. The characteristics of these three Phases will now be outlined:

Phase I: Pre-1143 ka (Pre MIS 34)

Phase I is dominated by high amplitude oscillations in U^{K}_{37}, with generally low but highly variable $C_{37:4}$ abundance (Figures 3.1B,C). SSTs oscillate with an amplitude of approximately 8°C (between 6 and 14°C) around the modern average of 9°C (Conkright et al., 2002). Glacials are associated with peaks in $\%C_{37:4}$, low U^{K}_{37} and low biomarker accumulation rates (Figure 3.1D-F).

Phase II: 1143 – 875 ka (MIS 34-22)

Phase II is characterised by cooling of interglacial SSTs of between 1.6-2.6°C, and a sustained increase in $\%C_{37:4}$ (Figures 3.1B,C). In contrast to Phase I, Interglacial SSTs during Phase II lay below the modern average of 9°C, and the amplitude of the SST oscillations has fallen slightly, to around 6°C (Figure 3.1B). Excluding interglacial maxima, the abundance of $C_{37:4}$ remained above 5% during Phase II, and reached its maximum value at 983 ka (24%) which corresponds to the coldest glacial $U^{K}_{37}{}'$ value of the 1500-500 interval of study. The $\%C_{37:4}$ record demonstrates that the Phase II cooling was also associated with the presence of Arctic Waters at ODP 983. The Phase I-II boundary occurs during an unusual glacial-interglacial cycle that correlates with MIS 35-32 (Figure 3.1). This cycle began at ca. 1212 ka with interglacial warming, and culminated in pronounced and sustained cooling by 1100 ka (MIS 34-32). This cycle is unusual because its duration, ca. 100-kyr, exceeds that of the glacial-interglacial oscillations during Phases I and II (Figure 3.1B). This trend can also be identified in the $\delta^{18}O$ global ice volume record (Figure 3.1A), and has been described as a 'premature 100-kyr cycle' (Mudelsee and Stattegger, 1997). The sustained cooling of Phase II is interrupted by MIS 31, which immediately followed the MIS 35-32 '100-kyr' cycle (Figure 3.1B). High U^{K}_{37} at ODP 983C and low global ice volume from $\delta^{18}O$ demonstrate that MIS 31 was one of the warmest interglacials of the 1500-500 ka interval (Figures 3.1A,B). MIS 31 is also marked by the maximum biomarker accumulation rates recorded at ODP 983C between 1500 and 500 ka (Figure 3.1D-F).

Phase III: post-875 ka (post-MIS 22)

Phase III is identified by a return to high variability in U^K_{37}, largely due to an increase in interglacial SSTs (Figure 3.1B). High $\%C_{37:4}$ continued to occur during glacials, and tended to exceed values observed during Phase I. Biomarker accumulation rates during Phase III continued to reach maxima during interglacial periods.

The time-series analysis results from ODP 983C are shown in Figure 3.2. Two methods were applied, harmonic analysis to determine the presence of periodic components above the background noise (Schulz and Stattegger, 1997) and evolutive analysis to identify changes in these periodic components through time (Pisias et al., 1995b). The details of the procedures are described in Section 2.6 (page 67). The reduced ability of the evolutive spectra to identify high-frequency signals (as discussed in Chapter 2) is clearly demonstrated when comparing the evolutive and harmonic spectra. The general absence of a precession-related signal in all spectra (except the harmonic spectrum of K37, Figure 3.2E) may be attributed to the resolution of the time-series from all of the cores analysed here. The ca. 5-kyr sampling resolution probably limits the identification of significant precessional periods (c.19-kyr and 23-kyr) above background noise. This problem has been encountered elsewhere with evolutive analysis (Liu and Herbert, 2004), and will affect all of the spectra presented in this Chapter. Some attentuation of the obliquity-related signals by the evolutive analysis is also apparent when the harmonic and evolutive spectra from ODP 983 are compared (e.g. 3.2A vs. 3.2B). A number of differences between the two analyses may also reflect the analysis of the complete data set by harmonic analysis (i.e. the interval 1500-500 ka), which contrasts with the analysis of shorter but overlapping intervals by the evolutive method (as outlined in Chapter 2). These issues arise for all four of the cores analysed here.

Despite these issues, the dominant periodicities in all time-series from ODP 983C correspond to the orbital parameters of obliquity and eccentricity (Figure 3.2,A,C,E). The dominance of eccentricity in the evolutive spectra is less clear in the harmonic results, and may be an artefact of the greater sensitivity of the evolutive analysis to lower frequency oscillations. The eccentricity signal weakened through time at ODP 983C (Figure 3.2B,D,F), until an obliquity-related signal dominated during Phase III. This trend is also visible in insolation (Figure 3.2H). However, the progressive

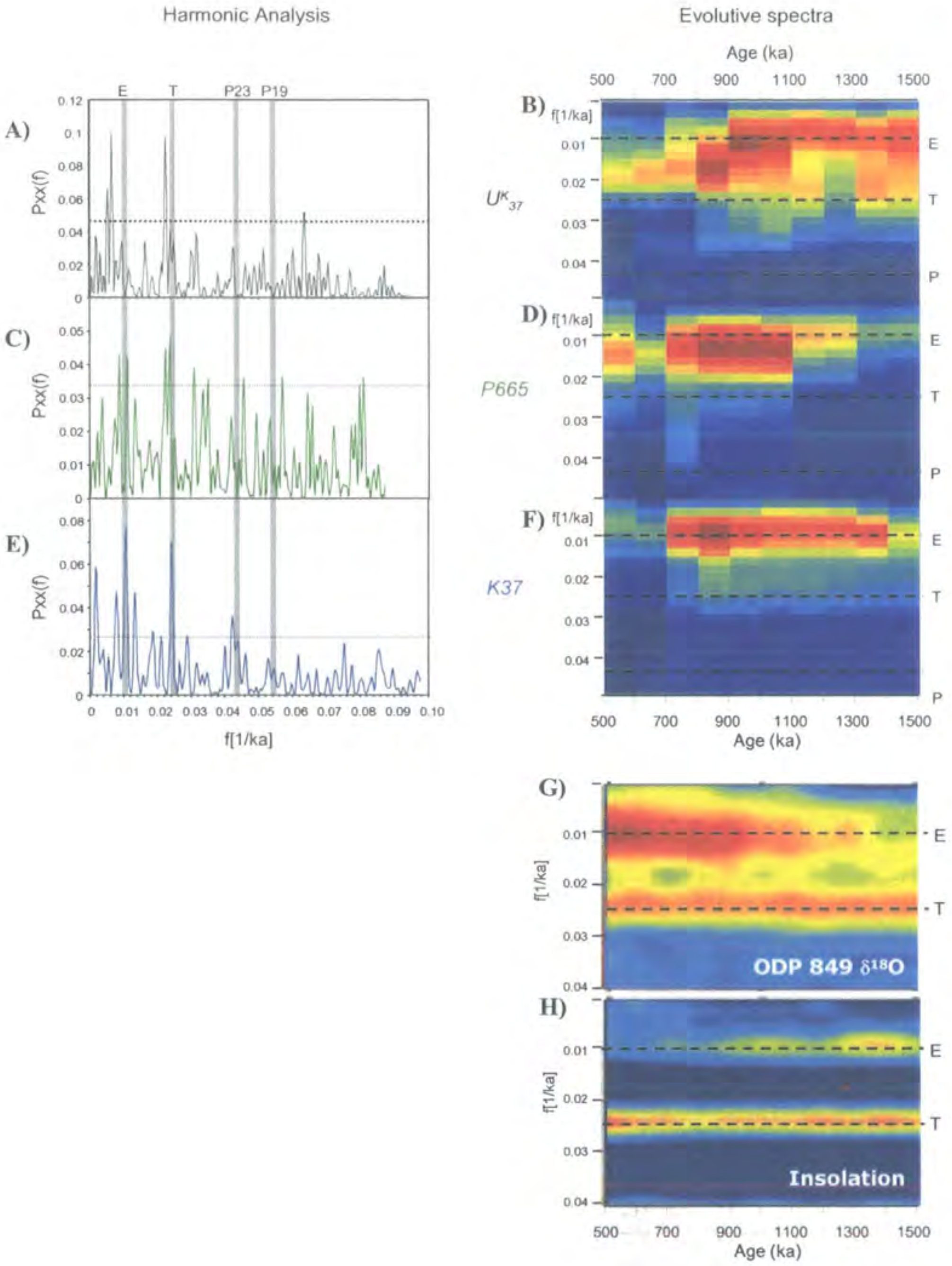

Figure 3-2 Spectral analysis results from ODP 983C. Milankovitch frequencies shown: E = eccentricity (ca.100-kyr), T = tilt ('obliquity', ca.41-kyr), P = precession (ca.23- and 19-kyr). Left: Harmonic analysis. Peaks lying above horizontal dashed line ('gs') represent periodic components that exceed background white noise (see Chapter 2 for discussion). Right: Evolutive spectra. Variance is identified with significance level of 90% (as described in Chapter 2). Red shading reveals high degree of variance at this significance level, blue reveals low degree of variance at this significance level. (A) U^K_{37} harmonic analysis; (B) U^K_{37} evolutive analysis; (C) P665 accumulation rate harmonic analysis; (D) P665 accumulation rate evolutive analysis; (E) K37 accumulation rate harmonic analysis; (F) K37 accumulation rate evolutive analysis; (G) Evolutive spectra of the benthic d18O ice volume record from ODP 849 (Mix et al.1995); (H) Evolutive spectra of eccentricity and tilt from Berger and Loutre (1991). G and H adapted from analysis by Dr. Nick Pisias presented in Clark et al. (1999).

weakening of the eccentricity signal in U^K_{37} contrasts with the $\delta^{18}O$ time-series, which reveal the emergence of 100-kyr cycles marking the MPT (Figure 3.2G). This result is surprising, given the impacts of global ice volume oscillations on surface ocean conditions in the northern North Atlantic through iceberg and freshwater discharges, and the expansion of sea-ice cover in response to regional cooling. However, a sensitive response of the surface ocean in the Nordic Seas to insolation variations was identified during the late Pleistocene (e.g. Koç and Jansen, 1994). Given the errors associated with the spectral analysis procedure at ODP 983C, it is not yet clear whether the mid-Pleistocene northern North Atlantic had greater sensitivity to long-term trends in insolation rather than global ice volume, or whether these trends are simply artefacts of the evolutive spectral analysis procedure.

In summary, glacial-interglacial oscillations in U^K_{37}, $\%C_{37:4}$ and biomarker accumulation rates are observed at ODP 983C. NSOW flow appears to have had minimal impact on the biomarker and coccolith accumulation rates, supporting the application of these proxies for reconstructing surface ocean conditions and export productivity at this site. A three-phase division of the interval 1500-500 ka has been determined. High amplitude variability in all time-series is evident in Phases I and III (pre-MIS 34 and post-MIS 22 respectively). Phase II (MIS 34-22) is marked by interglacial cooling and a sustained increase in $\%C_{37:4}$. The exception to this trend is the interglacial of MIS 31, which marks the warmest interglacial of the time-series and the maximum accumulation rates of the biomarkers.

3.3 ODP 1087A (Eastern South Atlantic)

All results from ODP 1087A are shown in Figure 3.3. The benthic $\delta^{18}O$ record from ODP 849D (Mix et al., 1995) is also shown for comparison. The core break of 2.58 m between cores 4H and 5H (Chapter 2) can be seen between 1255-1316 ka (MIS 39-40). A small gap centred on 920 ka also occurs. Sampling resolution throughout the core is ca.5-kyr, except between 500-600 ka where low sedimentation rates reduce the resolution to ca. 10-20-kyr. ODP 1087A sediments contained the highest abundances of pigments and alkenones of all the records analysed here, with the alkenones dominating the organic carbon compounds in the GC analyses.

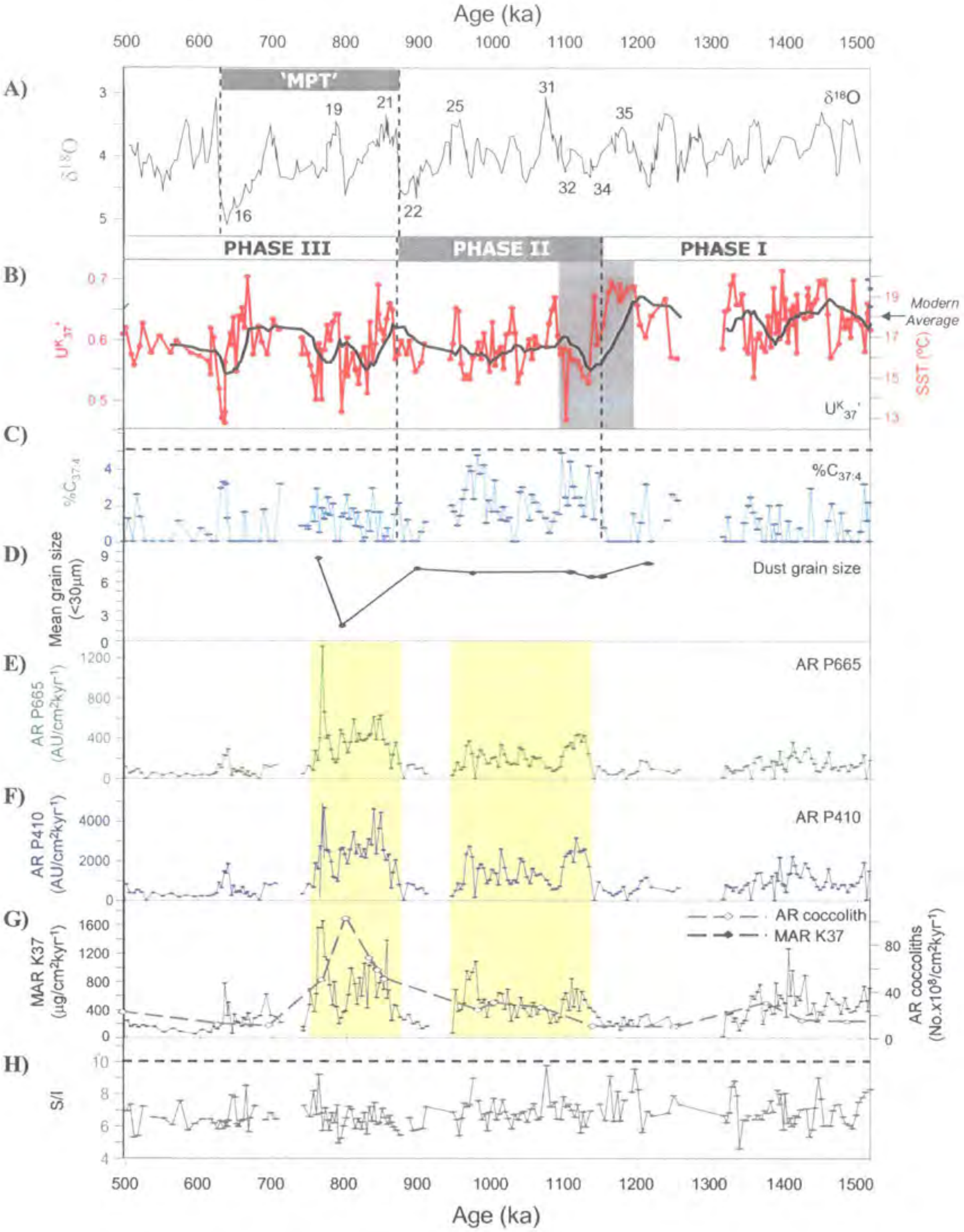

Figure 3-3 Results from ODP 1087A. The Mid-Pleistocene Transition as defined by Mudelsee and Schulz (1997) marked as 'MPT'. The three phases of surface circulation discussed the text are marked. Periods of significant carbon export are indicated by vertical yellow bars. A) δ^{18}O record from Mix et al. (1995). Selected isotope stages marked; B) U^{K}_{37}'. SST values are shown on the right-hand scale. A 10-pt running mean (i.e. a 50-kyr filter) is shown in black. The 'premature' 100-kyr cycle at the onset of Phase II is highlighted by grey shading; C) Abundance of the $C_{37:4}$ alkenone. The 5% level is marked by the horizontal dashed line; D) Mean grain size of aeolian dust fraction (<30 µm); E) Relative accumulation rate of P665; F) Relative accumulation rate of P410; G) accumulation rates of C_{37} alkenones ('K37') and coccoliths; H) S/I values. S/I = 10 marked by horizontal dashed line.

Periods of high ice volume are associated with low SSTs and high $C_{37:4}$ at ODP 1087A (Figure 3.3A-C). The abundance of $C_{37:4}$ is lower than found at ODP 983, with values never exceeding 5% (Figure 3.3C). High biomarker accumulation rates tend to occur during periods of high ice volume (Figure 3.3E-F), although the time-series are dominated by two periods of sustained increases between ca. 1140-944 ka and 858-740 ka. Consistently low S/I values (<10) indicate a chlorin origin for the pigments. Sediment redistribution processes are unlikely to have driven the biomarker accumulation rates at ODP 1087A. The fine-grained nature of the sediments (nannofossil ooze and clays, Wefer et al., 1998) suggests that they were not affected by the winnowing processes that redistribute organic carbon on the outer shelf to the north (Mollenhauer et al., 2002). Although sandy nannofossil beds are observed in ODP 1087A sediments, they occur on scales of 50-100 cm (Wefer et al., 1998) in contrast to the sustained periods of high biomarker accumulation rates that span several metres. As these intervals also span glacial and interglacial intervals, they cannot have been driven by the glacial remobilisation of exposed interglacial sediments, identified during MIS 2 and 4 off Namibia (Summerhayes et al., 1995). Variations to biomarker accumulation rates are therefore interpreted as representative of the strength of the biological carbon pump at ODP 1087A.

Close correlation between the pigment, alkenone and coccolith accumulation rates occurs throughout the interval of study (Figure 3.3D-F). This is clearly demonstrated by the harmonic spectral analysis results, which show near-identical power spectra between P665 and K37 (Figure 3.4C,E). An intriguing result of the harmonic spectral analysis is the dominance of the non-orbital 71-kyr period in U^{K}_{37}', P665 and K37, although significant variance can also be identified at 92-kyr and 42-kyr in U^{K}_{37}' (close to eccentricity and obliquity). These results are poorly reflected in the evolutive spectra, which fail to identify any significant periodicity at frequencies of less than that of eccentricity (Figure 3.4). As observed at ODP 983, the eccentricity-related signal in U^{K}_{37}' weakens through time. The significance of this trend is unclear, given that the evolutive spectra fail to identify the 71-kyr period dominating the harmonic spectra for biomarker accumulation rates (Figure 3.4). It should be noted that the disappearance of the 100-kyr cycle in U^{K}_{37}' corresponds to the onset of lower sampling resolution (from 5-kyr up to values of 20-kyr) after 800 ka, and the location of a 30-kyr coring gap at 710-740 ka (Figure 3.3). In this section of the core linear interpolation by the evolutive

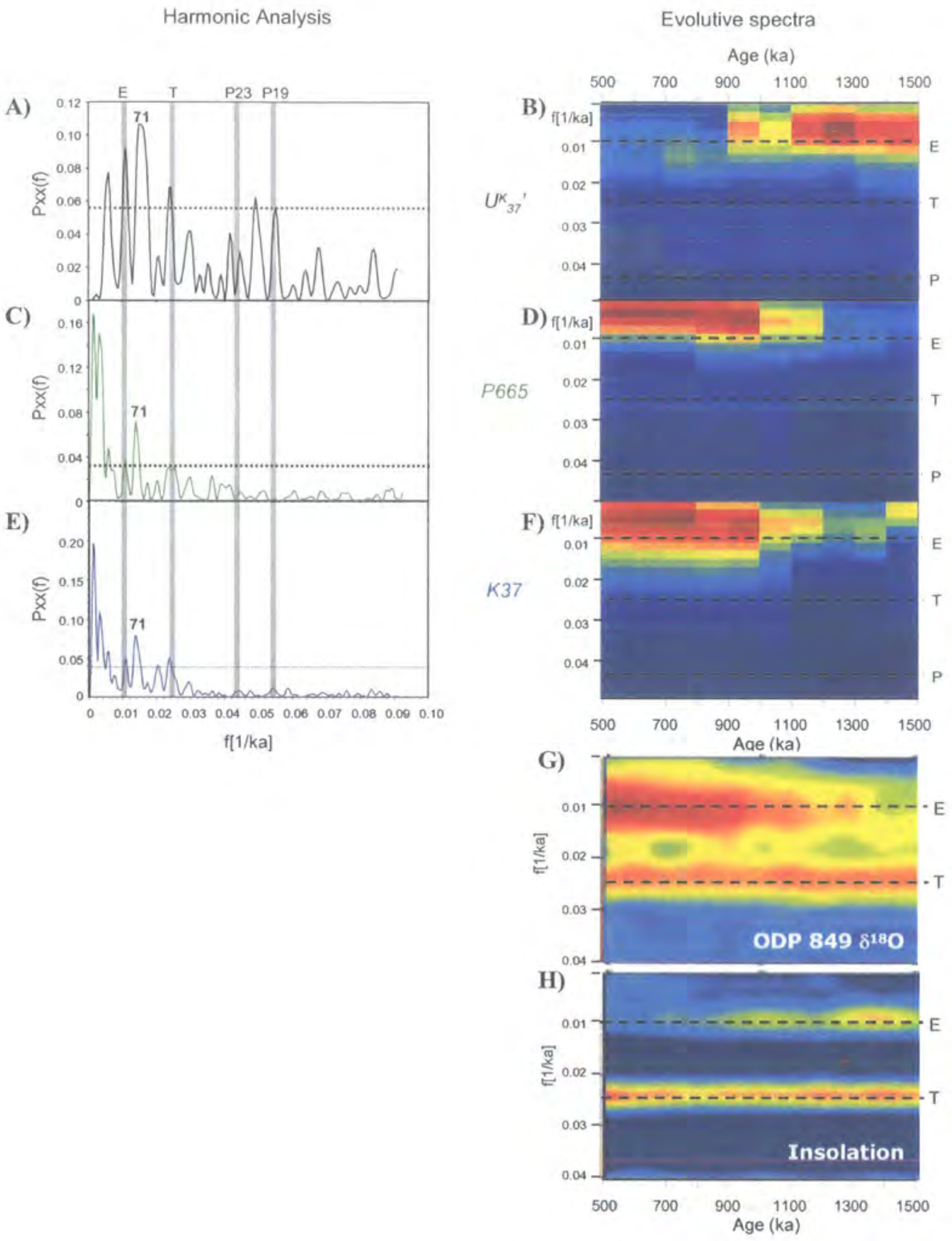

Figure 3-4 Spectral analysis results from ODP 1087A. Milankovitch frequencies shown: E = eccentricity (ca.100-kyr), T = tilt ('obliquity', ca.41-kyr), P = precession (ca.23- and 19-kyr). Other significant peaks are labelled. Left: Harmonic analysis. Peaks lying above horizontal dashed line ('gs') represent periodic components that exceed background white noise (see Chapter 2 for discussion). Right: Evolutive spectra. Variance is identified with significance level of 90% (as described in Chapter 2). Red shading reveals high degree of variance at this significance level, blue reveals low degree of variance at this significance level. (A) U^{K}_{37}' harmonic analysis; (B) U^{K}_{37}' evolutive analysis; (C) P665 accumulation rate harmonic analysis; (D) P665 accumulation rate evolutive analysis; (E) K37 accumulation rate harmonic analysis; (F) K37 accumulation rate evolutive analysis; (G) Evolutive spectra of the benthic d18O ice volume record from ODP 849 (Mix et al.1995); (H) Evolutive spectra of eccentricity and tilt from Berger and Loutre (1991). G and H adapted from analysis by Dr. Nick Pisias presented in Clark et al. (1999).

analysis between samples (see description of method in Section 2.6) may therefore have distorted or masked the dominant frequencies in the time-series.

Long-term trends in the U^{K}_{37}' time series at ODP 1087A, identified by the 50-kyr running mean and the amplitude of U^{K}_{37}' variations, allows the 1500-500 ka interval to be sub-divided into three phases (Figure 3.3). At ca. 1145 ka a shift towards cooler average SST, that lasts for the rest of the interval of study, and a 100-kyr U^{K}_{37}' cycle mark the onset of Phase II. A later shift toward higher amplitude SST variations with the onset of MIS 21 (ca. 880 ka) is used to define the transition between Phases II and III (Figure 3.3). The characteristics of these three Phases will now be outlined:

Phase I: Pre-1145 ka (Pre-MIS 34)

Phase I is characterised by relatively low amplitude (c.4°C) SST oscillations, around a median value of 18.1°C (U^{K}_{37}' = 0.642). %$C_{37:4}$ is low, generally below 2%, with occasional increases to 3% during cool intervals (Figure 3.3C). Biomarker accumulation rates are also relatively low. The strong periodicity identified by evolutive spectral analysis of U^{K}_{37}' at this time (Figure 3.4B) should be interpreted with care, as Phase I includes the 60-kyr core gap after 1316 ka.

Phase II: 1145-875 ka (MIS 34-22)

The onset of Phase II is identified by intense and sustained glacial cooling through MIS 34-32 (post-1145 ka; Figure 3.3B). During MIS 32, SSTs fell and remained below 16°C for the first time in the time-series, reaching a minimum SST of 12.8°C (U^{K}_{37}' = 0.437). %$C_{37:4}$ exceeded 3% for the first time in the time series. The intense cooling during MIS 34-32 is preceded by a prolonged interglacial that corresponds to MIS 35 (Figure 3.3B). The transition from peak interglacial to glacial conditions occurs over an interval of ca. 100-kyr (MIS 35-32), synchronous with the 100-kyr cycle identified at Site 983C.

Phase II is marked by a shift towards cooler average SSTs at ODP 1087A (Figure 3.3). Although SSTs continue to oscillate with an amplitude of around 4°C, the median SST value fell by c.1.7°C relative to Phase I, to a value of approximately 16.5°C (Figure 3.3B). SSTs continued to oscillate around this value for the rest of the time-series (Phases II and III). Interglacial values after this shift correspond more closely to the modern average of around 18°C (Conkright et al., 2002) although the glacial values of

15°C remain several degrees warmer than those of the LGM winter (11-12°C, Gersonde et al., 2003). A cooling signal is also evident in the sustained increase in the abundance of the cold water alkenone $C_{37:4}$ during Phase II, although its abundance never exceeded 5%. Maximum $C_{37:4}$ abundance was attained at 980 ka, synchronous with the maximum $\%C_{37:4}$ identified at ODP 983C (Figure 3.1C). Phase II is also clearly identified by the first phase of sustained high biomarker accumulation rates, which began with the pronounced cooling of MIS 34 but remained high until at least MIS 25 (Figure 3.3E-G). Accumulation rates were generally double those attained during Phase I. Although the record is of low resolution, there is little change in mean particle size during the glaciations of Phase II, suggesting that there was little change to the wind strength above the site.

Phase III: Post-875 ka (post-MIS 22)

Phase III is marked by an increase in the amplitude of SST oscillations to approximately 7°C. The median value of 16.5°C was maintained throughout Phase III (Figure 3.3B). $C_{37:4}$ abundance was more sporadic, highlighting the onset of warmer interglacial values (Figure 3.3C). Intensification of glacial cooling brought SSTs closer to those experienced during LGM winter (11-12°C, Gersonde et al., 2003). Phase III therefore marks the final step in the development of late Pleistocene conditions at ODP 1087A. The second phase of sustained high biomarker accumulation rates occurred during the first 120-kyr of Phase III, with values exceeding the levels attained in Phase II (Figure 3.3E-G). Average accumulation rates were at least three times the abundances of Phase I and the later stages of Phase III. Accumulation rates peaked in all records at ca. 767 ka, before falling abruptly to low levels.

In summary, variations in SST and biomarker accumulation rates associated with glacial-interglacial oscillations can be detected at ODP 1087A. Longer-term trends also prompt a three phase sub-division of the interval 1500-500 ka. Phase II is marked by a permanent cooling shift in average SSTs toward late Pleistocene values. The increasing amplitude of SST oscillations during Phase III results in further cooling during glaciations after MIS 22. The onset of Phase II is marked by pronounced glacial cooling during MIS 34-32, that represents the culmination of a 'premature' 100-kyr cycle similar to that observed at ODP 983C. The biomarker accumulation rate time-series are dominated by two periods of significant increases in accumulation rates, which occurred during Phase II and the onset of Phase III.

3.4 ODP 849D (Eastern Equatorial Pacific)

Figure 3.5 illustrates all results gained from ODP 849D and C. The benthic δ^{18}O record produced by Mix et al. (1995) for the same core is also shown. The U^{K}_{37}' SST record closely follows the δ^{18}O ice volume glacial-interglacial variability, with an amplitude of between 2-2.5°C (Figure 3.5A,B). This is similar to the U^{K}_{37}' SST shifts observed in the tropics at the LGM (Rosell-Melé et al., 2004). The close relationship between U^{K}_{37}' and δ^{18}O ice volume can also be identified in the evolutive spectra (Figure 3.6). Both records show strong variance in the obliquity band, although the signal is weaker in the U^{K}_{37}' time-series, with emergence of the dominant 100-kyr periodicity after ca. 1200 ka.

The accumulation rates of pigments and alkenones show good correlation (Figure 3.5D-F). Biomarker accumulation rates tend to be high during cool, glacial intervals. Although S/I values oscillate around the value of 10, these are not considered to represent terrigenous inputs to the site as observed in the North Atlantic. The principal source of terrigenous material to ODP 849 is from aeolian dust, but this accounts for less than 5% of sediments at the site (Hovan, 1995). The origin of the high S/I values can instead be traced to the presence of carotenoid-like pigments, which have high absorbance in the 470-475 nm range and thus distort absorbance at 410 nm (Figure 3.7). These pigments may be traced to primary production in modern phytoplankton, including blue-green algae, Prymnesiophytes, dinoflagellates and diatoms (Jeffrey et al., 1997). Mass spectrometry analysis is required to confirm their chemical structure and origin. In the absence of this data, and given the impact of these pigments on P410 values, the P665 time-series is applied here to reconstruct the accumulation rates of chlorins. Although strong variance in the obliquity band can be identified in the K37 harmonics record (Figure 3.6E), this signal is not identified in the evolutive analysis, which shows a stronger periodicity near 70-kyr (Figure 3.6F). The harmonic analysis of the chlorin accumulation rate time-series does not exhibit any strong variance at any orbital period, with only a weak signal at c. 53-kyr detected (Figure 3.6C). The differences between the alkenone and pigment spectra may reflect the operation of different controls over coccolithophore production in comparison to the total phytoplankton community. It may also be an artefact of the spectral analyses failing to identify higher frequency signals, as productivity in the tropics has previously been shown to show a strong relationship to

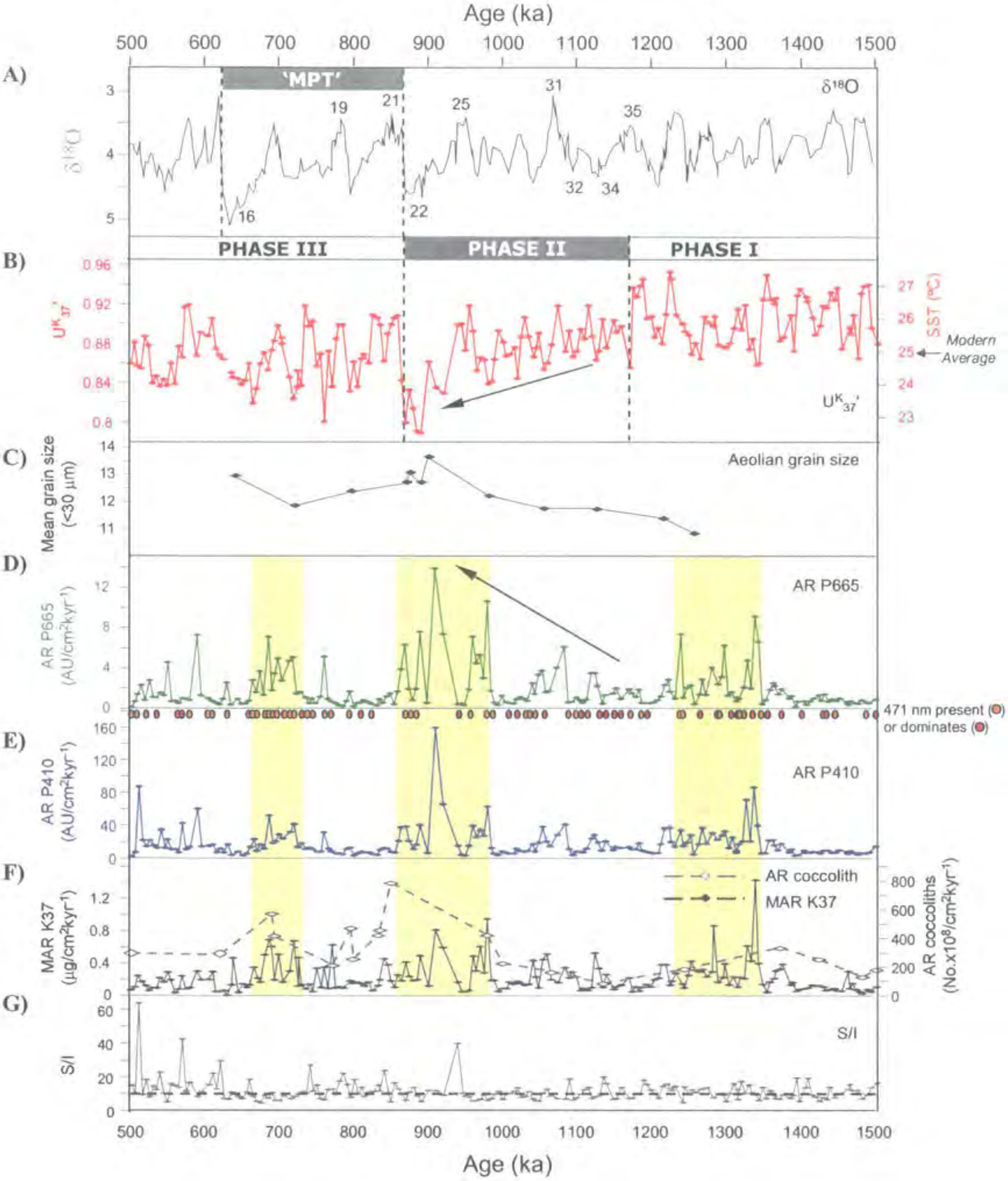

Figure 3-5 All results from ODP 849C and D. The Mid-Pleistocene Transition as defined by Mudelsee and Schulz (1997) marked as 'MPT'. The three phases of surface circulation discussed the text are marked. Periods of significant carbon export are indicated by vertical yellow bars. A) $\delta^{18}O$ record from Mix et al. (1995). Selected isotope stages marked; B) U^K_{37}'. SST values are shown on the right-hand scale. A 10-pt running mean (i.e. a 50-kyr filter) is shown in black; C) Mean grain size of aeolian dust fraction (<30 μm); D) Relative accumulation rate of P665; E) Relative accumulation rates of P410. Samples with absorbance at 471 nm shown by orange dots, samples where 471 nm dominates shown by red dots; F) Mass accumulation rates of C_{37} alkenones ('K37') and accumulation rate coccoliths; G) S/I values. S/I = 10 marked by horizontal dashed line.

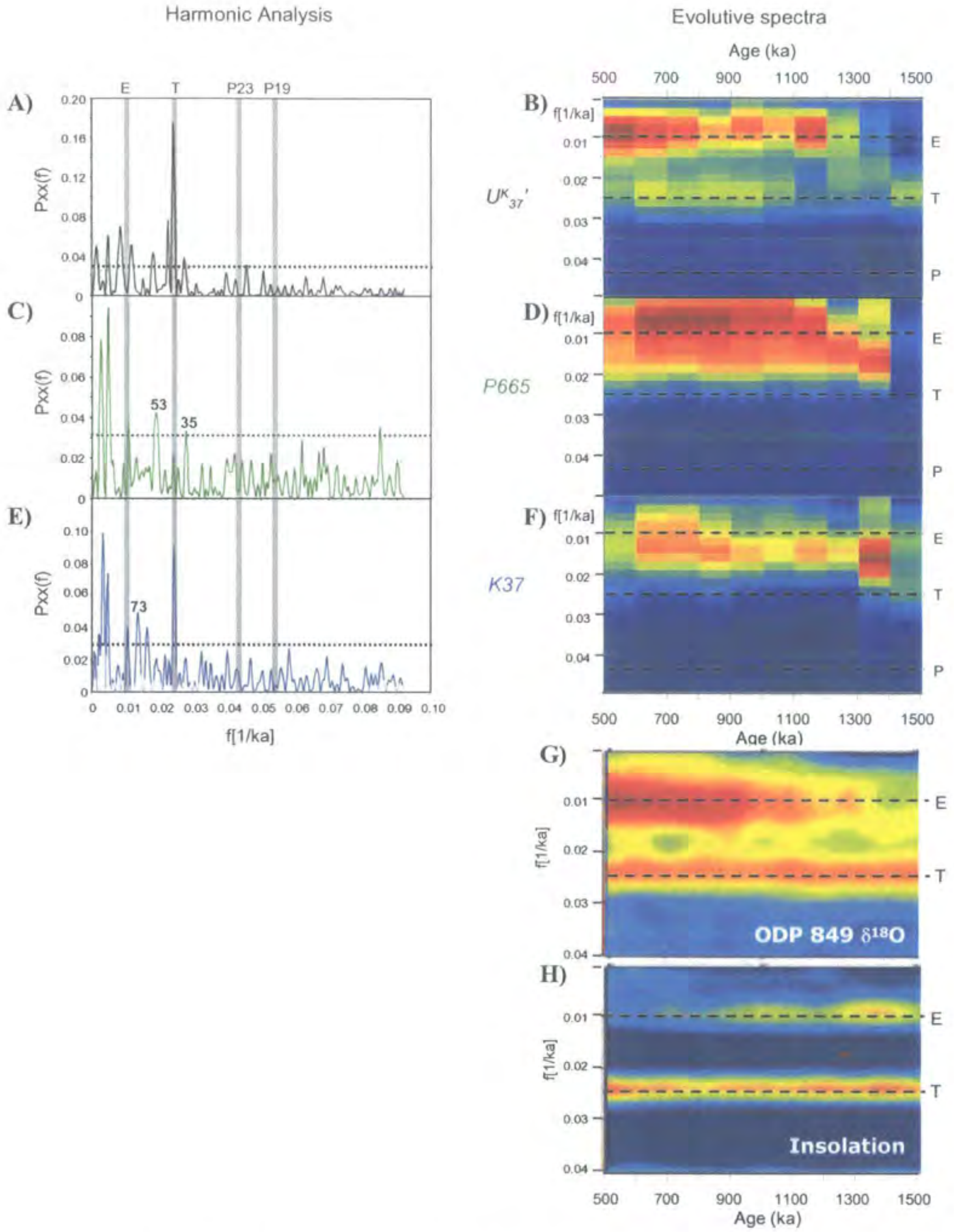

Figure 3-6 Spectral analysis results from ODP 849D. Spectral analysis results from ODP 849D. Milankovitch frequencies shown: E = eccentricity (ca.100-kyr), T = tilt ('obliquity', ca.41-kyr), P = precession (ca.23- and 19-kyr). Other significant peaks are labelled. Left: Harmonic analysis. Peaks lying above horizontal dashed line ('gs') represent periodic components that exceed background white noise (see Chapter 2 for discussion). Right: Evolutive spectra. Variance is identified with significance level of 90% (as described in Chapter 2). Red shading reveals high degree of variance at this significance level, blue reveals low degree of variance at this significance level. A) U^{K}_{37}' harmonic analysis; (B) U^{K}_{37}' evolutive analysis; (C) P665 accumulation rate harmonic analysis; (D) P665 accumulation rate evolutive analysis; (E) K37 accumulation rate harmonic analysis; (F) K37 accumulation rate evolutive analysis; (G) Evolutive spectra of the benthic d18O ice volume record from ODP 849 (Mix et al.1995); (H) Evolutive spectra of eccentricity and tilt from Berger and Loutre (1991). G and H adapted from analysis by Dr. Nick Pisias presented in Clark et al. (1999).

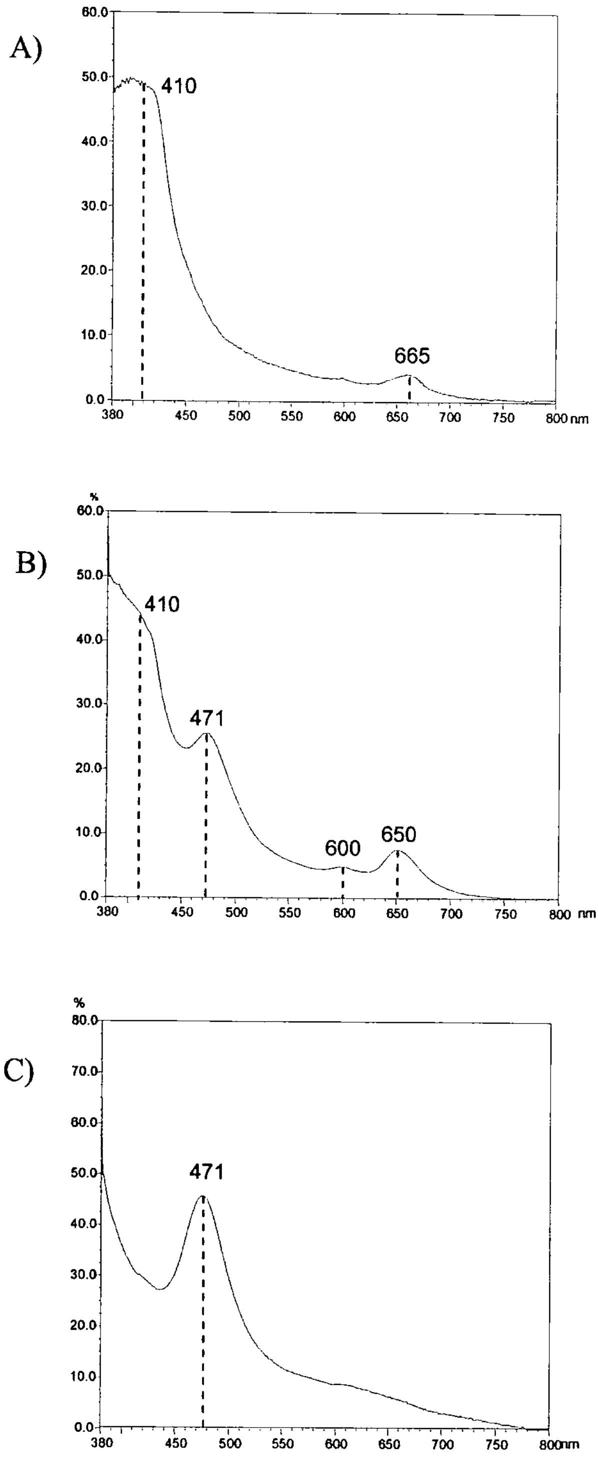

Figure 3-7 Typical absorbance spectra from ODP 849. Solvent: acetone. A) Typical chlorin-dominated spectrum, dominated by peaks at 410 nm and 665 nm (Sample 849C-2H-3W, 140-141; ca. 595 ka); B) Presence of additional peaks in the 471 nm wavelength, indicating the presence of carotenoid pigments (Sample 849D-2H-2W, 135-136; ca. 685 ka); C) 471 nm dominates (Sample 849D-4H-1W, 148-149; ca. 1435 ka).

precession and non-orbital frequencies e.g. 30-kyr (Pisias and Mix, 1997; Beaufort et al., 2001). No significant shifts in the dominant periodicities through time are detected in either biomarker accumulation rate evolutive spectra (Figure 3.6C,E).

The long-term trend in the U^{K}_{37}' time series at ODP 849D, as identified by the 50-kyr running mean, allows the 1500-500 ka interval to be sub-divided into three phases (Figure 3.5). At ca. 1170 ka (MIS 35) a progressive decline in average SSTs began, culminating in intense glacial cooling during MIS 22 (until 875 ka). A slight warming of average SSTs after MIS 22 and a shift toward higher amplitude SST variations with the onset of MIS 21 (ca. 875 ka) is used to define the transition between Phases II and III (Figure 3.5). The characteristics of these three Phases will now be outlined:

Phase I: 1500- 1170 ka (MIS 35 and earlier)

Phase I is dominated by glacial-interglacial variability in SST with a period of 41-kyr (Figures 3.5A, 3.6B). These oscillations occurred in phase with the $\delta^{18}O$ ice volume record (Figures 3.5A, 3.6G). Relatively high pigment and alkenone abundance occurred during the glacials between ca. 1345-1200 ka.

Phase II: 1170-875 ka (MIS 35-22)

Phase II is identified by a long-term cooling trend that gradually lowered SSTs by approximately 0.5°C between MIS 35 and 26 (Figure 3.5B). It culminated in pronounced glacial cooling during MIS 22, when SSTs fell as low as 22.5°C (Figure 3.5B). The period of the SST oscillations also shifted from 41-kyr to 30-35-kyr during Phase II. As a result, a weaker correlation to $\delta^{18}O$ variations developed, with SSTs generally leading $\delta^{18}O$ by ca. 15-kyr. Chlorin accumulation rates and the grain size of the dust fraction (a proxy for wind strength) reached their maxima at ca. 910 ka as the cooling intensified (Figure 3.5B-D). Unlike the two Atlantic records, a premature 100-kyr cycle during MIS 35-32 is not identified at ODP 849D, with cooling beginning earlier at ca. 1170 ka (within MIS 35).

Phase III: Post-875 ka (Post-MIS 22)

The long-term cooling trend of Phase II resulted in a permanent cooling shift at ODP 849D, with average SSTs during Phase III c.1.0-1.5°C lower than those of Phase I. Interglacial SSTs (around 26°C) in Phase III corresponded more closely to annual SSTs at the present day (modern annual range: between 23-26°C, Conkright et al., 2002).

Glacial SSTs during Phase III are also comparable to those reconstructed for the late Pleistocene (e.g. Lea et al., 2000; Rosell-Melé et al., 2004). Phase III marks an increased dominance of eccentricity-related SST variations, and a return to an in-phase relationship between oscillations in U^K_{37}' and $\delta^{18}O$ ice volume (visible by eye on Figure 3.5, and in Figure 3.6). The accumulation rates of pigments and alkenones returned to relatively low values during Phase III. A slight increase in accumulation rates was sustained between ca. 780-640ka (MIS 18-17). This interval is unusual for the time-series at ODP 849, as it occurred during an interglacial, when previous cycles of high accumulation rates occurred during cool intervals.

In summary, glacial-interglacial oscillations in SSTs and biomarker accumulation rates can be detected at ODP 849D during the early- and mid-Pleistocene. Long-term trends allow a three phase sub-division of the interval 1500-500 ka. Phase I exhibits relatively high-frequency, obliquity-related variations in SST and biomarker accumulation rates, which show good correlation to ice volume variations. Phase II is marked by a gradual but permanent cooling in average SSTs toward late Pleistocene values. This began at ca.1170 ka during MIS 35, earlier than the Phase II onset in the Atlantic cores. The progressive cooling during Phase II culminates in intense glacial cooling and a large increase in chlorin accumulation rates during MIS 22. Phase III is marked by the development of higher amplitude SST oscillations after MIS 22, and reduced biomarker accumulation rates.

3.5 ODP 806 (Western Equatorial Pacific)

All results from ODP 806B are shown in Figure 3.8. The benthic $\delta^{18}O$ record from ODP 849D (Mix et al., 1995) is also shown for reference. Although Pelejero and Calvo (2003) recommended that samples where $C_{37:3}$ could not be detected should not be displayed as $U^K_{37}' = 1$ (see Discussion in Chapter 1), they are shown on Figure 3.8 so that the warmest intervals, where SSTs exceeded 28.9°C, can be identified. This SST is produced based on the Müller et al. (1998) calibration (shown here in Section 1.6.3.1 page 45). At high U^K_{37}' values it has been demonstrated that this SST calibration may underestimate SST change compared to local or regional U^K_{37}'-SST calibrations in tropical waters (Pelejero and Calvoe, 2003). Here, the Müller et al. (1998) calibration is shown so that direct comparisons can be made with the three sites presented previously in this chapter. It should be noted that much of the variability in U^K_{37}' lies within the margin of error

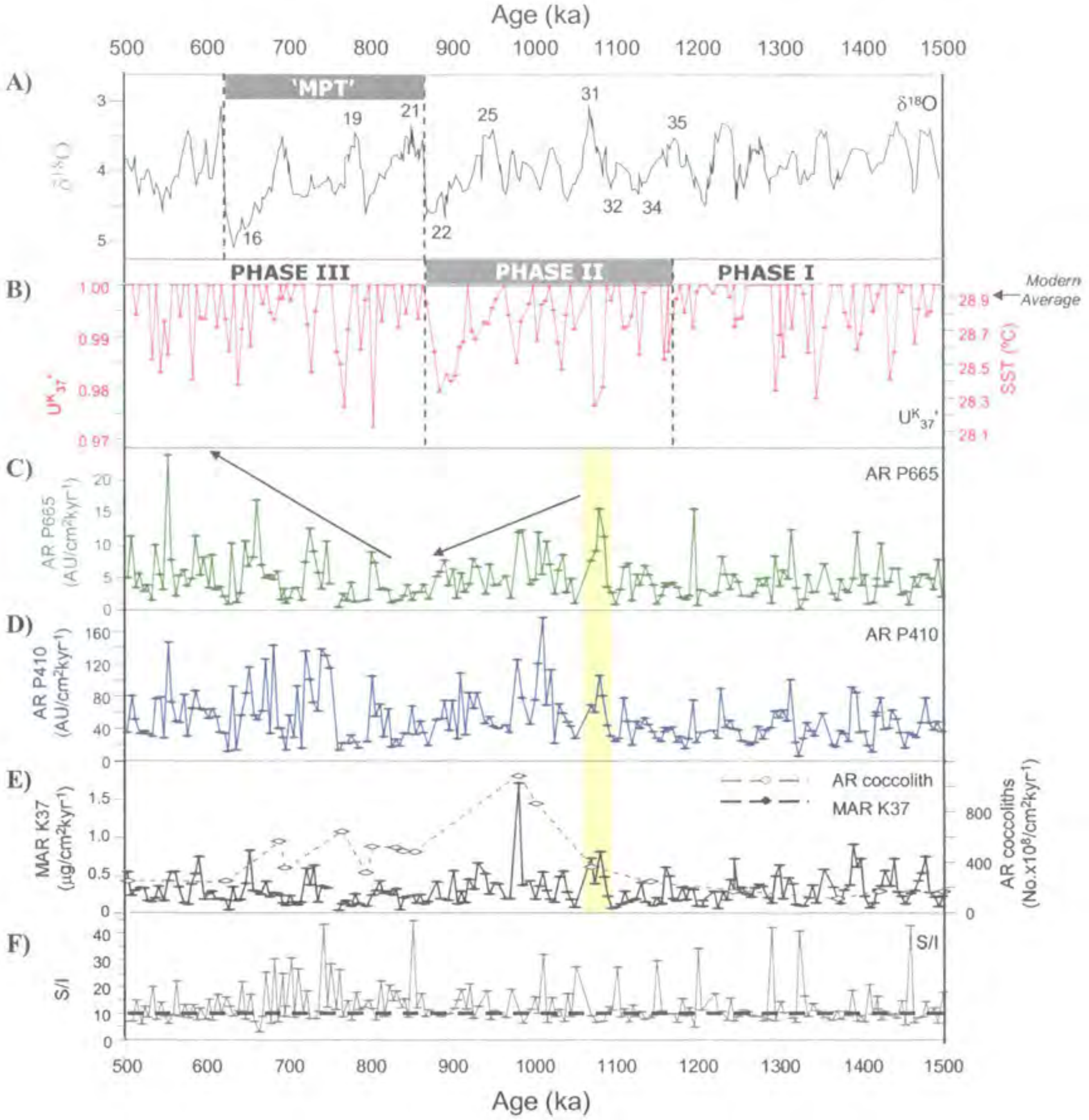

Figure 3-8 All results from ODP 806B. The Mid-Pleistocene Transition as defined by Mudelsee and Schulz (1997) marked as 'MPT'. The three phases of surface circulation discussed the text are marked. Periods of significant carbon export are indicated by vertical yellow bars. A) δ^{18}O record from Mix et al. (1995). Selected isotope stages marked; B) U^{K}_{37}'. SST values are shown on the right-hand scale. A 10-pt running mean (i.e. a 50-kyr filter) is shown in black. The error in U^{K}_{37}' values associated with the extraction and analysis (0.016 U^{K}_{37}' units, described in Chapter 2) is shown by the error bar. The grey shading highlights values lying within this error margin from a U^{K}_{37}' of 1.00; C) Relative accumulation rate of P665. Long-term trends in P665 maxima are shown by the arrows; D) accumulation rate of P410; E) Mass accumulation rate of C_{37} alkenones ('K37') and accumulation rate of coccoliths; F) S/I values. S/I = 10 marked by horizontal dashed line.

associated with the extraction and analytical methods (see discussion in section 2.2.5.4 in Chapter 2). Care should therefore be taken when interpreting the absolute SST values, acknowledging both the potential analytical and calibration errors.

Glacial-interglacial variability can still be detected using the U^K_{37}' time-series. Low U^K_{37}' values occur during intervals of high ice volume, and SSTs exceed the upper limit of U^K_{37}' during interglacials (Figure 3.8A,B). As the upper limit of U^K_{37}' can not be determined, the minimum range of glacial-interglacial SST variability at ODP 806 is 0.9°C based on the U^K_{37}' calibration of Müller et al. (1998). This variability lies within the 2-3°C variations reconstructed during late Pleistocene glacial-interglacial oscillations in this area (e.g. Lea et al., 2000 ; De Dekker et al., 2002; Stott et al., 2002; Rosell-Melé et al., 2004). The good relationship between the U^K_{37}' and $\delta^{18}O$ time-series is also clear in the spectral analysis. Both time-series have a dominant periodicity in the obliquity band for much of the interval of study, with the emergence of the 100-kyr period visible after 1200 ka (Figure 3.9B,D,I).

As observed at ODP 849, high S/I values (>10) occur throughout the record at ODP 806B. This cannot be attributed to terrigenous carbon inputs, as aeolian sediments are a minor component (<10%) of nearby ODP 805C (Krissek and Janecek, 1993). Carotenoid-like pigments of marine plankton origin are also detected at ODP 806B (Figure 3.10), which will increase the value of P410 (see discussion above). P665 is therefore used to represent chlorin accumulation rates at ODP 806B. There is good correlation throughout the interval of study between the accumulation rates of pigments and alkenones, and glacial-interglacial variability can be identified (Figure 3.8C-E).

Figure 3-9 (Overleaf) Spectral analysis results from ODP 806B. Milankovitch frequencies shown: E = eccentricity (ca.100-kyr), T = tilt ('obliquity', ca.41-kyr), P = precession (ca.23- and 19-kyr). Other significant peaks are labelled. A,C,E,G: Harmonic analysis. Peaks lying above horizontal dashed line ('gs') represent periodic components that exceed background white noise (see Chapter 2 for discussion). B,D,H,I,J: Right: Evolutive spectra. Variance is identified with significance level of 90% (as described in Chapter 2). Red shading reveals high degree of variance at this significance level, blue reveals low degree of variance at this significance level. (A) U^K_{37}' harmonic analysis, including samples with U^K_{37}' = 1; (B) U^K_{37}' evolutive analysis, including samples with U^K_{37}' = 1; (C) U^K_{37}' harmonic analysis, excluding samples with U^K_{37}' = 1; (D) U^K_{37}' evolutive analysis, excluding samples with UK37' = 1; (E) P665 accumulation rate harmonic analysis; (F) P665 accumulation rate evolutive analysis; (G) K37 accumulation rate harmonic analysis; (H) K37 accumulation rate evolutive analysis. I) Evolutive spectra of the ODP 849 benthic d18O ice volume record (Mix et al.1995); (J) Evolutive spectra of eccentricity and tilt (data: Berger and Loutre, 1991). I and J adapted from analysis by Dr. Nick Pisias presented in Clark et al. (1999).

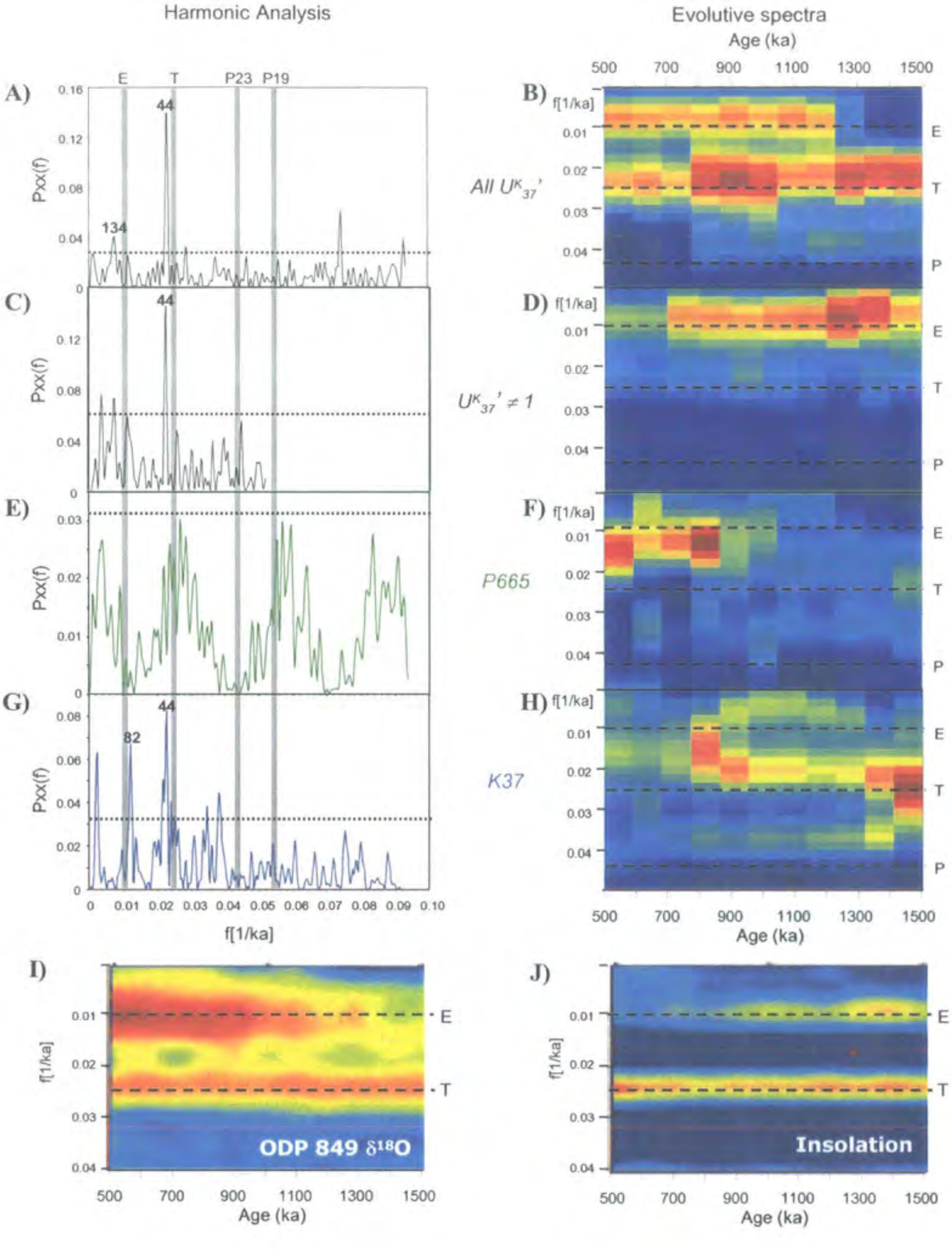

Figure 3.9 Spectral analysis results from ODP 806B. For explanation see the caption on the previous page.

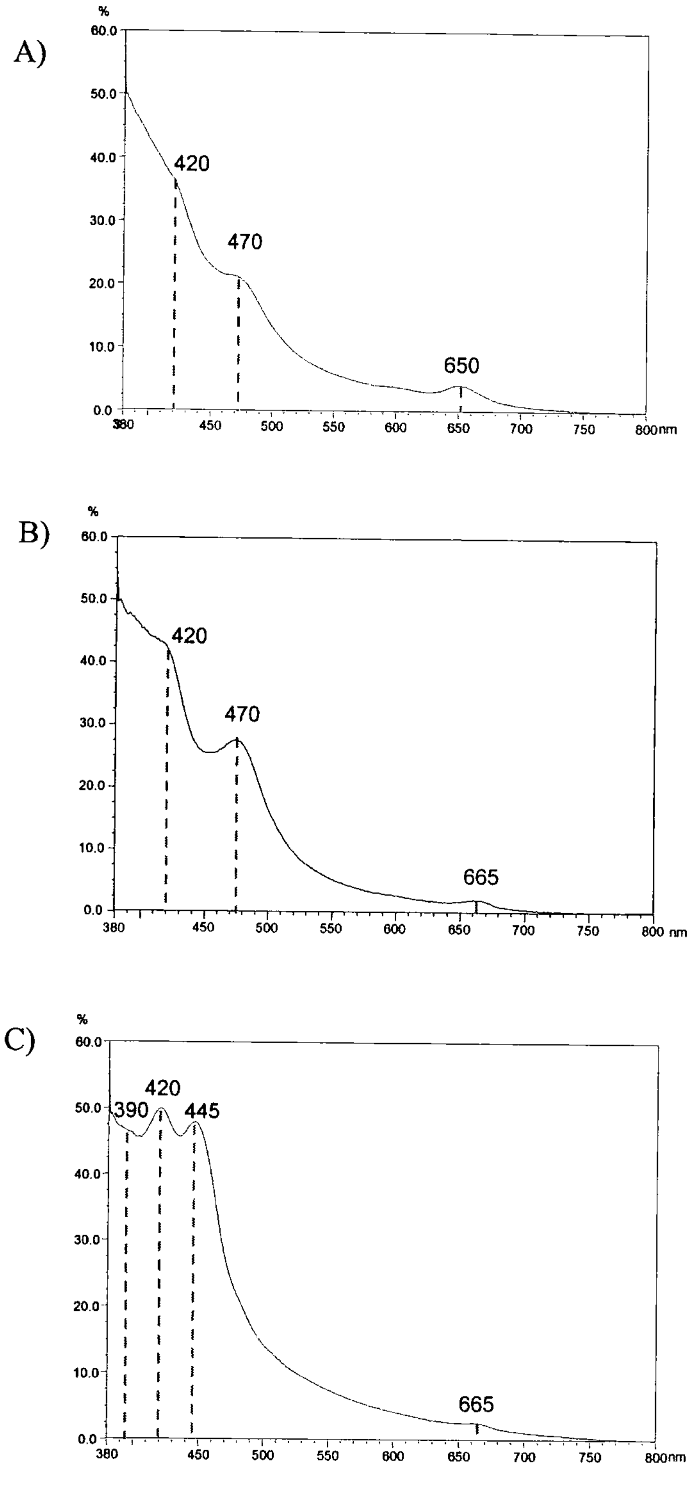

Figure 3-10 Typical absorbance spectra from ODP 806B. Solvent: acetone. A) Presence of 665 nm and 480 nm wavelengths (Sample 806B-4H-2W,13-14; ca. 1340 ka); B) 471 nm dominates, indicating the presence of carotenoid pigments (Sample 806B-4H-3W, 4-5; ca. 1410 ka); C) Additional peaks at low-wavelengths (Sample 806B-2H-6W,98-99; ca. 690 ka).

High biomarker accumulation rates are found during cool glacial intervals (Figure 3.8). The glacial-interglacial variability visible in Figure 3.8 is poorly identified in the spectral analysis results. The harmonic and evolutive spectra suggest that there is no strong periodicity in the chlorin accumulation rates until after ca. 800 ka (Figure 3.9E,F). A stronger signal is evident in the alkenone accumulation rates, which shows a strong signal near obliquity in the harmonic analysis (Figure 3.9G). This signal is weak in the evolutive spectrum however, which shows a shift from obliquity to eccentricity through time (Figure 3.9H). These differences may reflect the underlying forcing of tropical Pacific production by precessional and non-orbital frequencies (Pisias and Mix, 1997; Beaufort et al., 2001), which cannot be detected by the spectral analysis at the resolution of the time-series analysed here.

The long-term trend in the U^{K}_{37}' time series at ODP 806B, as identified by the 50-kyr running mean, allows the 1500-500 ka interval to be sub-divided into three phases (Figure 3.8). At ca. 1165 ka (MIS 35) average SSTs began to fall, marking the transition between Phases I and II. Two periods of apparent strong cooling occurred, at the transition between MIS 32-31 and during MIS 22. Average SSTs warmed after MIS 22 (ca. 880 ka). This warming is used to define the transition between Phases II and III (Figure 3.8). The characteristics of these three Phases will now be outlined:

Phase I: Pre-1165 ka (MIS 35 and earlier)

Phase I exhibits glacial-interglacial variability in U^{K}_{37}' and alkenone accumulation rates dominated by a ca. 41-kyr frequency (Figures 3.8, 3.9D). No significant signal could be detected in the pigment accumulation time-series (Figure 3.9,F), which oscillated below a maximum of approximately 12 AU/cm^2kyr^{-1} (Figure 3.8).

Phase II: 1165-880 ka (MIS 35-22)

The onset of Phase II is defined by a reduction in the abundance of values where $U^{K}_{37}' = 1$, suggesting of the onset of generally cooler surface ocean conditions (Figure 3.9B). The Phase I-II boundary is marked by the emergence of 100-kyr periodicity within the U^{K}_{37}' record, although the 41-kyr signal remains strong (Figure 3.8B). The Phase II cooling was most pronounced during MIS 22 (ca. 915-880 ka), synchronous with the intense cooling episode at ODP 849D (Figure 3.5B). An earlier cool interval correlates to the MIS 32-31 boundary (Figure 3.9B), and is also marked by high P665 accumulation rates that reach a maximum ca. 1080 ka (Figure 3.9C). After this time, Phase II exhibits a progressive long-term decline in chlorin accumulation rates (Figure 3.8C).

Phase III: Post-880 ka (Post-MIS 22)

The post-880 ka period is marked by a progressive increase in biomarker accumulation rates at ODP 806B (Figure 3.8C). A strong 100-kyr periodicity develops in the pigment accumulation rate time-series (Figure 3.9F). An increase in the frequency of U^{K}_{37}' values exceeding 1 suggests that interglacial SSTs warmed during Phase III (Figure 3.8B). Cool intervals continue to correlate with glaciations in the $\delta^{18}O$ record (Figure 3.8B). Strong variance at 100-kyr and 41-kyr continues to occur in the U^{K}_{37}' time-series, although the strength of the obliquity-related signal fell from Phase II (Figure 3.9B).

Biomarker accumulation rates at ODP 806B may be affected by current winnowing and sediment redistribution. The impacts of these processes have been identified at ODP 806B during the late Pleistocene and are proposed to account for the 100-kyr cyclicity in the deposition of interplanetary dust particles, previously used to support an orbital inclination origin for the 100-kyr climate cycles (Higgins et al., 2002). Higgins et al. (2002) proposed that the strength of the winnowing bottom currents at ODP 806 are determined by the strength of thermohaline circulation. A rapid and sustained reduction in the thermohaline inflow to the Pacific occurred after ca. 900 ka (Hall et al., 2001). The impact of this shift on sediment redistribution in the region of ODP 806B is not known, but it may have reduced the erosive power of the bottom currents at the site and encouraged the increased biomarker accumulation rates found during Phase III. However, Berger et al. (1994) found no relationship between sand content (suggestive of winnowing) and sedimentation rates at ODP 806B throughout the Pleistocene. They suggested that sedimentation rates were principally controlled by variations in surface ocean productivity. It is proposed here that while winnowing may have influenced sedimentation at ODP 806B, variations to the strength of the biological carbon pump dominate the biomarker accumulation rate records.

In summary, despite the upper limit of U^{K}_{37}' being exceeded during warm stages, glacial interglacial variability in SSTs and biomarker accumulation rates were detected at ODP 806B. Long-term trends result in a three-phase sub-division of the interval 1500-500 ka. Phase II is marked by sustained cooling during glacial times and a progressive decline in chlorin accumulation rates. The reduced frequency of unity values for U^{K}_{37}' suggests that interglacial SSTs may also have cooled. Variance at the 41-kyr period can be identified throughout the U^{K}_{37}' time-series, with 100-kyr cycles emerging during Phase II. The onset of Phase III is marked by the termination of the intense cooling during MIS 22, after which chlorin accumulation rates progressively rise, and develop a strong 100-kyr periodicity.

3.6 Synthesis and Conclusions

At all four sites examined here, changes in surface ocean conditions (temperatures and water mass domains) and biomarker accumulation rates have been detected during the early and mid-Pleistocene. The highest amplitude SST oscillations occur in the two Atlantic cores, ODP 983C and 1087A, with oscillations of at least 4°C. ODP 983C consistently exhibits the greatest amplitude of SST variations throughout the 1500-500 ka interval (approximately 8°C prior to MIS 35 and after MIS 22), although after MIS 22 SST oscillations at ODP 1087A reach an amplitude of around 7°C. SST oscillations at ODP 849D in the east equatorial Pacific were generally of a 2.0-2.5°C amplitude. Although the warmest SSTs could not be determined at ODP 806B, late Pleistocene SST reconstructions suggest that the amplitude of SST oscillations at the site probably did not exceed 2.0-3.0°C. ODP 1087A contained the highest abundances of biomarkers by at least an order of magnitude.

Variability was detected at two timescales: associated with glacial-interglacial oscillations, and over longer timescales. Significantly, the long-term trends allowed the records from all four sites to sub-division into three phases. The Phase I-II boundary between the four cores ranges from 1170-1145 ka, and the Phase II-III boundary ranges from 880-875 ka. Given that the margin of error in $\delta^{18}O$ age assignments between sites is up to 16 kyr (Table 1-3) the timing of the three phases is broadly synchronous between the four sites, although the Phase I-II boundary in the Pacific sites (1170 ka for ODP 849D, 1165 ka for ODP 806B) leads that of the Atlantic sites (1143 ka for ODP 983C, 1145 ka for ODP 1087A) outside this margin or error. All four records defined the Phase II-III boundary at the MIS 22-21 transition ca. 900 ka. The Phase I-II boundary was identified by the onset of cooling in all records, which occurs during MIS 34 at the two Atlantic sites (ca. 1145 ka), but during MIS 35 at the two Pacific sites (ca. 1170 ka). The difference between the timing of the Phase I-II boundary between the Atlantic and Pacific sites is also demonstrated by the presence of a '100-kyr' cycle in the Atlantic records, which is not found in the Pacific. This cycle is marked by a temporary decoupling of the SST time-series from the 41-kyr period during MIS 35-32. A sustained interglacial followed by pronounced glacial cooling marks the development of an extended interglacial to glacial cycle that has a duration of ca. 100-kyr. Significantly, a similar cycle has been detected at this time in both the $\delta^{18}O$ ice volume record (Figures 3.1, 3.3; Mudelsee and Stattegger, 1997) and a record of NADW circulation from the South Atlantic (Schmieder et al., 2000). Mudelsee and Stattegger (Mudelsee and Stattegger, 1997) proposed that this represented a 'premature' 100-kyr cycle developing prior to their dominance after MIS 22. The absence of this cycle from the two equatorial Pacific records suggests that the significance of this event may be restricted to the high latitudes and/or Atlantic Ocean circulation system.

Relatively high frequency oscillations in SST and biomarker accumulation rates characterise Phase I at all four sites. These oscillations correlate with the 41-kyr glacial-interglacial oscillations that dominate the global ice volume records prior to the MPT and which correlate with obliquity forcing. The common characteristic of Phase II at all four sites is sustained cooling. At ODP 983C and 806B this cooling is temporary for the duration of Phase II. A sustained but temporary increase in the abundance of the Arctic Water domain proxy $\%C_{37:4}$ also marks Phase II at ODP 983C. At ODP 849D, a progressive decline in SSTs also results in a permanent cooling shift of SSTs by around 0.5°C from Phase I to Phase III. The most significant long-term impact of the Phase II cooling trend is the permanent and rapid shift in SSTs at ODP 1087A, with average SSTs falling by 1.7°C. This occurs after intense glacial cooling during MIS 34-32. In the tropical Pacific, the cooling is most intense in the final stages of Phase II, with pronounced and synchronous cooling characterising MIS 22 at both ODP 849D and 806B. Phase II is also marked by intervals of high biomarker accumulation rates at all sites. This is particularly significant at ODP 1087A, where high accumulation rates are sustained for the duration of Phase II, irrespective of glacial-interglacial oscillations. At ODP 849D, high biomarker accumulation rates occur as the long-term cooling trend intensifies, through MIS 26-22. At ODP 983C and 806B, biomarker accumulation rates peak during the warm interglacial of MIS 35.

Phase III is marked by renewed interglacial warming at all four sites, at the termination of MIS 22. A second pulse of sustained high biomarker accumulation rates marks the first 200-kyr of Phase III at ODP 1087A. The amplitude of the glacial-interglacial oscillations at ODP 1087A increase in response to interglacial warming but intensification of glacial cooling during Phase III, and bring the amplitude of SST oscillations (around 7°C) close to those of ODP 983C in the north (around 8°C). Biomarker accumulation rates fall during Phase III at ODP 849D, but progressively rise at ODP 806B. The frequency of the SST and biomarker accumulation rate variations generally decreases during Phase III, in association with the development of longer glacial-interglacial oscillations in the global ice volume record. The exception to this trend is the SST record from ODP 983C, shows emergence of 41-kyr periodicity through time, similar to the shift identified in the insolation records. The significance of this trend at ODP 983C requires further investigation given a number of issues that arose with the spectral analysis of this core site.

The results presented in this Chapter therefore demonstrate that a number of significant changes occurred in surface ocean conditions and the strength of the biological carbon pump between 1500-500 ka. In the following three chapters, the causes and implications of these trends are discussed. First, the validity of the U^{K}_{37}' index for reconstructing SSTs before the late Pleistocene is evaluated in Chapter 4. This is followed in Chapter 5 by a comparison of all four SST records to discuss the occurrence of a global cooling trend. In Chapter 6, the biomarker accumulation rate time-series are compared, in an attempt to deduce a global trend and to examine the role that this may have played in driving the mid-Pleistocene climate changes discussed in Chapters 4 and 5. In Chapter 7, the behaviour of the tropical Pacific circulation system is examined. Chapter 8 provides a summary of the issues raised in the discussion chapters, and suggestions for further work.

4. Alkenone and coccolith records of the mid-Pleistocene in the South-east Atlantic: Testing the validity of the U^{K}_{37}' index

4.1 Introduction

Successful application of the alkenone palaeothermometer, the U^{K}_{37}' index, relies on past alkenone-synthesisers responding to growth-temperature changes in a similar manner to the modern alkenone producers, chiefly the coccolithophore *Emiliania huxleyi*. Combined analyses of coccolithophore assemblages and alkenones from sediments in the north-east and south-east Atlantic suggest that a similar biogeochemical response to changing SSTs occurs in alkenone producers back to ca. 400 ka (Müller et al., 1997; Weaver et al., 1999; Villanueva et al., 2002).

As outlined in Chapter 1, the final coccolithophore extinctions prior to the emergence of *E.huxleyi* occurred during the early- and mid-Pleistocene (Weaver, 1993). The impact of these evolutionary events on the U^{K}_{37}'-SST relationship has not been tested. This period of time is also marked by a series of zones where the coccolithophore assemblage is dominated by a single species of coccolithophore ('acme zones', Weaver, 1993). If during these events the nature of the U^{K}_{37}'-SST relationship was altered, application of the modern U^{K}_{37}'-SST calibration prior to the late Quaternary could be inappropriate.

This issue is addressed in this Chapter by comparing alkenone and coccolith records for the interval 1500-500 ka, following the approach of Müller et al. (1997), Villanueva et al. (2002), and Weaver et al. (1999). The records were generated from ODP Site 1087A, where coccoliths and alkenones are very abundant in the carbonate and organic fractions, allowing an excellent opportunity for comparison of the two records. The methods of alkenone and coccolith analysis have been described in Chapter 2.

4.2 Results and Discussion

4.2.1 U^{K}_{37}'

Figure 4.1A illustrates the U^{K}_{37}' record from ODP 1087A. Two significant events were described in Chapter 3: an increase in the amplitude of U^{K}_{37}' variations after ca. 875 ka, and a cooling shift of ca.1.67°C after ca.1150 ka. These are marked in Figure 4.1 by vertical dashed lines. This shift is permanent, and marks the development of interglacial SSTs that correlate more closely to modern annual values (ca. 18°C, Conkright et al., 2002). The abrupt nature of the cooling shift may have two origins.

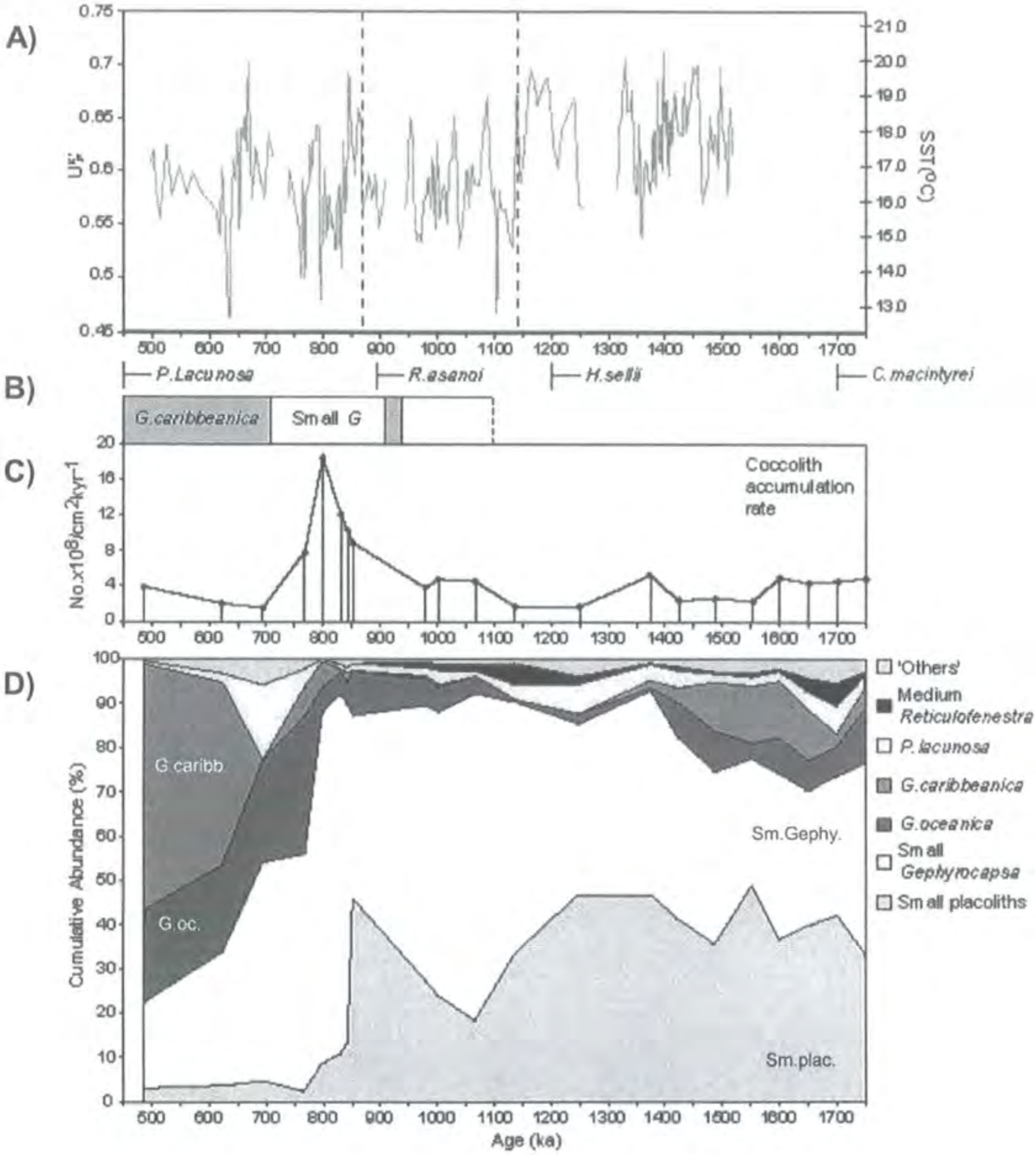

Figure 4-1 Comparison of U^{K}_{37}' and coccolith records from ODP 1087A. A) U^{K}_{37}' time-series (grey), as presented in Chapter 3 (Figure 3.3). SSTs generated using the Müller et al (1998) calibration are shown in scale on the right. The shift in median SSTs after ca. 1150 ka and the increase in amplitude of SST variations are marked by vertical dashed lines; B) Nannofossil last appearance datums (LADs) of *P.lacunosa*, *R.asanoi*, *H.sellii* and *C.macintyrei,* and acme zones of Hine and Weaver (1998). Dark shading indicates *G.caribbeanica* acmes, white indicates small *Gephyrocapsa* acmes. LAD datums as defined in Chapter 1; C) Coccolith accumulation rates, in numbers counted x 108/cm2kyr-1; D) Relative abundances of major coccolithophore groups

It may represent a change in the state of the surface ocean taking place at Site 1087 during the mid-Pleistocene, or it may demonstrate that a change in the structure of the coccolithophore assemblage altered the U^{K}_{37}' response to SSTs. If the dominant alkenone-synthesisers occupied a different habitat (e.g. increased depth in the water column, spring production rather than summer), and/or altered their biosynthetic mechanism for production of U^{K}_{37}' after ca. 1150 ka BP, the observed fall in U^{K}_{37}' may not reflect a 'real' palaeoclimate event. Rather, it may represent a change in the nature of the U^{K}_{37}'-SST relationship.

4.2.2 The coccolith assemblage

Figure 4.1B shows the timing and duration of the nannofossil acme zones (after Hine and Weaver, 1998) and the Last Appearance Datums (LADs) of mid-Pleistocene coccolithophores at ODP 1087A. Although a variety of LADs occur during the interval of study, Figure 4.1 shows that none correlate with the SST shift ca. 1150 ka. Although the last occurrence of *Helicosphaera sellii* is observed at ca. 1220 ka BP, this species is generally in low abundance (<2%), and a full glacial-interglacial cycle occurs between its extinction and the cooling shift. Nor does *H.sellii* belong to the Gephyrocapsaceae family whose ancestors are proposed to have produced the alkenones found in the sedimentary record back to ca. 45 Ma (Marlowe et al., 1990). These relationships suggest that the extinction of *H.sellii* had a minimal impact on the U^{K}_{37}' record.

Figure 4.1D illustrates the structure of the coccolithophore assemblage between ca.1700-500 ka at ODP 1087A. The assemblage at ODP 1087A closely resembles the nannofossil acme zonation (Figure 4.1B). Throughout the interval of study, *Gephyrocapsa* species dominate the coccolithophore assemblage. Prior to ca.800 ka, small placoliths and small *Gephyrocapsa* account for >70% of the population. Reduced abundance in one group is balanced by increased abundance in the other. Although the coccolith record is at a much lower resolution than the alkenone time-series, a number of changes to the coccolithophore assemblage can be detected.

The cooling shift after 1200 ka is associated with a reduction in the relative abundance of the small placoliths (Figure 4.1D). This is balanced by an increase in the abundance of the small *Gephyrocapsa*, so that the coccolithophore assemblage continues to be dominated by the smallest species. After ca. 800 ka, the most significant change to the coccolith assemblage occurs, marking the end of the dominance of the smaller species.

From ca. 800 ka, small *Gephyrocapsa* numbers decline sharply, replaced first by increases in *G.oceanica*, then *P.lacunosa* and finally by *G.caribbeanica*. The latter species dominates the record from ca. 620 ka (acme zone of QAZ4 of Hine and Weaver, 1998). Small *Gephyrocapsa* remain a significant component of the assemblage in this part of the record (20-40%), but no longer dominate. The small placoliths become a relatively minor component of the coccolithophore assemblage at this time, falling rapidly to values of less than 5% after ca. 800 ka.

The most significant non-*Gephyrocapsa* species throughout the interval of study is *Pseudoemiliania lacunosa* (Figure 4.1D). It reaches a peak in abundance of 17% at 693 ka. Although *P.lacunosa* belongs to the Gephyrocapsaceae family, and may therefore be expected to synthesise alkenones (Marlowe et al., 1990), no significant shifts in U^{K}_{37}' values are detected as its abundance declines sharply toward its extinction after 500 ka. Medium *Reticulofenestra* reach a maximum abundance of 5% during the pronounced cooling after 1150 ka, which marks the SST shift in the U^{K}_{37}' record. Although *Reticulofenestra* belongs to the Gephyrocapsaceae family (Marlowe et al., 1990), its overall low abundance suggests that it is unlikely to have affected U^{K}_{37}' values. The increase in the abundance of medium *Reticulofenestra* during the ca. 1150 ka cooling may therefore be a response to the cooler conditions, rather than an influence over the U^{K}_{37}'-SST relationship. ‘Other’ species identified in the core, with abundances of 2-3%, include *Coccolithus pelagicus* (a sub-Arctic and upwelling-thriving species in the Atlantic, Okada and McIntyre, 1977) and *Pontosphaera* species (warm water species), identified during glacial and interglacial intervals respectively. No change in their abundance could be identified before and after the SST shift at 1150 ka.

Figure 4.1 therefore demonstrates that no significant alteration to the coccolithophore assemblage could account for the shift in U^{K}_{37}' values from 1150 ka BP. Rather, the assemblage changes much later in the record, after both the SST shift and the increase in amplitude of the SST oscillations. This suggests that the U^{K}_{37}' record generated from ODP 1087A is a good representation of mid-Pleistocene SST changes, independent of any changes in its source organisms.

4.2.3 The validity of U^{K}_{37}' for mid-Pleistocene SST reconstructions

No changes in the coccolithophore assemblage could be identified at ODP 1087A to explain the trends in U^{K}_{37}' between 1500 and 500 ka. The dominance of *Gephyrocapsa* species throughout the interval of study also suggests that the modern U^{K}_{37}'-SST relationship can be applied, given that *Gephyrocapsa* species are also present in the modern biogeographical zones analysed in the global U^{K}_{37}' calibration of Müller et al. (1998).

The hypothesis that the modern U^{K}_{37}'-SST calibration can be applied to these sediments can be tested through the generation of a series of additional alkenone indices (Table 4-1). These indices describe the relationships between the C_{37} and the C_{38} alkenones. These relationships, like the U^{K}_{37}' index, are empirical and with no biological or theoretical basis. However, in a comparable manner to U^{K}_{37}' values, the indices defined in Table 4-1 show a restricted range of values throughout modern sediments and water column samples, which may be linked to the mechanism of alkenone synthesis (e.g. Conte et al, 2001; Prahl et al, 1988; Rosell-Melé et al, 1994; Sikes et al, 1997). If the sediments of Site 1087A also show these characteristics, further support for the application of the modern U^{K}_{37}'-SST calibration will be generated.

Table 4-1 Alkenone indices described in the text. [Cx:y] describes the abundance of an alkenone with x carbon atoms and y saturations. Me and Et describe alkenones with a methyl- or ethyl-group attached. References: 1: Prahl and Wakeham (1987), 2: Rosell-Melé et al. (1994), 3: Conte et al. (1998), 4: Prahl et al. (1988).

Index	Formula	Ref.
U^{K}_{37}'	$[C_{37:2}Me] / [C_{37:3}Me] + [C_{37:2}Me]$	1
U^{K}_{38}	$[C_{38:2}Me] + [C_{38:2}Et] / [C_{38:2}Me] + [C_{38:2}Et] + [C_{38:3}Me] + [C_{38:3}Et]$	2
U^{K}_{38}Et	$[C_{38:2}Et] / [C_{38:2}Et] + [C_{38:3}Et]$	3
K37	$[C_{37:2}Me] + [C_{37:3}Me]$	4
K38	$[C_{38:2}Me] + [C_{38:2}Et] + [C_{38:3}Me] + [C_{38:3}Et]$	4

The values for 3 alkenone indices at ODP 1087A through time are shown in Figure 4.2. The upper two figures describe the relationship between abundance of the C_{37} and C_{38} alkenones (K37 and K38 respectively). C_{38} alkenones contain both methyl and ethyl groups. Where only the ethyl-C_{38} alkenones are analysed, the index 'K38Et' (Conte et al., 1998) is applied. Throughout the interval of study, values for K37/K38 and K37/K38Et fall within a relatively restricted range (Figures 4.2 A and B). Significantly, no shifts in values are observed in either record that might correlate with the observed U^{K}_{37}' changes. Average values of both indices also fall close to those obtained in cultures (Prahl et al., 1988; Conte et al., 1998), and to those found in the late Quaternary

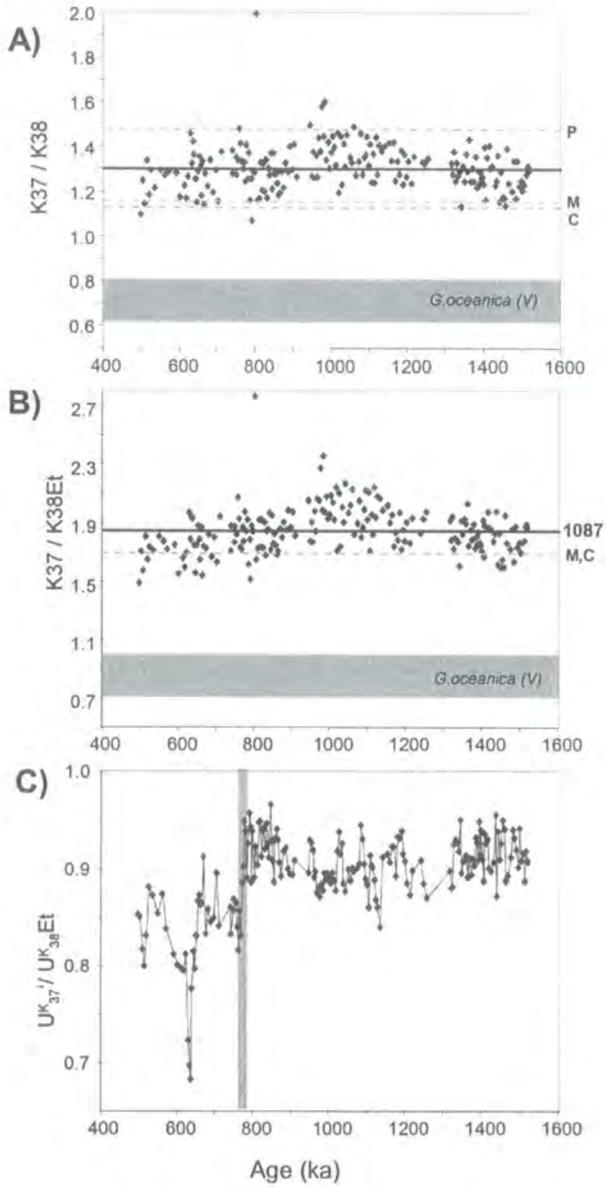

Figure 4-2 Alkenone indices from ODP 1087A, using formulae in Table 4.1. A) K37/K38. Solid black line shows ODP 1087A average, dashed lines show average values from cultures of *E.huxleyi* ('P': Prahl et al., 1988), cultures of both *E.huxleyi* and *G.oceanica* ('C' Conte et al., 1998), and late Quaternary sediments from Walvis Ridge ('M': Müller et al., 1998). Shaded area indicates the values attained from *G.oceanica* culture by Volkman et al. (1995). B) K37/K38Et. Lines and shading as in A). C) U^K_{37}' / U^K_{38}Et. Note the shift in ODP 1087A values at 770 ka.

sediments at Walvis Ridge to the north (Müller et al., 1997). The latter study used these indices to conclude that, even in the absence of *E.huxleyi* the mode of alkenone synthesis (and therefore the temperature dependence of U^{K}_{37}') was similar to that at present. The K37/K38 and K37/K38Et values from ODP 1087A also differ significantly from the *G.oceanica* culture of Volkman *et al.* (1995). This culture showed a different U^{K}_{37}'-SST relationship to that obtained by Müller et al. (1998). That Site 1087A values do not fall into this range therefore increases the support for application of the Müller et al. (1998) SST calibration across the mid-Pleistocene.

Figure 4.2C plots the $U^{K}_{37}'/U^{K}_{38}Et$ relationship at ODP 1087A through time. The $U^{K}_{38}Et$ index describes the relative abundance of C_{38} alkenones in a similar manner to the U^{K}_{37}' (Table 4-1), but includes only the ethyl C_{38} alkenones. A significant shift toward lower $U^{K}_{37}'/U^{K}_{38}Et$ values is observed at ca. 770 ka. Significantly this does not occur during the U^{K}_{37}' shift at ca.1150 ka, nor at the onset of the increase in U^{K}_{37}' variability at ca. 870 ka. The shift in the $U^{K}_{37}'/U^{K}_{38}Et$ ratio at ca. 770 ka occurs as the dominance of small *Gephyrocapsa* comes to an end, and the more diverse coccolithophore assemblage develops (Figure 4.1D). This clearly demonstrates that changes in coccolithophore species can have an impact on alkenone distributions, and that this occurred during the later part of the mid-Pleistocene.

To assess the impact that the shift in the $U^{K}_{37}'/U^{K}_{38}Et$ may have had on the temperature dependence of U^{K}_{37}', Figure 4.3 compares the relative abundance of U^{K}_{37}', $U^{K}_{38}Et$ and U^{K}_{38} with published ranges of values identified in modern cultures, sediments and water column samples (Conte and Eglinton, 1993; Rosell-Melé et al., 1994; Conte et al., 1995; Sikes et al., 1997; Ternois et al., 1997; Conte et al., 1998; Yamamoto et al., 2000; Conte et al., 2001). The shift identified in $U^{K}_{37}'/U^{K}_{38}Et$ at ca. 770 ka (Figure 4.2C) can be clearly identified in both plots (Figure 4.3). Critically, even with this shift, all of the values obtained from ODP 1087A plot within the field generated by sediments and water column samples that exhibit a modern U^{K}_{37}'-SST relationship. Prior to ca. 767 ka, the scatter between U^{K}_{37}' and $U^{K}_{38}Et$ (Figure 4.3A) lies outside the *E.huxleyi* field generated in cultures by Yamamoto et al. (2000) and from combined cultures and particulate matter by Conte et al. (2001). However, these samples plot close to the regression lines from Southern Ocean sediments identified by Sikes et al. (1997) in both U^{K}_{37}' and $U^{K}_{38}Et$ (Figure 4.3A), and U^{K}_{37}' and U^{K}_{38} (Figure 4.3B). These samples also plot close to the regression line between U^{K}_{37}' and U^{K}_{38} abundances from North Atlantic surface

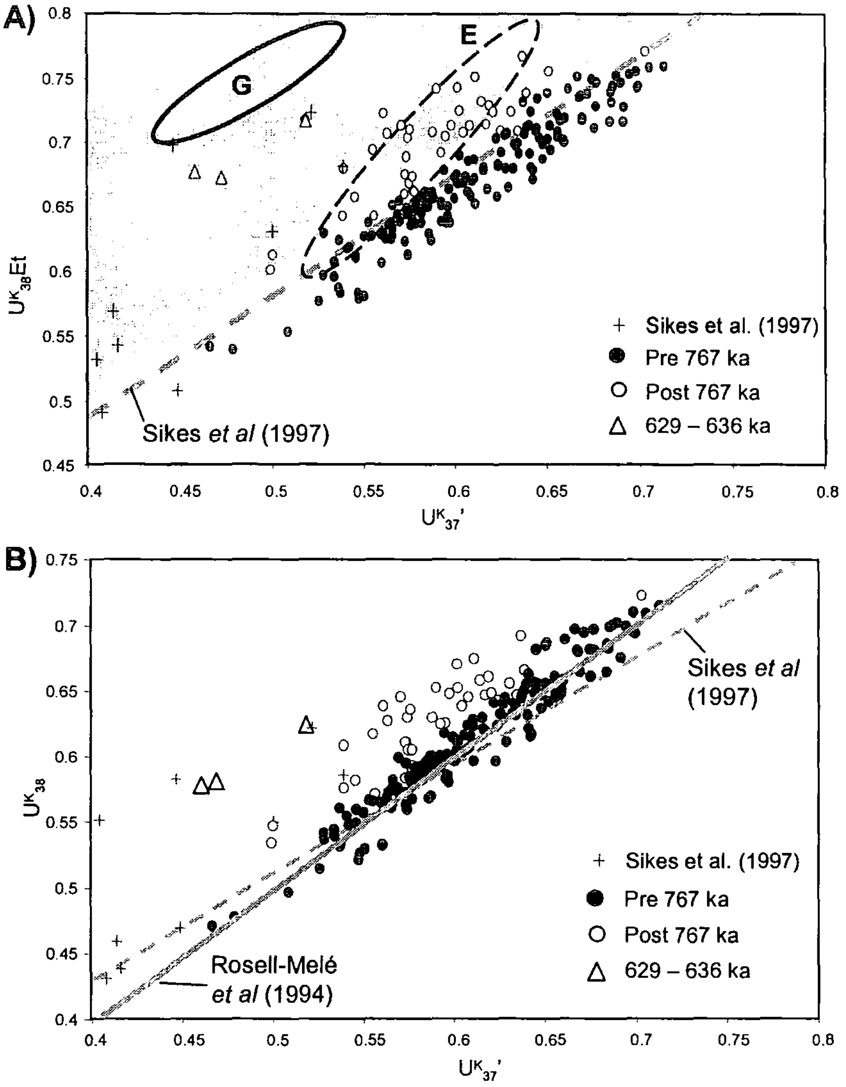

Figure 4-3 Scatter plots of A) U^{K}_{37}' vs U^{K}_{38}Et. B) U^{K}_{37}' vs U^{K}_{38}. Data grouped according to age. Shaded area in A) represents combined culture data (Conte et al., 1995; Conte et al., 1998), plus euphotic zone particulate matter from Bermuda (Conte et al., 2001), the north Atlantic (Conte and Eglinton, 1993), and the Mediterranean (Ternois et al., 1997). Area defined using scatter plot in Conte et al. (2001). Ovals define values identified in cultures of *G.oceanica* ('G') and *E.huxleyi* ('E') by Yamamoto et al. (2000). Crosses show values obtained from Southern Ocean sediments by Sikes et al. (1997), with their linear trend shown by the dashed grey line. In B) values obtained from Sikes et al. (1997) shown as in A), with the linear trend identified in north Atlantic sediments by Rosell-Melé et al. (1994) indicated by the solid line.

sediments (Figure 4.3B; Rosell-Melé et al. 1994). The good correlation between the relative abundances of the C_{37} and C_{38} alkenones to modern values at ODP 1087A throughout the 1500-500 ka time interval supports the application of the modern U^{K}_{37}'-SST calibration for reconstructing palaeo-SSTs. An interesting point to note is that values from ODP 1087A after the shift in U^{K}_{37}'/U^{K}_{38}Et fall within those of cultured *E.huxleyi*, rather than *G.oceanica* (Figure 4.3A). This is surprising given the increase in abundance (20%) of the latter after this time, but may reflect the dominance of the closely related *G.caribbeanica* in this part of the time-series (Figure 4.1D). This is not problematic for SST generation, however, as the both the *G.oceanica* and *E.huxleyi* cultures plotted on Figure 4.3A gave a U^{K}_{37}'-SST relationship that closely matched that of the Müller et al. (1998) calibration (Yamamoto et al., 2000).

4.3 Conclusions

A comparison of U^{K}_{37}' and coccolith records from ODP Site 1087A indicates that, despite a number of significant changes to the coccolithophore assemblage, the mechanism of alkenone-synthesis throughout the early and mid-Pleistocene closely resembles that of the modern alkenone-producers. Although the decline of small *Gephyrocapsa* at ca. 770 ka is accompanied by a shift in the ratio between U^{K}_{37}' and U^{K}_{38}Et, suggesting that changes to the mechanism of alkenone synthesis took place at this time, values still fall within those found in modern sediments. This suggests that the modern U^{K}_{37}'-SST calibrations can be applied with confidence to sediments where the modern coccolithophore assemblages are not present during the early- and mid-Pleistocene.

5. Global cooling precedes the mid-Pleistocene climate transition

5.1 Introduction

The mid-Pleistocene shift in the dominant periodicity of glacial-interglacials from 41- to 100-kyr is preceded by an increase in the mean global ice volume at ca. 920 ka, during MIS 22 (Mudelsee and Schulz, 1997). This marked the development of extensive northern hemisphere ice sheets, whose inertia may be critical to the increasing duration of the glacial cycles (e.g. Imbrie et al., 1993; Berger and Jansen, 1994; Raymo, 1997; Clark and Pollard, 1998; Paillard, 1998; Ruddiman, 2003). Increasing inertia in the ice-sheets is suggested by the immediate increase in the period of glacial-interglacial oscillations after the ice volume increase, first to ca. 77-kyr, and then to ca. 100-kyr after ca. 640 ka (Mudelsee and Schulz, 1997). It is this transitional state, between the 41- and 100-kyr systems, that is used to define the mid-Pleistocene climate transition ('MPT', Mudelsee and Schulz, 1997).

The increase in global ice volume has been attributed to an increase in the stability of the northern hemisphere ice sheets in response to progressive erosion of their basal substrates (Clark and Pollard, 1998). By this mechanism, the increasing severity of glaciations during and after the MPT were driven by the increase in mean global ice volume pushing the climate system into a cooler state. Alternative mechanisms for the MPT propose that the increase in mean global ice volume was a threshold response of the ice-sheets to a long-term global cooling trend, perhaps driven by falling atmospheric CO_2 concentrations (e.g. Berger and Jansen, 1994; Raymo, 1997; Paillard, 1998; Berger et al., 1999). A climatic origin for the transition is suggested by evidence for environmental change preceding the increase in global ice volume (Table 1.3, Chapter 1), including intensification of upwelling, periods of weaker thermohaline circulation, and increasing tropical aridity that may have begun as early as 1200 ka (e.g. Oppo et al., 1995; Marlow et al., 2000; Dupont et al., 2001; Durham et al., 2001). The 100-kyr ice-sheet cycles have also been proposed to be driven by climate processes, rather than by ice-sheet dynamics. These processes include variations in CO_2 (Shackleton, 2000; Ruddiman, 2003) and the extent of high-latitude sea-ice (Tziperman and Gildor, 2003), which may act to limit or regulate ice-sheet growth. A key issue for understanding the origin of the MPT is to determine whether the increase in mean global ice volume was a response to, or driver of, mid-Pleistocene climate change.

All four of the marine sediment records analysed in this thesis exhibit cooling trends that preceded the global ice volume increase during MIS 22 (Chapter 3). In the North

Atlantic, an expansion of sea-ice cover associated with the migration of the Arctic Front was also identified. The principal aim of this Chapter is to determine whether these sea-surface temperature (SST) changes resulted in a global cooling trend, and if this was the driving mechanism for the increase in the mean global ice volume that heralds the start of the MPT. The main objectives are:

1. To identify a global cooling trend from the SST records generated in this thesis and additional published data sets;
2. To assess the role played by global temperature change in driving the mid-Pleistocene expansion in global ice volume.

To achieve these objectives, a global temperature trend is reconstructed here by comparison of the U^{K}_{37} and U^{K}_{37}' time-series generated in this thesis. As the sites investigated in this thesis cover both the tropical and high-latitudes from two different circulation systems, the common temperature signal from these records is interpreted to be of global significance. The common temperature trend is generated through a stacking procedure, which is described in the following section. Additional available data sets, recording different regional signals to those generated here, are also compared and added to the stacked records. Finally, the extent of sea-ice is reconstructed by application of the $\%C_{37:4}$ proxy, to monitor the distribution of Arctic Waters in the northern hemisphere. This allows an assessment of the Tziperman and Gildor (2003) hypothesis that sea-ice extent is a critical factor in determining both the regulation of the 100-kyr cycles and their mid-Pleistocene development.

5.2 Stacking procedure

To identify a common trend within the reconstructed (SST) records, a stacking procedure was performed. This approach generates a 'standardised' palaeoclimate signal, by enhancing the signal-noise ratio and removing geographically-dependent features that may be present within individual records (Martinson et al., 1987; Heslop et al., 2002). The procedure has proved effective in determining 'average' northern and southern hemisphere temperature trends over the last 2 ka (Mann and Jones, 2003). Stacking of benthic $\delta^{18}O$ records was employed in the development of the first $\delta^{18}O$ timescale, the 'SPECMAP' timescale, to generate a global $\delta^{18}O$ signal (Imbrie et al., 1984). This procedure has proved to be valuable in the production of subsequent $\delta^{18}O$ stratigraphies (e.g. Martinson et al., 1987). Common trends in Chinese loess (Heslop et al., 2002) and Atlantic deep-water circulation (Schmieder et al., 2000) during the mid-Pleistocene have also been identified using this procedure.

The U^{K}_{37}' records presented in Chapter 3 (U^{K}_{37} for ODP 983C) are stacked with U^{K}_{37}' records from ODP 1084 in the Benguela upwelling system (Marlow et al., 2000), and ODP 882 in the North-west Pacific (Haug, 1996). The core locations are given in Figure 5.1. The U^{K}_{37}' records from ODP 846 (Emeis et al., 1995) and ODP 1081 (Marlow, 2001) were not used, as they generally provide the same signals in ODP 849C and ODP 1084 respectively. Their exclusion thus avoids biasing the stacked record to the trends in certain over-presented regions. Potential biases were tested by generating regional stacks, not shown here, which all showed a similar trend towards cooling developing from 1500 ka, although the magnitudes of cooling differed between stacks due to the difference in SST variation amplitudes between sites.

The approach followed here is based on the stacking procedures used by Schmieder et al. (2000) and Heslop et al. (2002). First, all time-series were smoothed with a 5-point running mean (ca. 25-kyr filter). This reduces the uncertainties associated with comparing time-series between sites, where age models may introduce errors of up to 16-kyr (Chapter 1). This smoothing was not undertaken for ODP 1084, where the resolution was ca. 50-kyr (Marlow et al., 2000). To compensate for variations in absolute U^{K}_{37}' values and the amplitude of their variation between sites, the smoothed records were normalised. Each time-series was normalised by subtracting the minimum value from each sample, and dividing by the amplitude of U^{K}_{37}' variation for that site. All records were then linearly interpolated onto a common time scale (500-1500 ka, at 5-kyr increments). The U^{K}_{37}' SST stack was generated by calculating the arithmetic mean of the normalised values for each time-point. This procedure was also followed to generate a $\%C_{37:4}$ stack from ODP 983 and 882.

Mann and Jones (2003) showed that regional sensitivities can be important for determining 'average' temperature change on both hemispheric and global scales. In order to determine the 'global average' SST change during the mid-Pleistocene, a stacked record of U^{K}_{37}' anomalies from each time-series was produced. From each smoothed record, the mean U^{K}_{37}' value of that time series was subtracted. The time-series were then linearly interpolated and stacked as above. This 'anomaly stack'

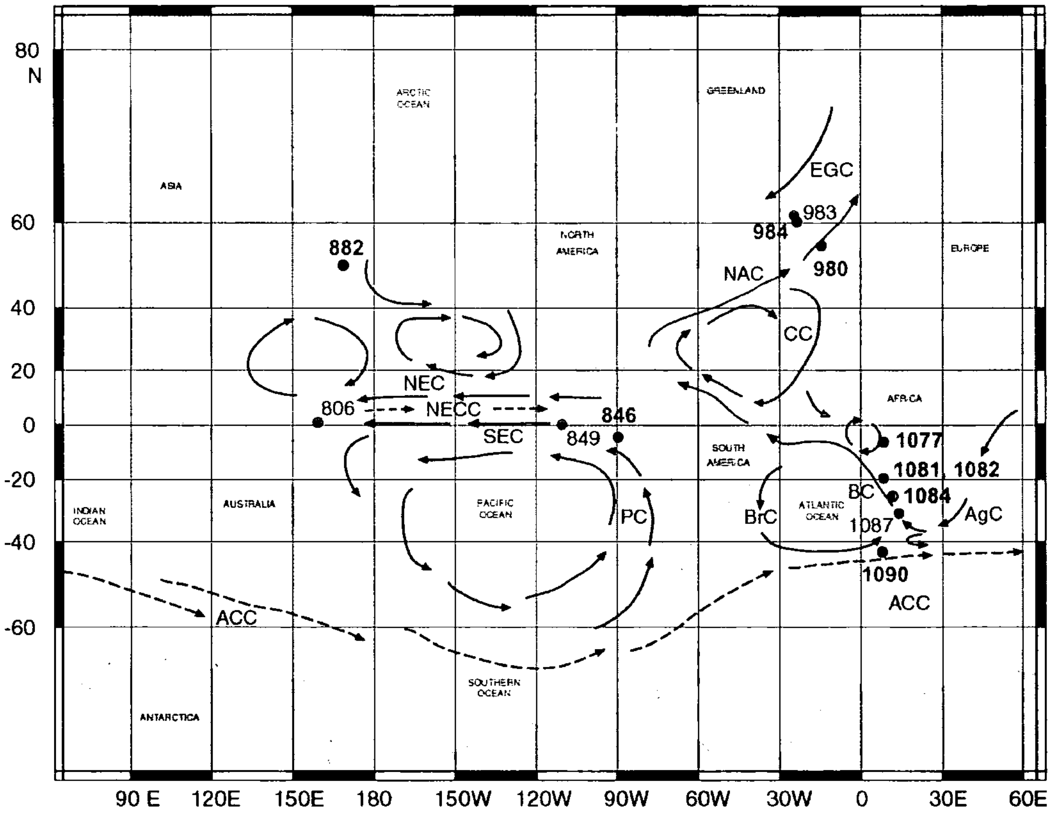

Figure 5-1 Major surface ocean circulation systems and the locations of the ODP cores discussed in this chapter. The heat transport pathways that link the Atlantic and Pacific cores analysed in this thesis are highlighted in blue, the core sites by red dots. Additional records used in the U^{K}_{37}' stack are highlighted in blue text and blue dots: ODP 882 (Haug, 1996), ODP 1084 (Marlow et al. 2000). Other cores discussed in the text are shown in dark green.

Base map source: www.odp-tamu.edu. Currents based on Open University (1989).

Current notation:

ACC: Antarctic Circumpolar Current; AgC: Agulhas Current; BC: Benguela Current; BrC: Brazil Current; CC: Canaries Current; EGC: East Greenland Current; NAC: North Atlantic Current; NEC: North Equatorial Current; NECC: North Equatorial Counter-current; PC: Peru Current; SEC: South Equatorial Current.

represents the average SST variation above and below the global average SST between 1500-500 ka.

5.3 Results and Discussion

5.3.1 Mid-Pleistocene cooling

The U^{K}_{37}' time-series generated in this thesis are presented in Figure 5.2. In Chapter 3, these time-series were divided into three 'phases', which are also marked in Figure 5.2. 'Phase II' occurs after MIS 35 (ca. 1200 ka) and is marked by cooling in all four U^{K}_{37}' records. The Phase I-II boundary occurs at ca. 1170 ka at the two Pacific sites investigated in this thesis, and slightly later at ca. 1145 ka in the two Atlantic sites (Figure 5.2). This difference in timing is greater than the 15-kyr maximum age estimation errors identified in Chapter 1 when comparing $\delta^{18}O$ stratigraphies (Table 1.3). However, if the $\delta^{18}O$ age model for ODP 849 'missed' a precessional cycle this could account for the 25-kyr age difference in the onset of cooling, and requires further investigation with higher resolution $\delta^{18}O$ analyses. A shift to cooler average SSTs occurred in the South-east Atlantic (ODP 1087A) and eastern equatorial Pacific (ODP 849C), although this was rapid in the former and progressive in the latter (Figure 5.2). In contrast, the northern North Atlantic (ODP 983C) and western equatorial Pacific (ODP 806B) showed temporary cooling during the same interval (Figure 5.2). All records define the end of phase II by an increase in the amplitude of the SST variations after MIS 22 (Figure 5.2).

Cooling during 'Phase II' cooling is also observed at a number of other locations, although the timing, magnitude and duration of the cooling trends differs between sites. The SST time-series for those sites where raw data was available or sent to the author

Figure 5-2 (Overleaf) U^{K}_{37}'-SST records between 1500-500 ka from the tropical Pacific, the Benguela upwelling system, and the mid-high latitudes of the North and South Atlantic and the North Pacific (U^{K}_{37}-SST from ODP 983 and 882). Time-series generated in this thesis shown in blue. Additional data sets from ODP 846 (Emeis et al., 1995), ODP 1081 and 1084 (Marlow, 2001) and ODP 882 (Haug, 1996). The three phases of major SST change as defined in Chapter 3 are marked by the vertical lines. The Phase I-II boundary ranges between ca. 1170-1145 ka, based on its onset at the Pacific sites (1170 ka, ODP 806, 849) and at the Atlantic sites (1145 ka, ODP 1087, 983). The 'preliminary 100-kyr cycle' from the Atlantic sites and the global ice volume record is shown by blue-grey shading for ODP 1087 and 983. The global ice volume record from ODP 849 (Mix et al., 1995) is shown for reference, with the MPT as defined by Mudelsee and Schulz (1997) marked as 'MPT'.

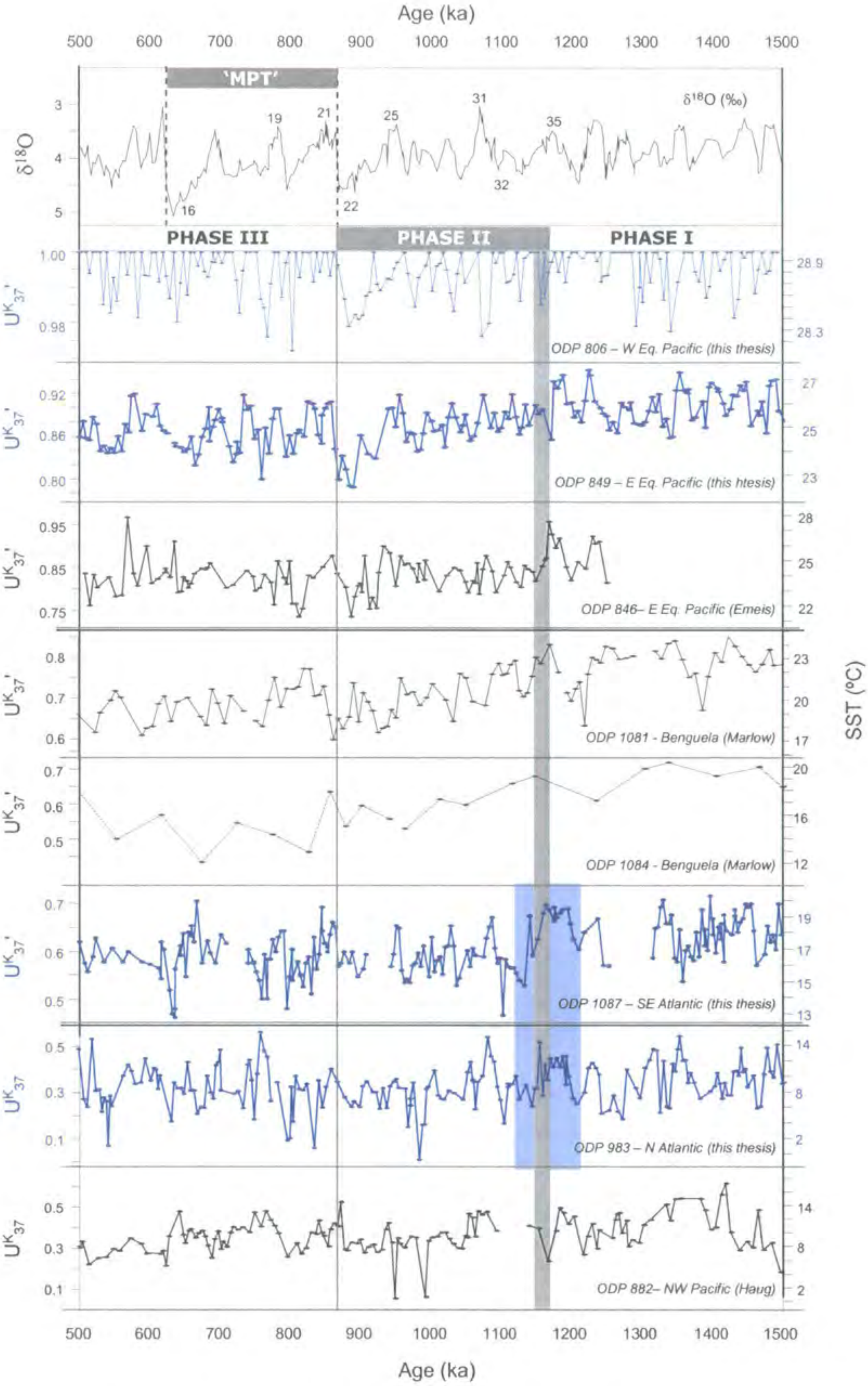

Figure 5.2 U^{K}_{37}'-SST records between 1500-500 ka from the tropical Pacific, the Benguela upwelling system, and the mid-high latitudes of the North and South Atlantic and the North Pacific (U^{K}_{37}–SST from ODP 983 and 882). For explanation see the caption on the previous page.

are shown in Figure 5.2 (see Figure 5.1 for core locations). ODP 882 in the north-west Pacific (Haug, 1996) exhibits a similar cooling trend to that of ODP 983, with lower interglacial SSTs during Phase II (Figure 5.2). Progressive cooling is visible in the two records influenced by Benguela upwelling, ODP 1084 and 1081 (Figure 5.2; Marlow et al., 2000; Marlow, 2001). A cooling trend is less clear at ODP 846 in the eastern equatorial Pacific in comparison to ODP 849, although both records show their greatest fall in SSTs during MIS 24-22, centred on ca. 900 ka (Figure 5.2; Emeis et al., 1995). The lack of a clear cooling signal at ODP 846 may be an artefact of the resolution of the ODP 846 record, as subsequent high-resolution analysis of this core reveals a decline in SSTs of approximately 1°C between 1200-800 ka (Liu and Herbert, 2004). Although not shown on Figure 5.2, progressive cooling of glacial SSTs building to intense cooling during MIS 22 was also observed at ODP 1077, which lies to the north of the Benguela upwelling region in the eastern tropical Atlantic (the core location is shown in Figure 5.1; Schefuß et al., 2003). Progressive cooling of glacial SSTs by around 2°C between ca. 800-450 ka was also reconstructed at ODP 1082 (Jahn, 2002). This site, like ODP 1087, is affected by the Benguela Current (see Figure 5.1 for the location). In contrast to ODP 1087, the ODP 1082 record revealed little SST change prior to ca. 800 ka (Jahn, 2002).

The normalised and anomaly U^{K}_{37}' stacks are shown in Figure 5.3. Glacial-interglacial variability is clearly visible when the records are compared to the benthic $\delta^{18}O$ record of global ice volume (Mix et al., 1995). Significantly, the stacked records demonstrate that global cooling occurred between ca. 1145 and 890 ka (MIS 34-22), which resulted in a permanent shift in mean SSTs. In the normalised stack, two periods of intense cooling are evident after 1000 ka (Figure 5.3B). The first, between ca. 1000 and 960 ka, reflects the U^{K}_{37}' minima reached in the two high-latitude sites (ODP 983 and 882, Figure 5.2). The second cooling, between 925-875 ka, marks the intense cooling that characterises the tropical Pacific records during MIS 24-22 (ODP 806B, 849C and 846, Figure 5.2). The impact of the latter cooling is reduced in the stacked U^{K}_{37}' anomaly record (Figure 3.5C), as the tropical records oscillate with an amplitude of only 1-2°C, in contrast to the >4°C variability in the mid- and high-latitude records (Figure 5.2). During MIS 22, when individual tropical records (Figure 5.2) and the normalised stack (Figure 5.3) exhibit significant cooling, the relatively minor cooling in the mid- and high-latitude sites (Figure 5.2), dampened the tropical impact on global temperatures. In contrast, the 'premature 100-kyr cycle' identified in the two Atlantic sites investigated here (ODP

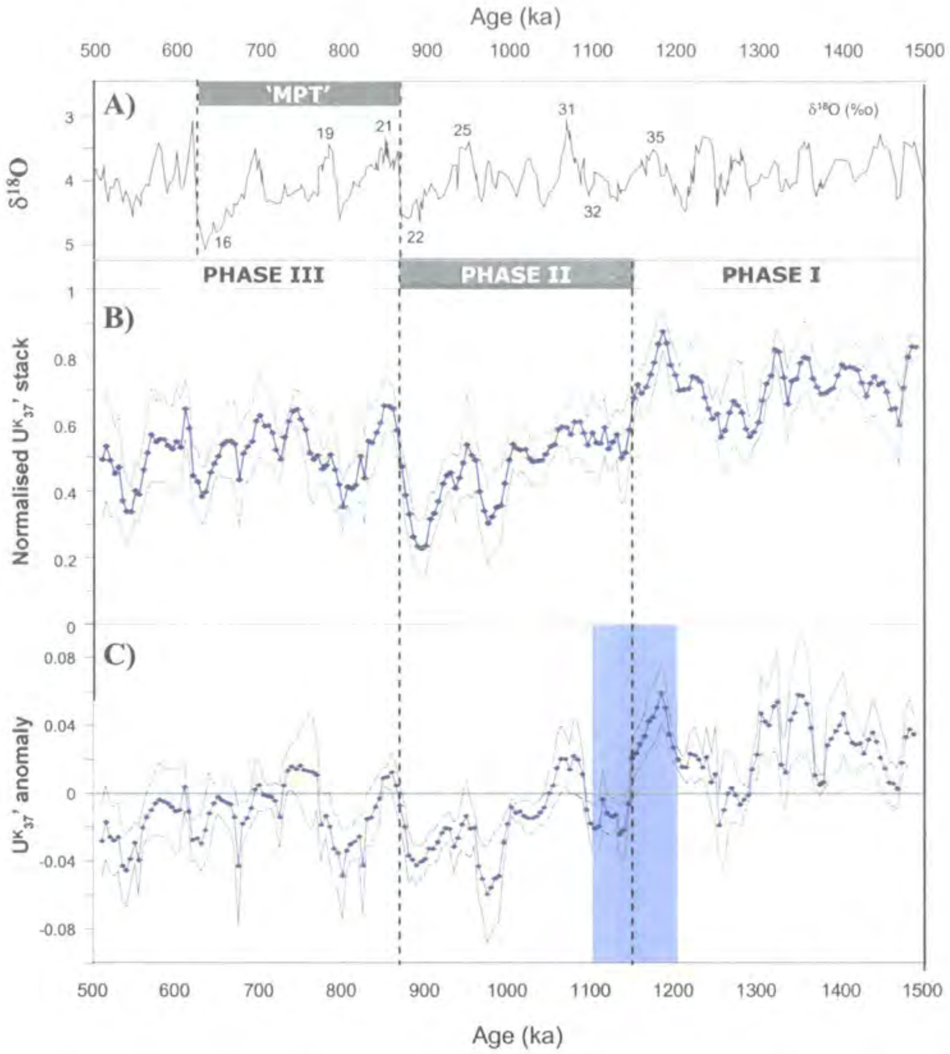

Figure 5-3 Stacked U^K_{37}' records between 1500-500 ka. The three phases of major SST change as shown in Figure 5.2 are marked. A) Global ice volume record from Mix et al. (1995). B) Stack of normalised U^K_{37}' from the four cores analysed in this thesis, plus ODP 1084 (Marlow et al., 2000) and 882 (Haug, 1996). Mean value shown in blue, standard deviation shown by grey lines. C) Stack of U^K_{37}' anomalies from the cores used for figure B. Standard deviation shown by grey lines. Horizontal grey line shows the mean U^K_{37}' for the stack. The 'premature' 100kyr cycle as shown in Figure 5.2 is marked by the blue-grey shading.

1087 and 983, see Figure 5.2 and discussion in Chapter 3) is absent from the tropical sites. As a result, its impact is dampened in the normalised stack (Figure 5.3B) but can still be detected in the anomaly stack (Figure 5.3C).

The U^{K}_{37}' anomaly stack can be used to calculate the magnitude of the shift in global SSTs (Figure 3.5C). Mean values after 1145 ka are 0.042 U^{K}_{37}' units below those prior to 1145 ka. This represents a fall in mean global SST of 1.25°C using the U^{K}_{37}'-SST calibration of Müller et al. . Significantly, this cooling occurred more than 200-kyr prior to the increase in the mean global ice volume from ca. 920 ka during MIS 22 (Mudelsee and Schulz, 1997). Although the first expansion of the Scandinavian ice-sheet into the North Sea Basin occurred in concert with the onset of the global cooling, no further advances of this magnitude are recorded until after ca. 500 ka (Sejrup et al., 2000). A delayed ice-sheet response to the global cooling is also evident in records of iceberg discharge to the North Atlantic and Nordic Seas. Although isolated intervals of iceberg discharge are identified after 1200 ka (e.g. Helmke et al., 2003a; Kleiven, 2000), there was no significant increase in the amount of deposited detritus or the length of the iceberg-rafting intervals. Rather, increased iceberg-rafted detritus from the Laurentide, Greenland, Scandinavian and Icelandic ice masses is found after ca. 1000 ka, in association with both the increase in mean global ice volume and the development of the 100-kyr cycles (Ruddiman et al., 1986; Bohrmann et al., 1990; Henrich and Baumann, 1994; Fronval and Jansen, 1996; Sejrup et al., 2000; St John and Krissek, 2002; Helmke et al., 2003a; Helmke et al., 2003b). A delayed response of the thermohaline circulation (THC) system to the global cooling can also be identified. Pronounced weakening of the THC has been reported to have occurred after 1000 ka (e.g. Gröger et al., 2003; Kleiven et al., 2003). Both ice volume and thermohaline circulation are important components within the global climate system. Their delayed response to global cooling in the surface ocean may therefore demonstrate that the latter had little impact over climate system behaviour, and to the development of the MPT. To test the hypothesis that the global cooling drove the MPT, two issues need to be addressed:

1. What mechanism(s) delayed the response of the ice sheets and the thermohaline circulation system to the global cooling after MIS 35?
2. What mechanism(s) drove the global cooling?

5.3.2 The delayed ice-sheet response to global cooling

Ice-sheet growth is dependent upon ambient temperatures and precipitation inputs. For ice sheets to grow, atmospheric temperatures need to be cold enough to enable precipitation to fall as snow, and for the accumulated snow and ice to survive summer melting. If cooling becomes too intense, reduced atmospheric humidity and the resulting fall in precipitation rates restrict growth: the precipitation-temperature feedback (Kallen et al., 1979; Miller and de Vernal, 1992). It seems unlikely that the global cooling identified in Figure 5.3 initiated this negative feedback to ice-sheet growth, as average SSTs after MIS 35 are comparable to those during the mean global ice volume increase during MIS 22 (Figure 5.3C).

In Chapter 3, a sustained increase in the abundance of $C_{37:4}$ was identified at ODP 983 in association with falling U^{K}_{37} values during Phase II (Figure 5.4B). By analogy with modern $\%C_{37:4}$ distributions (Rosell-Melé et al., 1998; Bendle, 2003), this was attributed to a sustained equatorward migration of the Arctic Front to the south of Iceland after ca. 1120 ka (from MIS 34). Modern waters to the north of the Arctic Front are associated with the presence of at least seasonal sea-ice cover (Swift, 1986). The $C_{37:4}$ record from ODP 983 is interpreted as evidence for a persistence of at least seasonal sea-ice cover to the south of Iceland between MIS 35-22, excluding interglacial maxima.

The extent of sea-ice cover plays an important role in influencing the moisture supply to ice-sheet source regions. Sea-ice cover limits evaporation and shifts moisture-bearing storm tracks equatorward, while its albedo further reduces humidity through atmospheric cooling (Smith et al., 2003; Tziperman and Gildor, 2003). The result is a reduction in the moisture available for precipitation in ice-sheet source regions. In the North Atlantic, the continued flow of the warm North Atlantic Current (NAC) to the eastern Nordic Seas is considered to be important for the supply of moisture to the circum-Atlantic ice-sheets during glacial inceptions (e.g. Ruddiman and McIntyre, 1979; Ruddiman et al., 1980; Sarnthein et al., 1995; McManus et al., 2002). This moisture source may also be restricted by more extensive sea-ice development diverting or reducing NAC flow to the Nordic Seas.

It is proposed here that the sustained expansion of sea-ice in the high latitudes of the northern North Atlantic introduced a negative feedback to ice-sheet growth despite global cooling after MIS 35 (post-1145 ka). The advance of the Scandinavian ice-sheet

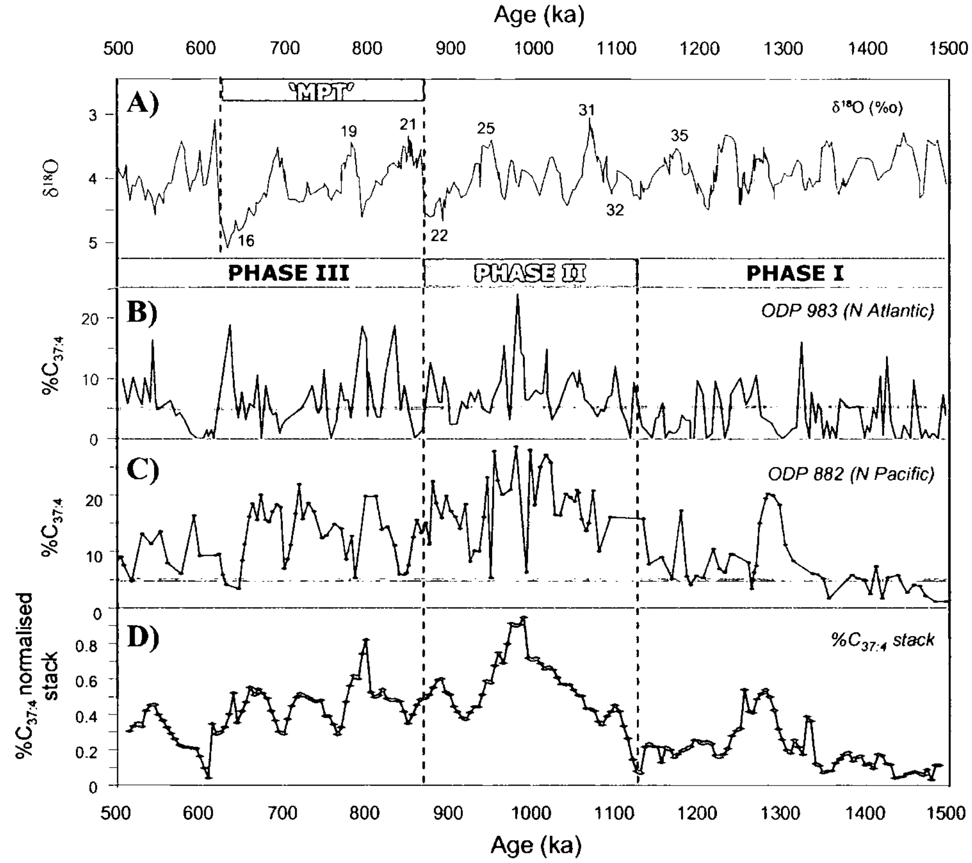

Figure 5-4 Stacked $\%C_{37:4}$ records between 1500-500 ka. The three phases of major SST change and the 'premature' 100kyr cycle as shown in Figures 5.2 and 5.3 are marked. A) Global ice volume record from Mix et al. (1995). B) $\%C_{37:4}$ record from ODP 983 (North Atlantic; this thesis). C) $\%C_{37:4}$ record from ODP 882 (North Pacific; Data from Haug, 1996). D) Stacked normalised $\%C_{37:4}$:4 record from ODP 983 and 882.

into the North Sea Basin that occurred with the onset of global cooling (Sejrup et al., 2000) may demonstrate that the sea-ice cover at this time was restricted to the west of the Nordic Seas and the North Atlantic, or that the moisture-bearing westerlies were positioned over the ice-sheet source region as they migrated southward in response to the increased equator-pole temperature gradient and/or sea-ice expansion. The presence of open water and/or inputs from the flow of the NAC to the east would have maintained the supply of moisture to the Scandinavian ice-sheet and encouraged its growth as global temperatures fell. Significantly, the North Atlantic may not have been alone in experiencing sea-ice expansion from MIS 34. Figure 5.4 shows that a similar trend in %$C_{37:4}$ also occurs at ODP 882, at around 50°N in the north-west Pacific (Haug, 1996). This confirms diatom data that suggest a southward migration of subarctic water masses into the North Pacific occurred between 1100 and 800 ka (Sancetta and Silvestri, 1986). The influence of the warm NAC at the higher-latitude site, ODP 983, is evident by its generally lower %$C_{37:4}$ values. Both sites exhibit a progressive increase in %$C_{37:4}$ after MIS 32 (ca. 1100 ka), reaching a peak at ca. 990 ka before steadily declining. This is demonstrated in the %$C_{37:4}$ stack, which shows a sustained expansion of sea-ice developing at high northern latitudes after MIS 32 (Figure 5.4D). The abundance of $C_{37:4}$ rapidly falls during MIS 25 (after 990 ka). Critically, this indicates that the glacial cycle that culminated in the global ice volume increase during MIS 22 was also associated with reduced high-latitude sea-ice cover. It is proposed that this reduction in sea-ice cover resulted in an increase in the supply of moisture to the northern hemisphere ice-sheet source regions, and thus played an important role in driving the MIS 22 expansion of global ice volume (Figure 5.3).

Although $C_{37:4}$ abundance declined after MIS 25, the $C_{37:4}$ stack shows that a shift toward higher average values had occurred, when compared to conditions prior to the global cooling (Figure 5.4C). This can also be identified in the individual $C_{37:4}$ records, where glacial values of $C_{37:4}$ during Phase III are generally higher than glacial values during Phase I (Figure 5.4B and C). This suggests that the global cooling after MIS 35 also marked the development of glacial migrations of the North Atlantic Arctic Front to the south of Iceland, a process observed during late Pleistocene glaciations (e.g. Ruddiman and McIntyre, 1981; Bard et al., 1987; Koç et al., 1993; Bond et al., 1997; Rosell-Melé et al., 1998; Calvo et al., 2001). Only during interglacial maxima in Phase III do $C_{37:4}$ values fall below 5% at ODP 983 (Figure 5.4A), suggesting that retreat of the Arctic Front (and seasonal sea-ice) to the north of Iceland was restricted to these times.

This trend was also identified in the foraminiferal records extending back to 1000 ka from ODP 980 and 984 by Wright and Flower (2002, site locations shown in Figure 5.1). These records provide evidence for the Arctic Front remaining to the south of Iceland from ca. 1000 ka to 660 ka (MIS 28-16), with temporary migrations northward during interglacial maxima. After MIS 16, they reconstructed a shift in the interglacial Arctic Front position to the north of Iceland, to a position similar to the present (Wright and Flower, 2002).

If more extensive sea-ice cover was effective in restricting ice-sheet growth between 1145-990 ka (MIS 35-25), the continued presence of sea-ice to the south of Iceland after this time may appear at odds with the increased severity of the glaciations that developed after MIS 22 (Ruddiman et al., 1986; Bohrmann et al., 1990; Fronval and Jansen, 1996; Sejrup et al., 2000; St John and Krissek, 2002; Helmke et al., 2003a; Helmke et al., 2003b). However, the spatial distribution of Arctic Waters and thus sea-ice cover appears to have changed after 990 ka. Before this time, only a small tongue of Atlantic water reached the eastern part of the Norwegian Sea (Henrich and Baumann, 1994). After ca. 1000 ka, a northward and westward migration of the Polar Front, that lies poleward of the Arctic Front at the present day, opened sea-ice during glacial summers and warmed interglacial SSTs (Henrich and Baumann, 1994; Henrich et al., 2002). It has been proposed that this increased the effective heat transport to the Scandinavian ice sheet, and drove the development of more severe glaciations on the Scandinavian mainland after 1000 ka (Henrich and Baumann, 1994). Wright and Flower (2002) also show that, although the Arctic Front lay to the south of Iceland after 1000 ka, it did not reach across the Atlantic to the British Isles. This would have allowed a route for the flow of Atlantic waters to the Nordic Seas to be maintained. Renewed interglacial inputs of Atlantic waters to the North Atlantic are also visible in the increase in interglacial SSTs at ODP 983 after MIS 22 (Figure 5.2).

It is proposed here that the extent of northern hemisphere sea-ice played a key role in both the delayed response of the northern hemisphere ice-sheets at the onset of global cooling, and their later expansion. First, in association with global cooling after MIS 35, southward migration of sea-ice in both the North Atlantic and North Pacific Oceans restricted the supply of moisture to the northern hemisphere ice sheets. In the North Atlantic, this migration was sufficient to limit the supply of warm, moisture bearing NAC waters to the eastern Nordic Seas. After reaching a maximum extent at ca. 990 ka, sea-ice cover retreated. Critically, although sea-ice cover was maintained at higher levels than experienced prior to the global cooling, its spatial distribution and seasonal melting enabled renewed flow of Atlantic waters into the Nordic Seas. This renewed supply of moisture to the high-latitudes encouraged expansion of the circum-Atlantic ice sheets. In order to test this hypothesis, similar time-series of the %$C_{37:4}$ proxy should be generated from additional sites in the northern North Atlantic in order to ascertain the spatial signal of $C_{37:4}$ during the mid-Pleistocene. If the advance of the Arctic Front occurred with the front lying west-east (in a manner comparable to the last glacial maximum e.g. Pflaumann et al., 2003), synchronous increases in %$C_{37:4}$ would be expected from sites lying at the same latitude. In contrast, later increases in %$C_{37:4}$ to the east would suggest that the Arctic Front advanced with a south-west to north-east orientation, comparable to the alignment at present and during previous interglacials (e.g. Swift, 1986; Wright and Flower, 2002). Evidence for Atlantic inputs to the Nordic Seas after 1000 ka (e.g. Henrich and Baumann, 1994; Henrich et al., 2002) suggest that at least the retreat of the sea-ice margins occurred fastest in the eastern Atlantic, enabling the flow of the NAC into the Nordic Seas. This suggests that %$C_{37:4}$ values will fall first in the eastern North Atlantic after 1000 ka. It is also important that the spatial signal of %$C_{37:4}$ in the north-east Pacific is generated, to assess in greater detail the impacts of sea-ice expansion in the North Pacific over the growth of the Laurentide ice-sheet. In the North Pacific, an earlier discharge of ice-rafted detritus to the North-west Pacific (ca. 1000 ka) relative to the north-east Pacific (ca. 900 ka, Rea and Snoeckx, 1995) has been attributed to local controls over ice-rafting between the east and west ice-masses and/or to the spatial distribution of the cool subarctic waters that had advanced into the North Pacific after 1100 ka (St. John and Krissek, 1999). %$C_{37:4}$ values may therefore rise later in sites from the North-east Pacific to those of the North-west and at ODP 882.

5.3.3 The South Atlantic record

SSTs at ODP 1087 are primarily influenced by the input of warm Indian Ocean waters from the Agulhas Retroflection, which may be reduced by northward migrations of the Antarctic Circumpolar Current (ACC) system (Figure 5.1; Wefer et al., 1996; Giraudeau et al., 2001; Kuhn and Diekmann, 2002; Gersonde et al., 2003). The extent of sea-ice cover around Antarctica may also be determined by the position of the ACC, with sea-ice expanding with a northward migration of the ACC. At ODP 1087, a permanent cooling occurs with the onset of global cooling after MIS 35. If this was the result of a northward shift of the ACC and a reduced input of Agulhas waters to ODP 1087, this may indicate that a synchronous expansion of sea-ice occurred in both hemispheres in association with the global cooling.

The surface ocean at ODP 1087 may also cool if intensification and seaward migration of the coastal Benguela upwelling cells reached the site. Figure 5.2 shows the SST records from two sites located within the Benguela upwelling system: ODP 1084, below the major upwelling cell near Lüderitz, and ODP 1081 in the Northern Benguela Region (see Figure 5.1 for their locations). Both records undergo a long-term cooling trend after MIS 35 (Figure 5.2). This is accompanied by increases in biomarker accumulation rates (chlorins and alkenones), indicative of higher export production (Marlow et al., 2000; Durham et al., 2001; Marlow, 2001). At ODP 1084, an increase in the abundance of diatom species associated with modern upwelling cells was also reported (Marlow et al., 2000). These results demonstrate an intensification of Benguela upwelling occurred after MIS 35 (Marlow et al., 2000; Durham et al., 2001; Marlow, 2001). The SST shift at ODP 1087 does not appear to reflect an upwelling signal at this site. To account for the permanent nature of the SST shift, upwelling would need to continue to influence the site after MIS 35, particularly during the more intense glacial cooling after MIS 22. However, even during glacial expansions of the Benguela upwelling cells during the late Pleistocene, newly upwelled waters rarely reached ODP 1087 (Giraudeau et al., 2001). This relatively minor influence of upwelling at the site developed as part of the Pliocene-Pleistocene transition, as the major upwelling cells migrated northwards *away* from ODP 1087 (Marlow, 2001; Giraudeau et al., 2002). Furthermore, interglacial SSTs after the cooling shift are similar to modern values, where upwelling has a minor influence over SST values at ODP 1087. Finally, the diatoms found during upwelling intensification at ODP 1084 (Marlow et al., 2000) were absent throughout the 1500-500 ka interval at ODP 1087A (J.A.Smith, University of Durham, pers.comm.).

A northward displacement of the ACC in the Southern Ocean by around 7° latitude by 1200 ka has been reconstructed from ODP 1090 (location shown in Figure 5.1), although it may have begun as early as 1830 ka (Becquey and Gersonde, 2002; Diekmann and Kuhn, 2002). The rapid cooling shift at ODP 1087A after MIS 35 is proposed here as a response to the ACC reaching a critical latitude that restricted the input of Agulhas waters to the Southern Benguela Region. After 870 ka (post-MIS 22) the southward retreat of the ACC lead to warming of interglacial SSTs to modern values, while glacials cooled by a few degrees (Becquey and Gersonde, 2002). This resulted in an increase in the amplitude of glacial-interglacial oscillations at ODP 1090, a trend also visible at ODP 1087 from 880 ka (Figure 5.2). This continued close coupling between the position of the ACC, as reconstructed from ODP 1090, and the SSTs at ODP 1087 further supports the proposal that SSTs at ODP 1087 are closely related to the position of the ACC. Significantly, the data from the South Atlantic region suggests that the global cooling that developed after MIS 35 was also associated with major expansions in sea-ice cover in both hemispheres. At ODP 1082, which lies to the north of ODP 1087 but is also under the influence of the Benguela Current (Figure 5.1), SSTs did not begin to cool until after 800 ka (Jahn, 2002). This may indicate that the initial restriction of Agulhas waters to the South-east Atlantic after MIS 35 has a limited impact on the temperature of the Benguela Current beyond the Southern Benguela Region. This hypothesis requires further investigation, and can be assessed by increasing the spatial resolution of analyses along the flow path of the Benguela Current.

5.3.4 The thermohaline circulation response to global cooling

By restricting the supply of warm and saline NAC to the Nordic Seas, and shifting centres of convection, the development of more extensive sea-ice cover in the North Atlantic has been linked to reductions in thermohaline circulation strength during late Pleistocene glaciations (Kellogg, 1980; Raymo et al., 1990a; Broecker, 1991; Venz et al., 1999). The interaction between the sea-ice expansion and deep-water circulation between 1500-500 ka is not straightforward. Weakening of *glacial* NADW formation as sea-ice cover expanded in the North Atlantic after MIS 35 (e.g. Raymo et al., 1990b; Oppo et al., 1995; de Menocal et al., 1997; Gröger et al., 2003) suggests that the late Pleistocene relationship between ice-cover and thermohaline strength may also have existed before 500 ka. Although the continued high abundance of $C_{37:4}$ during interglacials between MIS 35-22 suggests that sea-ice cover was also extensive during all except interglacial maxima during this interval (Figure 5.4), little change in interglacial NADW strength has been reported (e.g. Raymo et al., 1990b; Oppo et al., 1995; de Menocal et al., 1997; Gröger et al., 2003). Rather, when the overall abundance of $C_{37:4}$ at ODP 983 declines after MIS 22 (Figure 5.4), the glacial reductions in NADW formation intensify (Raymo et al., 1990b; Bickert et al., 1997; Hall et al., 2001; Forsberg et al., 2003; Gröger et al., 2003; Kleiven et al., 2003), with possible NADW stagnation identified during both glacial and interglacial intervals between MIS 22-16 (Schmieder et al., 2000). In the South Atlantic at ODP 1087, the fall in SSTs after MIS 35 has been interpreted here as a reduction in the input of the warm and saline Indian Ocean waters via the Agulhas retroflection. Gordon et al. (1992) proposed that such a reduction would have implications for the temperature and salinity of both the northward flowing Benguela Current and NAC. However, any reduction to the temperature and salinity of surface waters in the region of NADW formation, caused by the reduced input of Agulhas waters to the South-east Atlantic after MIS 35, appears to have had little impact on deep-water production.

This delayed response of the thermohaline circulation system to the global cooling may, like the ice-sheet mechanism outlined above, be related to the spatial distribution of the sea-ice cover. During and after MIS 22, the loci of deep-water convection followed the northward and westward migration of Atlantic Waters in the Nordic Seas introduced in Section 5.3.2 (Henrich et al., 2002). Gröger et al. (2003) propose that this brought the convection sites into closer proximity to Arctic Waters, and increased the sensitivity of convection centres to the position of the Arctic Front. The reduction in NADW strength after MIS 22 may therefore reflect a greater sensitivity of the convection process to any migrations of the Arctic Waters, even though the $C_{37:4}$ records suggest that sea-ice cover after MIS 22 was reduced in comparison to levels reached between MIS 32-35 (Figure 5.4). It has also been proposed that the mechanism of deep-water production may have changed after 1000 ka. Henrich and Baumann (1994) propose that prior to 1000 ka, deep-water formation was the result of brines generated by winter sea-ice formation. Thus, the extensive sea-ice suggested by the $\%C_{37:4}$ record presented here and the carbonate record of Henrich et al. (2002) may have been important in maintaining convection through brine formation. The migration of Arctic Waters after 1000 ka (Henrich et al., 2002) may therefore have reduced the extent of brine formation and had a greater impact on deep-water production. Furthermore, MIS 22 marks the increase in iceberg discharges that accompanied the development of larger northern hemisphere ice sheets (Ruddiman et al., 1986; St John and Krissek, 2002; Helmke et al., 2003b). The freshwater flux associated with large iceberg discharges has been identified as a key influence over deep-water convection in the North Atlantic, and in the operation of the bipolar seesaw (e.g. Broecker and Denton, 1990; Stocker, 2000; Ganopolski and Rahmstorf, 2001). The combination of relatively low freshwater discharges to the high latitudes of the North Atlantic due to smaller ice-sheets, and a lower sensitivity of the convection centres to this forcing and the position of the Arctic Front, may account for the more subdued response of thermohaline circulation to the global cooling and sea-ice expansion that followed MIS 35.

5.3.5 Implications for the MPT

A global cooling trend in the surface ocean that began after MIS 35, ca. 1145 ka, has been identified here. This began nearly 200-kyr prior to the expansion of global ice volume during MIS 22, ca. 920 ka. It is proposed here that this delay was the result of a synchronous expansion of sea-ice cover in the North Atlantic and North Pacific, and potentially also in the South Atlantic, which limited the supply of moisture to the high-latitude ice-sheet source regions. These results suggest that the MPT was driven by climate changes that began earlier than the defined onset of the MPT during MIS 22 (Mudelsee and Schulz, 1997), and that the MPT proper should therefore no longer be considered a single transition defined by ice volume changes. A two-stage transition is proposed here. First, global cooling and the appearance of the 'premature' 100-kyr cycle mark the onset of the first major climate change. The onset of this MPT 'Stage 1' by this definition is marked by the MIS 35-34 boundary ca. 1145 ka. If the start of the 'premature' 100-kyr cycle is used to mark the onset of Stage 1, this shifts its timing back to ca. 1200 ka. The second transition interval is defined by the increase in mean global ice volume during MIS 22, and the subsequent transition toward 100-kyr ice-sheet cycles. This MPT 'Stage 2' corresponds to the MPT as defined by Mudelsee and Schulz (1997). It was shown in Chapter 1 and in Figure 1.6 that there is some debate surrounding the timing of the MPT, because a number of climate changes have been detected that precede MIS 22. These early events even include a temporary emergence of 100-kyr cyclicity in the $\delta^{18}O$ record after ca. 1200 ka (Figure 1.5C, and Berger et al. 1993a). By considering the MPT as a two-stage transition in the manner described here these issues may be addressed, as the revised timing includes many of the events proposed to relate to the MPT but preceding the mean global ice volume increase, as shown in Figure 1.6.

The mechanism that drove the global cooling trend, and ultimately the shift toward 100-kyr cycles, is uncertain. In Figure 5.5, insolation variations driven by eccentricity, obliquity and precession are shown. No reduction in insolation can be detected to account for the permanent global cooling trend observed after MIS 35. Indeed, 'Phase

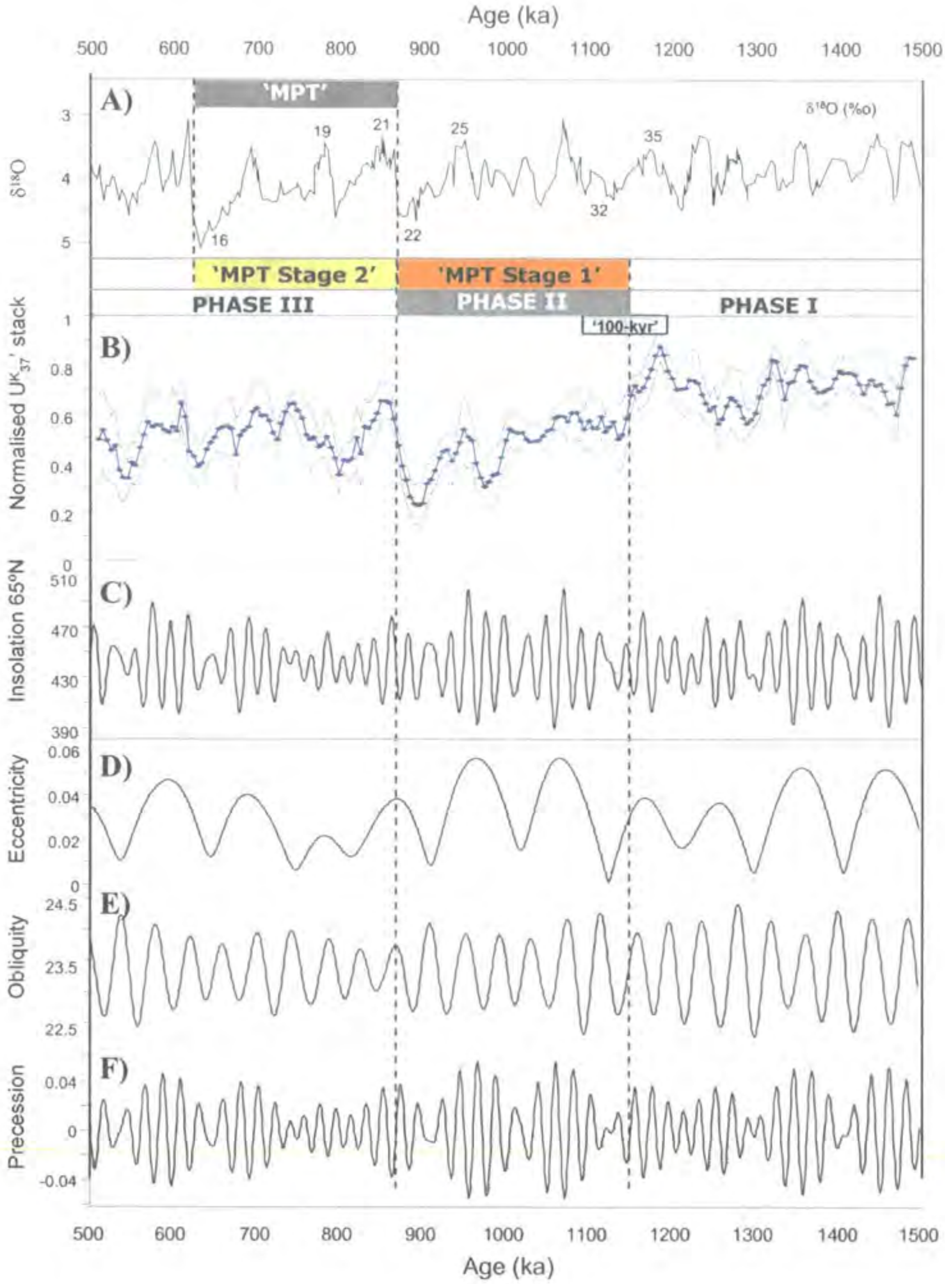

Figure 5-5 Comparison of the global cooling trend to orbitally driven insolation variations. The three phases of major SST change and the 'premature' 100kyr cycle as shown in Figures 5.2 and 5.3 are marked. The 'MPT Stage 1' and 'MPT Stage 2' as defined in this Chapter on page 138 are shown. A) Global ice volume record from Mix et al. (1995). B) Normalised U^{K}_{37}' stack, from Figure 5.2. C-F) Insolation variations, from (Berger and Loutre, 1991). C: Insolation at 65°N. D: Eccentricity. E: Obliquity. F: Precession.

II' is marked by a higher variability in insolation at 65°N (Figure 5.5). Although this resulted in a temporary intensification of insolation minima, it also increased the value of insolation maxima and seems unlikely to have resulted in long-term cooling. The origin of the global cooling trend must therefore lie with processes operating within the climate system itself. As outlined in Chapter 1 (Section 1.3.2 page 19), Tziperman and Gildor (2003) proposed that cooler deep-waters during the mid-Pleistocene resulted in a stronger vertical temperature gradient in the water column. In turn, they argue that this promoted restricted overturning and mixing of the water column, causing stratification and resulting in a surface water mass that was more sensitive to atmospheric cooling and thus sea-ice development. They propose that by encouraging the development of more extensive sea-ice cover during the mid-Pleistocene, the 'sea-ice switch' was activated, whereby increased sea-ice extent limits northern hemisphere ice sheet growth and initiates the rapid deglaciations characteristic of the 100-kyr cycles (Gildor and Tziperman, 2000; Gildor and Tziperman, 2001). Progressive cooling of deep-waters in the Atlantic relative to the Pacific has been identified from ca. 1500 ka (Tian et al., 2002). Gradual cooling of deep-waters in the tropical Pacific is also suggested by the progressive shoaling of the thermocline in the east after ca. 1500 ka (Cannariato and Ravelo, 1997). Although they did not present any mid-Pleistocene data, Dwyer et al. noted that glacial cooling of Atlantic deep-water was more intense during the late Pleistocene 100-kyr cycles in comparison to the 41-kyr cycles in the Pliocene.

Cooler deep-waters can account for the expansion of sea-ice and the decline in SSTs observed after MIS 35. As a result of the sea-ice expansion in the North Atlantic, the sensitivity of the region to insolation forcing would be reduced and the region would cool. Although not influenced directly by polar waters, the cooling trend that occurs at ODP 1087 can be linked to the northerly migration of the ACC, and to the expansion of sea-ice in the Southern Ocean. Deep-water cooling also explains the contemporaneous cooling in the eastern tropical Pacific (Figure 5.2, and Emeis et al., 1995) and in the Benguela upwelling cells (Marlow et al., 2000; Durham et al., 2001; Marlow, 2001). Upwelling brings cooler, deeper waters to the surface ocean in these two regions, and SSTs are therefore sensitive to changes in deep-water temperatures. The onset of sea-surface cooling occurs fairly rapidly, in contrast to the more gradual cooling reconstructed for the deep-waters. This suggests that after MIS 35, a critical deep-water temperature was reached that encouraged a rapid, threshold response in the surface ocean. Furthermore, the continued high levels of $C_{37:4}$ in the North Atlantic and Pacific during glacials after the initial onset of cooling supports the Tziperman and Gildor hypothesis that the mid-Pleistocene marked the development of more extensive sea-ice during glacials in response to deep-water cooling, and the potential development of the 'sea-ice switch' regulation of the 100-kyr cycles.

The cause of the modest decline in $C_{37:4}$ abundance after the maximum at 990 ka is uncertain. Once sea-ice cover reaches a critical extent and thickness, it insulates the surface ocean from the cold atmosphere, and growth is stopped (Gildor and Tziperman, 2000). The $C_{37:4}$ stack would suggest that this limit may have been reached at 990 ka, and could be sustained no longer. Alternatively, the more vigorous atmospheric circulation after 1145 ka suggested by more intense upwelling in the Benguela and eastern equatorial Pacific regions (visible by falling U^{K}_{37}' values at ODP 1084 and 849 in Figure 5.2) may have discouraged stratification, by increasing wind stress on the surface ocean in the high latitudes. An additional uncertainty for the sea-ice hypothesis, and for the global cooling trend presented here, is the mechanism that drove the fall in deep-water temperatures. Tziperman and Gildor (2003) suggested that it may relate to falling atmospheric CO_2 concentrations, that have also been proposed as a driving mechanism for the mid-Pleistocene expansion of the northern hemisphere ice-sheets (e.g. Berger and Jansen, 1994; Raymo, 1997; Paillard, 1998; Berger et al., 1999). Evaluating this mechanism is hampered by a limited data set of atmospheric CO_2 values from the period before the ice-core records began ca. 400 ka (Petit et al., 1999; Cuffey and Vimeux, 2001). Atmospheric CO_2 concentrations (pCO_2) exceeding those at present have been identified in the Pliocene, Miocene and earlier (Van Der Burgh et al., 1993; Pearson and Palmer, 2000), although 'modern' pCO_2 values were reconstructed during the Miocene by Pagani and co-workers (Pagani et al., 1999a; Pagani et al., 1999b). Only three data points from the Pleistocene were generated by Pearson and Palmer (2000), and show CO_2 concentrations (and the associated radiative forcing) rising towards the present. Two of these samples lie within glacial intervals (980 and 1490 ka), when lower pCO_2 would be expected compared to interglacials. The rise in pCO_2 may therefore be an artefact of the move from glacial to interglacial samples in the later stages of the Pleistocene.

The proposed long-term decline in pCO_2 relies upon theoretical relationships between tectonic uplift, particularly of the Tibetan Plateau, and the intensity of CO_2 draw-down by weathering processes (e.g. Raymo, 1994). Intensification of uplift may have a cooling impact on the climate system through mechanisms other than the proposed influence on the carbon cycle. Increased dust loading due to drier conditions in uplifted regions and more intense atmospheric circulation may encourage high-latitude cooling (Rea et al., 1998; An et al., 2001). Uplift may also affect pathways of tropospheric circulation, by splitting of shifting atmospheric circulation patterns (e.g. Wang and Li, 1985). Ruddiman and Kutzbach (1989) demonstrated that uplift of the Tibetan Plateau and the Sierra Nevada could cause cooling over North America, Asia, Europe, and the Arctic Ocean. Therefore, although a period of intensified Himalayan uplift is identified sometime between ca. 1320 ka and 1200 ka (e.g. Wu and An, 1996; Lu et al., 1999), its influence on the global climate state through the carbon cycle or high-latitude cooling is unclear. A strengthening of the Asian monsoon, consistent with intensification of Tibetan uplift, has been observed from ca. 1200 ka (Xiao and An, 1999; Heslop et al., 2002), although this appears to have become more pronounced later as part of the ice volume expansion from 920 ka (Wang and Zhao, 2000; Jian et al., 2003). In the absence of detailed records of carbon cycle behaviour and $p\mathrm{CO}_2$ reconstructions for the mid-Pleistocene, evaluation of the roles played by the carbon cycle and/or tectonic uplift in the global cooling trend identified here are limited.

A further issue that any potential driving mechanism for the onset of global cooling after MIS 35 needs to explain is the nature of MIS 35 itself. This isotope stage is a 'premature' 100-kyr cycle prior to the onset of their dominance after MIS 16. It is visible in the two high-latitude Atlantic SST records reconstructed here, ODP 1087 and 983 (Figure 5.2). It also corresponds to an unusual Chinese loess formation ('L_{15}') marking a major strengthening event in the Asian monsoon (Heslop et al., 2002), and by a 100-kyr cycle in both the global ice volume and NADW circulation records (Mudelsee and Stattegger, 1997; Schmieder et al., 2000). Temporary strengthening of the 100-kyr periodicity in δ^{18}O can also be observed after 1200 ka (Figure 1.5C and Berger et al., 1993a). The 'premature' 100-kyr cycle is not visible in the tropical SST records however (Figure 5.2), suggesting that within the surface ocean it is largely a high-latitude phenomenon. In addition to marking the onset of global cooling, this cycle also highlights a temporary decoupling of climate system components from the 41-kyr obliquity pacing that dominates the time-series prior to MIS 22 (Figure 5.5). Despite low obliquity at ca. 11745 ka, interglacial SSTs remain high, and instead closely follow eccentricity, although the latter is relatively weak at this time (Figure 5.5). MIS 35 may therefore mark the first non-linear climate system response to orbital forcing prior to the dominant 100-kyr periodicity after MIS 16. The continued dominant 41-kyr cyclicity in the climate system after MIS 35 shows that this was a temporary phenomenon. This may demonstrate that either the subsequent global cooling was necessary to permanently tip the climate system into this non-linear state, perhaps by increasing northern hemisphere ice sheet size, or that the expansion of sea-ice restricted the impact of this non-linear behaviour by dampening high-latitude climate change. The results presented here therefore show that that the surface ocean played an key role in the development of the MPT, by both driving and modulating the northern hemisphere ice-sheet response to global cooling.

5.3.6 Implications for the onshore record

It has been shown that the global cooling trend identified after MIS 35, and the prolonged and extensive expansion of sea-ice cover in both hemispheres, influenced heat and moisture transport within the climate system. These impacts are most clearly represented in the global ice volume records, but are also expected to have influenced the environments beyond the ice-sheets themselves. Significantly, a number of evolutionary events occurred onshore, including hominid evolution, that may be a response to environmental changes associated with the climate trends presented here. The temporal and spatial resolution of sedimentary archives onshore during this time period are considerably lower than those of the marine realm. Fragmentary sequences and uncertainties in dating also hamper comparisons of onshore events to those from the marine records. Tentative correlations are therefore made between environmental change onshore, and the surface ocean changes presented here.

The pronounced cooling that occurred in tropical SSTs during MIS 24-22, accompanied by the increase in mean global ice volume (Figure 5.1), correlates with cool episodes identified at a variety of sites in South America. The coldest stage of the mid-Pleistocene record in Bolivia is recorded by $\delta^{13}C$ analysis on mammalian teeth, which indicate a shift toward grazing of C_3 grasses, occurs during MIS 24 (MacFadden, 2000). The Funza pollen record from the high plain of Bogotá, Columbia, exhibits a decrease in mean annual temperature at this time, and also records a shift toward 100-kyr cyclicity (Hooghiemstra and Ran, 1994). A fall in the upper forest limit ca. 1000 ka in the Andes, and again during MIS 25-22, also indicates equatorial cooling (Hooghiemstra and Cleef, 1995). In the far south, the maximum extent of the Patagonian ice sheet was reached ca.

1100 ka (Singer et al., 2004). This correlates with the onset of global cooling, and may have been encouraged further by the northward migration of the ACC. During the last glacial maximum, the latter process is proposed to have pushed the moisture bearing westerlies equatorward towards the Patagonian ice-sheet source region (e.g. Hulton et al., 1994) as the equator-pole temperature gradient became 'squeezed' by global cooling and high-latitude ice-sheet expansion. However, climate may not have been the dominant control over the Patagonian advance, as tectonic uplift is believed to have increased the ice-sheet accumulation area after 1200 ka, with less extensive glaciations after this time attributed to tectonic and erosional removal of these accumulation areas over the rest of the Pleistocene (Singer et al., 2004).

An analogous equatorward migration of the moisture-bearing westerlies in the Northern Hemisphere has been proposed here to have driven the 1100 ka advance of the Scandinavian ice-sheet into the North Sea Basin (Section 5.3.2). One should expect that a similar advance may be recorded in the Rocky Mountain/Sierra Nevada range, which is also sensitive to the position of the westerlies. However, although the expansion of the northern hemisphere ice-sheets from ca. 920 ka (MIS 22) are associated with a thickening but spatial reduction in the Laurentide ice-sheet (Clark and Pollard, 1998) it is unclear how the other North American ice masses behaved. Furthermore, the change in the nature of the Laurentide ice-sheet has been attributed to changes in the basal substrate rather than to climatic control (Clark and Pollard, 1998). The chronological control over the Middle and Early Pleistocene glaciations in Canada are not tight enough to link with the climate changes discussed in this Chapter (Prof. John Clague, pers.comm. September 2004). Further north, iceberg-rafting into the North-east Pacific from Alaskan ice masses increased after 900 ka (Rea and Snoeckx, 1995). Improved dating and the analysis of stratigraphic archives documenting palaeo-environmental change are therefore required to assess the impact of the mid-Pleistocene cooling in North America.

In Europe, environmental records are limited by the extensive and repeated glacial advances that eroded interglacial sedimentary sequences, and restricted the distribution of non-glaciated environments during cold stages for generation of sedimentary archives bearing palaeoclimate information. Beyond the ice sheet limits, evidence for more intense fluvial erosion and a coupling of river terrace formation to glacial-interglacial oscillations in the Thames and the Somme are correlated to the emergence of the 100-

kyr cycles (see review by Bridgland, 2000). The fluvial response to the cooling and sea-ice expansion after MIS 35 is uncertain. In southern Europe, cooler climates develop during both glacial and interglacial intervals from about 900 ka (Bertini, 2003). The clearest picture of environmental change comes from the faunal records, which contain a number of significant evolutionary events that correlate more closely to the onset of cooling at ODP 983. Described as a 'major climate crisis' that affected Europe, the 'end-Villafranchian event' is marked by rapid replacement of the Late Villafranchian fauna by the more cold-adapted fauna comparable to modern types (Azzaroli, 1995). The associated mammalian migrations (Opdyke, 1995) probably helped to maintain faunal diversity by replacing disappearing species, which included extinction of over 20 large mammals (Azzaroli, 1995). Few sites exist where the a mix of the two faunal sets can be identified, indicating a rapid turnover of species (Azzaroli, 1995). The end-Villafranchian event begins in the high-latitudes of Europe from around 1200 ka (Azzaroli, 1995), as ODP 983 underwent cooling and sea-ice expansion (Figures 5.1, 5.4). The turnover reached the mid-latitudes sometime later, dated between 1050-900 ka (Azzaroli, 1995; Opdyke, 1995; Napoleone et al., 2003). This correlates to the interval between the maximum abundance of $C_{37:4}$ (and the coldest SSTs at ODP 983), and the expansion of the northern hemisphere ice masses. These correlations suggest that changes to the surface ocean of the North Atlantic after MIS 35 may have played a key role in driving the end-Villafranchian 'crisis'.

Significant changes within the hominid evolution record in Europe and Asia also occurred at this time. The first major geographical expansion of the *Homo* lineage from Africa into the Eurasian region occurred around 1000 ka (de Menocal and Bloemendal, 1995). This expansion of *Homo erectus* beyond Africa has been attributed to the development of fire, which would be a valuable tool under the cooler climate regime of Europe relative to Africa (Haviland, 1994). If 1000 ka is an accurate date for the *Homo* expansion, it correlates with the waning of the sea-ice extent in the North Atlantic, and consequent warming in interglacials, although glacial cooling may have intensified with the expansion of the northern hemisphere ice sheets. Renewed moisture supplies to Europe and warmer interglacials may therefore have made the region more habitable in comparison to the preceding 200-kyr.

The expansions of *Homo* from Africa ca. 1000 ka may also have been driven by environmental change in Africa. In Section 5.3.3, intensification of Benguela upwelling was identified after MIS 35. The presence of cooler upwelled waters offshore reduces precipitation and increases aridity onshore, and is associated with more vigorous atmospheric circulation (Dowsett and Willard, 1996). More intense atmospheric circulation is also suggested by the synchronous expansion of sea-ice and high-latitude cooling observed in both hemispheres, which may have increased the equator-pole temperature gradients given the smaller SST decline in the tropical sites (Figure 5.2, 5.3). Strengthening atmospheric circulation and increasing aridity in both east and west Africa have been identified in marine records from ca. 1000-900 ka (de Menocal, 1995; Schefuß et al., 2003). Increasing aridity is also suggested by a shift towards C_4 grasslands in the subtropical region from ca. 920 ka, identified in marine records from the west (Schefuß et al., 2003) and onshore records from the east (Sikes, 1999). Reduced inputs from the Kunene and Congo rivers into the South-east Atlantic occur from 1100 ka and 1050 ka respectively (Dupont et al., 2001; Durham et al., 2001), accompanied by increased terrigenous inputs of Namibian desert origin between 1500 and 580 ka (Jahn et al., 2003). More vigorous atmospheric circulation is also suggested by the intensification of the Asian monsoon systems, although these become more pronounced after MIS 22 (Xiao and An, 1999; Wang and Zhao, 2000; Heslop et al., 2002), which would be expected to affect precipitation patterns in Asia and India (e.g. Wang et al., 2003).

The widespread changes in the palaeoenvironment of southern Africa seem likely to have had an impact on living populations. Although the onshore archives are of relatively low-resolution, some significant changes can be identified. In particular, a number of extinctions mark the hominid records between 1500 and 1000 ka (e.g. *Australopithecus robustus*, *Australopithecus boisei*), so that by 1000 ka *Homo erectus* was the only known living hominid (Kimbel, 1995). Extinctions in the mouse record, and a reduction in suid (pig) diversity, are also observed during this time (Bishop, 1999; Denys, 1999). These evolutions have been attributed to the development of increasingly open landscapes, or the increased seasonality that may have developed as the amplitude of climate oscillations increased (Bishop, 1999; Owen-Smith, 1999; Sikes, 1999). Although a tentative conclusion, the global cooling trend and its associated environmental changes onshore may have driven a number of significant evolutionary events onshore. However, these links remain speculative, further encouraging the need for better spatial and temporal resolution of onshore records during the mid-Pleistocene.

5.4 Conclusions

A global cooling trend has been identified in the SST records reconstructed in this thesis. This trend is also confirmed in a number of additional data sets, which together cover a wide variety of oceanographic regimes. Significantly, the onset of this cooling after MIS 35 preceded the increase in mean global ice volume during MIS 22 that heralds the transition to 100-kyr ice-sheet cycles. This delayed response can be attributed to the expansion of sea-ice that accompanied the global cooling restricting ice-sheet growth. The later increase in global ice volume is associated with a reduction in sea-ice cover, that enabled the supply of moisture to ice-sheet source regions to increase. Accompanied by cooler global temperatures, this enhanced moisture flux encouraged the development of larger northern hemisphere ice masses during and after MIS 22. A delayed response in thermohaline circulation to the global cooling was also identified. This was attributed to the increasing sensitivity of deep-water convection to the extent of sea-ice in the North Atlantic, due to migration of convection loci towards the Arctic Front after 1000 ka.

The delayed response of the ice-sheets to the global cooling suggests that the MPT should no longer be considered as a single transition between the mean global ice volume increase at ca. 920 ka and the first dominant 100-kyr cycle at ca. 640 ka (Mudelsee and Schulz, 1997). Rather, the shift toward the 100-kyr climate system occurred in two stages. The onset of the first stage is marked by global cooling in the surface ocean and an expansion of sea-ice. These changes may have played a role in a number of environmental changes observed onshore. The second stage of the transition is represented by the MPT after MIS 22 as defined by Mudelsee and Schulz (1997). The most intense climate changes within the thermohaline circulation system, Asian monsoon strength and further environmental changes onshore are identified during this stage.

Further research is required to address a number of issues. First, an increase in the spatial resolution of sea ice cover (estimated here using $\%C_{37:4}$) at high-latitudes after MIS 35 is necessary in order to determine the extent of the proposed migrations of Arctic Waters and sea-ice cover. Second, the cause of the cooling and sea-ice expansion remains uncertain. It may relate to falling atmospheric CO_2 concentrations, variations in atmospheric circulation due to tectonic changes, or to cooling of the deep-waters. The data presented here most strongly support the latter proposal, but further analysis of the behaviour of the carbon cycle, and reconstructions of atmospheric CO_2 concentrations are required to evaluate the CO_2 hypothesis further.

6. Organic carbon export from the surface ocean during the mid-Pleistocene

6.1 Introduction

The mid-Pleistocene climate transition (MPT) has conventionally been defined as the shift in the dominant periodicity of glacial-interglacial oscillations from 41-kyr to 100-kyr. This occurs across the time interval ca. 920-640 ka (Mudelsee and Schulz, 1997). The transition occurs with no significant change to the strength of the corresponding orbital parameters of obliquity and eccentricity (e.g. Berger and Loutre, 1991). The MPT therefore represents a change in the response of the climate system to insolation forcing, driven by processes and components within the climate system itself (Imbrie et al., 1993). The emergence of the 100-kyr oscillations is preceded by an increase in the mean global ice volume during MIS 22, ca. 920 ka (Mudelsee and Schulz, 1997). This marks the development of more extensive northern hemisphere ice-sheets, whose greater inertia is thought to be critical in increasing the duration of the glacial-interglacial oscillations (e.g. Imbrie et al., 1993; Berger and Jansen, 1994; Raymo, 1997; Clark and Pollard, 1998; Paillard, 1998; Ruddiman, 2003). In Chapter 5, it was proposed that this increase in mean global ice volume was driven by sustained global cooling in the surface ocean that developed after MIS 35, ca. 1145 ka (Section 5.3.1). The onset of the global cooling preceded the expansion of the northern hemisphere ice-sheets during MIS 22 (ca. 920 ka) by over 200-kyr (Chapter 5). This delayed response in the ice-sheets is proposed to result from the synchronous expansion of sea-ice cover in the North Atlantic and North Pacific with the onset of the cooling, which acted to reduce the supply of moisture to the ice-sheet source regions. These earlier climate changes imply that the MPT was much longer than had previously been stated, and in response a revised two-stage model for the MPT was proposed (Section 5.3.5). The onset of the MPT 'Stage 1' is marked by the onset of global cooling and the expansion of sea-ice cover from ca. 1145 ka (MIS 34). 'Stage 2' defines the interval between the MIS 22 increase in mean global ice volume and the MIS 16 appearance of the first dominant and recurrent 100-kyr cycle i.e. the MPT as defined by Mudelsee and Schulz (1997).

The driving mechanism for the global decline in sea-surface temperature (SST) and the expansion of sea-ice cover in the high-latitudes of both hemispheres is not clear. In Chapter 5, these trends were attributed to falling deep-water temperatures encouraging vertical stratification and sea-ice growth, as proposed by Tziperman and Gildor (2003). A decline in deep-water temperature in the Atlantic has been identified from 1500 ka (Tian et al., 2002), which may also account for the pronounced cooling in upwelling regions (Chapter 5). Tziperman and Gildor (2003) propose that the deep-water cooling may have been driven by a fall in atmospheric CO_2 concentration (pCO_2). By driving global cooling, pCO_2 decline has also been proposed as a driving mechanism for the mid-Pleistocene expansion of the northern hemisphere ice-sheets (e.g. Berger and Jansen, 1994; Raymo, 1997; Paillard, 1998; Berger et al., 1999). The evaluation of this hypothesis is limited by the lack of pCO_2 data before ca. 400 ka (Petit et al., 1999; Cuffey and Vimeux, 2001). Only three Pleistocene data points were generated by Pearson and Palmer (2000), which show a rise in pCO_2 after 1490 ka. As discussed in Chapter 5, the proposed long-term (Plio-Pleistocene) decline in pCO_2 relies instead upon theoretical relationships between tectonic uplift and CO_2 draw-down by weathering processes (e.g. Raymo, 1994), which are themselves controversial.

The global ocean is the largest carbon reservoir in the modern climate system, and therefore plays an important role within the carbon cycle (Siegenthaler, 1993; Levin and Hesshaimer, 2000). The 'biological carbon pump' exports organic carbon produced by photosynthetic utilisation of upper ocean CO_2 by phytoplankton to the deep-ocean (Shaffer, 1993; Falkowski et al., 2000). A strong biological carbon pump removes CO_2 from surface waters, and thus promotes dissolution and draw-down of CO_2 from the atmosphere. An increase in biological carbon pump strength through higher surface productivity has been proposed to account for glacial reductions in pCO_2 during the late Pleistocene (e.g. Sarnthein et al., 1988). This may be key at sites where modern productivity is high but nutrient-limited. This includes the eastern equatorial Pacific, where a low supply of iron from continental sources is considered a limiting factor (Chavez et al., 1991; Martin et al., 1991). During glaciations, enhanced aeolian dust flux to the eastern equatorial Pacific due to increased aridity onshore and more intense atmospheric circulation is proposed to increase the supply of iron to the surface ocean, triggering an increase in primary production and a consequent draw-down of pCO_2 (e.g. Martin, 1990; Watson et al., 2000; Ridgwell and Watson, 2002; e.g. Bopp et al., 2003; Ruddiman, 2003). Ruddiman (2003) proposed that this feedback may be particularly strong at the obliquity frequency, due to the impact of ice-sheet size on trade wind intensity and dust flux to the tropics. He proposed that this feedback may be key to driving the climate system into a deeper glacial state and the development of a 100-kyr cycle when low obliquity coincides with low precession and eccentricity.

The principal aim of this Chapter is to assess the role played by the biological carbon pump in driving the mid-Pleistocene climate changes presented in Chapter 5. The main objectives are:

1. To identify global variability in the strength of the biological carbon pump between 1500-500 ka;
2. To assess the role played by the global variability in biological carbon pump strength in driving the mid-Pleistocene global cooling and/or the expansion of the northern hemisphere ice-sheets.

To achieve these objectives, the strength of the biological carbon pump at each of the four sites considered in this thesis is estimated using the accumulation rates of the chlorin pigments ('P665'). As discussed in Chapter 3, the abundance of chlorins within sediments reflects the interaction between production in the surface ocean and a suite of degradation processes that act on the organic carbon as it travels through the water column and into sediments. It is this balance that controls the export of organic carbon from the surface ocean to the underlying sediments and defines the strength of the biological carbon pump, and is recorded in the abundance of chlorins in the sediments. The variability in organic carbon export at a global scale is measured here by applying a stacking procedure to the chlorin accumulation rate time-series generated in this thesis. Additional data sets are added to the stack from the Benguela upwelling system and the North-west Pacific (ODP 1084 and 882; core locations shown in Figure 6.1). Each of the sites examined here have different local controls over surface production (Figure 6.1) and chlorin accumulation rates in the underlying sediments. The common trend between these sites may therefore be representative of a 'global' response of the ocean driving changes in the accumulation rates of organic carbon in deep-sea sediments.

6.2 Stacking procedure

The chlorin accumulation rate time-series for each core were stacked following the procedure outlined in Chapter 5. In summary, each time-series was smoothed using a 5-pt (ca. 25-kyr) running mean. Each smoothed series was normalised by subtracting the minimum value and dividing by the amplitude of the variations (i.e. the maximum-minimum value) for that series. The same ODP sites used for the U^{K}_{37}' stacks were used

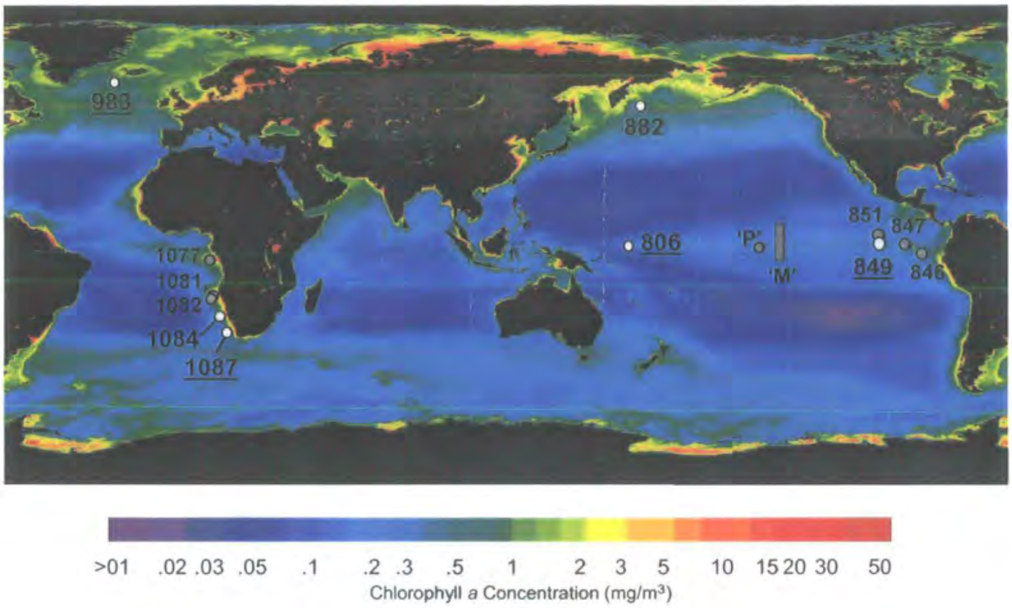

Figure 6-1 Modern chlorophyll-*a* concentrations in surface waters (annual mean), and the locations of cores discussed in this chapter. The four sites investigated in this thesis are underlined (ODP 983, 1087, 849 and 806). The sites used in the chlorin pigment stack are shown by white circles. This includes data from ODP 882 (Haug, 1996) and ODP 1084 (Marlow et al. 2000). Additional sites discussed in the text are shown by black circles. The vertical grey bar 'M' marks the transect of sites analysed by Murray et al. (2000). Site 'P' marks the location of the core discussed by Pearson and Palmer (2003). Map source: http://seawifs.gsfc.nasa.gov/SEAWIFS/IMAGES/IMAGES.html.

to generate the chlorin stack i.e. the four cores analysed in this thesis (P665 analyses), plus chlorin accumulation rate data from Benguela core ODP 1084 (P410, Marlow et al., 2000) and North-west Pacific core ODP 882 (P670, Haug, 1996). The ODP 1084 record was not smoothed, due to its relatively low resolution (ca. 50-kyr).

It should be noted that the biological pumping and the physical exchange of CO_2 between the ocean and atmosphere at each site vary in their effectiveness. For example, in the North Atlantic, the sinking of surface waters during deep-water formation prevents surface waters from equilibrating to atmospheric CO_2 levels. The result is that surface waters are undersaturated in CO_2, and the region is a CO_2 *sink* (Bigg, 1998). Biological production in these areas may therefore enhance CO_2 draw-down. In contrast, upwelling regions release CO_2 to the atmosphere and are thus *sources* of CO_2. Although high nutrient levels in upwelling zones are associated with high levels of biological production, the latter must be high enough to utilise the excess CO_2 in order to draw-down CO_2 (Lampitt et al., 1995; Schneider and Müller, 1995). Thus, high chlorin accumulation rates under upwelling zones require careful interpretation. The sites analysed here encompass a range of oceanographic regimes. Sites ODP 1084 and 849 are influenced by upwelling, while ODP 983 lies in the northern North Atlantic, close to regions of deep-water formation. Sites ODP 806, 1087, 882 are not affected by either of these processes, where the physical exchange of CO_2 between the ocean and atmosphere is in / close to equilibrium, and thus changes in the biological pump strength have potentially greater impacts on pCO_2. One region that is not included in the stacked record but which plays an important role in ocean-atmosphere CO_2 exchange is the Southern Ocean (Figure 6.1). A reduction in the degassing of CO_2 in upwelling waters of the Southern Ocean due to an expansion of sea-ice cover has been proposed to account for some of the glacial fall in pCO_2 (Stephens and Keeling, 2000). In Chapter 5 it was noted that a northward migration of the Antarctic Circumpolar Current (ACC) occurred during the mid-Pleistocene that may have been associated with more extensive sea-ice cover. The potential role of the Southern Ocean and its impact over pCO_2 during the mid-Pleistocene will be discussed later in this Chapter.

6.3 Results & Discussion

6.3.1 Organic carbon export during the mid-Pleistocene

Figure 6.2 presents the chlorin accumulation rate time-series generated in this thesis, and those from the Benguela upwelling system (Marlow, 2001), and the North-west Pacific (Haug, 1996). All cores were analysed using UV-Vis spectrophotometry (following the method described in Chapter 2) and show changes in relative accumulation rates down-core ('area units'/cm^2kyr^{-1}). At ODP 882, in the North-west Pacific, these values were calibrated to the extinction coefficient of the chlorin phaeophorbide using the Beer-Lambert law to give absolute chlorin accumulation rates, $\mu g/cm^2kyr^{-1}$ (following the method described in Harris and Maxwell, 1995; Haug, 1996). Chlorin accumulation rate data was not available from ODP 846 (Emeis et al., 1995). The mass accumulation rate of total organic carbon (MAR TOC) generated by Emeis et al. (1995) is displayed instead in Figure 6.2 as a measure of organic carbon export, given the low inputs of terrigenous detritus to the site (Hovan, 1995). In Chapters 3 and 5, the global cooling trend and sea-ice expansion between MIS 35-22 (ca. 1145-880 ka) was used to divide the 1500-500 ka interval into three phases of surface ocean circulation that were broadly synchronous between sites. To assess the relationship between the long-term trends in SST and chlorin accumulation rates, these three phases are displayed on Figure 6.2. 'Phase II' corresponds to the global cooling of 'MPT Stage 1' as discussed above.

There is in appearance little correspondence in the long-term trends of the chlorin accumulation rate time-series between sites in Figure 6.2, demonstrating the operation of strong local controls over chlorin accumulation rates. For example, the long-term decline in glacial chlorin accumulation rates between MIS 32-22 (ca.1080-880 ka) and

Figure 6-2 (Overleaf) Chlorin accumulation rate records between 1500-500 ka from the tropical Pacific, the Benguela upwelling system, and the mid-high latitudes of the North and South Atlantic and the North Pacific. Time-series generated in this thesis shown in green. Additional data sets from ODP 846 (mass accumulation rate of total organic carbon; Emeis et al., 1995), ODP 1081 and 1084 (Marlow, 2001) and ODP 882 (Haug, 1996). The three phases of major SST change as defined in Chapter 5 are marked by the vertical lines. The global ice volume record from ODP 849 (Mix et al., 1995) is shown for reference, with the MPT as defined by Mudelsee and Schulz (1997) marked as 'MPT'. Periods of relatively high chlorin accumulation rates (identified by eye) that occur between three or more sites are highlighted with the vertical grey bars. Potentially significant increases in chlorin accumulation rates that are isolated to one site are highlighted with vertical yellow bars, also identified by eye.

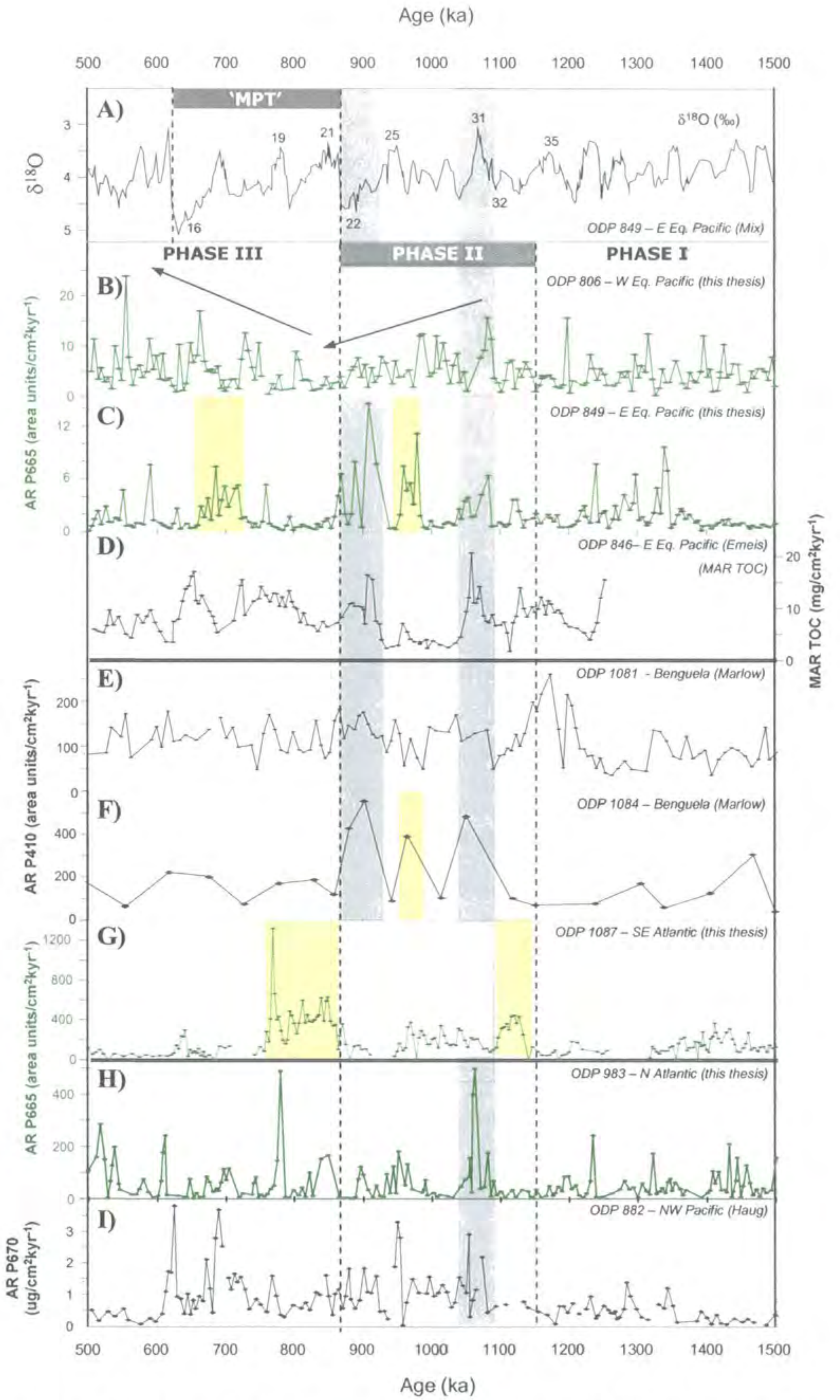

Figure 6.2 Chlorin accumulation rate records between 1500-500 ka from the tropical Pacific, the Benguela upwelling system, and the mid-high latitudes of the North and South Atlantic and the North Pacific. For explanation see the caption on the previous page.

subsequent progressive increase in glacial values after from MIS 20 (post-800 ka) at ODP 806 in the western Pacific is not represented at any other site in Figure 6.2. Two periods of high chlorin accumulation rates can be identified at ODP 1087 in the South-east Atlantic (Figure 6.2G), between MIS 34-26 (ca. 1135-960 ka) and MIS 21-19 (ca. 880-760 ka), but they have poor correlations to the other time-series displayed in Figure 6.2. Significantly, Figure 6.2 also shows two periods where chlorin accumulation rates increased synchronously between three or more sites. The first occurred during MIS 31-30, ca. 1090-1040 ka, when high chlorin accumulation rates are recorded at all sites except ODP 1087 (Figure 6.2). This is followed during MIS 24-22 (ca. 950-880 ka) by high chlorin accumulation rates at ODP 849, 846, and 1084 (Figure 6.2).

These events are clearly identified in the chlorin accumulation rate stack (hereafter the 'chlorin stack'). The chlorin stack reached its maximum value during MIS 31, with values remaining high until after MIS 22 (Figure 6.3B). The chlorin stack demonstrates that despite the strong regional signals apparent in Figure 6.2, a rapid and permanent increase in organic carbon export at a global scale occurred after ca. 1150 ka (after MIS 35). This is accompanied by an increase in inter-regional variability, demonstrated by the greater standard deviation (Figure 6.3B) and larger difference between minimum and maximum values (Figure 6.3C) after MIS 32 (ca. 1100 ka). This increase in the export of organic carbon from the surface ocean after MIS 35 suggests that the biological carbon pump at a global scale strengthened at this time. Superimposed on this long-term trend the chlorin stack also shows variability at glacial-interglacial timescales (Figure 6.2B).

As discussed above, a stronger biological carbon pump has been suggested as a potential mechanism for driving global cooling during glacial stages through reducing $p\mathrm{CO}_2$. The global SST signal generated in Chapter 5 by stacking $\mathrm{U}^{\mathrm{K}}_{37}{}'$ values from the same sites analysed in this Chapter is shown in Figure 6.2D. Significantly, there is a negative correlation between the level of organic carbon export and SSTs at a global scale throughout the 1500-500 ka interval. This relationship holds over both the glacial-interglacial and longer-term timescales, and suggests that a strong biological carbon

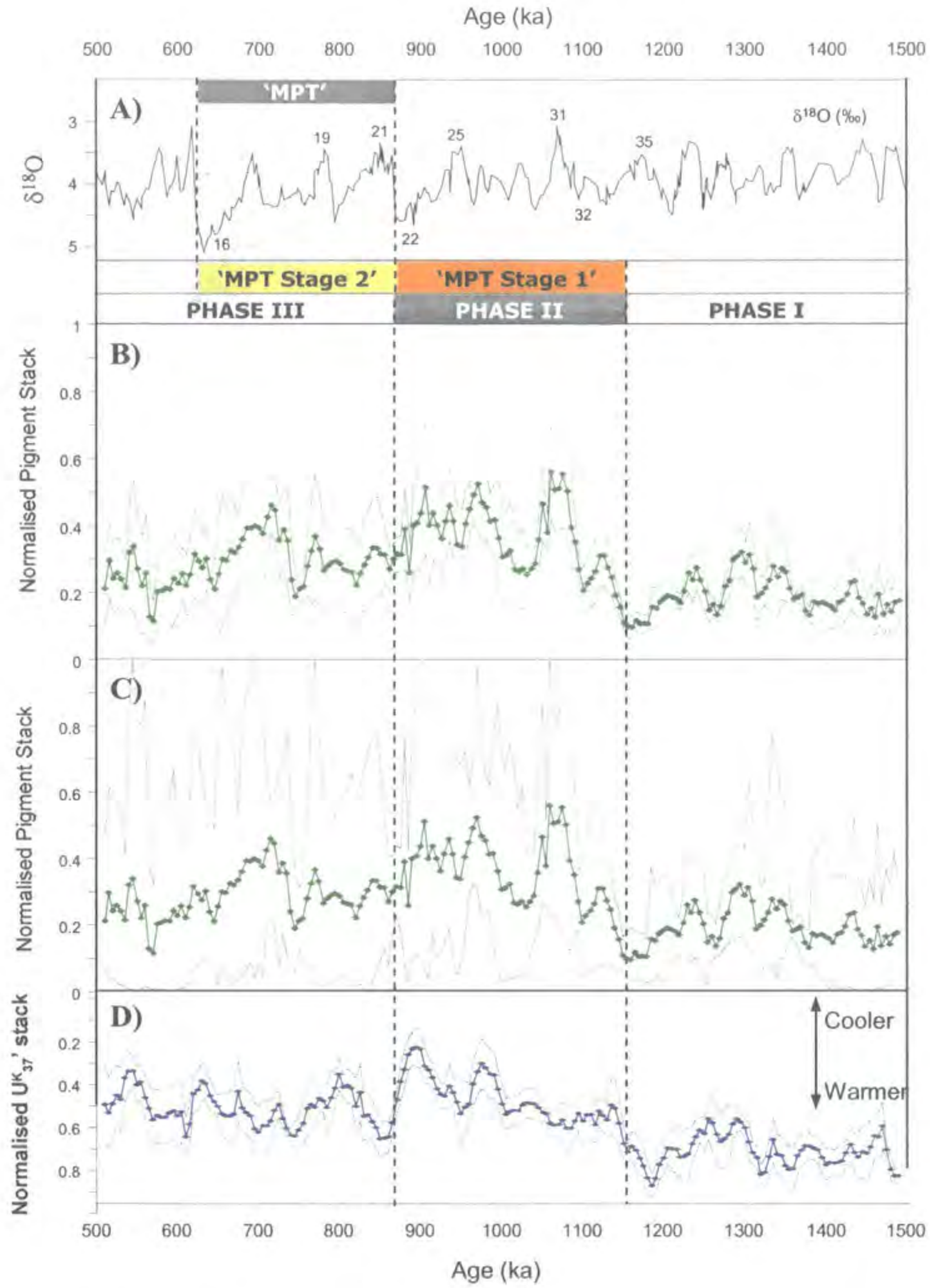

Figure 6-3 Stacked chlorin accumulation rate time-series between 1500-500 ka. The three phases of major SST change and the revised two-stage model of the MPT as described in Chapter 5 are marked. A) Global ice volume record from Mix et al. (1995); B) Stack of normalised pigment accumulation rates from the four cores analysed in this thesis, plus ODP 1084 (Marlow, 2001) and ODP 882 (Haug, 1996). The mean value is shown in green, the standard deviation by the thin grey lines; C) Stack of normalised pigment accumulation rates from the four cores analysed in this thesis, plus ODP 1084 (Marlow, 2001) and ODP 882 (Haug, 1996). The mean value is shown in green, the maximum and minimum values for each age point by the thin grey lines; D) Stack of normalised U^{K}_{37}' from the four cores analysed in this thesis, plus ODP 1084 (Marlow et al., 2000) and 882 (Haug, 1996), from Chapter 5. Mean value shown in blue, standard deviation shown by grey lines. Note that the scale has been reversed relative to Figure 5.3.

pump may play an important role in driving or modulating global cooling through its impact over $p\mathrm{CO}_2$. Significantly, the strengthening of the biological carbon pump after ca. 1150 ka suggested by the chlorin stack correlates to the onset of global cooling that was identified in Chapter 5 from ca. 1145 ka (Figure 6.3D). This raises the possibility that the sustained global cooling was driven by a reduction in $p\mathrm{CO}_2$ in response to a stronger biological carbon pump. A potential problem for this hypothesis arises with the timing of the chlorin stack maximum during the interglacial MIS 31 (Figure 6.3B). MIS 31 is marked by the warmest interglacial of the 1500-500 ka interval at ODP 983 in the northern North Atlantic (Chapter 3), and has the lowest global ice volume of this interval (Figure 6.3A). However, the duration of the interglacial maximum, as recorded by $\delta^{18}O$, is relatively short in comparison to other interglacial stages during this time (Figure 6.3A). The U^{K}_{37}' stack also fails to show any significant rise in global temperature during this interval (Figure 7.2D) despite low global ice volume (Figure 6.3A). This may demonstrate the effectiveness of the strong biological carbon pump in reducing $p\mathrm{CO}_2$ and maintaining relatively low global SSTs during this interglacial.

The chlorin stack in Figure 6.3 suggests that organic carbon export from the surface ocean, and thus the strength of the biological carbon pump, may have driven and/or maintained the global cooling from MIS 35 that was identified in Chapter 5. At a regional scale, high chlorin accumulation rates in the Benguela region of the South-east Atlantic (ODP 1087, 1084, 1081) and the equatorial upwelling region of the eastern Pacific (ODP 849) correlate with both the onset of global cooling and the later increase in global ice volume during MIS 22 (Figure 6.2). These regions may therefore have played an important role in driving the climate events associated with the MPT. In the following sections, the potential impacts of regional scale changes in organic carbon export over $p\mathrm{CO}_2$ are examined for the four sites investigated in this thesis.

6.3.2 The Benguela Region

The Benguela records can be divided into two sub-systems based on the surface oceanography. ODP 1084 and 1081 are located beneath the cool and nutrient-rich Benguela upwelling cells, whilst ODP 1087 lies beyond the region of upwelling, where SSTs are controlled by the relative inputs of warm Agulhas waters from the Indian Ocean and cooler Southern Ocean waters from the Antarctic Circumpolar Current system (see Figure 6.1 for core locations; Shannon et al., 1989; Gordon et al., 1996).

This division could be identified in the U^{K}_{37}' time-series presented in Chapter 5, where progressive cooling in the upwelling sites after MIS 35 contrasted with rapid cooling at ODP 1087 (Figure 5.2). The division is also reflected in the chlorin accumulation rate time-series (Figures 6.2E-G). This is most clear between ODP 1087 and ODP 1084, the latter lying below the major upwelling cell (Figures 6.2F,G).

The contrasting chlorin accumulation rate records between ODP 1087 and ODP 1084 supports the proposal put forward in Chapter 5 that ODP 1087 was not affected by upwelling between 1500-500 ka. In Chapter 5, the post-MIS 35 cooling shift that occurred at the site was attributed to a reduced input of warm Agulhas waters to the Southern Benguela Region in response to the northward migration of the Antarctic Circumpolar Current (ACC, Becquey and Gersonde, 2002; Diekmann and Kuhn, 2002). This process may also account for the periods of sustained high organic carbon export at ODP 1087. The subtropical front that forms the northern margin of the ACC is identified in modern surface waters to the south of ODP 1087 by high levels of chlorophyll and hence high primary production (Figure 6.1, and shown in greater detail in Figure 1.9). The position of the ACC migrated southward during interglacials between 1500-500 ka (Becquey and Gersonde, 2002; Diekmann and Kuhn, 2002), which is reflected in higher interglacial SSTs at ODP 1087 (Figure 5.2). However, chlorin accumulation rates are sustained at high levels for two periods at ODP 1087, independently of glacial-interglacial oscillations. The onset of the first period is marked by high chlorin accumulation rates during MIS 34 (ca. 1135-1096 ka). Although values fall after this initial pulse, they remain double those of 'Phase I' (Figure 6.2G). The second period occurs between MIS 21-19 (ca. 880-760 ka), where accumulation rates at ODP 1087 are triple those of 'Phase I'. The mechanism driving the periods of sustained high levels of organic carbon export after MIS 35 at ODP 1087 is therefore unclear.

The two periods of increased organic carbon export at ODP 1087 may have contributed to a fall in pCO_2 after MIS 35. In addition to a stronger biological carbon pump, the permanent cooling at ODP 1087 after MIS 35 may also have drawn down atmospheric CO_2 into the surface ocean, as CO_2 has a higher solubility in cooler waters. A similar coupling of high productivity and cool SSTs was proposed to account for the weaker glacial flux of CO_2 to the atmosphere from the Angola Current over the last 160-kyr (Müller et al., 1994). As the two periods of increased organic carbon export at ODP 1087 occur after the onset of global cooling and the MIS 22 global ice volume increase

(Figure 6.2), they could not have driven these events. However, the two periods of high export production (and thus a strong biological carbon pump) after 1145 ka may have played an important role in mid-Pleistocene climate change by maintaining lower pCO_2 and thus the low global temperatures after MIS 35.

Between MIS 31-22 (ca. 1100-880 ka), a rapid increase in the chlorin accumulation rate maxima occurs at ODP 1084 (Figure 6.2F). This occurs with falling SSTs and an increase in the abundance of diatoms found within the modern Benguela upwelling cells (Marlow et al., 2000). These results suggest that the intensity of upwelling increased in the Benguela region between MIS 31-22 (Marlow et al., 2000). A pulse of high chlorin accumulation rates occurs during MIS 35-34 (ca. 1240-1100 ka) at ODP 1081 in the Northern Benguela region (Figure 6.2; Marlow, 2001). This increase occurs at the onset of progressive cooling of the surface waters, which suggests that upwelling at this site also intensified (Marlow, 2001). Strengthening of upwelling-favourable winds between 1500-580 ka in the Northern Benguela Region was proposed to account for the sustained increase in both terrigenous-derived iron inputs and MAR TOC at ODP 1082 after ca.1100 ka (see Figure 6.1 for site location; Jahn et al., 2003).

The impact of more intense Benguela upwelling on pCO_2 is not clear, due to the complicated relationship between upwelling intensity and the exchange of CO_2 between the ocean and the atmosphere. This is due to the interaction between the pressure- and temperature-driven release of CO_2 to the atmosphere from upwelling waters, and the utilisation of surface water CO_2 by enhanced primary productivity (Lampitt et al., 1995; Schneider and Müller, 1995). A draw-down of CO_2 from the atmosphere in the presence of more intense upwelling is only possible where the increase in primary productivity is of a sufficient magnitude to remove the enhanced concentrations of CO_2 in the upwelling waters (Lampitt et al., 1995; Schneider and Müller, 1995). This process is not impossible, as Westerhausen et al. (1994) demonstrated that the glacial biological carbon pump in the equatorial Atlantic over the past 300-kyr was successful in reducing the release of CO_2 to the atmosphere from increased upwelling. High levels of productivity after MIS 35 may have been encouraged by the enhanced flux of aeolian iron into the Benguela region, identified at ODP 1082 (Jahn et al., 2003). The effectiveness of these processes in reducing the upwelling-driven flux of CO_2 from the surface ocean to the atmosphere is not known in the absence of pCO_2 data. However, chlorin accumulation rates at ODP 1084 show a positive correlation to global ice volume between MIS 31-22, including the development of the large northern hemisphere ice-sheets during MIS 22 (Figure 6.2). This suggests that a strong biological carbon pump in the Benguela upwelling cells between MIS 31-22 may have maintained the global cooling and perhaps even played a role in driving the cooling and ice-sheet expansion of MIS 22 by reducing the flux of CO_2 to the atmosphere. As export productivity does not increase until after the onset of the global cooling trend, it appears not to have played a role in driving the early fall in SSTs from 1145 ka. However, the results presented here suggest that the strengthening of the biological pump in the Benguela upwelling cells may have played an important role in maintaining the global cooling trend during the mid-Pleistocene.

6.3.3 The eastern equatorial Pacific

The upwelling zone of the eastern equatorial Pacific is a key region within the modern carbon cycle. The upwelling of cool and nutrient-rich waters within the equatorial divergence, including ODP 849, drives some of the highest rates of biological production in the open-ocean (Chavez and Barber, 1987). However, unused nitrogen and phosphorous in surface waters demonstrates that the modern rates of primary production could still be higher, and must be limited at present by relatively low levels of one or more additional nutrients. Due to this limitation, primary production fails to utilise all of the available dissolved CO_2 in the upwelling waters, resulting in a net flux of CO_2 to the atmosphere (Chavez et al., 1991; Loubere et al., 2003). The major limiting factor over primary production is considered to be the relatively low supply of iron to the region from continental sources (Chavez et al., 1991; Martin et al., 1991). An increase in the supply of iron from aeolian dust, due to increased aridity onshore with more intense atmospheric circulation, has been proposed to account for some of the glacial lowering of pCO_2 by enhancing production in the eastern equatorial Pacific during the late Pleistocene (e.g. Martin, 1990; Watson et al., 2000; Ridgwell and Watson, 2002; Bopp et al., 2003; Ruddiman, 2003). The sensitivity of pCO_2 to low-latitude export production was also demonstrated in a modelling study by Rich *et al.* (1999). They showed that small changes to export production in the low-latitudes could generate a greater CO_2 draw down than a comparable change in export production in the high latitudes. This was attributed to the greater sequestration of exported carbon by the deep-ocean (a stronger biological carbon pump) in response to increased glacial stratification in the low-latitudes (Rich et al., 1999). Berger and Wefer (1991) proposed that the mechanical action of stronger glacial winds may also have encouraged production by increasing upwelling, and may have supplied additional micro-nutrients to the region in addition to iron.

Changes to export production and the strength of the biological carbon pump in the eastern equatorial Pacific may therefore be an important component in the glacial reductions of $p\mathrm{CO}_2$. Four periods can be identified between 1500-500 ka at ODP 849 where relatively high chlorin accumulation rates are also associated with periods of significant climate change associated with the MPT (Figure 6.2C). First, during MIS 31-30, after the shift toward cooler global SSTs. The second and third periods occurred between MIS 26-22 (ca. 1000-880 ka; Figure 6.2C) where glacial chlorin accumulation rates reach their maximum values of the 1500-500 ka interval. The maximum chlorin accumulation rate occurs at ca. 910 ka, immediately prior to the intense cooling in the tropical Pacific (Chapter 3) and the increase in mean global ice volume during MIS 22 (Figure 6.2A). The fourth period is marked by a more moderate but sustained increase in chlorin accumulation rates between MIS 18-17 (ca. 780-640 ka; Figure 6.2C). This immediately precedes the onset of the first 100-kyr cycle during MIS 16 (Figure 6.2A).

These correlations between periods of enhanced organic carbon export at ODP 849 and global climate change suggest that the biological pump at this site was important in driving the mid-Pleistocene increase in mean global ice volume and the later development of the 100-kyr cycles, through its impact over $p\mathrm{CO}_2$. However, ODP 849 lies within the upwelling zone of the equatorial divergence, and thus to reduce $p\mathrm{CO}_2$, any productivity increases driven by more intense upwelling must be sufficient to remove the excess CO_2 brought to the surface ocean. Palmer and Pearson (2003) recently demonstrated that a rise in CO_2 concentrations in the central equatorial Pacific (ca. 156°W; site location shown in Figure 6.1) was coincident with the sharp rise in $p\mathrm{CO}_2$ during the last deglaciation. They attributed this trend to intensification of upwelling in the eastern equatorial Pacific, and the consequent expansion of CO_2-rich upwelling waters, and suggested that it may have been important in driving the deglaciation (Palmer and Pearson, 2003). However, Figure 6.4 shows that the first period of high chlorin accumulation rates between 1000-880 ka coincides with a pronounced fall in SSTs at ODP 849. This occurs with an increase in the grain-size of the dust fraction (Figure 6.4D), suggesting that the strength of the South-east Trade Winds increased at this time. These results suggest that the increase in organic carbon

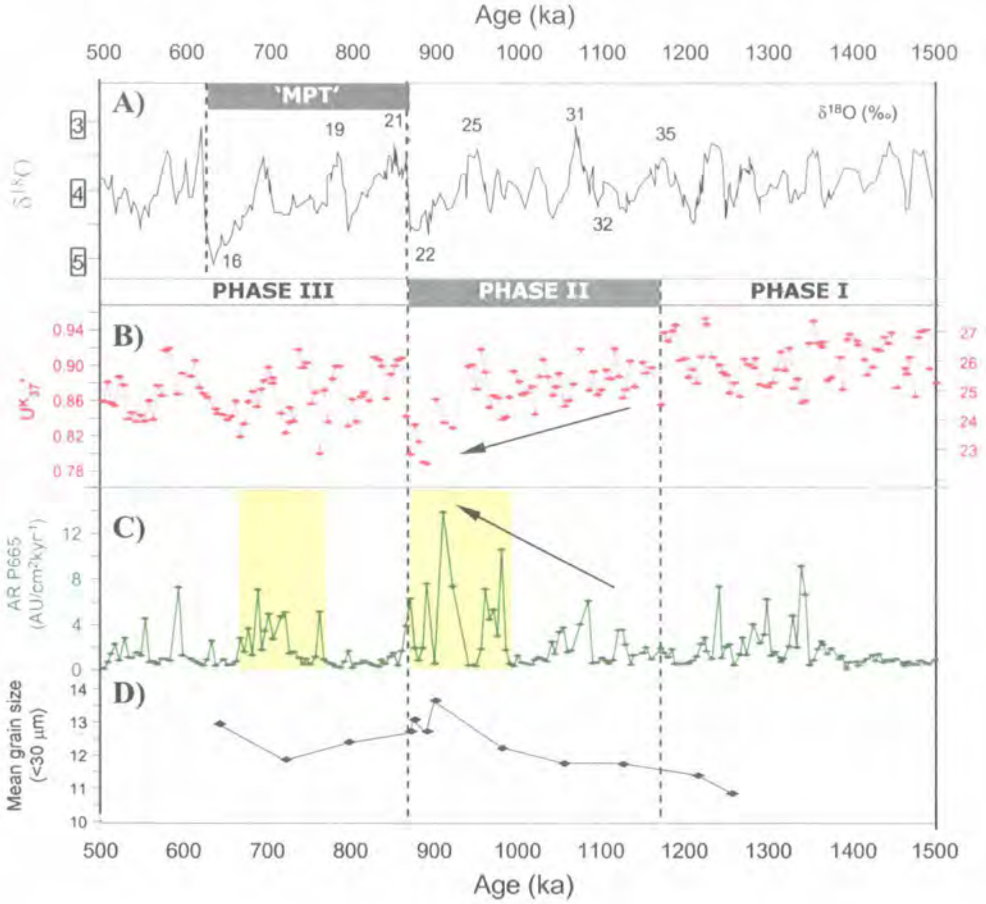

Figure 6-4 Time-series of U^{K}_{37}', chlorin accumulation rate and mean particle size of aeolian dust from ODP 849 (eastern equatorial Pacific) between 1500-500 ka. The Mid-Pleistocene Transition as defined by Mudelsee and Schulz (1997) marked as 'MPT'. (A) Benthic oxygen isotope curve, from ODP 849 (Mix et al., 1995). Selected isotope stages marked; (B) U^{K}_{37}' SST time-series from ODP 849C and D; (C) Accumulation rate of chlorins at ODP 849. Phases of high accumulation rates marked by yellow shading; (D) Mean grain size of fine sediment fraction (<30µm).

export between 1000-800 ka was driven by more intense upwelling in response to stronger South-east Trade Winds. This period coincides with the intensification of Benguela upwelling revealed by high chlorin accumulation rates at ODP 1084 (Figure 6.2), which also reflects South-east Trade Wind strength (Shannon, 1985). If the strengthening of the South-east Trade Winds also brought more aeolian iron to the eastern equatorial Pacific, the increase in organic carbon export that occurred between MIS 26-22 would have been effective in utilising the additional CO_2 in the surface ocean as upwelling intensified. That this process was effective in drawing down atmospheric CO_2 is suggested by the timing of the maximum chlorin accumulation rate, immediately prior to the pronounced global cooling and increase in mean global ice volume that mark MIS 22 (ca. 900-880 ka; Figure 6.3).

High levels of export production are not restricted to ODP 849, but also occur in sites to the west (Murray et al., 2000) and are suggested by high accumulation rates of carbonate and TOC in the east (Emeis et al., 1995; Murray et al., 1995). This suggests that the biological carbon pump may have increased in strength at a regional scale in the eastern equatorial Pacific between MIS 26-22, 1000-880 ka. Significantly, the chlorin maximum at ca. 910 ka (MIS 23) is synchronous with high values of obliquity that should have driven the climate system back toward warmer, interglacial values by analogy with the previous glacial-interglacial oscillations. The relationship between global cooling and high organic carbon export in the eastern equatorial Pacific during MIS 23-22 (ca. 910-880 ka) therefore suggests that the increase in export productivity in the region was effective in reducing pCO_2 during MIS 23. By maintaining low global temperatures during MIS 23 this would have enabled intensification of glacial conditions to occur with the subsequent fall in insolation during MIS 22. The biological pump in the eastern equatorial Pacific may therefore have been important in the mid-Pleistocene expansion of global ice volume during MIS 22.

The fourth period of high chlorin abundance at ODP 849 is unusual for the interval of study, as it occurs during an interglacial and with relatively warm SSTs. This suggests that it was not driven by intensification of equatorial upwelling. This conclusion is supported by the poor correlation that develops after MIS 22 between chlorin abundance at ODP 849 and the accumulation of biogenic sediments (TOC, carbonate, opal, alkenones) at ODP sites 847 and 846 in the upwelling zone to the east (Emeis et al., 1995; Murray et al., 1995; Liu and Herbert, 2004). This period does correlate well with a period of high export production centred on ca. 700 ka identified at 140°W (site locations shown in Figure 6.1; Murray et al., 2000). Murray et al. (2000) found that the increase in export production was most pronounced in the sites that lay to the south of the equator (2°S and 5°S). These sites lie within the SEC that also determines the conditions of the surface ocean at ODP 849 (Figure 6.1). No explanation for this increase in export production was proposed (Murray et al., 2000). Significantly, this pulse immediately precedes the pronounced glacial ice volume increase during MIS 16 that heralds the onset of the first 100-kyr cycle in $\delta^{18}O$ (Figure 6.2, 6.4). By driving a decline in pCO_2, the strong biological carbon pump in the central and eastern equatorial Pacific between MIS 18-16 may have been important in driving this glacial intensification.

A period of high glacial chlorin accumulation rates is also evident between ca. 1350-1200 ka (Figure 6.2C), although its relationship to mid-Pleistocene climate change appears more complex. This period correlates with high carbonate accumulation rates and the maximum opal accumulation rate of the last 1500 ka at ODP 847, also located within the SEC (site location shown in Figure 6.1; Murray et al., 1995). This suggests that high productivity drove high levels of organic carbon export within the eastern equatorial Pacific between ca. 1350-1200 ka. It occurs with little change to SSTs at ODP 849 (Figure 6.4), suggesting that it was not driven by more intense upwelling. Planktic foraminifer $\delta^{13}C$ values from ODP 851 suggest that the nutrient contents of the upwelling waters increased at this time (Cannariato and Ravelo, 1997). As this increase in the rate of organic carbon export occurred without an increase in upwelling intensity, it may have been effective in reducing pCO_2. The impact of this process on mid-Pleistocene climate change is unclear. Although it precedes the onset of the global cooling phase during MIS 35 (Figure 6.3D), chlorin accumulation rates had already fallen to low values by the onset of MIS 35 at ca. 1200 ka (Figure 6.4). This may have driven a precursory fall in pCO_2 values that contributed to the later development of global cooling after MIS 35. However, there is little change to either global SSTs (Figure 6.3D) nor glacial ice volumes (Figure 6.3D) during this interval. This suggests that the strengthening of the glacial biological carbon pump between 1350-1200 ka may have little impact on pCO_2 and mid-Pleistocene climate change. However, in the absence of pCO_2 data this hypothesis is difficult to assess.

6.3.4 The western equatorial Pacific

The first significant increase in chlorin accumulation rates at ODP 806 occurs during MIS 31, ca. 1080 ka (Figure 6.2B). After MIS 31, glacial chlorin accumulation rates steadily decline until MIS 21 (ca. 800 ka), before progressively increasing until their maximum values of the 1500-500 ka interval are reached at ca. 550 ka (Figure 6.2B). Throughout the 1500-500 ka interval, high chlorin accumulation rates correlate with cool SSTs as recorded by U^K_{37}' (Chapter 3). This includes the interglacial MIS 31, where U^K_{37}' indicates that SSTs were relatively low (Chapter 3). High chlorin accumulation rates also correlate with intervals of high diatom abundance at ODP 806 (Lange and Berger, 1993), suggesting that they reflect increases in primary productivity.

The surface waters of ODP 806 are not affected by equatorial and coastal upwelling. The increases in organic carbon export at the site may therefore have been important contributors to any decline in $p\text{CO}_2$ during MIS 31, and during the glacial intervals after MIS 21. However, export productivity at ODP 806 is unlikely to have played a role in maintaining global cooling between MIS 31-22 given that organic carbon export fell during this period (Figure 6.2B). The strengthening of the glacial biological carbon pump at ODP 806 after MIS 21 may have been important in driving larger glacial ice volumes that developed after MIS 22. Higher export productivity after MIS 22 may also represent a response of the surface ocean at ODP 806 to this increase in glacial ice volume. The surface layers of the modern western tropical Pacific are capped by a low-salinity layer that isolates surface waters from the nutrient-rich thermocline below, driving relatively low surface productivity (Mackey et al., 1997). During the LGM, lower sea-level and reduced precipitation resulted in an increase in surface salinity in the region (Martinez et al., 1997). The mean global ice volume increase during MIS 22 represents an increase in glacial sea-level fall of between 20-40 m for late Pleistocene glaciations (Raymo, 1997; Raymo et al., 1997). This may have driven greater production at ODP 806 after MIS 22 by increasing surface salinity, reducing thermocline depth, and increasing the supply of nutrients to the surface at ODP 806. The enhanced organic carbon export may then have acted as a positive feedback by maintaining low glacial temperatures through its impact on $p\text{CO}_2$. As discussed in Chapter 1, the δ^{18}O value of planktic foraminifera reflect both the temperature and salinity of surface waters. This hypothesis may therefore be tested through comparison of the δ^{18}O values of planktic foraminifera to proxies for SST (e.g. U^K_{37}', Sr/Ca in foraminifera carbonates, foraminifera transfer functions). This approach was followed by Martinez et al. (1997)

in their reconstruction of the LGM salinity variations in the western equatorial Pacific, by using a combination of planktic foraminifera $\delta^{18}O$ values and transfer function-derived SSTs. This procedure could not applied in this thesis to test this hypothesis due to the general absence of interglacial SST values through the U^{K}_{37}' results from ODP 806, which prevents any correction of $\delta^{18}O$ for glacial-interglacial variations in SSTs. However, the positive relationship between the increase in global ice volume and export production after MIS 21 suggests that the biological carbon pump in the western equatorial Pacific may affected $p\text{CO}_2$ and influenced ice-sheet growth during the conventional 'MPT' (Figure 6.2).

6.3.5 The northern North Atlantic

There is little variation to the amplitude of the glacial-interglacial oscillations in chlorin accumulation rates at ODP 983 between 1500 to 500 ka (Figure 6.2H). This suggests that organic carbon export from this site played a minor role in the mid-Pleistocene climate changes. High chlorin accumulation rates occur during interglacials throughout the 1500-500 ka interval of study (Figure 6.2H). This suggests that any draw down of $p\text{CO}_2$ at ODP 983 by the biological carbon pump is balanced by the transfer of CO_2 to the atmosphere by other regions or processes to increase global interglacial temperatures. Only two intervals are marked by significant increases in organic carbon export, during MIS 31 (ca. 1065 ka) and MIS 19 (ca. 780 ka; Figure 6.2H). The duration of these two events is relatively short, at ca. 15-kyr each. MIS 19 is not marked by an significant change to either global ice volume or global temperatures (Figure 6.2), suggesting that any climatic impact of this increase in the strength of the biological carbon pump at ODP 983 through $p\text{CO}_2$ was minor. Only during MIS 31 is the biological carbon pump at ODP 983 likely to have had a potentially more significant role. The high chlorin accumulation rates at this time form part of the global increase in organic carbon export proposed above to have been important in the global cooling that followed MIS 35.

Changes to the strength of the biological carbon pump at ODP 983 therefore appear to have had a limited impact over the mid-Pleistocene climate changes through $p\text{CO}_2$. High chlorin accumulation rates occur during interglacials, and correlate with periods of high diatom abundance at ODP 983 (Koç et al., 1999) and high biogenic carbonate deposition in the Nordic Seas (Helmke et al., 2003). This suggests that the chlorin accumulation rates at ODP 983 reflect increases in interglacial production in the surface waters. Glacial intervals at ODP 983 are marked by cool SSTs and the development of sea-ice cover at the site (Chapter 3). The development of these conditions during the annual cycle tends to limit production in Arctic Waters (Longhurst, 1998). The interglacial increases in chlorin accumulation rates may therefore represent a response of primary production to climate amelioration during interglacials, rather than acting as a driving mechanism for global cooling. This includes the increase in chlorin accumulation rate during MIS 31, which marks the warmest interglacial in the surface ocean at ODP 983 (Chapter 3).

6.3.6 Issues & Implications

Throughout the 1500-500 ka interval of study, high levels of organic carbon export at a global scale correlate with low global SSTs over glacial-interglacial timescales. An increase in the levels of organic carbon export from the surface ocean at a global scale also develops after MIS 35, in concert with the onset of the global cooling described in Chapter 5. It is proposed here that these correlations reflect an influence of the strength of the biological carbon pump over $p\mathrm{CO}_2$ and thus over global temperatures. The increase in export productivity after MIS 35 is proposed to have driven and/or maintained the global cooling after MIS 35. As these two processes occur synchronously, it is difficult to determine whether falling $p\mathrm{CO}_2$ was the sole driving mechanism for the global cooling. These results therefore do not preclude the cooling of deep-water temperatures as a potential driving mechanism for global cooling after MIS 35 (proposed in Chapter 5), but raise the possibility that lowering of $p\mathrm{CO}_2$ by the biological carbon pump may also have played an important role.

This interpretation is complicated by the intensification of upwelling identified in both the Benguela region and the eastern equatorial Pacific, as this may have acted to increase the flux of CO_2 from the ocean to the atmosphere. However, it is proposed here that the regional scale increase in export production in the eastern equatorial Pacific between MIS 26-22 may have been effective in reducing this flux, as pronounced glacial cooling and the increase in mean global ice volume of MIS 22 occur with the intensification of upwelling recorded at ODP 849. High levels of organic carbon export at ODP 1084, below the major Benguela upwelling cell, also correlate with intervals of low global temperatures. The biological carbon pump here may also have been effective in reducing the CO_2 flux to the atmosphere. Two periods of sustained high organic carbon export have also been identified at ODP 1087 in the eastern South Atlantic. It is proposed here that the biological carbon pump here may also have been effective in maintaining the lower global temperatures after MIS 35. These results therefore support the proposal here that increases in export production may have played an important role in lowering pCO_2 and driving the climate changes associated with the MPT.

In Chapter 5, an expansion of sea-ice cover in the high northern latitudes was reconstructed using the relative abundance of the $C_{37:4}$ alkenone (Figure 5.4). It was proposed that a similar trend may have occurred in the southern hemisphere: U^{K}_{37}' data from ODP 1087 (Figure 5.2) and published SST reconstructions from the Southern Ocean (Becquey and Gersonde, 2002) showed that the position of the ACC migrated northward during the mid-Pleistocene, restricting the supply of warm Agulhas waters to the south-east Atlantic by 1145 ka. An expansion of sea-ice cover in the Southern Ocean could also have significant impacts over the exchange of CO_2 between the ocean and atmosphere. Stephens and Keeling (2000) have proposed that expanded sea-ice in the Southern Ocean may have contributed to the lowering of pCO_2 during the last glacial maximum, by preventing upwelling waters from reaching the surface ocean and degassing. Furthermore, vertical stratification of the polar oceans, as suggested by the sea-ice development in the North Atlantic and North Pacific after 1145 ka (Figure 5.4) will also act to reduce deep-water exposure to the surface ocean and consequent degassing (Sigman et al., 2004). When these changes to high latitude surface water masses are coupled with the higher export productivity at a global scale, as proposed in this Chapter, the marine carbon cycle during the mid-Pleistocene emerges as a potential key player in driving a fall in pCO_2, in turn driving or maintaining the global cooling trend that developed from 1145 ka.

Two issues have arisen in this Chapter that should be addressed to evaluate further the role played by the biological carbon pump in the MPT. The first relates to the spatial resolution of the time-series presented here, and whether the sites that have been examined are representative of regional scale changes in organic carbon export. In Chapter 3, issues of sediment redistribution were addressed for each site, and were considered to have a minor impact on the four chlorin accumulation rate time-series generated in this thesis. This conclusion should be tested, through increasing the spatial resolution of chlorin accumulation rate data at each of the four sites investigated in this thesis, and/or correcting the time-series for sediment redistribution processes, for example by application of the ^{230}Th normalisation method (Francois et al., 2004) described in Chapter 1.

The second issue that limits interpretation of the impact of increased organic carbon export over global climate change is the scarcity of $p\text{CO}_2$ data for the 1500-500 ka interval. The result of the balance between more intense upwelling and a stronger biological carbon pump in the eastern equatorial Pacific and the South-east Atlantic is therefore not known. To understand fully the role played by the biological carbon pump, $p\text{CO}_2$ reconstructions are necessary for the 1500-500 ka interval. Progress has been made in extending the $p\text{CO}_2$ ice-core records into the mid-Pleistocene, with the Dome Concordia record in Dronning Maud Land, Antarctica potentially reaching 780 ka (European Project for Ice Coring in Antarctica, 'EPICA': http://www.awi-bremerhaven.de/GPH/EPICA/index.html). To address the uncertainties raised in this Chapter, application of CO_2 proxies is required to extend this record back to at least 1500 ka. A proxy that shows great promise for this issue is the analysis of δ^{13}C in alkenones. The fractionation of ^{13}C and ^{12}C in alkenones during photosynthesis by coccolithophores has been shown to correlate well to ocean CO_2 concentrations (e.g. Bidigare et al., 1997; Popp et al., 1998; Pagani et al., 1999; Pagani et al., 2002). Although coccolithophore growth rates must also be taken into account, these can be estimated using Sr/Ca analyses of coccolith carbonate (e.g. Stoll et al., 2002). Finally, generation of $p\text{CO}_2$ requires calibration of the ocean CO_2 concentrations to SSTs, which can be generated simultaneously using $\text{U}^{\text{K}}_{37}{}'$. The $\delta^{13}\text{C}_{\text{alkenone}}$ method has been effective in reconstructing $p\text{CO}_2$ during the late Pleistocene (e.g. Jasper and Hayes, 1990; Andersen et al., 1999), and even during the Miocene (Pagani et al., 1999). This approach therefore shows great potential for increasing our understanding of $p\text{CO}_2$ variability across the MPT. However, as the EPICA record measures $p\text{CO}_2$ within gas bubbles contained within the ice (i.e. not a proxy reconstruction) this record may be more robust, if it can extend back toward and beyond 1200 ka, than one from $\delta^{13}\text{C}_{\text{alkenone}}$, which will contain a number of assumptions and uncertainties for each stage of the $p\text{CO}_2$ value generation. Although there is 120 m of ice to drill below the present EPICA core, it is unclear how good the record obtained will be, given that ice at this depth is close to melting point (EPICA community members, 2004). Estimates also place the base of this additional ice to MIS 26, ca. 960 ka (EPICA community members, 2004). It therefore seems likely that we shall have to rely on proxy methods to test the proposed fall in $p\mathrm{CO}_2$ after 1145 ka outlined here.

6.4 Conclusions

It has been shown that a number of significant increases in the export of organic carbon from the surface ocean occurred during the mid-Pleistocene. On a global scale, this is expressed as a permanent increase in organic carbon export, and thus the strength of the biological carbon pump, after MIS 35 (ca. 1150 ka). MIS 31 (ca. 1080 ka) marks the maximum level of global organic carbon export of the 1500-500 ka interval, This event can be identified by high chlorin accumulation rates in all of the sites presented here, except ODP 1087 in the South-east Atlantic. Significant increases to organic carbon export have been identified in the eastern equatorial Pacific, and the South-east Atlantic. These are two regions that at present, and during the late Pleistocene, may play a key role in the transfer of CO_2 between the ocean and atmosphere. The increases in organic carbon export in these two regions occur in close association with the two climate phases that mark the shift toward a 100-kyr world: the global cooling that develops after the premature 100-kyr cycle during MIS 35, and the expansion of the northern hemisphere ice sheets and the transition towards 100-kyr glacial-interglacial oscillations that occurs between MIS 22-16. In the absence of $p\mathrm{CO}_2$ data, the direct impact of these increases in organic carbon export over $p\mathrm{CO}_2$ through the biological carbon pump is not clear. However, the results presented here demonstrate that through its potential impact over $p\mathrm{CO}_2$, the biological carbon pump at a global scale may have played a key role in driving or modulating the climate changes associated with the MPT.

7. Intensification of Walker Circulation during the mid-Pleistocene climate transition

7.1 Introduction

A major debate in climate research is the role played by the tropics in modulating global climate change at a variety of timescales. A potential key player that has emerged is the closely coupled ocean-atmosphere circulation system of the tropical Pacific, which influences heat and moisture transport within the climate system (Cane, 1998; Pierrehumbert, 2000). It may also regulate concentrations of greenhouse gases within the atmosphere through its impacts on tropical soil distributions, and the intensity of upwelling systems in the east (Flückiger et al., 1999; Stott et al., 2002).

In the modern tropical Pacific, the South-east Trade Winds drive surface waters westward as part of the Walker Circulation system (Figure 7.1). In response, upwelling brings cold and nutrient-rich waters to the surface of the eastern Pacific (the eastern Pacific 'cold-tongue'). In the west, the warmest SSTs of the surface ocean are found, with mean annual values >29°C defining the 'West Pacific Warm Pool' (Martinez et al., 1997; Conkright et al., 2002). Inter-annual to decadal variability in the strength of this system are described by the El Niño/Southern Oscillation (ENSO). Weaker Walker Circulation during an 'El Niño' event is associated with the collapse of the cold-tongue in the east, and an eastward expansion and migration of the warm waters. The opposite extreme, a 'La Niña' event, exhibits strong Trades and more intense upwelling in the east. The oscillations between these two extremes are associated with significant perturbations in SST and precipitation patterns that may extend beyond the tropics (illustrated in Figure 1.11, Chapter 1). ENSO-like variations may also persist on decadal scales, between warm 'El Niño' or cold 'La Niña' states (e.g. Diaz and Markgraf, 2000).

In light of the modern teleconnections between the region and high-latitude climate, and evidence for a sensitive response of the system to precessional forcing (e.g. Clement et al., 1999), the tropical Pacific may play a key role in global climate change at a number of timescales. ENSO-like variations have been identified at both millennial and orbital timescales during the late Pleistocene (e.g. McCulloch et al., 1999; Lea et al., 2000; Tudhope et al., 2001; Koutavas et al., 2002; Stott et al., 2002; Koutavas and Lynch-Stieglitz, 2003). The development of stronger Walker Circulation during the Pliocene has been proposed as a potential driving mechanism for the onset of northern hemisphere glaciation after 3 Ma (Molnar and Cane, 2002). By analogy with modern teleconnections, Molnar and Cane (2002) propose that a weakening of the Hadley circulation developed in

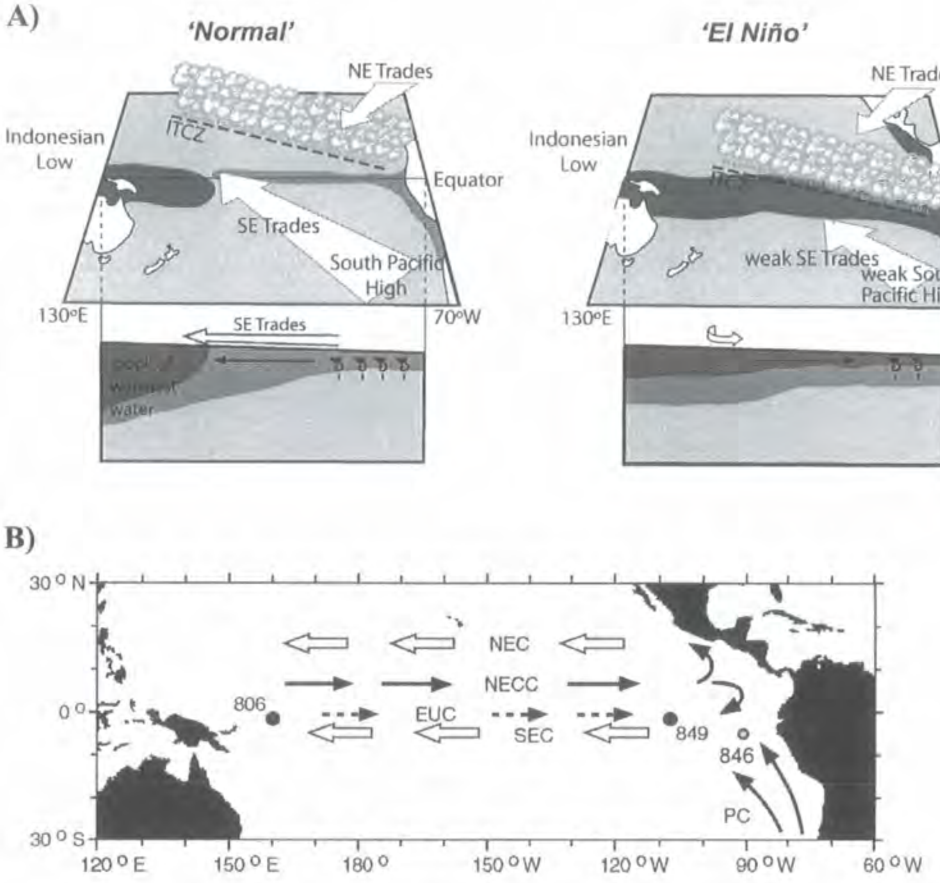

Figure 7-1 The ENSO system and the locations of cores discussed in this Chapter. (A) Comparison of 'normal' ocean-atmosphere circulation in the tropical Pacific (left) to circulation exhibited during an El Niño year. Warm surface waters indicated by dark grey shading. The eastern Pacific cold tongue is visible with the grey shading along the equator and coastline of the Americas in the left figure. An El Niño event is marked by weaker South-east Trades and collapse of the east-west gradients in SST and thermocline depth. *Source:* Wilson et al. (2000, p.34). (B) The locations of the two cores analysed in this thesis (ODP 806 and 849) and ODP 846. Surface and subsurface ocean currents: SEC: South-east Current, NECC: North-east Counter Current, NEC: North Equatorial Current, PC: Peru Current. The eastward flow of the Equatorial Undercurrent (EUC) also marked. The positions of the SEC and NEC systems are closely related to the position and strength of the South-east and North-east Trade Winds. Based on Pisias et al. (1995a) and Open University (1989).

response to more intense Walker Circulation, resulting in a reduction to the heat flux to the ice-sheet source regions and the growth of the northern hemisphere ice-sheets.

The mid-Pleistocene climate transition (MPT), as redefined in this thesis, comprises global cooling after MIS 35 (ca.1145 ka; Chapter 5), followed after MIS 22 by an expansion of the northern hemisphere ice sheets and a shift toward 100-kyr glacial-interglacial oscillations (Mudelsee and Schulz, 1997). The role played by the tropical Pacific circulation system in these climate changes is not clear. Rutherford and D'Hondt (2000) argue that the 100-kyr cycles are driven by the propagation of semi-precessional cycles (ca.11.5-kyr) from the tropics to the high-latitudes. They propose that this relationship developed in the mid-Pleistocene in response to increased heat transport across or along the equator (Rutherford and D'Hondt, 2000). The latter is suggestive of stronger Walker Circulation in the tropical Pacific, which may also have driven the expansion of the northern hemisphere ice-sheets by reducing the heat flux to the high-latitudes.

Since the Pliocene, progressive shoaling of the thermocline in the eastern equatorial Pacific, accompanied by deepening in the west, suggests that a long-term intensification of Walker Circulation has occurred (Cannariato and Ravelo, 1997; Chaisson and Ravelo, 2000). Evidence for an increase in organic carbon export at ODP 849 during the MIS 35-22 global cooling phase (ca.1145-880 ka) has also been identified in this thesis in Chapter 6. This trend suggests that the intensity of upwelling in the eastern Pacific increased at this time. The principal aim of this Chapter is to assess the role played by the tropical Pacific circulation system in the MPT. The main objectives are:

1. To reconstruct the strength of Walker Circulation in the tropical Pacific between 1500-500 ka;
2. To assess the role played by the Walker Circulation in driving the mid-Pleistocene expansion of the northern hemisphere ice sheets.

By analogy with modern oscillations of the ENSO system, the past strength of Walker Circulation can be determined by reconstructing SST gradients between sites located in the eastern and western tropical Pacific (e.g. Chaisson, 1995; Chaisson and Ravelo, 2000; Lea et al., 2000). This approach is followed here, by comparing the U^{K}_{37}' time-series presented in Chapter 3 from ODP 806 in the West Pacific Warm Pool, and ODP 849 from the eastern equatorial Pacific. ODP 849 is influenced by the South Equatorial

Current, whose properties are determined by the South-east Trade Winds. It is therefore ideally situated for monitoring the strength of the Trades. Aeolian intensity is also examined through analysis of the grain-size of dust within the sediments of ODP 849, following the methods of Hovan (1995). Finally, the strength of Walker Circulation also affects the intensity of upwelling in the eastern Pacific, and the depth of the thermocline across the region. As thermocline depth may influence the supply of nutrients to the surface ocean, and thus levels of primary production, the strength of the biological pump at ODP 806 and 849 may give further insight into the behaviour of the tropical Pacific circulation system for the interval of study.

7.2 Results & Discussion

7.2.1 Tropical Pacific circulation 1500-500 ka

The SST oscillations at ODP 849 in the eastern equatorial Pacific closely follow the benthic $\delta^{18}O$ global ice volume glacial-interglacial variability (Figures 7.2A and C). Although interglacial SSTs at ODP 806 in the west exceeded the upper limit of the U^{K}_{37}' proxy, at ca. 28.9°C (Pelejero and Calvo, 2003), the coldest intervals correspond to cool stages at ODP 849 (Figure 7.2B). The co-variance of tropical SSTs and global ice volume is reflected in the strong variance at the 41-kyr obliquity period and the emergence of ca.100-kyr periodicity after 1200 ka in both SST time-series (Figure 7.3).

The amplitude of the SST variations at ODP 849 is approximately 2-2.5°C throughout the interval of study, and does not change with the emergence of variance at the 100-kyr

---

Figure 7-2 (Overleaf) Time-series of U^{K}_{37}' and chlorin accumulation rates in the eastern and western equatorial Pacific between 1500-500 ka. The Mid-Pleistocene Transition as defined by Mudelsee and Schulz (1997) marked as 'MPT'. The three phases of surface circulation and the revised two-stage definition of the MPT discussed in Chapter 5 are marked. Note that the onset of 'MPT Stage 1' begins at 1145 ka, 25-kyr after the onset of cooling at ODP 849 used to define Phase II (for discussion see Chapter 3). (A) Benthic oxygen isotope curve, from ODP 849 (Mix et al 1995). Selected isotope stages marked; (B) U^{K}_{37}' from ODP 806B, western equatorial Pacific. Note exaggerated U^{K}_{37}' scale compared to ODP 849. SSTs shown on right y-axis, which reach a maximum where $U^{K}_{37}' \geq 1$; (C) U^{K}_{37}' from ODP 849C and D, eastern equatorial Pacific. SSTs shown on right y-axis; (D) Minimum west-east SST gradient, between ODP 806 minus ODP 849. Median shown by grey horizontal line. Mean annual value: ca. 4°C (Conkright et al, 2002); (E) Mean grain size of fine sediment fraction (<30μm); (F) Accumulation rate of chlorins at ODP 806; (G) Accumulation rate of chlorins at ODP 849; (H) Normalised chlorin stack from ODP 806 and 849, following procedures described in Chapter 6.

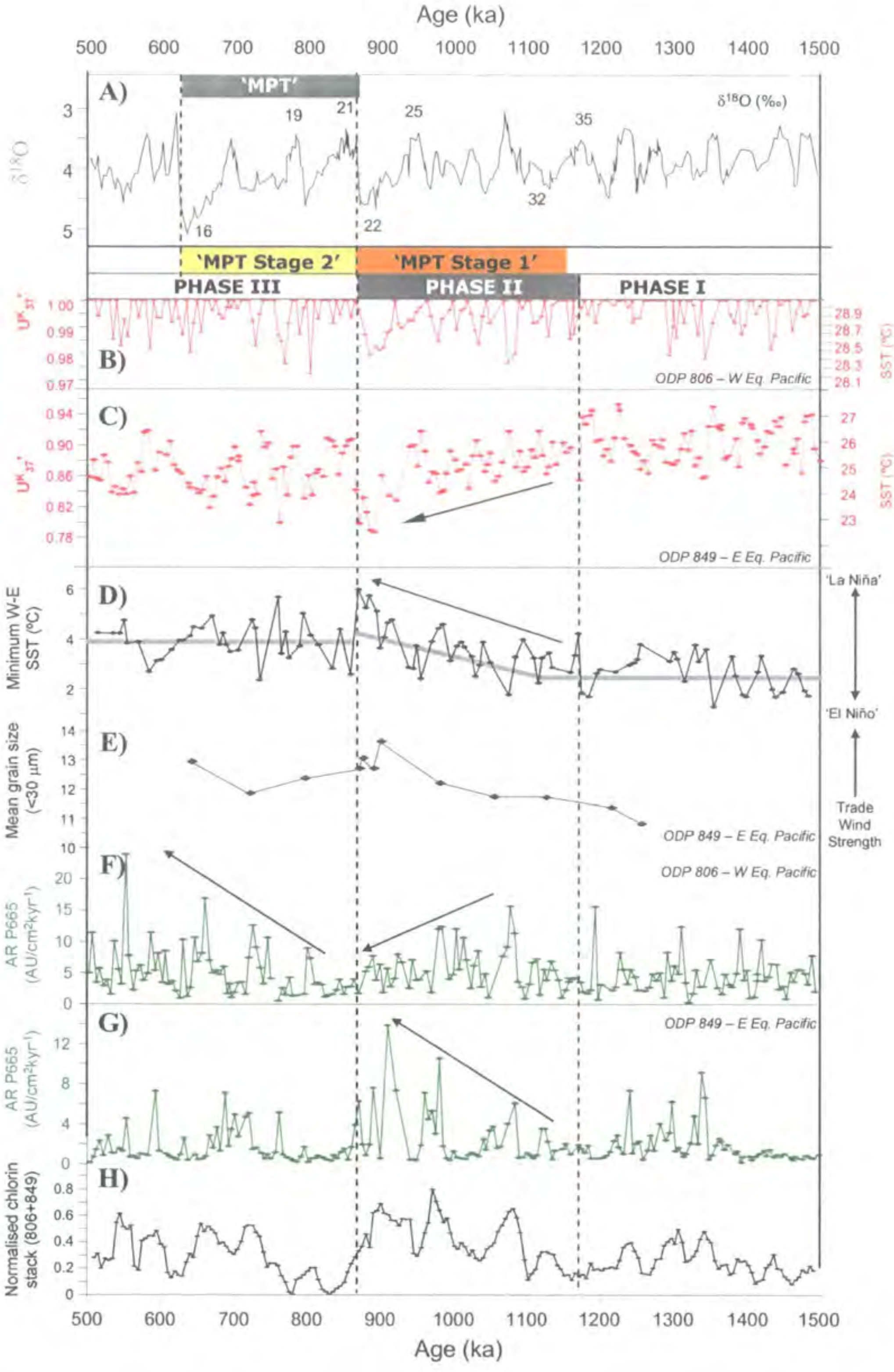

Figure 7.2 Time-series of U^{K}_{37}' and chlorin accumulation rates in the eastern and western equatorial Pacific between 1500-500 ka. For explanation see the caption on the previous page.

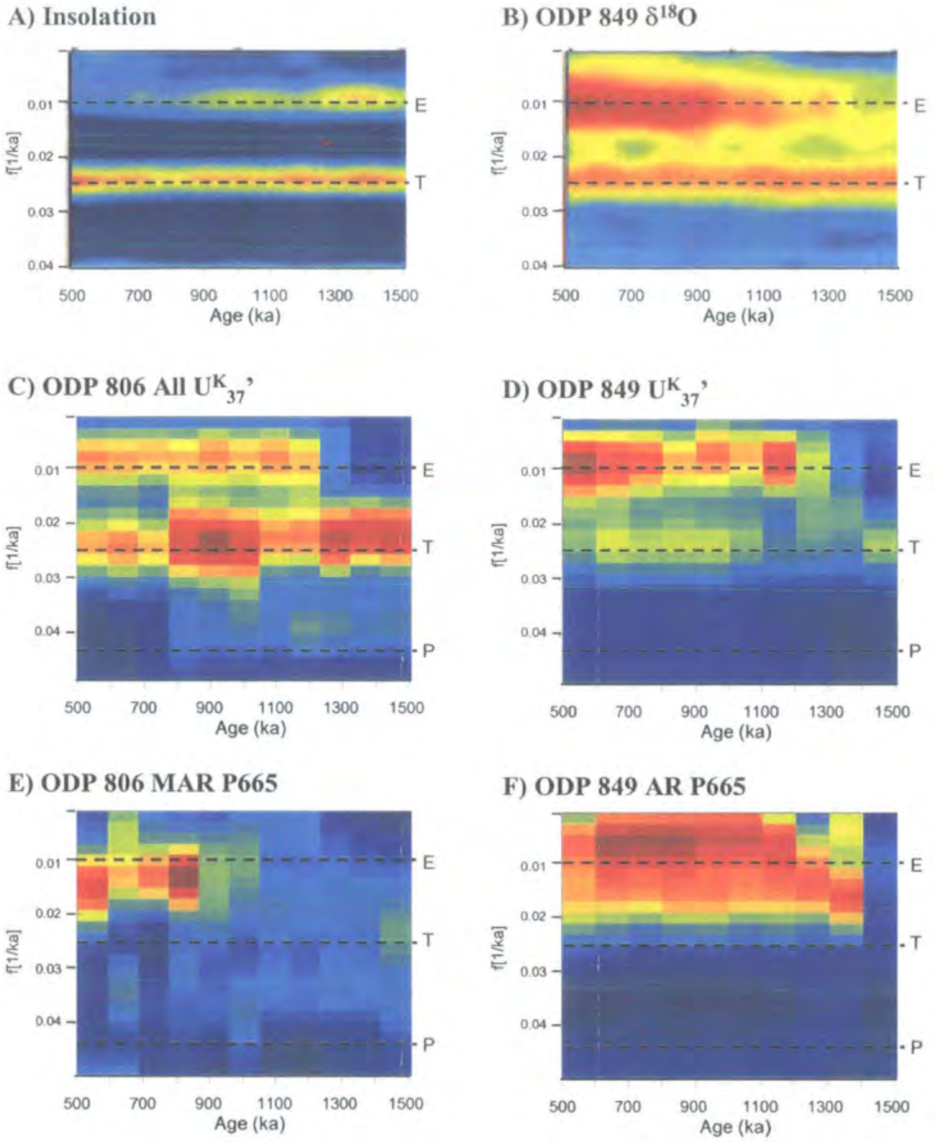

A) Insolation

B) ODP 849 $\delta^{18}O$

C) ODP 806 All U^{K}_{37}'

D) ODP 849 U^{K}_{37}'

E) ODP 806 MAR P665

F) ODP 849 AR P665

Figure 7-3 Evolutive spectral analysis of U^{K}_{37}' and chlorin accumulation rate time-series from ODP 849 and 806. Red shading highlights a high degree of variance at the 90% significance level, blue highlights a low degree of variance (as described in Chapter 2). A) Eccentricity and tilt; B) ODP 849 $\delta^{18}O$; C) ODP 806 U^{K}_{37}' (all values); D) ODP 849 U^{K}_{37}'; E) ODP 806 chlorin accumulation rate (P665); F) ODP 849 chlorin accumulation rate (P665). The spectral analysis for A) and B) performed by N.Pisias for Clark et al. (1999), using data for eccentricity and obliquity (Berger and Loutre, 1991) and the ODP 849 $\delta^{18}O$ time-series (Mix et al., 1995).

period. This amplitude is comparable to reconstructed SST anomalies in the region for the Last Glacial Maximum (Lea et al., 2000; Rosell-Melé et al., 2004). As the maximum SSTs at ODP 806 cannot be determined, a minimum amplitude of 0.9°C is suggested by the U^{K}_{37}' data (Figure 7.2B). The phase of global cooling between MIS 35-22 (ca. 1145-880 ka) and discussed in Chapter 5 ('Phase II' on Figure 7.2) is reflected by a decline in SSTs at both sites. At ODP 849, a relatively warm interglacial during MIS 23 (ca.26°C) is followed by an intense glacial cooling during MIS 22 that lowered SSTs to a minimum of 22.5°C (Figure 7.2C). Pronounced cooling during MIS 22 is also recorded at ODP 806 (Figure 7.2B). This unusual glacial-interglacial cycle at ODP 849 was preceded by a longer-term decline in average SSTs that began during MIS 35 ca. 1170 ka, slightly earlier than the onset of global cooling at ca. 1145 ka (Figure 7.2B; see discussion in Chapter 5). Average SSTs at ODP 849 permanently fell by approximately 1.5°C during this period. As a result, the cooler glacial and interglacial SSTs after MIS 22 show a better correlation to late Pleistocene and modern values than those before MIS 35 (Lea et al., 2000; Conkright et al., 2002; Rosell-Melé et al., 2004). A similar cooling shift has been identified at ODP 846, located to the east of ODP 849 but also within the eastern Pacific cold-tongue (Liu and Herbert, 2004).

Between 1500-500 ka SSTs at ODP 806 always exceeded those of ODP 849, as observed in modern SST distributions. This is demonstrated by the positive W-E SST gradient throughout the interval of study (Figure 7.2D). This gradient was produced by subtracting SST values at ODP 849 from those at ODP 806, but excluding those samples where U^{K}_{37}' had a value of 1 at ODP 806. This generally removes interglacial values from the W-E SST gradient, so that the gradient broadly corresponds to glacial periods (including their terminations and onsets). However, during the Phase II cooling at ODP 806, fewer values of unity for U^{K}_{37}' result in a W-E SST gradient that reflects both glacial and interglacial boundary conditions (Figure 7.2D). Due to the greater amplitude of SST variations at ODP 849, the W-E SST gradient increased during cool, glacial intervals (Figure 7.2D). Significantly, a longer-term intensification of the SST gradient can be identified after MIS 35, in response to the progressive cooling at ODP 849 in the east (Figure 7.2D). This trend suggests that the Walker Circulation in the tropical Pacific intensified during the global cooling phase after MIS 35. Strengthening of the South-east Trades is also suggested by the increase in the mean grain-size of dust at ODP 849 (Figure 7.2E). These changes are most pronounced after MIS 31, when a progressive decline in maximum chlorin accumulation rates occurs at ODP 806 until MIS 22, and the opposite trend is observed at ODP 849 (Figures 7.2F and G). This anti-phase behaviour in the long-term levels of organic carbon export between the two sites is consistent with a deepening of the thermocline in the western Pacific, and the reverse trend in the east. This would drive a reduction in the supply of nutrients (and hence, productivity) to the surface ocean of the western Pacific, but an increase in the east. These trends are also associated with more intense Walker Circulation in the modern tropical Pacific (Figure 7.1). Despite this anti-phasing, the chlorin accumulation rate stack from ODP 806 and 849 (Figure 7.2H; stacking method as described in Chapter 6) demonstrates that on a regional scale, the overall level of export production in the tropical Pacific increased between MIS 31-22.

The progressive intensification of the W-E SST gradient between MIS 35-22 resulted in a permanent increase by an average of approximately 2°C by MIS 22 (Figure 7.2D). This demonstrates that a shift away from a prevailing El Niño-like state in the tropical Pacific occurred as part of the mid-Pleistocene global cooling. Significantly, this shift resulted in a mean SST gradient that closely resembles the modern 'average' value i.e. neither extreme El Niño or La Niña conditions (ca.4°C, Conkright et al., 2002). This suggests that, although the east-west SST and thermocline gradients were developing during the Pliocene and early Pleistocene (Cannariato and Ravelo, 1997; Chaisson and Ravelo, 2000), the modern intensity of the SST gradient (and therefore the strength of the Walker Circulation system) evolved in association with the MPT.

During and prior to MIS 22 (pre-880 ka), low glacial SSTs are accompanied by high chlorin accumulation rates at ODP 849 in the east (Figures 7.2C and F). This suggests that the intensity of upwelling in the eastern equatorial Pacific increased during glaciations. After MIS 22, relatively small increases to glacial chlorin accumulation rates occur despite cooler SSTs at ODP 849 (Figures 7.2C and F). A similar trend was identified at ODP 846 to the east (Figure 7.1), where high alkenone abundance developed a weaker correlation to cool SSTs after 600 ka (Liu and Herbert, 2004). This may reflect a weaker glacial upwelling in the equatorial divergence after MIS 22 in response to the expansion of the northern hemisphere ice-sheets. In the modern annual circulation cycle of the tropical Pacific (e.g. Wyrtki, 1965), cooling in the northern hemisphere during boreal winter shifts the position of the ITCZ to the south, in turn reducing the strength of the South-east Trades and thus equatorial upwelling. It is proposed here that the expansion of the northern hemisphere ice-sheets from MIS 22 may have reduced the glacial intensity of upwelling in the eastern equatorial Pacific by driving a southward migration of the ITCZ and a relative weakening of the South-east Trades. This mechanism has been proposed to account for a similar weakening of upwelling in the eastern equatorial Pacific during the LGM (Koutavas *et al.* 2002). Koutavas et al. (2002) and Koutavas and Lynch-Stieglitz (2003) demonstrated that although SSTs in the eastern cold-tongue fell during the LGM, the SST gradients at the boundary of the cold-tongue were reduced, suggestive of less intense upwelling and El Niño-like conditions. This challenges earlier views that intensification of the W-E SST and thermocline depth gradients during glaciations were the result of stronger Walker Circulation (Andreasen and Ravelo, 1997; Lea et al., 2000). At ODP 849, although the chlorin accumulation rate increases are small after MIS 22, they generally continue to peak during cool, glacial intervals (Figure 7.2). This suggests that although upwelling was on average less intense after MIS 22, glacial periods may still have been associated with an increase in upwelling at the site. To test this hypothesis, the spatial resolution of SST and chlorin accumulation rate data after MIS 22 should be increased in the eastern equatorial Pacific.

7.2.2 Implications for the MPT

The shift toward a La Niña state after MIS 35 preceded the expansion of the northern hemisphere ice-sheets that occurred during MIS 22 (Figure 7.2). Although interglacial cooling in the tropics may have a minimal direct impact on temperatures over the Laurentide ice-sheet source region (Rodgers et al., 2003), stronger Walker Circulation reduces the flux of heat to the high-latitudes (e.g. Trenberth et al., 1998; Molnar and Cane, 2002; Philander and Fedorov, 2003). The Pliocene growth of northern hemisphere ice-sheets was attributed to a similar shift away from a sustained El Niño-state after 3 Ma (Molnar and Cane, 2002; Philander and Fedorov, 2003). Stronger Walker Circulation after MIS 35 may therefore have played an important role in driving the mid-Pleistocene expansion of the northern hemisphere ice-sheets. Although the Walker Circulation began to strengthen after MIS 31 (ca. 1070 ka), there is a delayed ice-sheet response until MIS 24-22 (ca.920-880 ka; Figure 7.2). This delay does not preclude the Walker Circulation as a driving mechanism for the ice-sheet growth however, as in Chapter 5 it was demonstrated that between MIS 35-25 both the North Atlantic and Pacific Oceans experienced a sustained expansion of sea-ice cover. This would have reduced the supply of moisture to the ice-sheet source regions, and prevented their growth prior to MIS 25 (e.g. Smith et al., 2003; Tziperman and Gildor, 2003). The critical combination of a reduction in sea-ice cover after MIS 25, coupled with further cooling in the high-latitudes through stronger Walker Circulation, may have driven the subsequent ice-sheet expansion.

Intensification of Walker Circulation increases heat flow along the equator. Rutherford and D'Hondt (2000) propose this as a potential mechanism to propagate semi-precessional cycles to the high-latitudes and the consequent development of 100-kyr cycles. They propose that this occurs as teleconnections are increased between low and high latitudes and thus the tropical signal is propagated outward. However, it is unclear which processes and mechanisms Rutherford and D'Hondt (2000) envisage to accomplish this propagation. The 5-kyr resolution of the data sets in Figure 7.2 is insufficient to identify semi-precessional cycles (ca.11.5-kyr), and the evolutive spectral analysis fails to identify variance at the precessional period (Figure 7.3; see discussion in Chapter 2). This hypothesis should be tested further both by increasing the resolution of analysis during the 1500-500 ka interval, to identify variance in the precession period, and by extending the result to sediments younger than 500 ka, to test whether this trend continues when glacial-interglacial oscillations with an eccentricity period dominate.

Tropical Pacific circulation may also have played a role in the mid-Pleistocene cooling through the operation of the biological carbon pump. The chlorin accumulation rate stack (Figure 7.2H) from ODP 849 and 806 demonstrates that an overall increase in the export of organic carbon to sediments, and hence the strength of the biological carbon pump, occurred in the equatorial Pacific. This is most pronounced between MIS 31-22 (Figure 7.2H), when organic carbon export is high in both equatorial sites. This regional increase in organic carbon export may potentially have been important in driving or maintaining the global cooling that followed MIS 35. As a result of the anti-phasing between the two Pacific sites, the high values in the chlorin stack between MIS 35-22 are dominated by the signal from ODP 849 (Figure 7.2H). The potential impact of this trend on $p\text{CO}_2$ values is unclear. The high chlorin accumulation rates at ODP 849 are accompanied by falling SSTs and increasing dust grain-size (Figure 7.2C,E). These trends are indicative of more intense upwelling in the eastern Pacific and the shift toward La Niña conditions. As discussed in Chapter 6, more intense upwelling in the eastern Pacific is associated with a greater concentration of dissolved CO_2 in surface waters that may also extend westward, as observed during La Niña events (Palmer and Pearson, 2003). To limit or prevent the consequent increase in the flux of CO_2 from the surface ocean to the atmosphere, primary production must increase by a sufficient magnitude to utilise this additional CO_2 in surface waters (e.g. Lampitt et al., 1995; Schneider and Müller, 1995). As discussed in Chapter 6, the increase in organic carbon export from the eastern equatorial Pacific may have been effective in utilising the additional dissolved CO_2, and thus may have contributed to a fall in pCO_2. This is suggested by the intensification of global cooling and global ice volume increase into MIS 22, which follows the increase in organic carbon export during MIS 23 (ca. 910 ka; Figure 7.2). As outlined in Chapter 6, this hypothesis should be tested through the generation of pCO_2 values between 1500 and 500 ka.

7.2.3 Driving Mechanisms

The strength of the Walker Circulation is closely coupled to the strength of the South-east Trade Winds. The latter may intensify in response to changes in global ice volume and sea-ice extent, which increases the equator-pole temperature gradients and drives more vigorous atmospheric circulation (Bush and Philander, 1998). These processes may account for the dominance of the 41-kyr periodicity in the SST records before MIS 35 from both 806 and 849 (Figure 7.3), and also observed at ODP 846 to the east (Liu and Herbert, 2004). This periodicity cannot be attributed to a direct response of the tropical Pacific to insolation forcing, as local insolation is dominated by precession (Liu and Herbert, 2004). An extra-tropical origin for this signal is suggested by the strong 41-kyr periodicity within the global ice volume record (Figure 7.2, 7.3), which can also be detected in records of NADW strength and North Atlantic SST variations (Ruddiman et al., 1986; Raymo et al., 1990b).

No significant changes to global ice volume can be detected prior to MIS 22 that could account for the strengthening of Walker Circulation after MIS 35. An expansion of sea-ice cover in the North Pacific and North Atlantic has been identified in this thesis after MIS 35 (Chapter 5). This occurs in synchrony with the sustained migration northward of the Antarctic Circumpolar Current (ACC) after 1200 ka (Becquey and Gersonde, 2002; Diekmann and Kuhn, 2002). This synchronous expansion of sea-ice in the northern and southern hemispheres should have increased the equator-pole temperature gradients and thus intensified atmospheric circulation. The strength of the Walker Circulation continues to increase after MIS 25 (990 ka), despite the retreat of sea-ice in the North Atlantic and North Pacific and an inferred reduction in the pole-equator temperature gradient in the northern hemisphere (Chapter 5). However, this occurred with little change in the position of the ACC (Becquey and Gersonde, 2002; Diekmann and Kuhn, 2002), suggesting that the South-east Trades should have remained strong. The intensification of upwelling within the Benguela upwelling cells between MIS 35-22 supports this hypothesis, as this upwelling system is also driven by the South-east Trades (Chapter 5; Marlow, 2001; Marlow et al. 2000). During the modern annual cycle, the coincidence of relatively strong South-east Trades but weaker North-east Trades in the equatorial Pacific shifts the ITCZ northward, driving more intense upwelling in the east and stronger Walker Circulation (Wyrtki, 1965). The retreat of the northern hemisphere sea-ice may therefore have been an important factor in the intensification of Walker Circulation after MIS 25. It cannot account for the continued high W-E Pacific SST gradient after MIS 22 however, as MIS 22 marks the expansion of the northern hemisphere ice-sheets (Figure 7.2A). By analogy with the modern annual cycle in the tropical Pacific, cooling in the northern hemisphere (e.g. through the development of larger ice masses) would be expected to reduce the glacial intensity of upwelling by shifting the ITCZ southward and reducing the strength of the South-east Trades. The sustained increase in the strength of the Walker circulation during the mid-Pleistocene therefore requires an alternative or additional mechanism to be operating.

An alternative explanation for the onset of cooling in the eastern equatorial Pacific lies with the temperature of the upwelled waters themselves. A shallow thermocline in the region results in cooler and deeper waters being brought to the surface with only a minor increase in trade wind strength (Philander and Fedorov, 2003). This also makes the upwelled waters sensitive to changes to deep-water temperatures. Philander and Federov (2003) propose that during the Pliocene, a long-term cooling of deep-waters (e.g. Lear et al., 2000; Tian et al., 2002) caused the thermocline to shoal in the eastern equatorial Pacific. They propose that this occurred as cooling of the deep-water by increased the vertical temperature gradient between the surface and deep-ocean, in turn increasing the density difference between surface and deeper waters, and thus driving the thermocline to shallower depths (Philander and Fedorov, 2003). Cooler waters were then brought to the surface with little change in wind strength. They argued that the resulting increase in SST gradient caused Walker Circulation to strengthen and maintain the eastern upwelling. A similar mechanism may explain the initial onset of mid-Pleistocene cooling at ODP 849, as suggested by the progressive shoaling of the thermocline in the eastern Pacific after 1500 ka (Cannariato and Ravelo, 1997; Chaisson and Ravelo, 2000). It is proposed here that when the thermocline reached a critical depth, cooler deep waters were brought to the surface of ODP 849. In turn, this triggered an intensification of Walker Circulation, which not only maintained the eastern upwelling but may also have driven the increase in global ice volume and/or the development of the 100-kyr cycles. This mechanism is also consistent with the cooling of the Benguela upwelling cells at this time (Chapter 5; Marlow, 2001; Marlow et al., 2000), which are also influenced by this sensitive relationship between deep and surface water temperatures. Progressive cooling of deep-waters was also proposed in Chapter 5 to account for the synchronous expansion of sea-ice cover in both hemispheres, which was attributed to the increased stability and stratification of the water column as deep-water cool (c.f. Tziperman and Gildor, 2003).

7.3 Conclusions

The MPT as defined in this thesis (Chapter 5) marks an intensification of Walker Circulation in the tropical Pacific. This represents a shift away from the El Niño-like state that prevailed before ca.1200 ka, and occurs in association with the global cooling phase that began after MIS 35. Significantly, both SSTs in the eastern equatorial Pacific and the W-E SST gradient reached modern values at the culmination of the cooling phase during MIS 22. It is proposed here that the intensification of Walker Circulation may have been triggered by falling deep-water temperatures and a shoaling of the thermocline. This process would bring cooler waters to the surface ocean with little change in wind intensity. Intensification of Walker circulation may also have been encouraged by strengthening of the South-east Trades in response to the northward migration of the ACC after 1200 ka.

Through reducing the flux of heat to the ice-sheet source regions, the intensification of Walker Circulation is proposed to have played a key role in driving the mid-Pleistocene development of larger northern hemisphere ice-sheets from MIS 22. It may also have enhanced the propagation of semi-precessional cycles to the high-latitudes, a mechanism proposed by Rutherford and D'Hondt (2000) to account for the emergence of 100-kyr glacial-interglacial oscillations. The strengthening of the biological carbon pump across the region between MIS 31-22 may also have been important in maintaining or driving the global cooling through its impacts on $p\text{CO}_2$. However, this hypothesis requires further testing due to the complicated relationship between upwelling systems and $p\text{CO}_2$. The results presented here therefore demonstrate that the MPT was not simply a development within the northern hemisphere ice-sheets and high-latitude climates, but had significant impacts on tropical climate. Furthermore, the tropical Pacific circulation system may have played an important role in driving the MPT, through its potential influence over both the development of more extensive ice-sheets, and the shift toward the 100-kyr world.

8. Summary and Conclusions

8.1 Summary

The mid-Pleistocene climate transition (MPT) marks a change in the nature of the climate system response to insolation forcing. The principal aim of this thesis was to understand the causes of the MPT through the reconstruction of surface ocean circulation and the strength of the biological carbon pump in the Atlantic and tropical Pacific circulation systems. These two systems were examined as they exert important influences over global climate change, through their impacts on heat and moisture transports, and carbon cycling. Strong surface ocean circulation patterns characterise the Atlantic and Pacific Oceans, which transport heat northward in the Atlantic, and westward in the Pacific. The circulation of these two systems was reconstructed for the mid-Pleistocene by analysing sites that represented end-members of each surface ocean circulation system. Four Ocean Drilling Program (ODP) sites were selected: ODP 983 (northern North Atlantic), ODP 1087 (South-east Atlantic), ODP 849 (East equatorial Pacific) and ODP 806 (West equatorial Pacific). The interval of study at all sites was from 1500 to 500 ka. This time interval spans the MPT as defined by Mudelsee and Schulz (1997; ca. 920-640 ka) but allowed an evaluation of the role played by any longer-term climate trends in the MPT to be undertaken. All sites were analysed at a resolution of ca. 5-kyr, to allow identification of variance at orbital frequencies (from the ca. 19-kyr precession to 413-kyr eccentricity periods).

Sea-surface temperature (SST) reconstructions were obtained through application of the alkenone palaeotemperature proxy U^{K}_{37}'. Alkenones (C_{37} to C_{39} ketones) are synthesised by a restricted group of algae, the *Prymnesiophyceae*, which include the coccolithophores. Prior to this thesis, U^{K}_{37}' had been demonstrated to remain a robust SST proxy during the late Pleistocene, despite changes to the coccolithophore assemblages that are likely to produce alkenones (Müller et al., 1997; Weaver et al., 1999; Villanueva et al., 2002). The objective of Chapter 4 was to assess the impact of the many mid- and early-Pleistocene coccolithophore extinction events on the temperature dependence of U^{K}_{37}'. This was undertaken through comparison of the U^{K}_{37}' and coccolith species time-series from ODP 1087A in the South-east Atlantic. The results show that evolutionary events and changes in species dominance within the coccolithophore populations had little impact on the U^{K}_{37}' record during the mid- and early-Pleistocene. The relative abundances of the C_{37} and C_{38} alkenones at ODP 1087A also fall within the ranges found within modern cultures, surface sediments and water column samples. These results demonstrate that the early and mid-Pleistocene coccolithophores exhibited a similar biogeochemical response to growth temperature to that of modern alkenone-synthesisers. The analyses presented in Chapter 4 therefore validate the application of the U^K_{37}' index for reconstructing palaeo-SSTs during the early- and mid-Pleistocene.

The principal aim of Chapter 5 was to determine a global temperature trend for the early- and mid-Pleistocene using alkenone palaeo-SST time-series. This enabled the hypothesis that the MPT was driven by global cooling to be tested (e.g. Berger and Jansen, 1994; Raymo, 1997; Paillard, 1998; Berger et al., 1999). At every site, variations to SSTs were identified that correlate to glacial-interglacial oscillations. At all four sites, longer-term trends in SSTs were also identified, that enabled the 1500-500 ka interval to be sub-divided into three phases that are broadly synchronous between sites. Phase I, pre-MIS 35 (pre-ca. 1170 ka) was characterised by relatively high frequency oscillations in SSTs. Phase II, from MIS 35-22 (ca. 1170-880 ka) was marked by cooling at every core site. The cooling was permanent at ODP 1087 (South-east Atlantic) and ODP 849 (eastern equatorial Pacific), but temporary at ODP 983 (North Atlantic) and ODP 806 (western equatorial Pacific). Phase III, after MIS 22 (post-ca. 880 ka) was marked by the development of high amplitude glacial-interglacial oscillations. A global temperature trend was determined by combining the four SST time-series investigated in this thesis, and SST records from the Benguela upwelling cells (from Marlow et al., 2000; Marlow, 2001) and a site in the North-west Pacific (ODP 882, from Haug, 1996). The U^K_{37}' stack reveals a global cooling signal from MIS 34 (ca. 1140 ka) hitherto not described in the literature (Figure 8.1B). The cooling was sustained long-term, and lowered global SSTs by around 1.25°C. Significantly, the onset of the global cooling precedes the expansion of the northern hemisphere ice-sheets during MIS 22 by ca. 300-kyr.

The $\%C_{37:4}$ time-series generated in this thesis from ODP 983 (North Atlantic) was combined with the record from ODP 882 in the North-west Pacific (Haug, 1996). High abundances (>5%) of the $C_{37:4}$ alkenone in the modern North Atlantic correlate to the Arctic and Polar water mass domains, which have at least seasonal sea-ice cover (Rosell-Melé, 1998; Bendle, 2003). Variations to the values of the $\%C_{37:4}$ stack were interpreted in Chapter 5 to infer the dominance of different oceanographic domains in the study sites, reflecting the strengthening of arctic conditions and hence the seasonal extent of sea-ice cover in the northern hemisphere oceans. The $\%C_{37:4}$ stack is interpreted as showing a rapid expansion of sea-ice cover in the high northern latitudes,

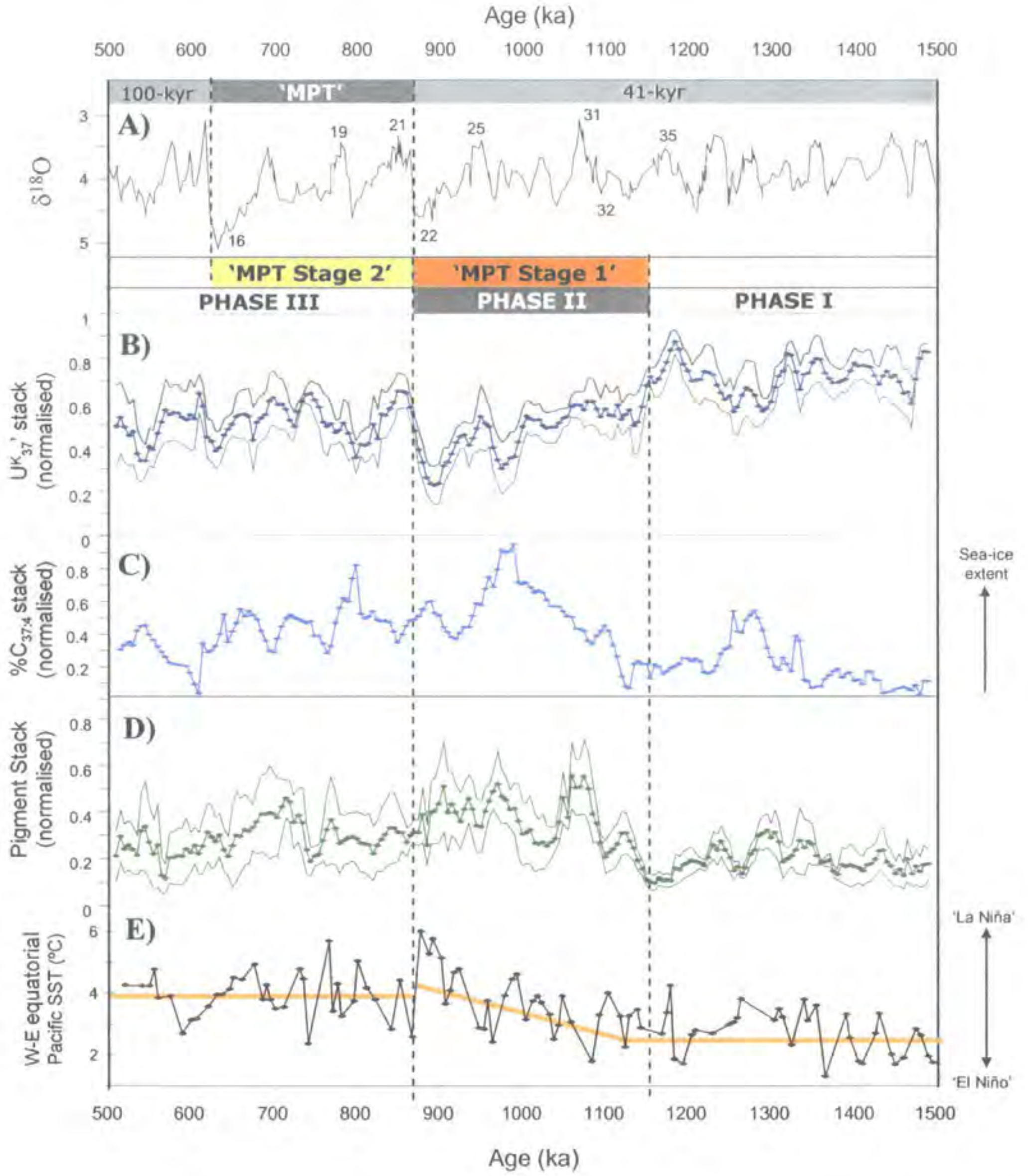

Figure 8-1 Mid-Pleistocene climate change in the surface ocean. A) Global ice volume record from Mix et al. (1995); B) Stack of normalised U^{K}_{37}' , representing global SST variability (Chapter 5). Mean value shown in blue, standard deviation shown by grey lines; C) Stack of $\%C_{37:4}$ from the North Atlantic and North Pacific, representing the extent of sea-ice cover in the northern high latitudes (Chapter 5); D) Stack of normalised pigment accumulation rates, representing organic carbon export from the surface ocean at a global scale (Chapter 6). The mean value is shown in green, the standard deviation by the thin grey lines; E) The minimum west-east SST gradient in the equatorial Pacific, representing the strength of the Walker circulation (Chapter 7). The mid-Pleistocene climate transition (MPT) as defined by Mudelsee and Schulz (1997) is marked. The three phases of surface ocean circulation identified in this thesis are identified by the vertical dashed lines. The revised boundaries of the MPT proposed in Chapter 5 are also shown by 'MPT Stage 1' and 'MPT Stage 2', as discussed in the text.

which occurred in association with the onset of the global cooling trend (Figure 8.1C). The highest values of %$C_{37:4}$ stack are found between 990-975 ka, suggesting that sea-ice reached its maximum at this time. Although there is subsequently a decline in the values of the %$C_{37:4}$ stack, values remain higher than those pre-MIS 35, and suggest that the global cooling trend was accompanied by the development of more extensive sea-ice cover in the long-term. This trend is attributed in Chapter 5 to the progressive cooling of deep-waters after 1500 ka (e.g. Tian et al., 2002), which Tziperman and Gildor (2003) proposed would have encouraged more extensive sea-ice development during the mid-Pleistocene by increasing the stratification between the surface and deep-ocean.

The principal aim of Chapter 6 was to assess the potential role of the carbon cycle in driving the published climate changes associated with the MPT and those presented in Chapter 5. The biological carbon pump, which transports organic carbon from the surface ocean to sea-floor sediments, provides a potential mechanism for lowering atmospheric CO_2 concentrations (pCO_2) and thus for driving global cooling and ice-sheet growth. Processes of sediment redistribution are considered to have played a minor role in biomarker accumulation rates at all sites (Chapter 3). These time-series were thus interpreted as proxies for the strength of the biological carbon pump because they are driven by the balance between export production in surface waters and biomarker diagenesis in the water column and sediments.

Variability at glacial-interglacial timescales was identified in all four of the sites investigated here. Stacking was performed to combine the chlorin accumulation rate time-series generated in this thesis with those from the Benguela upwelling cells (from Marlow et al., 2000; Marlow, 2001) and the North-west Pacific site (ODP 882, from Haug, 1996). A consideration to bear in mind is that the magnitude of the chlorin accumulation rates differs greatly between sites, and the stacking procedure normalises all records removing any weight on the relative importance of each setting as a carbon sink. Thus, in upwelling sites the rates of organic carbon drawdown are much larger than in oligotrophic areas. The chlorin stack suggests that, on a global scale, the strength of the biological carbon pump increased from MIS 34, in association with the global cooling trend described in Chapter 5 (Figure 8.1D). It is proposed here that this may have driven or maintained global cooling after MIS 35 by reducing pCO_2. The onset of the relative increase in the accumulation rates of chlorins is not synchronous between individual sites, although all sites excluding ODP 1087 (South-east Atlantic) have high chlorin accumulation rates during MIS 31 (ca. 1080 ka). Strong local controls over biomarker accumulation rates raise uncertainties about the effectiveness of the biological carbon pump for reducing pCO_2. This issue is particularly important at ODP 849 in the eastern equatorial Pacific, where high biomarker accumulation rates were attributed to stronger upwelling. Even with higher levels of production in the surface ocean, increased upwelling of CO_2-rich upwelled waters may increase the flux of CO_2 to the atmosphere. However, the high biomarker accumulation rates at ODP 849 during Phase II occur with low global SSTs, and immediately prior to the expansion of the northern hemisphere ice-sheets. This relationship suggests that the biological carbon pump at this site may have been effective in reducing pCO_2, thus maintaining or even driving global cooling during the mid-Pleistocene.

The role played by the tropics in driving or modulating global climate change has recently become a major issue in the climate research community. Stronger equatorial circulation has also been proposed as a key driving mechanism for the emergence of the 100-kyr glacial-interglacial oscillations associated with the MPT (Rutherford and D'Hondt, 2000). This hypothesis was tested in Chapter 7, through reconstruction of the strength of the closely coupled ocean-atmosphere circulation system of the tropical Pacific. Within the modern climate system, oscillations in the strength of this system are described by the El Niño/Southern Oscillation (ENSO) index, which oscillates between a strong La Niña state and weaker El Niño state. A comparison of SSTs from ODP 849 and 806, in the eastern and western tropical Pacific, demonstrated in Chapter 7 that the global cooling after MIS 35 was also associated with a long-term shift toward a stronger circulation system in the tropical Pacific (Figure 8.1E). By analogy with the modern climate system, this results in a shift toward a 'La Niña'-like state after MIS 34. The development of stronger tropical Pacific circulation is also accompanied by the strengthening of the biological carbon pump, first in the eastern equatorial Pacific during Phase II, and then in the west during Phase III.

Figure 8.1 demonstrates that the mid-Pleistocene is marked by significant changes to surface water conditions (SST and sea-ice extent), organic carbon export (the strength of the biological carbon pump) at a global scale, and the strength of the tropical Pacific circulation system. Significantly, the onset of these changes occurred during 'Phase II' of the four records analysed here, and thus preceded the MIS 22 expansion of the northern hemisphere ice-sheets by up to ca.300-kyr (Figure 8.1). The results presented here prompt a number of questions that need addressed to determine the role played by the climate changes presented in Figure 8.1 in the MPT. In particular, what caused the delayed ice-sheet response to the onset of global cooling, and what drove or maintained the global cooling?

The delayed response of the ice-sheets to the Phase II cooling is proposed here to reflect the influence of the supply of moisture to ice-sheet source regions in order to generate ice-sheet growth. Figures 8.1B and C demonstrate that the onset of global cooling was accompanied by an expansion of sea-ice over in both the Northern Atlantic and North Pacific. More expansive sea-ice cover reduces moisture inputs to ice-sheet source regions, by reducing evaporation and atmospheric humidity, and diverting storm tracks equatorward (Smith et al., 2003; Tziperman and Gildor, 2003). It is proposed here that even with global cooling after MIS 34, the northern hemisphere ice-sheets were unable to expand due to moisture limitation. A similar process may also have occurred within the Antarctic region, where a sustained northward expansion of the Antarctic Circumpolar Current (and presumably also the sea-ice cover to the south) has also been identified between ca. 1200-900 ka (Becquey and Gersonde, 2002; Diekmann and Kuhn, 2002).

After ca. 990 ka (MIS 25) sea-ice retreat is recorded by %$C_{37:4}$ (Figure 8.1C). The cause of this trend is unclear, but may be due to self-limitation on sea-ice growth due to its insulating effect over the surface ocean and/or to the more vigorous atmospheric circulation identified here in the tropical Pacific and Benguela upwelling, which would have acted to increase wind stress at high latitudes and thus discourage stratification. The removal or reduction of the moisture limitation from sea-ice as it retreated after ca. 990 ka is proposed to have played a key role in driving the expansion of the northern hemisphere ice-sheets during MIS 25-22 (Figure 8.1). It is proposed that the decline in sea-ice cover, as suggested by the %$C_{37:4}$ stack, encouraged accumulation in the ice-sheet source regions. The reduction in the sea-ice extent is accompanied by the long-term strengthening of the ENSO circulation system (Figure 8.1E). By analogy with modern 'La Niña' conditions, this should also have reduced the flux of heat to the ice-sheet source regions and encouraged further cooling. After MIS 22, the global U^{K}_{37}' stack also shows warmer glacial SSTs had developed when compared to the intense cooling of MIS 26 and 22 (Figure 8.1B). This apparently contradictory rise in SSTs with the onset of larger northern hemisphere ice-sheets may reflect an increase in effective heat transport toward the high-latitude ice-sheet source regions. Warmer surface waters encourage greater evaporation and humidity in the atmosphere, increasing potential precipitation. In the North Atlantic, the rise in SSTs at ODP 983 after MIS 22 reflects enhanced inputs of warm Atlantic waters to the region, which is proposed to be key to effective heat transport to the circum-Atlantic region during glacial inceptions (e.g. McManus et al., 2002). Furthermore, average global SSTs still remain below those prior to MIS 35 (Figure 8.1B), suggesting that the global climate system still remained cooler after MIS 22 than pre-MIS 35. These interactions suggest that the combination of high-latitude and tropical processes appears to have been key to the mid-Pleistocene expansion of the northern hemisphere ice-sheets (Figure 8.2). The increased inertia of these larger ice-sheets may be critical to the increasing duration of the glacial-interglacial cycles during the mid-Pleistocene, as the ice volume increase during MIS 22 is immediately followed by 77-kyr cycles until the 100-kyr cycles dominate from MIS 22 (Mudelsee and Schulz, 1997). By driving the expansion of the northern hemisphere ice-sheets, the climate changes identified in this thesis may therefore have played an important role in driving the MPT. The interaction between these processes in the mid-Pleistocene climate changes is summarised in Figure 8.2.

The driving mechanism for the cooling itself is less clear to identify. The increase in organic carbon export at a global scale suggests that the biological carbon pump may have driven global cooling through reducing reducing $p\mathrm{CO}_2$. The increase in organic carbon export associated with more intense upwelling in the eastern equatorial Pacific and the Benguela upwelling region complicates the evaluation of this hypothesis, given the complicated relationship between reducing $p\mathrm{CO}_2$ and upwelling outlined above. However, high chlorin accumulation rates in these regions tend to correlate with cooling events, suggesting that they may have been effective in driving a fall in reducing $p\mathrm{CO}_2$. The sustained high biomarker accumulation rates at a non-upwelling site, ODP 1087 in the South-east Atlantic, shows potential for reducing $p\mathrm{CO}_2$. The increase in chlorin accumulation rates here increase after the onset of cooling, suggesting that the biological carbon pump may have been effective in maintaining rather than driving the global cooling.

An alternative mechanism was proposed in Chapter 5 that relates the surface ocean changes identified in this thesis to those of the deep ocean. Tziperman and Gildor (2003) proposed that gradual cooling of the deep-ocean encouraged vertical stratification and

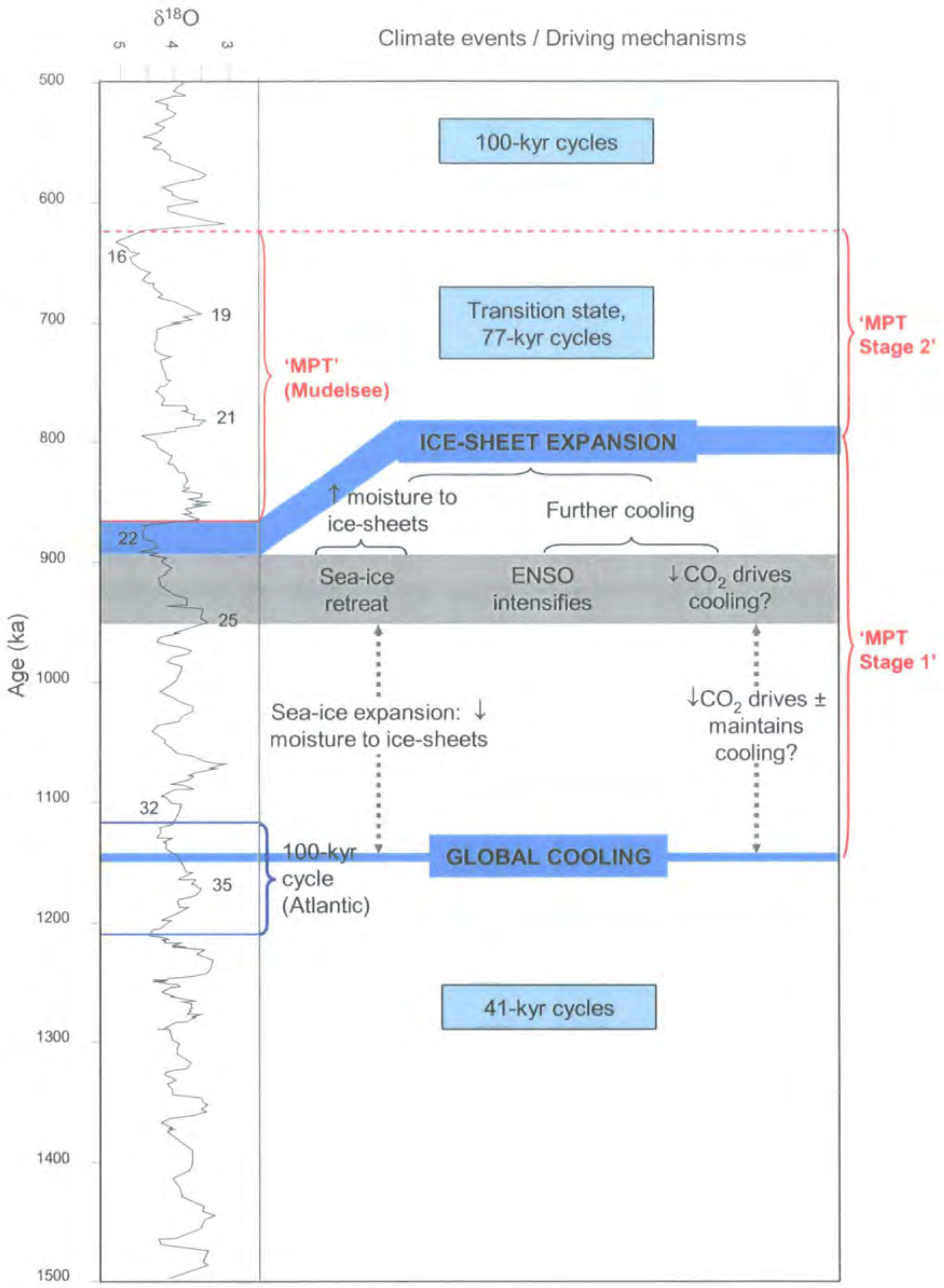

Figure 8-2 Summary of the mid-Pleistocene climate changes identified in this thesis and their potential driving mechanisms. On the left the global ice volume record from Mix et al. (1995) is shown, with selected isotope stages marked. The MPT as defined by Mudelsee and Schulz (1997) is marked on the $\delta^{18}O$ record. The revised boundaries of the MPT as proposed here are shown to the right.

sea-ice expansion during the mid-Pleistocene. This mechanism could account for the synchronous expansion of the sea-ice cover in the North Pacific and North Atlantic, and potentially also in the Antarctic region. It may also explain the synchronous cooling that is identified within upwelling regions (e.g. ODP 849, this study; ODP 1084, Marlow, 2001), where deep-waters are brought to the surface. Shoaling of the thermocline in the eastern Pacific, consistent with deep-water cooling, has also been reconstructed after 1500 ka (Cannariato and Ravelo, 1997). Cooling of deep-waters in the Atlantic relative to the Pacific has been identified after 1500 ka (Tian et al., 2002), and late Pleistocene glacial deep-water temperatures are lower than those of the Pliocene (Dwyer et al., 1995). A greater number of deep-water temperature reconstructions are required in order to evaluate this mechanism further.

The results from this thesis have demonstrated that significant changes to surface ocean circulation and the biological carbon pump occurred prior to the expansion of the northern hemisphere ice-sheets that is commonly used to delineate the onset of the MPT. Significantly, these events may have been key to driving the ice-sheet expansion and consequently to the MPT itself. An secondary aim of this thesis was to attempt to clarify the timing of the MPT. Revised boundaries for the MPT are proposed in Chapter 5 to incorporate the precursory climate changes identified in the surface ocean. A two-stage MPT is proposed (Figures 8.1, 8.2). Stage I was marked by the onset of global cooling from MIS 34 (ca.1140 ka), and corresponds to 'Phase II' of the 1500-500 ka interval described earlier. 'MPT Stage 1' is identified by global cooling, an increase in high-latitude sea-ice extent, increased organic carbon export at a global scale, and intensification of the Walker circulation in the tropical Pacific. Significantly, this 'MPT Stage 1' also includes a temporary strengthening of the 100-kyr cycle in global ice volume after 1145 ka, shown in Figure 1.5 and discussed by Berger et al. (1993a). This temporary and early emergence of the 100-kyr $\delta^{18}O$ signal has hitherto not been described by the conventional definition of the MPT using global ice volume change that spans MIS 22-16 (Mudelsee and Schulz, 1997). The 'MPT Stage 2' is proposed here to begin with the expansion of the northern hemisphere ice-sheets during MIS 22, which was driven by the interaction between reduced high latitude sea-ice cover and more intense circulation in the tropical Pacific. Stage II also marks a series of perturbations to deep-water and monsoon circulation that may have been triggered by the ice-sheet expansion. The termination of this second stage occurs with the onset of the first 100-kyr cycle during MIS 16. The 'MPT Stage 2' corresponds to the MPT as defined by

Mudelsee and Schulz (1997) based on an increase in mean global ice volume during MIS 22 and the onset of the first dominant 100-kyr cycle. This two-stage MPT incorporates MIS 34-16. It may therefore address many of the issues surrounding the timing of the MPT, as it covers the majority of the temporal ranges for the MPT proposed within the existing literature (e.g. Table 1.1).

8.2 Concluding remarks

In addition to fulfilling the principal aim of this thesis, to understand the causes of the MPT and the role played by the surface ocean in these events, this thesis has demonstrated the value of biomarker proxies, and the validity of the U^{K}_{37}' palaeo-SST proxy, for reconstructing surface ocean change during the early- and mid-Pleistocene, and given new boundaries with which to define the MPT. The results generated in this thesis demonstrate that significant changes to surface ocean circulation and the biological carbon pump occurred during the mid-Pleistocene. It is proposed here that these processes played a key role in driving the onset and pace of the MPT. Although the results support the hypothesis that the MPT was driven by global cooling, they also demonstrate the key role played by the supply of moisture in enabling the expansion of the northern hemisphere ice-sheets. It is proposed here that the balance between sea-ice extent and tropical circulation strength played an important role in controlling the supply of moisture and heat flux to the ice-sheets. These conclusions thus support the hypotheses of Rutherford and D'Hondt (2000) and Tziperman and Gildor (2003). In light of these results, a new definition of the MPT has been proposed, that incorporates the global cooling, the expansion of the northern hemisphere ice-sheets and the transition to 100-kyr cycles.

The results from this thesis have also raised a number of issues that require further assessment. First, how extensive was the sea-ice cover in the North Atlantic and North Pacific? The spatial resolution of the $\%C_{37:4}$ records in these regions should be increased, to determine the spatial distribution of the sea-ice cover and how this may have changed through time. This will enable further assessment of the impact that expanded sea-ice cover during the mid-Pleistocene may have had over surface circulation and the supply of moisture to the northern hemisphere ice sheets. Second, what caused the cooling of the deep-water temperature proposed to account for this sea-ice expansion? Tziperman and Gildor (2003) suggested that falling pCO_2 may have played a role, but were unable to propose a controlling mechanism. Finally, did pCO_2 actually fall during the mid-Pleistocene? And if so, what drove it? The latter issue may be addressed by increasing the spatial resolution of the biomarker accumulation rate time-series, to address fully the potential impacts of local processes on each of the records. The potential impact(s) of the biological carbon pump on pCO_2 at each site may then be realised. A greater understanding of the role played by changes to the biological carbon pump in the MPT is likely to be achieved by the generation of pCO_2 reconstructions to encompass at least the MIS 35-15 interval. Although there are currently limited pCO_2 reconstructions spanning this interval, a number of emerging proxies, particularly the analysis of $\delta^{13}C$ in alkenones and the possibility of the EPICA ice core reaching MIS 22 and perhaps earlier, show great promise for providing high-resolution records of pCO_2 across the MPT.

References

An, Z., Kutzbach, J. E., Prell, W. L., and Porter, S. C. (2001). Evolution of Asian monsoons and phased uplift of the Himalaya-Tibetan plateau since Late Miocene times. *Nature* **411**, 62-66.

Andersen, N., Müller, P. J., Kirst, G., and Schnieder, R. R. (1999). Alkenone $\delta^{13}C$ as a Proxy for Past PCO_2 in Surface Waters: Results from the Late Quaternary Angola Current. *In* "Use of Proxies in Paleoceanography: Examples from the South Atlantic." (G. Wefer, Ed.), pp. 469-488. Springer-Verlag Berlin Heidelberg.

Andreasen, D. J., and Ravelo, A. C. (1997). Tropical Pacific Ocean thermocline depth reconstructions for the last glacial maximum. *Paleoceanography* **12,** 395-413, 10.1029/97PA00822.

Andruleit, H. (1996). A filtration technique for quantitative studies of coccoliths. *Micropaleontology* **42,** 403-406.

Archer, D., Winguth, A., Lea, D. W., and Mahowald, N. (2000). What caused the glacial/interglacial pCO_2 cycles? *Reviews of Geophysics* **38,** 159-189.

Azzaroli, A. (1995). The 'Elephant-Equus' and the 'End-Villafranchian' Events in Eurasia. *In* "Paleoclimate and Evolution: with Emphasis on Human Origins." (E. S. Vrba, G. H. Denton, T. C. Partridge, and L. H. Burckle, Eds.), pp. 311-318. Yale University Press.

Balco, G., Patterson, C., and Stone, J. O. (2003). The fate of preglacial regolith beneath the Laurentide ice sheet. *In* "INQUA XVI Congress." Reno, Nevada.

Bard, E. (2001a). Comparison of alkenone estimates with other paleotemperature proxies. *Geochemistry Geophysics Geosystems* **2,** art. no.-2000GC000050.

Bard, E. (2001b). Paleoceanographic implications of the difference in deep-sea sediment mixing between large and fine particles. *Paleoceanography* **16,** 235-239.

Bard, E., Arnold, M., Maurice, P., Duprat, J., Moyes, J., and Duplessy, J.-C. (1987). Retreat veolicty of the North Atlantic polar front during the last deglaciation determined by ^{14}C accelerator mass spectrometry. *Nature* **328,** 791-794.

Bassinot, F. C., Beaufort, L., Vincent, E., and Labeyrie, L. (1997). Changes in the dynamics of western equatorial Atlantic surface currents and biogenic productivity at the "Mid-Pleistocene Revolution" (~930 ka). *In* "Proceedings of the Ocean Drilling Program, Scientific Results." (N. J. Shackleton, W. B. Curry, C. Richter, and T. J. Bralower, Eds.), pp. 269-284.

Beaufort, L. (1994). Climatic importance of the modulation of the 100-k.y.r. cycle inferred from 16 m.y. long Miocene records. *Paleoceanography* **9,** 821-834.

Beaufort, L., and Aubry, M.-P. (1990). Fluctuations in the composition of Late Miocene calcareous nannofossil assemblages as a response to orbital forcing. *Paleoceanography* **5,** 845-865.

Beaufort, L., de Garidel-Thoron, T., Mix, A. C., and Pisias, N. G. (2001). ENSO-like Forcing on Oceanic Primary Production During the Late Pleistocene (abstract). *Science* **293,** 2440-2444.

Becquey, S., and Gersonde, R. (2002). Past hydrographic and climate changes in the Subantarctic Zone of the South Atlantic - the Pleistocene record from ODP Site 1090. *Palaeogeography, Palaeoclimatology, Palaeoecology* **182,** 221-239.

Beer, J., Mende, W., and Stellmacher, R. (2000). The role of the sun in climate forcing. *Quaternary Science Reviews* **19,** 403-415.

Bendle, J. A. P. (2003). "Palaeoceanography of the Late-Glacial and Holocene N.E. Atlantic: Development and application of biomarker proxies of environmental change." Unpublished PhD thesis, University of Durham.

Benn, D. I., and Evans, D. J. A. (1998). "Glaciers and Glaciation." Arnold, Bath.

Bentaleb, I., Fontugne, M., and Beaufort, L. (2002). Long-chain alkenones and U^{K}_{37}' variability along a north-south transect in the Western Pacific Ocean. *Global and Planetary Change* **34,** 173-183.

Berger, A., and Loutre, M. F. (1991). Insolation values for the climate of the last 10 Million years. *Quaternary Science Reviews* **10,** 297-317.

Berger, A., Li, X. S., and Loutre, M. F. (1999). Modelling northern hemisphere ice volume over the last 3 Ma. *Quaternary Science Reviews* **18,** 1-11.

Berger, W. H., and Jansen, E. (1994). Mid-Pleistocene Climate Shift- The Nansen Connection. *In* "The Polar Oceans and Their Role in Shaping the Global Environment. Geophysical Monograph Series 84." (O. M. Johannessen, R. D. Muench, and J. E. Overland, Eds.), pp. 295-311. American Geophysical Union.

Berger, W. H., and Wefer, G. (1991). Productivity of the glacial ocean: Discussion of the iron hypothesis. *Limnology and Oceanography* **36,** 1899-1918.

Berger, W. H., Bickert, T., Schmidt, H., and Wefer, G. (1993a). Quaternary oxygen isotope record of pelagic foraminifers: Site 806, Ontong Java Plateau. *In* "Proceedings of the Ocean Drilling Program, Scientific Results, vol.130." (W. H. Berger, L. W. Kroenke, L. A. Mayer, and Shipboard Scientific Party, Eds.), pp. 381-395. College Station, TX (Ocean Drilling Program).

Berger, W. H., Bickert, T., Schmidt, H., Wefer, G., and Yasuda, M. (1993b). Quaternary oxygen isotope record of pelagic foraminifers: Site 805, Ontong Java Plateau. *In* "Proceedings of the Ocean Drilling Program, Scientific Results." (W. H. Berger, L. W. Kroenke, and L. A. e. a. Mayer, Eds.), pp. 363-379. College Station, TX (Ocean Drilling Program).

Berger, W. H., Lange, C. B., and Wefer, G. (2002). Upwelling history of the Benguela-Namibia system: a synthesis of Leg 175 results. *In* "Proceedings of the Ocean Drilling Program, Scientific Results v 175." (G. Wefer, Berger, W.H., and C. Richter, Eds.), pp. 1–103 [Online]. Available from World Wide Web: <http://www-odp.tamu.edu/publications/175_SR/VOLUME/SYNTH/SR175SYN.PDF>.

Berger, W. H., Yasuda, M. K., Bickert, T., Wefer, G., and Takayama, T. (1994). Quaternary time scale for the Ontong Java Plateau: Milankovitch template for Ocean Drilling Program Site 806. *Geology* **22,** 463-467.

Bertini, A. (2003). Early to Middle Pleistocene Changes of the Italian Flora and Vegetation in the Light of a Chronostratigraphic Framework. *Il Quaternario: Italian Journal of Quaternary Sciences* **16,** 19-36.

Bickert, T., Curry, W. B., and Wefer, G. (1997). Late Pliocene to Holocene (2.6-0 Ma) western equatorial Atlantic deep-water circulation: inferences from benthic stable isotopes. *In* "Proceedings of the Ocean Drilling Program, Scientific Results." (N. J. Shackleton, W. B. Curry, C. Richter, and T. J. Bralower, Eds.), pp. 239-254.

Bidigare, R. R., Fluegge, A., Freeman, K. H., Hanson, K. L., Hayes, J. M., Hollander, D., Jasper, J. P., King, L. L., Laws, E. A., Milder, J., Millero, F. J., Pancost, R., Popp, B. N., Steinberg, P. A., and Wakeham, S. G. (1997). Consistent fractionation of C-13 in nature and in the laboratory: Growth-rate effects in some haptophyte algae. *Global Biogeochemical Cycles* **11,** 279-192.

Bigg, G. R. (1998). "Oceans and Climate." Cambridge University Press.

Bishop, L. C. (1999). Suid Paleoecology and Habitat Preferences at African Pliocene and Pleistocene Hominid Localities. *In* "African Biogeography, Climate Change, and Human Evolution." (T. G. Bromage, and F. Schrenk, Eds.), pp. 216-225. Oxford University Press.

Bloemendal, J., Liu, X. M., and Rolph, T. C. (1995). Correlation of the magnetic susceptibility stratigraphy of Chinese loess and the marine oxygen isotope record: chronological and palaeoclimatic implications. *Earth and Planetary Science Letters* **131,** 371-380.

Blunier, T., and Brook, E. J. (2001). Timing of Millenial-Scale Climate Change in Antarctica and Greenland During the Last Glacial Period. *Science* **291,** 109-112.

Blunier, T., Chappellaz, J., Schwander, J., Dällenbach, A., Stauffer, B., Raynaud, D., Jouzel, J., Clausen, H. B., Hammer, C. U., and Johnsen, S. J. (1998). Asynchrony of Antarctic and Greenland climate change during the last glacial period. *Nature* **394,** 739-743.

Bohrmann, G., Henrich, R., and Thiede, J. (1990). Miocene to Quaternary Paleoceanography in the Northern North Atlantic: Variability in Carbonate and Biogenic Opal Accumulation. *In* "Geological History of the Polar Oceans: Arctic versus Antarctic." (U. Bleil, and J. Thiede, Eds.), pp. 647-675. NATO ASI Series C. Kluwer, Dordrecht.

Bond, G., Showers, W., Cheseby, M., Lotti, R., Almasi, P., de Menocal, P., Priore, P., Cullen, H., Hajdas, I., and Bonani, G. (1997). A Pervasive Millenial-Scale Cycle in North Atlantic Holocene and Glacial Climates. *Science* **278,** 1257-1266.

Bopp, L., Kohfeld, K. E., Le Quéré, C., and Aumont, O. (2003). Dust impact on marine biota and atmospheric CO2 during glacial periods. *Paleoceanography* **18,** 1046.

Boyle, E. A., and Keigwin, L. D. (1987). North Atlantic thermohaline circulation during the past 20,000 years linked to high-latitude surface temperature. *Nature* **330,** 35-40.

Bradley, R. S. (2000). Past global changes and their significance for the future. *Quaternary Science Reviews* **19,** 391-402.

Brassell, S. C., Dumitrescu, M., and ODP Leg 198 Shipboard Scientific Party. (2004). Recognition of alkenones in a lower Aptian porcellanite from the west-central Pacific. *Organic Geochemistry* **35,** 181-188.

Brassell, S. C., Eglinton, G., Marlowe, I. T., Pflaumann, U., and Sarnthein, M. (1986). Molecular stratigraphy: a new tool for climatic assessment. *Nature* **320,** 129-133.

Bridgland, D. R. (2000). River terrace systems in north-west Europe: an archive of environmental change, uplift and early human occupation. *Quaternary Science Reviews* **19,** 1293-1303.

Broecker, W. S. (1991). The Great Ocean Conveyor. *Oceanography* **4,** 79-89.

Broecker, W. S. (1998). Paleocean circulation during the last deglaciation: A bipolar seesaw? *Paleoceanography* **13,** 119-121.

Broecker, W. S., and Denton, G. H. (1990). The role of ocean-atmosphere reorganizations in glacial cycles. *Quaternary Science Reviews* **9,** 305-341.

Bromage, T. G., and Schrenk, F. (1999). African Biogeography, Climate Change, and Human Evolution.

Bush, A. B. G., and Philander, S. G. H. (1998). The Role of Ocean-Atmosphere Interactions in Tropical Cooling During the Last Glacial Maximum. *Science* **279,** 1341-1344.

Calvo, E., Villanueva, J., Grimalt, J. O., Boelaert, A., and Labeyrie, L. (2001). New insights into the glacial latitudinal temperature gradients in the North Atlantic. Results from U^{K}_{37}' sea surface temperatures and terrigenous inputs. *Earth and Planetary Science Letters* **188,** 509-519.

Cane, M. A. (1998). A Role for the Tropical Pacific. *Science* **282,** 59-61.

Cannariato, K. G., and Ravelo, A. C. (1997). Pliocene-Pleistocene evolution of eastern tropical Pacific surface water circulation and thermocline depth. *Paleoceanography* **12,** 805-820.

Chaisson, W. (1995). Planktonic foraminiferal assemblages and paleoceanographic change in the trans-tropical Pacific Ocean: A comparison of west (Leg 130) and east (Leg 138), latest Miocene to Pleistocene. *In* "Proceedings of the Ocean Drilling Program, Scientific Results, vol.138." (N. G. Pisias, L. A. Mayer, T. R. Janecek, A. Palmer-Julson, and T. H. van Andel, Eds.), pp. 555-. College Station, TX (Ocean Drilling Program).

Chaisson, W. P., and Ravelo, A. C. (2000). Pliocene development of the east-west hydrographic gradient in the equatorial Pacific. *Paleoceanography* **15,** 497-505.

Channell, J. E. T., and Kleiven, H. F. (2000). Geomagnetic palaeointensities and astrochronological ages for the Matuyama-Brunhes boundary and the boundaries of the Jaramillo Subchron: palaeomagnetic and oxygen isotope records from ODP Site 983. *Philosophical Transactions of the Royal Society of London A* **358,** 1027-1047.

Chavez, F. P., and Barber, R. T. (1987). An estimate of new production in the equatorial Pacific. *Deep-Sea Research I* **34,** 1229-1243.

Chavez, F. P., Buck, K. R., and Barber, R. T. (1990). Phytoplankton taxa in relation to primary productivity in the upper Equatorial Pacific Ocean. *Journal of Physical Oceanography* **37,** 1733-1752.

Chavez, F. P., Buck, K. R., Coale, K. H., Martin, J. H., Di Tullio, G. R., Welschmeyer, N. A., Jacobson, A. C., and Barber, R. T. (1991). Growth rates, grazing, sinking, and iron limitation of equatorial Pacific phytoplankton. *Limnology and Oceanography* **36,** 1816-1833.

Clark, P. U., Alley, R. B., and Pollard, D. (1999). Northern Hemisphere Ice-Sheet Influences on Global Climate Change. *Science* **286,** 1104-1111.

Clark, P. U., and Pollard, D. (1998). Origin of the middle Pleistocene transition by ice sheet erosion of regolith. *Paleoceanography* **13,** 1-9.

Clemens, S. C., Murray, D. W., and Prell, W. L. (1996). Nonstationary Phase of the Plio-Pleistocene Asian Monsoon. *Science* **274,** 943-948.

Clement, A. C., Seager, R., and Cane, M. A. (1999). Orbital controls on the El Niño/Southern Oscillation and the tropical climate. *Paleoceanography* **14,** 441-456.

CLIMAP Project Members. (1976). The surface of ice-age earth. *Science* **191,** 1131-1137.

Conkright, M. E., Locarnini, R. A., Garcia, H. E., O'Brien, T. D., Boyer, T. P., Stephens, C., and Antonov, J. I. (2002). "World Ocean Atlas 2001: Objective Analyses, Data Statistics, and Figures, CD-ROM Documentation, MD, 17pp." National Oceanographic Data Center, Silver Spring, MD.

Conte, M. H., and Eglinton, G. (1993). Alkenone and alkenoate distributions within the euphotic zone of the eastern north Atlantic: correlation with production temperature. *Deep-Sea Research I* **40,** 1935-1961.

Conte, M. H., Eglinton, G., and Madureira, L. A. S. (1992). Long-chain alkenones and alkyl alkenoates as palaeotemperature indicators: their production, flux and early sedimentary diagenesis in the Eastern North Atlantic. *Organic Geochemistry* **19,** 287-298.

Conte, M. H., Thompson, A., Eglinton, G., and Green, J. C. (1995). Lipid biomarker diversity in the coccolithophorid *Emiliania huxleyi* (Prymnesiophyceae) and the related species *Gephyrocapsa oceanica*. *Journal of Phycology* **31,** 272-282.

Conte, M. H., Thompson, A., Lesley, D., and Harris, R. P. (1998). Genetic and physiological influences on the alkenone/alkenoate versus growth temperature relationship in *Emiliania huxleyi* and *Geophyrocapsa oceanica*. *Geochimica et Cosmochimica Acta* **62,** 51-68.

Conte, M. H., Weber, J. C., King, L. L., and Wakeham, S. G. (2001). The alkenone temperature signal in western North Atlantic surface waters. *Geochimica et Cosmochimica Acta* **65,** 4275-4287.

Croll, J. (1875). "Climate and time in their geological relations. A theory of secular changes of the Earth's climate." London, Daldy, Isbister & Co.

Crowley, T. J., Kim, K.-Y., Mengel, J. G., and Short, D. A. (1992). Modelling 100,000-Year Climate Fluctuations in Pre-Pleistocene Time Series. *Science* **255,** 705-707.

Cuffey, K. M., and Vimeux, F. (2001). Covariation of carbon dioxide and temperature from the Vostok ice core after deuterium-excess correction. *Nature* **412,** 523-526.

Curry, W. B., Marchitto, T. M. J., McManus, J. F., Oppo, D. W., and Laarkamp, K. L. (1999). Millennial-scale Changes in Ventilation of the Thermocline, Intermediate and Deep Waters of the Glacial North Atlantic. *In* "Chapman Conference on Mechanisms of Millennial-scale Global Climate Change." (P. U. Clark, R. S. Webb, and L. D. Keigwin, Eds.), pp. 59-76. Volume 112, Geophysical Monography, American Geophysical Union.

De Dekker, P., Tapper, N. J., and van der Kaars, S. (2002). The status of the Indo-Pacific Warm Pool and adjacent land at the Last Glacial Maximum. *Global and Planetary Change* **35,** 25-35.

de Menocal, P. B. (1995). Plio-Pleistocene African climate. *Science* **270,** 53-59.

de Menocal, P. B., and Bloemendal, J. (1995). Plio-Pleistocene Climatic Variability in Subtropical Africa and the Paleoenvironment of Hominid Evolution: A Combined Data-Model Approach. *In* "Paleoclimate and Evolution: with Emphasis on Human Origins." (E. S. Vrba, G. H. Denton, T. C. Partridge, and L. H. Burckle, Eds.), pp. 262-288. Yale University Press.

de Menocal, P., Archer, D., and Leth, P. (1997). Pleistocene variations in deep Atlantic circulation and calcite burial between 1.2 and 0.6 Ma: a combined data-model approach. *In* "Proceedings of the Ocean Drilling Program, Scientific Results." (N. J. Shackleton, W. B. Curry, C. Richter, and T. J. Bralower, Eds.), pp. 285-297.

de Vernal, A., and Hillaire-Marcel, C. (2000). Sea-ice cover, sea-surface salinity and halo-/thermocline structure of the northwest North Atlantic: modern versus full glacial conditions. *Quaternary Science Reviews* **19,** 65-85.

Denys, C. (1999). Of Mice and Men: Evolution in East and South Africa during Plio-Pleistocene Times. *In* "African Biogeography, Climate Change, and Human Evolution." (T. G. Bromage, and F. Schrenk, Eds.), pp. 226-252. Oxford University Press.

Diaz, H. F., and Markgraf, V. (2000). El Niño and the southern oscillation : multiscale variability and global and regional impacts. Cambridge : Cambridge University Press.

Diekmann, B., and Kuhn, G. (2002). Sedimentary record of the mid-Pleistocene climate transition in the southeastern South Atlantic (ODP Site 1090). *Palaeogeography, Palaeoclimatology, Palaeoecology* **182,** 241-258.

Dowsett, H., and Willard, D. (1996). Southeast Atlantic marine and terrestrial response to middle Pliocene climate change. *Marine Micropaleontology* **27,** 181-193.

Duplessy, J.-C., Labeyrie, L., Arnold, M., Paterne, M., Duprat, J., and van Weering, T. C. E. (1992). Changes in surface salinity of the North Atlantic Ocean during the last deglaciation. *Nature* **358,** 485-487.

Dupont, L. M., Donner, B., Scheider, R., and Wefer, G. (2001). Mid-Pleistocene environmental change in tropical Africa began as early as 1.05 Ma. *Geology* **29,** 195-198.

Durham, E. L., Maslin, M. A., Platzman, E., Rosell-Melé, A., Marlow, J. R., Leng, M., Lowry, D., Burns, S. J., and Party, a. t. O. L. S. S. (2001). Reconstructing the climatic history of the western coast of Africa over the past 1.5 m.y.: a comparison of proxy records from the Congo Basin and the Walvis Ridge and the search for the Mid-Pleistocene Revolution. *In* "Proceedings of the Ocean Drilling Program, Scientific Results." (G. Wefer, W. H. Berger, and C. Richter, Eds.), pp. 1-46 [Online].

Dwyer, G. S., Cronin, T. M., Baker, P. A., Raymo, M. E., Buzas, J. S., and Correge, T. (1995). North Atlantic Deepwater Temperature Change During Late Pleistocene and Late Quaternary Climatic Cycles. *Science* **270,** 1247-1351.

Eglinton, T. I., Conte, M. H., Eglinton, G., and Hayes, J. M. (2001). Proceedings of a workshop on alkenone-based paleoceanographic indicators. *Geochemistry Geophysics Geosystems* **2,** art. no.-2000GC000122.

Ehleringer, J. R., Cerling, T. E., and Helliker, B. R. (1997). C_4 photosynthesis, atmospheric CO_2, and climate. *Oecologia* **112,** 285-299.

Emeis, K.-C., Doose, H., Mix, A. C., and Schulz-Bull, D. (1995). Alkenone sea-surface temperatures and carbon burial at Site 846 (Eastern equatorial Pacific Ocean): the last 1.3 m.y. *In* "Proceedings of the Ocean Drilling Program, Scientific Results." (N. G. Pisias, L. A. Mayer, A. Palmer-Julson, and T. H. van Andel, Eds.), pp. 605-613.

Emiliani, C. (1955). Pleistocene temperatures. *Journal of Geology* **66,** 264-275.

EPICA community members. (2004). Eight glacial cycles from an Antarctic ice core. *Nature* **429,** 623-628.

Esper, O., Versteegh, G. J. M., Zonneveld, K. A. F., and Willems, H. (2004). A palynological reconstruction of the Agulhas Retroflection (South Atlantic Ocean) during the Late Quaternary. *Global and Planetary Change* **41,** 31-62.

Everitt, D. A., Wright, S. W., Volkman, J. K., Thomas, D. P., and Lindstrom, E. J. (1990). Phytoplankton community compositions in the western equatorial Pacific determined from chlorophyll and carotenoid pigment distributions (abstract). *Deep-Sea Research I* **37,** 975-997.

Falkowski, P., Scholes, R. J., Boyle, E., Canadell, J., Canfield, D., Elser, J., Gruber, N., Hibbard, K., Högberg, O., Linder, S., Mackenzie, F. T., Moore III, B., Pedersen, T., Rosenthal, Y., Seitzinger, S., Smetacek, V., and Steffen, W. (2000). The Global Carbon Cycle: A Test of Our Knowledge of Earth as a System. *Science* **290,** 291-296.

Farley, K. A., and Patterson, D. B. (1995). A 100-kyr periodicity in the flux of extraterrestrial ^{3}He to the sea floor. *Nature* **378,** 600-603.

Farrimond, P., Eglinton, G., and Brassell, S. C. (1986). Alkenones in Cretaceous black shales, Blake-Bahama Basin, wesatern North Atlantic. *Organic Geochemistry* **10,** 897-903.

Flückiger, J., Dallenbach, A., Blunier, T., Stauffer, B., Stocker, T. F., Raynaud, D., and Barnola, J.-M. (1999). Variation in atmospheric N_2O concentration during abrupt climatic changes. *Science* **285,** 227.

Forsberg, C. F., LØvlie, R., Jansen, E., Solheim, A., Sejrup, H. P., and Lie, H. E. (2003). A 1.3-Myr palaeoceanographic record from the continental margin off Dronning Maud Land, Antarctica. *Palaeogeography, Palaeoclimatology, Palaeoecology* **198,** 223-235.

Francois, R., Frank, M., Rutgers van der Loeff, M., and Bacon, M. P. (2004). ^{230}Th normalization: An essential tool for interpreting sedimentary fluxes during^{230} the late Quaternary. *Paleoceanography* **19,** PA1018, doi:10.1029/2003PA000939.

Fronval, T., and Jansen, E. (1996). Late Neogene Paleoclimates and Paleoceanography in the Iceland-Norwegian Sea: Evidence from the Iceland and Vøring Plateaus. *In* "Proceedings of the Ocean Drilling Program, Scientific Results 151." (J. Thiede, A. M. Myhre, J. V. Firth, G. L. Johnson, and W. F. Ruddiman, Eds.), pp. 455-468.

Gagan, M. K., Ayliffe, L. K., Beck, J. W., Cole, J. E., Druffel, E. R. M., Dunbar, R. B., and Schrag, D. P. (2000). New views of tropical paleoclimates from corals. *Quaternary Science Reviews* **19,** 45– 64.

Ganopolski, A., and Rahmstorf, S. (2001). Rapid changes of glacial climate simulated in a coupled climate model. *Nature* **409,** 153-158.

Gartner, S. (1977). Calcareous nannofossils biostratigraphy and revised zonation of the Pliocene. *Marine Micropaleontology* **2,** 1-25.

Gersonde, R., Abelmann, A., Brathauer, U., Becquey, S., Bianchi, C., Cortese, G., Grobe, H., Kuhn, G., Niebler, H.-S., Segl, M., Sieger, R., Zielinski, U., and Fütterer, D. K. (2003). Last glacial sea surface temperatures and sea-ice extent in the Southern Ocean (Atlantic-Indian Sector): A multiproxy approach. *Paleoceanography* **18,** 1061.

Gildor, H., and Tziperman, E. (2000). Sea ice as the glacial cycles' climate switch: Role of seasonal and orbital forcing. *Paleoceanography* **15,** 605-615.

Gildor, H., and Tziperman, E. (2001). A sea ice climate switch mechanism for the 100-kyr glacial cycles. *Journal of Geophysical Research* **106 C5,** 9117-9133.

Giraudeau, J., Cremer, M., Manthe, S., Labeyrie, L., and Bond, G. (2000). Coccolith evidence for instabilities in surface circulation south of Iceland during Holocene times. *Earth and Planetary Science Letters* **179,** 257-268.

Giraudeau, J., Meyers, P. A., and Christensen, B. A. (2002). Accumulation of organic and inorganic sediments in Pliocene-Pleistocene sediments along the SW African margin. *Marine Geology* **180,** 49-69.

Giraudeau, J., Pierre, C., and Herve, L. (2001). A late Quaternary, high resolution record of planktonic foraminiferal species distribution in the southern Benguela region: Site 1087. *In* "Proceedings of the Ocean Drilling Program, Scientific Results 175." (G. Wefer, W. H. Berger, and C. Richter, Eds.), pp. 1-26 [Online]. Available from World Wide Web: <http://www-odp.tamu.edu/publications/175_SR/VOLUME/CHAPTERS/SR175_07.PDF>.

Gordon, A. L., Weiss, R. F., Smethie, W. M. J., and Warner, M. J. (1992). Thermocline and Intermediate Water Communication Between the South Atlantic and Indian Oceans. *Journal of Geophysical Research* **97,** 7223-7240.

Grice, K., Klein Breteler, W. M., Schouten, S., Grossi, V., de Leeuw, J. W., and Sinninghe Damsté, J. S. (1998). Effects of zooplankton herbivory on biomarker proxy records. *Paleoceanography* **13,** 686-693.

Grimalt, J. O., Calvo, E., and Pelejero, C. (2001). Sea surface paleotemperature errors in U^{K}_{37}' estimation due to alkenone measurements near the limit of detection. *Paleoceanography* **16,** 226-232.

Gröger, M., Henrich, R., and Bickert, T. (2003). Variability of silt grain size and planktonic foraminiferal preservation in Plio/Pleistocene sediments from the western equatorial Atlantic and Caribbean. *Marine Geology* **201,** 307-320.

Guilderson, T. P., Fairbanks, R. G., and Rubenstone, J. L. (1994). Tropical Temperature Variations Since 20,000 Years Ago: Modulating Interhemispheric Climate Change. *Science* **263,** 663-665.

Hall, I. R., McCave, I. N., Shackleton, N. J., Weedon, G. P., and Harris, S. E. (2001). Intensified deep Pacific inflow and ventilation in Pleistocene glacial times. *Nature* **412,** 809-812.

Hansen, B., and Østerhus, S. (2000). North Atlantic - Nordic Seas exchanges. *Progress in Oceanography* **45,** 109-208.

Harris, P. G., and Maxwell, J. (1995). A novel method for the rapid determination of chlorin concentrations at high stratigraphic resolution in marine sediments. *Organic Geochemistry* **23,** 853-856.

Harris, P. G., Zhao, M., Rosell-Melé, A., Tiedemann, R., Sarnthein, M., and Maxwell, J. R. (1996). Chlorin accumulation rate as a proxy for Quaternary marine primary productivity. Nature 383, 63-65.

Haug, G. H. (1996). "Paleoceanography and sedimentation history in the Northwest Pacific during the last 6 Mio years (ODP Site 882)." Unpublished Ph.D. thesis, Geol.Palaontol.Inst.Kiel,78.

Haug, G. H., Hughen, K. A., Sigman, D. M., Peterson, L. C., and Röhl, U. (2001). Southward Migration of the Intertropical Convergence Zone Through the Holocene. *Science* **293,** 1304-1308.

Haviland, W. A. (1994). "Human Evolution and Prehistory."

Hay, W. H., and Brock, J. C. (1992). Temporal variation in intensity of upwelling off southwest Africa. *In* "Upwelling Systems: Evolution Since the Early Miocene." (C. P. Summerhayes, W. L. Prell, and K.-C. Emeis, Eds.), pp. 463-497. Geological Society Special Publication No 64.

Hays, J. D., Imbrie, J., and Shackleton, N. J. (1976). Variations in the Earth's Orbit: Pacemaker of the Ice Ages. *Science* **194,** 1121-1132.

Helmke, J. P., Bauch, H. A., and Erlenkeuser, H. (2003). Development of glacial and interglacial conditions in the Nordic seas between 1.5 and 0.35 Ma. *Quaternary Science Reviews* **22,** 1717-1728.

Helmke, J. P., Bauch, H. A., and Mazaud, A. (2003b). Evidence for a mid-Pleistocene shift of ice-drift pattern in the Nordic Seas. *Journal of Quaternary Science* **18,** 183-191.

Henrich, R., and Baumann, K.-H. (1994). Evolution of the Norwegian Current and the Scandinavian Ice Sheets during the past 2.6 m.y.: evidence from ODP Leg 104 biogenic carbonate and terrigenous records. *Palaeogeography, Palaeoclimatology, Palaeoecology* **108,** 75-94.

Henrich, R., Baumann, K.-H., Huber, R., and Meggers, H. (2002). Carbonate preservation records of the past 3 Myr in the Norwegian-Greenland Sea and the northern North Atlantic: implications for the history of NADW production. *Marine Geology* **184,** 17-39.

Herbert, T. D., and Schuffer, J. D. (1998). Alkenone unsaturation estimates of late Miocene through late Pliocene sea-surface temperatures at Site 958. *In* "Proceedings of the Ocean Drilling Program, Scientific Results, vol 195." pp. 17-21.

Heslop, D., Dekkers, M. J., and Langereis, C. G. (2002). Timing and structure of the mid-Pleistocene transition: records from the loess deposits of northern China. *Palaeogeography, Palaeoclimatology, Palaeoecology* **185,** 133-143.

Higgins, S. M. (2001). "Extraterrestrial Tracer in the Sea: Evaluation and Application of ^{3}He in Interplanetary Dust Particles as a Constant Flux Tracer in Marine Sediments." Unpublished Ph.D. thesis, Columbia University, New York.

Higgins, S. M., Anderson, R. F., Marcantonio, F., Schlosser, P., and Stute, M. (2002). Sediment focussing creates 100-kyr cycles in interplanetary dust accumulation on the Ontong Java Plateau. *Earth and Planetary Science Letters* **203,** 283-397.

Higginson, M. J. (1999). "Chlorin pigment stratigraphy as a new and rapid palaeoceanographic proxy in the Quaternary." University of Bristol.

Hine, N., and Weaver, P. P. E. (1998). Quaternary. *In* "Calcareous Nannofossil Biostratigraphy." (P. Bown, Ed.), pp. 266- 283. Chapman and Hall.

Hoefs, M. J. L., Versteegh, G. J. M., Rijpstra, W. I. C., de Leeuw, J. W., and Sinninghe-Damsté, J. S. (1998). Postdepositional oxic degradation of alkenones: implications for the measurement of palaeo sea surface temperatures. *Paleoceanography* **13,** 42-49.

Hooghiemstra, H., and Cleef, A. M. (1995). Pleistocene climatic change and environmental and generic dynamics in the North Andean montane forest and Páramo. *In* "Biodiversity and conservation of neotropical montane forests." (S. P. Churchill, and e. al, Eds.), pp. 35-49. New York Botanical Garden, New York.

Hooghiemstra, H., and Ran, E. T. H. (1994). Late Pliocene-Pleistocene high resolution pollen sequence of Columbia: An overview of climatic change. *Quaternary International* **21,** 63-80.

Hovan, S. (1995). Late Cenozoic atmospheric circulation intensity and climatic history recorded by eolian deposition in the eastern equatorial Pacific Ocean, Leg 138. *In* "Proceedings of the Ocean Drilling Program, Scientific Results, vol.138." (N. G. Pisias, L. A. Mayer, T. R. Janecek, A. Palmer-Julson, and T. H. van Andel, Eds.), pp. 615-625. College Station, TX (Ocean Drilling Program).

Hulton, N., Sugden, D., Payne, A., and Clapperton, C. (1994). Glacier Modeling and the Climate of Patagonia during the Last Glacial Maximum. *Quaternary Research* **42,** 1-19.

Hyun, S., Ortiz, J. D., Raymo, M. E., and Taira, A. (1999). Low-frequency oscillations in Site 983 sediments: relationships between carbonate and productivity proxies. *In* "Proceedings of the Ocean Drilling Program, Scientific Results, vol 162." (M. E. Raymo, E. Jansen, P. Blum, and T. D. Herbert, Eds.), pp. 197-207. College Station, TX (Ocean Drilling Program).

Imbrie, J., Berger, A., Boyle, E. A., Clemens, S. C., Duffy, A., Howard, W. R., Kukla, G., Kutzbach, J., Martinson, D. G., McIntyre, A., Mix, A. C., Molfino, B., Morley, J. J., Peterson, L. C., Pisias, N. G., Prell, W. L., Raymo, M. E., Shackleton, N. J., and Toggweiler, J. R. (1992). On the structure and origin of major glaciation cycles. Part I: Linear responses to Milankovitch forcing. *Paleoceanography* **7,** 701-738.

Imbrie, J., Hays, J. D., Martinson, D. G., McIntyre, A., Mix, A. C., Morley, J. J., Pisias, N. G., Prell, W. L., and Shackleton, N. J. (1984). The orbital theory of Pleistocene climate: support from a revised chronology of the marine $\delta^{18}O$ record. *In* "Milankovitch and Climate, Part I." (A. L. e. a. Berger, Ed.), pp. 269-305. D.Riedel Publishing Company.

Imbrie, J., McIntyre, A., and Mix, A. C. (1989). Oceanic response to orbital forcing in the late Quaternary: observational and experimental strategies. *In* "Climate and Geo-Sciences." (A. Berger, Ed.), pp. 121-164. Kluwer Academic, Norwell, Mass.

Jahn, B. (2002). "Mid to Late Pleistocene Variations of Marine Productivity and Terrigenous Input to the Southeast Atlantic." Universitat Bremen.

Jahn, B., Donner, B., Müller, P. J., Röhl, U., Schneider, R. R., and Wefer, G. (2003). Pleistocene variations in dust input and marine productivity in the northern Benguela Current: Evidence of evolution of global glacial-interglacial cycles. *Palaeogeography, Palaeoclimatology, Palaeoecology* **193,** 515-533.

Janecek, T. R., and Rea, D. K. (1985). Quaternary fluctuations in the Northern Hemisphere tradewinds and westerlies. *Quaternary Research* **24,** 150-163.

Jansen, E., Raymo, M. E., Blum, P., and Shipboard Scientific Party. (1996). Site 983. *In* "Proceedings of the Ocean Drilling Program, Initial Reports 162." (Shipboard Scientific Party, Ed.), pp. 139-167. College Station, TX (Ocean Drilling Program).

Jasper, J. P., and Hayes, J. M. (1990). A carbon isotope record of CO_2 levels during the late Quaternary. *Nature* **347,** 462-464.

Jeffrey, S. W., Mantoura, R. F. C., and BjØrnland, T. (1997). Data for the identification of 47 key phytoplankton pigments. *In* "Phytoplankton pigments in oceanography: guidelines to modern methods." (S. W. Wright, Ed.), pp. 149-559.

Jian, Z., Wang, P., Chen, M.-P., Li, B., Zhao, Q., Bühring, C., Laj, C., Lin, H.-L., Pflaumann, U., Bian, Y., Wang, R., and Cheng, X. (2000). Foraminiferal responses to major Pleistocene paleoceanographic changes in the southern South China Sea. *Paleoceanography* **15,** 229-243.

Jian, Z., Zhao, Q., Cheng, X., Wang, J., Wang, P., and Su, X. (2003). Plio-Pleistocene stable isotope and paleoceanographic changes in the northern South China Sea. *Palaeogeography, Palaeoclimatology, Palaeoecology* **193,** 425-442.

Kallen, E., Crafoord, C., and Ghil, M. (1979). Free-oscillations in a climate model with ice-sheet dynamics. *Journal of Atmospheric Science* **36,** 2292-2303.

Keely, B. J., Harris, P. G., Popp, B. N., Hayes, J. M., Meischner, D., and Maxwell, J. (1994). Porphyrin and chlorin distributions in a Late Pliocene lacustrine sediment. *Geochimica et Cosmochimica Acta* **58,** 3691-3701.

Kellogg, T. B. (1980). Paleoclimatology and paleo-oceanography of the Norwegian and Greenland seas: Glacial-interglacial contrasts. *Boreas* **9,** 115-136.

Kim, J.-H., Schneider, R. R., Müller, P. J., and Wefer, G. (2002). Interhemispheric comparison of deglacial sea-surface temperature patterns in Atlantic eastern boundary currents. *Earth and Planetary Science Letters* **194,** 383-393.

Kimbel, W. H. (1995). Hominid Speciation and Pliocene Climatic Change. *In* "Paleoclimate and Evolution: with Emphasis on Human Origins." (E. S. Vrba, G. H. Denton, T. C. Partridge, and L. H. Burckle, Eds.), pp. 425-437. Yale University Press.

Kissel, C., Laj, C., Clemens, S. C., and Solheid, P. (2003). Magentic signature of environmental changes in the last 1.2 Myr at ODP Site 1146, South China Sea. *Marine Geology* **201,** 119-132.

Kleiven, H. F. (2000). "Orbital and millennial-scale ice sheet and ocean variability in the North Atlantic during the Pliocene and Pleistocene climate transitions." University of Bergen.

Kleiven, H. F., Jansen, E., Curry, W. B., Hodell, D. A., and Venz, K. A. (2003). Atlantic Ocean thermohaline circulation changes on orbital to suborbital timescales during the mid-Pleistocene. *Paleoceanography* **18,** 1008.

Koç, N., and Jansen, E. (1994). Response of the high-latitude Northern Hemisphere to orbital climate forcing: Evidence from the Nordic Seas. *Geology* **22,** 523-526.

Koç, N., Hodell, D. A., Kleiven, H. F., and Labeyrie, L. D. (1999). High-resolution Pleistocene diatom stratigraphy of Site 983 and correlations with isotope stratigraphy. *In* "Proceedings of the Ocean Drilling Program, Scientific Results, vol.162." (M. E. Raymo, E. Jansen, P. Blum, and T. D. Herbert, Eds.), pp. 51-62. College Station, TX (Ocean Drilling Program).

Koç, N., Jansen, E., and Haflidason, H. (1993). Paleoceanographic reconstructions of surface ocean conditions in the Greenland, Iceland and Norwegian Seas through the last 14 ka based on diatoms. *Quaternary Science Reviews* **12,** 115-140.

Kornilova, O., and Rosell-Melé, A. (2003). Application of microwave-assisted extraction to the analysis of biomarker climate proxies in marine sediments. *Organic Geochemistry* **34,** 1517-1523.

Koutavas, A., and Lynch-Stieglitz, J. (2003). Glacial-interglacial dynamics of the eastern equatorial Pacific cold tongue-Intertropical Convergence Zone reconstructed from oxygen isotope records. *Paleoceanography* **18,** 1089, doi:10.1029/2003PA000894.

Koutavas, A., Lynch-Stieglitz, J., Marchitto, T. M. J., and Sachs, J. P. (2002). El Niño-Like Pattern in Ice Age Tropical Pacific Sea Surface Temperature. *Science* **297,** 226-230.

Krissek, L. A., and Janecek, T. R. (1993). Eolian deposition on the Ontong Java Plateau since the Oligocene: unmixing a record of multiple dust sources. *In* "Proceedings of the Ocean Drilling Program, Scientific Results, vol.130." (Shipboard Scientific Party, Ed.), pp. 471-489. College Station, TX (Ocean Drilling Program).

Kroenke, L. W., Berger, W. H., Janecek, T. R., and Shipboard Scientific Party. (1991). Site 806. *In* "Proceedings of the Ocean Drilling Program, Initial Reports, vol.130." (L. W. Kroenke, W. H. Berger, T. R. Janecek, and Shipboard Scientific Party, Eds.), pp. 291. College Station, TX (Ocean Drilling Program).

Kuhn, G., and Diekmann, B. (2002). Late Quaternary variability of ocean circulation in the southeatern South Atlantic inferred from the terrigenous sediment record of a drift deposit in the southern Cape Basin (ODP Site 1089). *Palaeogeography, Palaeoclimatology, Palaeoecology* **182,** 287-303.

Lampitt, R. S., Fahrbach, E., Schneider, B., Schneider, R. R., Smith, S. V., Toggweiler, J. R., Watson, A. J., and Zeitschel, B. (1995). Group Report: Does Upwelling Have a Significant Influence on the Global Carbon Cycle? *In* "Upwelling in the Ocean: Modern Processes and Ancient Records." (C. P. Summerhayes, K.-C. Emeis, M. V. Angel, R. L. Smith, and B. Zeitschel, Eds.), pp. 383-404. John Wiley.

Lange, C. B., and Berger, W. H. (1993). Diatom productivity and preservation in the western equatorial Pacific: the Quaternary record. *In* "Proceedings of the Ocean Drilling Program, Scientific Results, vol.130." (W. H. Berger, L. W. Kroenke, L. A. Mayer, and Shipboard Scientific Party, Eds.), pp. 509-521. College Station, TX (Ocean Drilling Program).

Lea, D. W., Pak, D. K., and Spero, H. J. (2000). Climate Impact of Late Quaternary Equatorial Pacific Sea-Surface Temperature Variations. *Science* **289,** 1719-1724.

Lear, C. H., Elderfield, H., and Wilson, P. A. (2000). Cenozoic Deep-Sea Temperatures and Global Ice Volumes from Mg/Ca in Benthic Foraminiferal Calcite. *Science* **287,** 269-272.

Levin, I., and Hesshaimer, V. (2000). Radiocarbon - a unique tracer of global carbon cycle dynamics. *Radiocarbon* **42,** 69-80.

Little, M. G., Schneider, R. R., Kroon, D., Price, B., Summerhayes, C. P., and Segl, M. (1997). Trade wind forcing of upwelling, seasonality, and Heinrich events as a response to sub-Milankovitch climate variability. *Paleoceanography* **12,** 568-576.

Liu, Z., and Herbert, T. D. (2004). High-latitude influence on the eastern equatorial Pacific climate in the early Pleistocene epoch. *Nature* **427,** 720-724.

Longhurst, A. R. (1998). "Ecological Geography of the Sea." Acacdemic Press.

Loubere, P. (1999). A multiproxy reconstruction of biological productivity and oceanography in the eastern equatorial Pacific for the past 30,000 years. *Marine Micropaleontology* **37,** 173-198.

Loubere, P., Fariduddin, M., and Murray, R. W. (2003). Patterns of export production in the eastern equatorial Pacific over the past 130,000 years. *Paleoceanography* **18,** 1028.

Lowe, J. J., and Walker, M. J. C. (1994). "Reconstructing Quaternary Environments." Longman, Second Edition.

Lu, H., Liu, X., Zhang, F., An, Z., and Dodson, J. (1999). Astronomical calibration of the loess-paleosol deposits at Luochuan, central Chinese Loess Plateau. *Palaeogeography, Palaeoclimatology, Palaeoecology* **154,** 237-246.

Lutjeharms, J. R. E. (1996). The exchange of water between the South Indian and the South Atlantic. *In* "The South Atlantic: Present and Past Circulation." (G. Wefer, W. H. Berger, G. Siedler, and D. Webb, Eds.), pp. 125-162. Springer, Berlin.

MacFadden, B. J. (2000). Middle Pleistocene Climate Change Recorded in Fossil Mammal Teeth from Tarija, Bolivia, and Upper Limit of the Ensenaden Land-Mammal Age. *Quaternary Research* **54,** 121-131.

Mackey, D. J., Parslow, J. S., Griffiths, F. B., Higgins, H. W., and Tilbrook, B. (1997). Phytoplankton productivity and the carbon cycle in the western Equatorial Pacific under El Niño and non-El Niño conditions. *Deep-Sea Research II* **44,** 1951-1978.

Mackey, D. J., Parslow, J., Higgins, H. W., Griffiths, F. B., and O'Sullivan, J. E. (1995). Plankton productivity and biomass in the western equatorial Pacific: Biological and physical controls. *Deep-Sea Research II* **42,** 499-533.

Mann, M. E., and Jones, P. D. (2003). Global surface temperatures over the past two millennia. *Geophysical Research Letters* **20,** 1820.

Marcantonio, F., Andersen, N., Higgins, S. M., Stute, M., and Schlosser, P. (2001). Sediment focussing in the central equatorial Pacific Ocean. *Paleoceanography* **16,** 260-267.

Marcantonio, F., Andersen, N., Stute, M., Kumar, P., Schlosser, P., and Mix, A. C. (1996). Extraterrestrial 3He as a tracer of marine sediment transport and accumulation. *Nature* **383,** 705-707.

Marlow, J. R. (2001). "Application of U^{K}_{37}' for Long-term (Pliocene-Pleistocene) Palaeoclimate Reconstruction." University of Newcastle upon Tyne.

Marlow, J. R., Lange, C. B., Wefer, G., and Rosell-Melé, A. (2000). Upwelling intensification as part of the Pliocene-Pleistocene climate transition. *Science* **290,** 2288-2291.

Marlowe, I. (1984). "Lipids as palaeoclimatic indicators." Unpublished Thesis thesis, University of Bristol.

Marlowe, I. T., Brassell, S. C., Eglinton, G., and Green, J. C. (1990). Long-chain alkenones and alkyl alkenoates and the fossil coccolith record of marine sediments. *Chemical Geology* **88,** 349-375.

Martin, J. H. (1990). Glacial-interglacial CO_2 change: The iron hypothesis. *Paleoceanography* **5,** 1-13.

Martin, J. H., Gordon, R. M., and Fitzwater, S. E. (1991). The case for iron. *Limnology and Oceanography* **36,** 1793-1802.

Martinez, J. I., De Dekker, P., and Chivas, A. R. (1997). New estimates for salinity changes in the Western Pacific Warm Pool during the Last Glacial Maximum: oxygen-isotope evidence. *Marine Micropaleontology* **32,** 311-340.

Martinson, D. G., Pisias, N. G., Hays, J. D., Imbrie, J., Moore, T. C. J., and Shackleton, N. J. (1987). Ade-Dating and the Orbital Theory of the Ice Ages: Development of a High-Resolution 0 to 300,000-Year Chronostratigraphy. *Quaternary Research* **27,** 1-30.

Maslin, M., Shackleton, N. J., and Pflaumann, U. (1995). Surface water temperature, salinity and density changes in the NE Atlantic during the last 45 000 years: Heinrich events, deep water formation and climatic rebounds. *Paleoceanography* **10,** 527-544.

Mayer, L. A. (1994). Surface area control of organic carbon accumulation in continental shelf sediments. *Geochimica et Cosmochimica Acta* **58,** 1271-1284.

Mayer, L. A., Pisias, N. G., Janecek, T. R., and Shipboard Scientific Party. (1992). Site 849. *In* "Proceedings of the Ocean Drilling Program, Initial Reports, vol.138." (L. A. Mayer, N. G. Pisias, T. R. Janecek, and Shipboard Scientific Party, Eds.), pp. 735-767. College Station, TX (Ocean Drilling Program).

McCulloch, M. T., Tudhope, A. W., Esat, T. M., Mortimer, G. E., Chappell, J., Pillans, B., Chivas, A. R., and Omura, A. (1999). Coral record of equatorial sea-surface temperatures during the penultimate deglaciation at Huon Peninsula. *Science* **283,** 202-204.

McIntyre, A. (1970). *Gephyrocapsa* protohuxleyi sp.m., a possible phyletic link and index fossil for the Pleistocene. *Deep-Sea Research* **17,** 187-190.

McIntyre, A., Ruddiman, W. F., Karlin, K., and Mix, A. C. (1989). Surface water response of the equatorial Atlantic Ocean to orbital forcing. *Paleoceanography* **4,** 19-55.

McManus, J. F., Oppo, D. W., Keigwin, L. D., Cullen, J., and Bond, G. C. (2002). Thermohaline Circulation and Prolonged Interglacial Warmth in the North Atlantic. *Quaternary Research* **58,** 17-21.

Milankovitch, M. (1930). Mathematische Klimalehre und astronomische Theorie der Klimaschwankungen. *In* "Handbuch der Klimatologie, vol. 1." (W. Köppen, and R. Geiger, Eds.), pp. 1-176. Gebrüder Bornträger, Berlin.

Miller, G., and de Vernal, A. (1992). Will greenhouse warming lead to Northern Hemisphere ice-sheet growth? *Nature* **355,** 244-246.

Mix, A. C., Pisias, N. G., Rugh, W., Wilson, J., Morey, A., and Hagelberg, T. K. (1995). Benthic foraminifer stable isotope record from Site 849 (0-5 Ma): local and global climate changes. *In* "Proceedings of the Ocean Drilling Program, Scientific Results, Vol 138." (N. G. Pisias, L. A. Mayer, T. R. Janecek, A. Palmer-Julson, and T. H. van Andel, Eds.), pp. 371-389.

Mollenhauer, G., Eglinton, T. I., Ohkouchi, N., Schneider, R. R., Müller, P. J., Grootes, P. M., and Rullkötter, J. (2003). Asynchronous alkenone and foraminifera records from the Benguela Upwelling System. *Geochimica Et Cosmochimica Acta* **67,** 2157-2171.

Mollenhauer, G., Schneider, R. R., Müller, P. J., Spieß, V., and Wefer, G. (2002). Glacial/interglacial variability in the Benguela upwelling system: Spatial distribution and budgets of organic carbon accumulation. *Global Biogeochemical Cycles* **16,** 1134.

Molnar, P., and Cane, M. A. (2002). El Niño's tropical climate and teleconnections as a blueprint for pre-Ice Age climates. *Paleoceanography* **17,** 11.

Morley, J. J., and Hays, J. D. (1979). Comparison of Glacial and Interglacial Oceanographic Conditions in the South Atlantic from Variations in Calcium Carbonate and Radiolarian Distributions. *Quaternary Research* **12,** 396-408.

Morley, J. J., and Heusser, L. E. (1997). Role of orbital forcing in east Asian monsoon climates during the last 350 kyr: Evidence from terrestrial and marine climate proxies from core RC14-99. *Paleoceanography* **12,** 483-493.

Mudelsee, M. (2001). The phase relations among atmospheric CO_2 content, temperature and global ice volume over the past 420 ka. *Quaternary Science Reviews* **20,** 583-589.

Mudelsee, M., and Schulz, M. (1997). The Mid-Pleistocene climate transition: onset of 100ka cycle lags ice volume build-up by 280ka. *Earth and Planetary Science Letters* **151,** 117-123.

Mudelsee, M., and Stattegger, K. (1997). Exploring the structure of the mid-Pleistocene Revolution with advanced methods of time-series analysis. *Geologische Rundschau* **86,** 499-511.

Müller, P. J., Cepek, M., Ruhland, G., and Schneider, R. R. (1997). Alkenone and coccolithophorid species changes in late Quaternary sediments from the Walvis Ridge: Implications for the alkenone paleotemperature method. *Palaeogeography Palaeoclimatology Palaeoecology* **135,** 71-96.

Müller, P. J., Cepek, M., Ruhland, G., and Schneider, R. R. (1997). Alkenone and coccolithophorid species changes in late Quaternary sediments from the Walvis Ridge: Implications for the alkenone paleotemperature method. *Palaeogeography Palaeoclimatology Palaeoecology* **135,** 71-96.

Müller, P. J., Kirst, G., Ruhland, G., von Storch, I., and Rosell-Melé, A. (1998). Calibration of the alkenone paleotemperature index U^{K}_{37}' based on core-tops from the eastern South Atlantic and the global ocean (60 degrees N-60 degrees S). *Geochimica Et Cosmochimica Acta* **62,** 1757-1772.

Müller, P. J., Schneider, R., and Ruhland, G. (1994). Late Quaternary PCO_2 variations in the Angola Current: Evidence from organic carbon δ^{13}C and alkenone temperatures. *In* "Carbon Cycling in the Glacial Ocean." (R. e. a. Zahn, Ed.), pp. 343-366. NATO ASI Series.

Muller, R. A., and MacDonald, G. J. (1995). Glacial cycles and orbital inclination. *Nature* **377,** 107-108.

Muller, R. A., and MacDonald, G. J. (1997). Simultaneous presence of orbital inclination and eccentricity in proxy climate records from Ocean Drilling Program Site 806. *Geology* **25,** 3-6.

Murray, D. W., Farrell, J. W., and McKenna, V. S. (1995). Biogenic sedimentation at Site 847, eastern equatorial Pacific Ocean, during the past 3 m.y. *In* "Proceedings of the Ocean Drilling Program, Scientific Results, vol.138." (N. G. Pisias, L. A. Mayer, T. R. Janecek, A. Palmer-Julson, and T. H. van Andel, Eds.), pp. 429-457. College Station, TX (Ocean Drilling Program).

Murray, R. W., Knowlton, C., Leinen, M., Mix, A. C., and Polsky, C. H. (2000). Export production and carbonate dissolution in the central equatorial Pacific Ocean over the past 1 Myr. *Paleoceanography* **15,** 570-592.

Napoleone, G., Albianelli, A., Azzaroli, A., Bertini, A., Magi, M., and Mazzini, M. (2003). Calibration of the Upper Valdarno Basin to the Plio-Pleistocene for Correlating the Apennine Continental Sequences. *Il Quaternario: Italian Journal of Quaternary Sciences* **16,** 131-166.

Ohkouchi, N., Eglinton, T. I., Keigwin, L. D., and Hayes, J. M. (2002). Spatial and Temporal Offsets Between Proxy Records in a Sediment Drift. *Science* **298,** 1224-1228.

Okada, H. (2000). Neogene and Quaternary Calcareous Nannofossils from the Blake Ridge, Sites 994, 995 and 997. *In* "Proceedings of the Ocean Drilling Program, Scientific Results, 164." (W. P. Dillon, Ed.), pp. 331-341.

Okada, H., and Honjo, S. (1973). The distribution of oceanic coccolithophorids in the Pacific. *Deep-Sea Research* **26,** 355-374.

Okada, H., and McIntyre, A. (1977). Modern coccolithophores of the Pacific and North Atlantic Oceans. *Micropaleontology* **23,** 1-55.

Opdyke, N. D. (1995). Mammalian Migration and Climate over the Last Seven Million Years. *In* "Paleoclimate and Evolution: with Emphasis on Human Origins." (E. S. Vrba, G. H. Denton, T. C. Partridge, and L. H. Burckle, Eds.), pp. 109-114. Yale University Press.

Open University. (1989). "Ocean Circulation." Pergamon Press.

Oppo, D. W., and Lehmann, S. J. (1995). Suborbital timescale variability of North Atlantic Deep Water during the last 200,000 years. *Paleoceanography* **10,** 901-910.

Oppo, D. W., Raymo, M. E., lohmann, G. P., Mix, A. C., wright, J. D., and Prell, W. L. (1995). A δ^{13}C record of Upper North Atlantic Deep Water during the past 2.6 million years. *Paleoceanography* **10,** 373-394.

Owen-Smith, N. (1999). Ecological Links between African Savanna Environments, Climate Change, and Early Hominid Evolution. *In* "African Biogeography, Climate Change, and Human Evolution." (T. G. Bromage, and F. Schrenk, Eds.), pp. 138-149. Oxford University Press.

Pagani, M., Arthur, M. A., and Freeman, K. H. (1999). Miocene evolution of atmospheric carbon dioxide. *Paleoceanography* **14,** 273-292.

Pagani, M., Freeman, K. H., and Arthur, M. A. (1999b). Late Miocene Atmospheric CO_2 Concentrations and the Expansion of C_4 Grasses. *Science* **285,** 876-879.

Pagani, M., Freeman, K. H., Ohkouchi, N., and Caldeira, K. (2002). Comparison of water column [CO_{2aq}] with sedimentary alkenone-based estimates: A test of the alkenone-CO_2 proxy. *Paleoceanography* **17,** 1069.

Paillard, D. (1998). The timing of Pleistocene glaciations from a simple multiple-state climate model. *Nature* **391,** 378-381.

Palmer, M. R., and Pearson, P. N. (2003). A 23,000-Year Record of Surface Water pH and PCO2 in the Western Equatorial Pacific Ocean. Science 300, 480-482.

Patience, A. J., and Kroon, D. (1991). Oxygen-isotope chronostratigraphy. *In* "Quaternary Dating Methods - A User's Guide." (P. L. Smart, and P. D. Frances, Eds.), pp. 199-228. Technical Guide 4, Quaternary Research Association, Cambridge.

Patterson, D. B., and Farley, K. A. (1998). Extraterrestrial ^{3}He in sea-floor sediments: Evidence for correlated 100 kyr periodicity in the accretion rate of interplanetary dust, orbital parameters, and Quaternary climate. *Geochimica et Cosmochimica Acta* **62,** 3669-3682.

Pearson, P. N., and Palmer, M. R. (2000). Atmospheric carbon dioxide concentrations over the past 60 million years. *Nature* **406,** 695-699.

Pelejero, C., and Calvo, E. (2003). The upper end of the U^K_{37}' temperature calibration revisited. *Geochemistry, Geophysics, Geosystems* **4,** 1014, doi:10.1029/2002GC000431, 2003.

Pelejero, C., Grimalt, J. O., Heilig, S., Kienast, M., and Wang, L. (1999). High-resolution U^K_{37} temperature reconstructions in the South China Sea over the past 220 kyr. *Paleoceanography* **14,** 224-231.

Petit, J. R., Jouzel, J., Raynaud, D., Barkov, N. I., Barnola, J.-M., Basile, I., Bender, M., Chappellax, J., Davis, M., Delaygue, G., Delmotte, M., Kotlyakov, V. M., Legrand, M., Lipenkov, V. Y., Lorius, C., Pepin, L., Ritz, C., Saltzman, E., and Stievenard, M. (1999). Climate and atmospheric history of the past 420,000 years from the Vostok ice core, Antarctica. *Nature* **399,** 429-436.

Pflaumann, U., Sarnthein, M., Chapman, M., d'Abreu, L., Funnell, B., Huels, M., Kiefer, T., Maslin, M., Schulz, H., Swallow, J., van Kreveld, S., Vautravers, M., Vogelsang, E., and Weinelt, M. (2003). Glacial North Atlantic: Sea-surface conditions reconstructed by GLAMAP 2000. *Paleoceanography* **18,** 1065.

Philander, S. G., and Fedorov, A. V. (2003). Role of tropics in changing the response to Milankovitch forcing some three million years ago. *Paleoceanography* **18,** 1045.

Pierre, C., Saliege, J. F., Urrutiaguer, M. J., and Giraudeau, J. (2001). Stable isotope record of the last 500 k.y. at Site 1087 (Southern Cape Basin). *In* "Proceedings of the Ocean Drilling Program, Scientific Results 175." (C. Richter, Ed.), pp. 1-22 [Online]. Available from World Wide Web: <http://www-odp.tamu.edu/publications/175_SR/VOLUME/CHAPTERS/SR175_12.PDF>.

Pierrehumbert, R. T. (2000). Climate change and the tropical Pacific: The sleeping dragon wakes. *Proceedings of the National Academy of Science* **97,** 1355-1358.

Pisias, N. G., and Mix, A. C. (1997). Spatial and temporal oceanographic variability of the eastern equatorial Pacific during the late Pleistocene: Evidence from Radiolaria microfossils. *Paleoceanography* **12,** 381-393.

Pisias, N. G., Mayer, L. A., Janecek, T. R., Palmer-Julson, A., and van Andel, T. H. (1995a). "Proceedings of the Ocean Drilling Program, Scientific Results, vol.138." College Station, TX (Ocean Drilling Program).

Pisias, N. G., Mayer, L. A., and Mix, A. C. (1995b). Paleoceanography of the eastern equatorial Pacific during the Neogene: Synthesis of Leg 138 Drilling Results. *In* "Proceedings of the Ocean Drilling Program, Scientific Results, vol.138." (N. G. Pisias, L. A. Mayer, T. R. Janecek, A. Palmer-Julson, and T. H. van Andel, Eds.), pp. 5-21. College Station, TX (Ocean Drilling Program).

Popp, B. N., Kenig, F., Wakeham, S. G., Laws, E. A., and Bidigare, R. R. (1998). Does growth rate affect ketone unsaturation and intracellular carbon isotopic variability in Emiliani huxleyi? *Paleoceanography* **13,** 35-41.

Prahl, F. G., and Wakeham, S. G. (1987). Calibration of unsaturation patterns in long-chain ketone compositions for palaeotemperature assessment. *Nature* **320,** 367-369.

Prahl, F. G., Collier, R. B., Dymond, J., Lyle, M., and Sparrow, M. A. (1993). A Biomarker Perspective on Prymnesiophyte Productivity in the Northeast Pacific-Ocean. *Deep-Sea Research Part I-Oceanographic Research Papers* **40,** 2061-2076.

Prahl, F. G., Cowie, G. L., de Lange, G. J., and Sparrow, M. A. (2003). Selective organic matter preservation in "burn-down" turbidites on the Madeira Abyssal Plain. *Paleoceanography* **18,** 1052.

Prahl, F. G., Delange, G. J., Lyle, M., and Sparrow, M. A. (1989). Post-Depositional Stability of Long-Chain Alkenones under Contrasting Redox Conditions. *Nature* **341,** 434-437.

Prahl, F. G., Muehlhausen, L. A., and Zahnle, D. I. (1988). Further evaluation of long-chain alkenones as indicators of paleoceanographic conditions. *Geochimica et Cosmochimica Acta* **52,** 2303-2310.

Prahl, F. G., Pilskaln, C. H., and Sparrow, M. A. (2001). Seasonal record for alkenones in sedimentary particles from the Gulf of Maine. *Deep-Sea Research Part I-Oceanographic Research Papers* **48,** 515-528.

Prahl, F. G., Wolfe, G. V., and Sparrow, M. A. (2004). Physiological impacts on alkenone paleothermometry. *Paleoceanography* **18,** 1025, doi.10.1029/2002PA000803.

Prell, W. L., and Kutzbach, J. E. (1987). Monsoon variability over the past 150,000 yars. *Journal of Geophysical Research* **92,** 8411-8425.

Rahmstorf, S. (2002). Ocean circulation and climate during the past 120,000 years. *Nature* **419,** 207-214.

Raymo, M. E. (1994). The Himalayas, organic carbon burial, and climate in the Miocene. *Paleoceanography* **9,** 399-404.

Raymo, M. E. (1994). The Initiation of Northern Hemisphere Glaciation. *Annual Review of Earth and Planetary Sciences* **22,** 353-383.

Raymo, M. E. (1997). The timing of major climate terminations. *Paleoceanography* **12,** 577-585.

Raymo, M. E., and Niscancioglu, K. (2003). The 41 kyr world: Milankovitch's other unsolved mystery. *Paleoceanography* **18,** 1011.

Raymo, M. E., Oppo, D. W.,and Curry, W. (1997). The mid-Pleistocene climate transition: A deep sea carbon isotope perspective. Paleoceanography 12, 546-559.

Raymo, M. E., Rind, D., and Ruddiman, W. F. (1990a). Climatic effects of reduced Arctic sea ice limits in the GISS II general circulation model. Paleoceanography 5, 367-382.

Raymo, M. E., Ruddiman, W. F., Shackleton, N. J., and Oppo, D. W. (1990b). Evolution of Atlantic-Pacific $\delta^{13}C$ gradients over the last 2.5 m.y. *Earth and Planetary Science Letters* **97,** 353-368.

Rea, D. K., and Snoeckx, H. (1995). Sediment fluxes in the Gulf of Alaska: Paleoceanographic record from Site 887 on the Patton-Murray Seamount Platform. *In* "Proceedings of the Ocean Drilling Program, Scientific Results 145." pp. 247-256.

Rea, D. K., Snoeckx, H., and Joseph, L. H. (1998). Late Cenozoic eolian deposition in the North Pacific: Asian drying, Tibetan uplift, and cooling of the northern hemisphere. *Paleoceanography* **13,** 215-224.

Rechka, J. A., and Maxwell, J. R. (1988). Characterisation of alkenone temperature indicators in sediments and organisms. *Organic Geochemistry* **13,** 727-734.

Rich, J. J., Hollander, D., and Birchfield, G. E. (1999). Role of bioproductivity in atmospheric CO_2 changes. *Global Biogeochemical Cycles* **13,** 531-553.

Richardson, P. L., Lutjeharms, J. R. E., and Boebel, O. (2003). Introduction to the "Inter-ocean exchange around southern Africa". *Deep Sea Research Part II: Topical Studies in Oceanography* **50,** 1-12.

Ridgwell, A. J., and Watson, A. J. (2002). Feedback between aeolian dust, climate, and atmospheric CO_2 in glacial time. *Paleoceanography* **17,** 1059.

Rodgers, K. B., Lohmann, G., Lorenz, S., Schneider, R., and Henderson, G. M. (2003). A tropical mechanism for Northern Hemisphere deglaciation. *Geochemistry, Geophysics, Geosystems* **4,** 1046.

Rogers, J., and Bremner, J. M. (1991). The Benguela ecosystem, Part VII: Marine geological aspects. *Marine Biology Annual Review* **29,** 1-85.

Rosell-Melé, A. (1994). "Long-chain alkenones, alkyl alkenoates and total pigment abundances as climatic proxy-indicators in the Northeastern Atlantic." Unpublished Thesis thesis, University of Bristol.

Rosell-Melé, A. (1998). Interhemispheric appraisal of the value of alkenone indices as temperature and salinity proxies in high-latitude locations. *Paleoceanography* **13,** 694-703.

Rosell-Melé, A. (2000). Examination of the Use of Biomarker Proxies for the Reconstruction of Paleoceanographic Conditions in the Northern North Atlantic. *In* "The Northern North Atlantic: A Changing Environment." (P. Schäfer, W. Ritzrau, M. Schlüter, and J. Thiede, Eds.), pp. 353-363. Springer, Berlin.

Rosell-Melé, A., and Koç, N. (1997). Paleoclimatic significance of the stratigraphic occurrence of photosynthetic biomarker pigments in the Nordic Seas. *Geology* **25,** 49-52.

Rosell-Melé, A., Bard, E., Emeis, K.-C., Farrimond, P., Grimalt, J., Müller, P. J., and Schneider, R. (1998a). Project takes a new look at past sea surface temperatures. *Eos Transactions of the AGU* **79,** 393-394.

Rosell-Melé, A., Bard, E., Emeis, K.-C., Grieger, B., Hewitt, C., Müller, P. J., and Schneider, R. R. (2004). Sea surface temperature anomalies in the oceans at the LGM estimated from the alkenone-U^K_{37}' index: comparison with GCMs. *Geophysical Research Letters* **31,** L03208.

Rosell-Melé, A., Bard, E., Emeis, K.-C., Grimalt, J. O., Müller, P. J., Schneider, R. R., Bouloubassi, I., Epstein, B., Fahl, K., Fluegge, A., Freeman, K., Goñi, M., Güntner, U., Hartz, D., Hellebust, S., Herbert, T. D., Ikehara, M., Ishiwatari, R., Kawamura, K., Kenig, F., de Leeuw, J. W., Lehman, S., Mejanelle, L., Ohkouchi, N., Pancost, R. D., Pelejero, C., Prahl, F. G., Quinn, J., Rontani, J.-F., Rostek, F., Rullkötter, J., Sachs, J., Blanz, T., Sawada, K., Schulz-Bull, D., Sikes, E., Sonzogni, C., Ternois, Y., Versteegh, G. J. M., Volkman, J. K., and Wakeham, S. G. (2000). Precision of the current methods to measure the alkenone proxy U^K_{37}' and absolute alkenone abundance in sediments: Results of an interlaboratory comparison study. *Geochemistry, Geophysics, Geosystems* **6,** 2000GC000141.

Rosell-Melé, A., Carter, J. F., Parry, A. T., and Eglinton, G. (1995a). Determination of the U^K_{37} Index in Geological Samples. *Analytical Chemistry* **67,** 1283-1289.

Rosell-Melé, A., Carter, J., and Eglinton, G. (1994). Distributions of long-chain alkenones and alkyl alkenoates in marine surface sediments from the North East Atlantic. *Organic Geochemistry* **22,** 501-509.

Rosell-Melé, A., Eglinton, G., Pflaumann, U., and Sarnthein, M. (1995b). Atlantic core-top calibration of the U^K_{37} index as a sea-surface palaeotemperature indicator. *Geochimica et Cosmochimica Acta* **59,** 3099-3107.

Rosell-Melé, A., Jansen, E., and Weinelt, M. (2002). Appraisal of a molecular approach to infer variations in surface ocean freshwater inputs into the North Atlantic during the last glacial. *Global and Planetary Change* **34,** 143-152.

Rosell-Melé, A., Maslin, M. A., Maxwell, J. R., and Schaeffer, P. (1997). Biomarker evidence for "Heinrich" events. *Geochimica et Cosmochimica Acta* **61,** 1671-1678.

Rosell-Melé, A., Weinelt, M., Sarnthein, M., Koc, N., and Jansen, E. (1998). Variability of the Arctic front during the last climatic cycle: application of a novel molecular proxy. *Terra Nova* **10,** 86-89.

Roy, M., Clark, P. U., Raisbeck, G. M., and Yiou, F. (2004). Geochemical constraints on the regolith hypothesis for the middle Pleistocene transition. *Earth and Planetary Science Letters* **227**, 281-296.

Ruddiman, W. F. (2003). Orbital insolation, ice volume, and greenhouse gases. Quaternary Science Reviews 22, 1597-1629.

Ruddiman, W. F., and Kutzbach, J. E. (1989). Forcing of Late Cenozoic Northern Hemisphere Climate by Plateau Uplift in Southern Asia and the American West. *Journal of Geophysical Research* **94**, 18409-18427.

Ruddiman, W. F., and McIntyre, A. (1979). Warmth of the subpolar North Atlantic Ocean during Northern Hemisphere ice-sheet growth. *Science* **204**, 173-175.

Ruddiman, W. F., and McIntyre, A. (1981). Oceanic mechanisms for amplifcation of the 23,000-year ice-volume cycle. *Science* **212**, 617-627.

Ruddiman, W. F., and McIntyre, A. (1981). The North Atlantic ocean during the last deglaciation. *Palaeogeography, Palaeoclimatology, Palaeoecology* **35**, 145-214.

Ruddiman, W. F., McIntyre, A., and Raymo, M. E. (1986). Paleoenvironmental Results from North Atlantic Sites 607 and 609. *In* "Initial Reports, DSDP 94." (W. F. Ruddiman, R. B. Kidd, E. Thomas, and etal, Eds.), pp. 855-878. U.S. Govt. Printing Office, Washington.

Ruddiman, W. F., McIntyre, A., Niebler-Hunt, V., and Durazzi, J. T. (1980). Ocean evidence for the mechanism of rapid northern hemisphere glaciation. *Quaternary Research* **13**, 33-64.

Ruddiman, W. F., Raymo, M. E., and McIntyre, A. (1986). Matuyama 41,000-year cycles: North Atlantic Ocean and northern hemisphere ice sheets. *Earth and Planetary Science Letters* **80**, 117-129.

Rühlemann, C., Mulitza, S., Müller, P. J., Wefer, G., and Zahn, R. (1999). Warming of the tropical Atlantic Ocean and slowdown of thermohaline circulation during the last deglaciation. *Nature* **402**, 511-514.

Rutherford, S., and D'Hondt, S. (2000). Early onset and tropical forcing of 100,000-year Pleistocene glacial cycles. *Nature* **408**, 72-75.

Sachs, J. P., and Anderson, R. F. (2003). Fidelity of alkenone paleotemperatures in southern Cape Basin sediment drifts. *Paleoceanography* **18**, 1082.

Sancetta, C., and Silvestri, S. (1986). Pliocene-Pleistocene evolution of the North Pacific ocean-atmosphere system, interpreted from fossil diatoms. *Paleoceanography* **1**, 163-180.

Sarnthein, M., Jansen, E., Weinelt, M., Arnold, M., Duplessy, J.-C., Erlenkeuser, H., FlatØy, A., Johannessen, G., Johannessen, T., Jung, S., Koc, N., Labeyrie, L., Maslin, M., Pflaumann, U., and Schulz, H. (1995). Variations in Atlantic surface ocean paleoceanography, 50°-80°N: A time-slice record of the last 30,000 years. *Paleoceanography* **10**, 1063-1094.

Sarnthein, M., Winn, K., Duplessy, J.-C., and Fontugne, M. R. (1988). Global variations of surface ocean productivity in low and mid latitudes: Influence on CO_2 reservoirs of the deep-ocean and atmosphere during the last 21,000 years. *Paleoceanography* **3,** 361-399.

Sato, T., and Takayama, T. (1992). A Stratigraphically Significant New Species of the Calcareous Nannofossil *Reticulofenestra asanoi. In* "Centenary of Japanese Micropaleontology." (T. Sato, Ed.), pp. 457-460.

Sawada, K., Handa, N., Shiraiwa, Y., Danbara, A., and Montani, S. (1996). Long-chain alkenones and alkyl alkenoates in the coastal and pelagic sediments of the northwest North Pacific, with special reference to the reconstruction of Emiliania huxleyi and gephyrocapsa oceanica ratios. *Organic Geochemistry* **24,** 751-764.

Schefuß, E. (2003). "Paleo-environmental effects of the Mid-Pleistocene Transition in the tropical Atlantic and equatorial Africa." Universiteit Utrecht.

Schefuß, E., Schouten, S., Jansen, J. H. F., and Sinninghe Damsté, J. S. (2003). African vegetation controlled by tropical sea surface temperatures in the mid-Pleistocene period. *Nature* **422,** 416-421.

Schmieder, F., von Dobeneck, T., and Bleil, U. (2000). The Mid-Pleistocene climate transition as documented in the deep South Atlantic Ocean: Initiation, interim state, and terminal event. *Earth and Planetary Science Letters* **179,** 539-549.

Schmitz, W. J., and McCartney, M. S. (1993). On the North Atlantic Circulation. *Reviews of Geophysics* **31,** 29-49.

Schneider, R. (2001). Alkenone temperature and carbon isotope records: Temporal resolution, offsets, and regionality. *Geochemistry Geophysics Geosystems* **2,** art. no.-2000GC000060.

Schneider, R. R., and Müller, P. J. (1995). What Role Has Upwelling Played in the Global Carbon and Climatic Cycles on a Million-Year Time Scale? *In* "Upwelling in the Ocean: Modern Processes and Ancient Records." (C. P. Summerhayes, K.-C. Emeis, M. V. Angel, R. L. Smith, and B. Zeitschel, Eds.), pp. 361-380. John Wiley.

Schulz, H. M., Schoner, A., and Emeis, K. C. (2000). Long-chain alkenone patterns in the Baltic Sea - an ocean- freshwater transition. *Geochimica et Cosmochimica Acta* **64,** 469-477.

Schulz, M., and Stattegger, K. (1997). SPECTRUM: Spectral Analysis of Unevenly Spaced Paleoclimate Time Series. *Computers and Geosciences* **23,** 929-945.

Segar, D.A. (1998). Introduction to Ocean Sciences. *Wadsworth.*

Sejrup, H. P., Larsen, E., Landvik, J., King, E. L., Haflidason, H., and Nesje, A. (2000). Quaternary glaciations in southern Fennoscandia: evidence from southwestern Norward and the northern North Sea region. *Quaternary Science Reviews* **19,** 667-685.

Shackleton, N. J. (2000). The 100,000-Year Ice-Age Cycle Identified and Found to Lag Temperature, Carbon Dioxide, and Orbital Eccentricity. *Science* **289,** 1897-1902.

Shackleton, N. J., and Opdyke, N. D. (1976). Oxygen isotope and paleomagnetic stratigraphy of Pacific core V28-239. Late Pliocene to Latest Pleistocene. *Geological Society of America Memoir* **145,** 449-464.

Shackleton, N. J., Berger, A., and Peltier, W. R. (1990). An alternative astronomical calibration of the lower Pleistocene timescale based on ODP Site 677. *Transactions of the Royal Society of Edinburgh, Earth Sciences* **81,** 251-261.

Shaffer, G. (1993). Effects of the marine biota on global carbon cycling. *In* "The Global Carbon Cycle." (M. Heimann, Ed.), pp. 431-456. NATO ASI Series I: Global Environmental Change. Springer-Verlag.

Shankle, A. M., Goericke, R., Franks, P. J. S., and Levin, L. A. (2002). Chlorin distribution and degradation in sediments within and below the Arabian Sea oxygen minimum zone. *Deep-Sea Research I* **49,** 953-969.

Shannon, L. V. (1985). The Benguela ecosystems: Part I. Evolution of the Benguela, physical features and processesq. *Annual Review of Oceanography and Marine Biology* **23,** 105-182.

Shannon, L. V., Lutjeharms, J. R. E., and Agenbag, J. J. (1989). Episodic input of Subantarctic water into the Benguela region. *South African Journal of Marine Science* **8,** 317-322.

Sicre, M. A., Bard, E., Ezat, U., and Rostek, F. (2002). Alkenone distributions in the North Atlantic and Nordic sea surface waters. *Geochemistry Geophysics Geosystems* **3,** art. no.-1013.

Siegenthaler, U. (1993). Modelling the present day oceanic carbon cycle. *In* "The Gloabl Carbon Cycle." (M. Heimann, Ed.), pp. 367-396. NATO ASI Series I: Global Environmental Change. Springer-Verlag.

Sigman, D. M., Jaccard, S. L., and Haug, G. H. (2004). Polar ocean stratification in a cold climate. *Nature* **428,** 59-62.

Sikes, E. L., and Sicre, M. A. (2002). Relationship of the tetra-unsaturated C_{37} alkenone to salinity and temperature: Implications for paleoproxy applications. *Geochemistry Geophysics Geosystems* **3,** art. no.-1063.

Sikes, E. L., Volkman, J. K., Robertson, L. G., and Pichon, J. J. (1997). Alkenones and alkenes in surface waters and sediments of the Southern Ocean: Implications for paleotemperature estimation in polar regions. *Geochimica Et Cosmochimica Acta* **61,** 1495-1505.

Sikes, N. E. (1999). Plio-Pleistocene Floral Context and Habitat Preferences of Sympatric Hominid Species in East Africa. *In* "African Biogeography, Climate Change, and Human Evolution." (T. G. Bromage, and F. Schrenk, Eds.), pp. 301-315. Oxford University Press.

Singer, B. S., Ackert, R. P. J., and Guillou, H. (2004). ^{40}Ar/^{39}Ar chronology of Pleistocene glaciations in Patagonia. *GSA Bulletin* **116,** 434-450.

Smith, L. M., Miller, G. H., Otto-Bliesner, B., and Shin, S.-I. (2003). Sensitivity of the Northern Hemisphere climate system to extreme changes in Holocene Arctic sea-ice. *Quaternary Science Reviews* **22,** 645-658.

Sonzogni, C., Bard, E., Rostek, F., Dollfus, D., Rosell-Melé, A., and Eglinton, G. (1997). Temperature and salinity effects on alkenone ratios measured in surface sediments from the Indian Ocean. *Quaternary Research* **47,** 344-355.

St John, K. E., and Krissek, L. A. (2002). The late Miocene to Pleistocene ice-rafting history of southest Greenland. *Boreas* **31,** 28-35.

St. John, K. E. K., and Krissek, L. A. (1999). Regional patterns of Pleistocene ice-rafted debris flux in the North Pacific. *Paleoceanography* **14,** 653-662.

Stauffer, B., Blunier, T., Dällenbach, A., Indermühle, A., Schwander, J., Stocker, T. F., Tschumi, J., Chappellaz, J., Raynaud, D., Hammer, C. U., and Clausen, H. B. (1998). Atmospheric CO2 concentration and millenial-scale climate change during the last glacial period. *Nature* **392,** 59-62.

Stephens, B. B., and Keeling, R. F. (2000). The influence of Antarctic sea ice on glacial-interglacial CO_2 variations. *Nature* **404,** 171-174.

Stocker, T. F. (1998). The Seesaw Effect. *Science* **282,** 61-62.

Stocker, T. F. (2000). Past and future reorganizations in the climate system. *Quaternary Science Reviews* **19,** 301-319.

Stoll, H. M., Ziveri, P., Geisen, M., Probert, I., and Young, J. R. (2002). Potential and limitations of Sr/Ca ratios in coccolith carbonate: new perspectives from cultures and monospecific samples from sediments. *Philosophical Transactions of the Royal Society of London A* **360,** 719-747.

Stott, L., Poulsen, C., Lund, S., and Thunell, R. (2002). Super ENSO and Global Climate Oscillations at Millennial Time Scales. *Science* **297,** 222-226.

Summerhayes, C. P., Kroon, D., Rosell-Melé, A., Jordan, R. W., Schrader, H.-J., Hearn, R., Villanueva, J., Grimalt, J. O., and Eglinton, G. (1995). Variability in the Benguela Current upwelling system over the past 70,000 years. *Progress in Oceanography* **35,** 207-251.

Swift, J. (1986). The Arctic Waters. *In* "The Nordic Seas." (B. G. Hurdle, Ed.), pp. 129-151. Springer, New York.

Teece, M. A., Getliff, J. M., Leftley, J. W., Parkes, R. J., and Maxwell, J. R. (1998). Microbial degradation of the marine prymnesiophyte *Emiliania huxleyi* under oxic and anoxic conditions as a model for early diagenesis: long chain alkadienes, alkenones and alkyl alkenoates. *Organic Geochemistry* **29,** 863-880.

Ternois, Y., Sicre, M. A., Boireau, A., Conte, M. H., and Eglinton, G. (1997). Evaluation of long-chain alkenones as paleo-temperature indicators in the Mediterranean Sea. *Deep-Sea Research I* **44,** 271-286.

Thierstein, H. R., Geitzenauer, K. R., and Molfino, B. (1977). Global synchroneity of late Quaternary coccolith datum levels: Validation by oxygen isotopes. *Geology* **5,** 400-404.

Tian, J., Wang, P., Cheng, X., and Li, Q. (2002). Astronomically tuned Plio-Pleistocene benthic $\delta^{18}O$ record from the South China Sea and Atlantic-Pacific comparison. *Earth and Planetary Science Letters* **203,** 1015-1029.

Toggweiler, J. R., Dixon, K., and Broecker, W. (1991). The Peru upwelling and th ventilation of the South Pacific thermocline. *Journal of Geophysical Research* **96,** 20467-20497.

Trenberth, K. E., Branstator, G. W., Karoly, D., Kumar, A., Lau, N.-C., and Ropelewski, C. (1998). Progress during TOGA in understanding and modeling global teleconnections associated with tropical sea surface temperatures. *Journal of Geophysical Research* **103,** 14291-14324.

Tudhope, A. W., Chilcott, C. P., McCulloch, M. T., Cook, E. R., Chappell, J., Ellam, R. M., Lea, D. W., Lough, J. M., and Shimmield, G. B. (2001). Variability in the El Nino - Southern oscillation through a glacial-interglacial cycle. *Science* **291,** 1511-1517.

Turney, C. S. M., Kershaw, A. P., Clemens, S. C., Branch, N., Moss, P. T., and Fifield, L. K. (2004). Millennial and orbital variations of El Nino/Southern Oscillation and high-latitude climate in the last glacial period. *Science* **428,** 306-310.

Tziperman, E., and Gildor, H. (2003). On the mid-Pleistocene transition to 100-ky glacial cycles and the asymmetry between glaciation and deglaciation times. *Paleoceanography* **18,** 1-8.

Van Der Burgh, J., Visscher, H., Dilcher, D. L., and Kürschner, W. M. (1993). Paleoatmospheric signatures in Neogene fossil leaves. *Science* **260,** 1788-1790.

Venz, K. A., Hodell, D. A., Stanton, C., and Warnke, D. A. (1999). A 1.0 Myr record of Glacial North Atlantic Intermediate Water variability from ODP site 982 in the northeast Atlantic. *Paleoceanography* **14,** 42-52.

Villanueva, J., and Grimalt, J. O. (1996). Pitfalls in the chromatographic determination of the alkenone U^{K}_{37} index for paleotemperature estimation. *Journal of Chromatography A* **723,** 285-291.

Villanueva, J., Flores, J. A., and Grimalt, J. O. (2002). A detailed comparison of the U^{K}_{37}' and coccolith records over the past 290 years: implications to the alkenone paleotemperature method. *Organic Geochemistry* **33,** 897-905.

Villanueva, J., Grimalt, J. O., Labeyrie, L. D., Cortijo, E., Vidal, L., and Louis-Turon, J. (1998). Precessional forcing of productivity in the North Atlantic Ocean. *Paleoceanography* **13,** 561-571.

Visser, K., Thunell, R., and Stott, L. (2003). Magnitude and timing of temperature change in the Indo-Pacific warm pool during deglaciation. *Nature* **421,** 152-155.

Volkman, J. K., Barrett, S. M., Blackburn, S. I., and Sikes, E. L. (1995). Alkenones in *Gephyrocapsa oceanica*: Implications for studies of paleoclimate. *Geochimica et Cosmochimica Acta* **59,** 513-520.

Volkman, J. K., Eglinton, G., Corner, E. D. S., and Sargent, J. R. (1980). Novel unsaturated straight-chain C37-C39 methyl and ethyl ketones in marine sediments and coccolithophore Emiliana huxleyi. *In* "Advances in Organic Geochemistry 1979." (A. G. Douglas, and J. R. Maxwell, Eds.), pp. 219-227. Pergamon, Oxford.

Vrba, E. S., Denton, G. H., Partridge, T. C., and Burckle, L. H. (1995). Paleoclimate and Evolution: with Emphasis on Human Origins. Yale University Press.

Wang, B., Clemens, S. C., and Lui, P. (2003). Contrasting the Indian and East Asian monsoons: implications on geologic timescales. *Marine Geology* **201,** 5-21.

Wang, F. B., and Li, B. Y. (1985). The lower boundary of the Quaternary in the Himalaya region in China. *In* "Quaternary Geology and Environment of China." (T. S. Liu, Ed.), pp. 18-26. China Ocean Press, Beijing.

Wang, H., and McCave, I. N. (1990). Distinguishing climatic and current effects in mid-Pleistocene sediments of Hatton and Gardar Drifts, NE Atlantic. *Journal of the Geological Society of London* **147,** 373-383.

Wang, R., and Zhao, Q. (2000). Abrupt variations of the radiolarian fauna at Mid-Pleistocene climate transition in the South China Sea. *Chinese Science Bulletin* **45,** 952-955.

Wang, R., Clemens, S. C., Huang, B., and Chen, M. (2003b). Quaternary palaeoceanographic changes in the northern South China Sea (ODP Site 1146): radiolarian evidence. *Journal of Quaternary Science* **18,** 745-756.

Watson, A. J., Bakker, D. C. E., Ridgwell, A. J., Boyd, P. W., and Law, C. S. (2000). Effect of iron supply on Southern Ocean CO_2 uptake and implications for glacial atmospheric CO_2. *Nature* **407,** 730-733.

Weaver, A. J., Bitz, C. M., Fanning, A. F., and Holland, M. M. (1999a). Thermohaline Circulation: High-Latitude Phenomena and the Difference Between the Pacific and Atlantic. *Annual Review of Earth and Planetary Sciences* **27,** 231-285.

Weaver, P. P. E. (1993). High resolution stratigraphy of marine Quaternary sequences. *In* "High Resolution Stratigraphy." (R. B. Kidd, Ed.), pp. 137-153. Geological Society Special Publication No 70.

Weaver, P. P. E., Chapman, M. R., Eglinton, G., Zhao, M., Rutledge, D., and Read, G. (1999b). Combined coccolith, foraminiferal, and biomarker reconstruction of paleoceanographic conditions over the last 120 kyr in the northern North Atlantic (59°, 23°W). *Paleoceanography* **14,** 336-349.

Wefer, G., Berger, W. H., and Richter, C. (2001). "Proceedings of the Ocean Drilling Program, Scientific Results, 175." College Station, TX (Ocean Drilling Program).

Wefer, G., Berger, W. H., Bickert, T., Donner, B., Fischer, G., Kemle-v Mücke, S., Meinecke, G., Müller, P. J., Mulitza, S., Niebler, H.-S., Patzold, J., Schmidt, H., Schneider, R. R., and Segl, M. (1996). Late Quaternary Surface Circulation of the South Atlantic: The Stable Isotope Record and Implications for Heat Transport and Productivity. *In* "The South Atlantic: Present and Past Circulation." (G. Wefer, W. H. Berger, G. Siedler, and D. Webb, Eds.), pp. 363-410. Springer, Berlin.

Wefer, G., Berger, W. H., Bijma, J., and Fischer, G. (1999). Clues to Ocean History: a Brief Overview of Proxies. *In* "Use of Proxies in Paleoceanography: Examples from the South Atlantic." (G. Wefer, Ed.), pp. 1-68. Springer-Verlag, Berlin Heidelberg.

Wefer, G., Berger, W. H., Richter, C., and Shipboard Scientific Party. (1998). Site 1087. *In* "Proceedings of the Ocean Drilling Program, Initial Reports 175." (G. Wefer, W. H. Berger, C. Richter, and Shipboard Scientific Party, Eds.), pp. 457-484.

Westerhausen, L., Sarnthein, M., Struck, U., Erlenkeuser, H., and Poynter, J. (1994). PCO_2 variations of equatorial surface water over the last 330,000 years: the $\delta^{13}C$ record of organic carbon. *In* "Carbon Cycling in the Glacial Ocean." (R. e. a. Zahn, Ed.), pp. 367-384. NATO ASI Series.

Wilson, R. C. L., Drury, S. A., and Chapman, J. L. (2000). "The Great Ice Age: Climate Change and Life." Routledge, London.

Wright, A. K., and Flower, B. P. (2002). Surface and deep ocean circulation in the subpolar North Atlantic during the mid-Pleistocene revolution. *Paleoceanography* **17,** 1068.

Wu, X. H., and An, Z. S. (1996). Loess–paleosol sequence on Loess Plateau and uplift of the Qinghai–Xizang Plateau. *Sci. Chin.(Ser. D).* **39,** 121–133.

Wyrtki, K. (1965). Oceanography of the eastern equatorial Pacific Ocean. *Oceanography and Marine Biology* **4,** 33-68.

Wyrtki, K. (1981). An estimate of equatorial upwelling in the Pacific. *J.Phys.Res.* **11,** 1205-1214.

Xiao, J., and An, Z. (1999). Three large shifts in East Asian monsoon circulation indicated by loess-paleosol sequences in China and late Cenozoic deposits in Japan. *Palaeogeography, Palaeoclimatology, Palaeoecology* **154,** 179-189.

Yamamoto, M., Shiraiwa, Y., and Inouye, I. (2000). Physiological responses of lipids in *Emiliania huxleyi* and *Gephyrocapsa oceanica* (Haptophyceae) to growth status and their implications for alkenone paleothermometry. *Organic Geochemistry* **31,** 799-811.

Yan, X.-H., Ho, C.-R., Zheng, Q., and Klemas, V. (1992). Temperature and size variabilities of the Western Pacific warm pool. *Science* **258,** 1643-1645.

Zhao, M., Eglinton, G., Haslett, S. K., Jordan, R. W., Sarnthein, M., and Zhang, Z. (2000). Marine and terrestrial biomarker records for the last 35,000 years at ODP site 658C off NW Africa. Organic Geochemistry 31, 919-930.

Appendices

A1: Results from ODP 983. ODP labelling is Site-Core-Section, depth interval (cm). All other terms defined in Chapters 1 and 2.

A2: Results from ODP 1087 Site A. ODP labelling is Core-Section, depth interval (cm). All other terms defined in Chapters 1 and 2.

A3: Biomarker indices from ODP 1087 Site A (Chapter 4). ODP labelling is Core-Section, depth interval (cm). All other terms defined in Chapters 2 and 4.

A4: Coccolith results from ODP 1087 Site A (Chapter 4). ODP labelling is Core-Section, depth interval (cm). All other terms defined in Chapters 2 and 4.

A5: Results from ODP 849. ODP labelling is Site-Core-Section, depth interval (cm). All other terms defined in Chapters 1 and 2.

A6: Results from ODP 806 Site B. ODP labelling is Site-Core-Section, depth interval (cm). All other terms defined in Chapters 1 and 2. The samples from ODP 805 Site C used to bridge a coring gap are also shown (as discussed in Chapters 1 and 2), with labelling Site-Core-Section, depth interval (cm). U^{K}_{37}' and SST values are shown only for those samples where the $C_{37:3}$ alkenone could be detected.

A1: Results from ODP 983. ODP labelling is Site-Core-Section, depth interval (cm). All other terms defined in Chapters 1 and 2.

ODP 983	**Depth**	**Age**	**Bulk MAR**	**P410**	**AR P410**	**P665**	**AR P665**	**S/I**	**K37**	**MAR K37**	**U^{K}_{37}**	**U^{K}_{37}'**		**SST**	**C37:4**
ODP Sample Label	(Mcd)	(ka)	(g/cm^2/kyr)	(AU/g)	(AU/cm^2/kyr)	(AU/g)	(AU/cm^2/kyr)		(ng/g)	(µg/cm^2/kyr)		(CIMS *)		(°C)	(%K37)
C-6H-6W, 36-37	57.69	493.98	8.876	39.97	354.75	2.37	21.02	16.88	1092.69	9.70	0.056	0.290		0.3	18.2
C-6H-6W,116-117	58.49	500.41	6.901	106.24	733.12	15.35	105.93	6.92	520.79	3.59	0.483	0.498	*	13.3	1.0
C-6H-7W, 48-49	59.28	506.78	6.886						257.10	1.77	0.271	0.300	*	6.9	2.3
B-7H-2W,136-137	60.07	512.66	7.455	125.19	933.29	21.00	156.57	5.96	590.64	4.40	0.236	0.311		5.8	5.7
C-7H-1W,32-33	60.86	518.52	7.479	188.41	1409.11	37.97	284.00	4.96	468.09	3.50	0.525	0.530	*	14.6	0.3
C-7H-1W,112-113	61.65	524.38	7.468	142.31	1062.75	20.01	149.41	7.11	678.42	5.07	0.306	0.402		7.9	6.9
C-7H-2W, 24-25	62.29	529.79	6.573	14.10	92.66	0.35	2.32	39.94	203.55	1.34	0.311	0.387		8.1	5.5
C-7H-2W,88-89	62.92	532.83	11.477	92.26	1058.84	5.77	66.20	15.99	531.95	6.11	0.217	0.288	*	5.2	5.5
C-7H-3W,0-1	63.55	535.87	11.518	180.54	2079.51	10.93	125.91	16.52	343.20	3.95	0.277	0.313	*	7.1	2.7
C-7H-3W,64-65	64.19	538.95	11.522	98.31	1132.75	17.08	196.76	5.76	489.78	5.64	0.262	0.342		6.6	6.0
C-7H-3W, 123-129	64.82	541.98	11.522						595.24	6.86	0.072	0.257	*	0.9	14.7
C-7H-4W,40-41	65.45	545.00	11.560	41.58	480.67	4.87	56.32	8.54	479.05	5.54	0.283	0.376		7.2	6.7
C-7H-4W, 104-105	66.09	546.37	25.980	11.89	309.01	1.29	33.55	9.21	189.65	4.93	0.240	0.300		5.9	4.6
C-7H-5W,80-81	67.35	563.82	4.007	29.14	116.77	3.89	15.58	7.49	346.28	1.39	0.370	0.404	*	9.9	2.4
C-7H-5W,144-145	67.99	570.28	5.493	35.05	192.52	2.93	16.11	11.95	337.57	1.85	0.417	0.434	*	11.3	1.2
C-7H-6W, 56-57	68.62	574.80	7.732	36.23	280.11	4.88	37.76	7.42	332.55	2.57	0.390	0.413	*	10.5	1.6
C-7H-6W,120-121	69.26	581.02	5.710	158.93	907.46	12.70	72.52	12.51	193.11	1.10	0.335	0.374		8.8	2.9
C-7H-7W,36-37	69.90	588.23	4.923	59.85	294.64	4.85	23.88	12.34	252.32	1.24	0.340	0.351		9.0	0.9
C-7H-CCW,28-29	70.53	595.32	4.931	20.16	99.38	0.85	4.20	23.69	111.66	0.55	0.442	0.442		12.0	0.0
B-8H-3W,44-45	71.27	602.97	5.369	21.10	113.29	1.75	9.38	12.07	270.59	1.45	0.348	0.351	*	9.2	0.2
C-8H-1W,60-61	71.80	607.23	6.888	75.08	517.21	9.63	66.32	7.80	266.12	1.83	0.402	0.422		10.8	1.5
C-8H-1W, 124-125	72.44	610.27	11.692	77.33	904.13	14.99	175.21	5.16	413.41	4.83	0.395	0.399		10.6	0.3
C-8H-2W,56-57	73.27	613.15	15.988	104.75	1674.73	15.01	239.92	6.98	418.58	6.69	0.314	0.334		8.2	1.5
C-8H-2W,140-141	74.11	615.40	20.711	23.02	476.74	0.62	12.90	36.95	50.99	1.06	0.372	0.372		9.9	0.0
C-8H-3W,72-73	74.94	632.00	2.774	62.83	174.27	3.70	10.27	16.96	77.64	0.22	0.175	0.371		4.0	14.3
C-8H-3W, 128-129	75.48	635.57	8.384						92.94	0.78	0.342	0.440	*	9.0	6.8
C-8H-4W, 32-33	76.03	640.36	6.370	40.15	255.74	1.01	6.45	39.64	0.00	0.00	0.316	0.444		8.2	8.9
C-8H-4W, 88-89	76.57	645.06	6.378	25.90	165.17	0.67	4.25	38.86	65.24	0.42	0.319	0.364		8.3	3.3

ODP 983 ODP Sample Label	Depth (Mcd)	Age (ka)	Bulk MAR (g/cm^2/kyr)	P410 (AU/g)	AR P410 (AU/cm^2/kyr)	P665 (AU/g)	AR P665 (AU/cm^2/kyr)	S/I	K37 (ng/g)	MAR K37 (μg/cm^2/kyr)	U^{K}_{37}	U^{K}_{37}' (CIMS *)		SST (°C)	C37:4 (%K37)
C-8H-4W,140-141	77.12	649.86	6.362	145.34	924.62	11.81	75.16	12.30	107.91	0.69	0.292	0.402		7.5	7.8
C-8H-5W,44-45	77.66	654.55	6.379	13.95	88.97	0.18	1.13	78.66	95.98	0.61	0.426	0.442	*	11.6	1.1
C-8H-5W,100-101	78.20	659.25	6.371	74.97	477.64	3.33	21.20	22.53	105.84	0.67	0.306	0.387		7.9	5.8
C-8H-6W, 4-5	78.74	663.96	6.366	19.34	123.10	0.54	3.45	35.65	181.12	1.15	0.307	0.377		8.0	5.1
C-8H-6W,56-57	79.29	668.72	6.384	24.73	157.85	1.14	7.25	21.77	0.00	0.00	0.208	0.350		5.0	10.6
C-8H-6W,112-113	79.83	673.60	6.164	135.78	836.93	13.53	83.39	10.04	365.61	2.25	0.236	0.236		5.8	0.0
C-8H-7W,16-17	80.38	678.55	6.164	70.12	432.25	10.09	62.17	6.95	295.88	1.82	0.234	0.352		5.7	8.8
C-8H-CCW,8-9	80.92	682.95	6.813	34.43	234.53	3.71	25.30	9.27	338.74	2.31	0.369	0.388	*	9.9	1.3
B-9H-3W,8-9	81.46	688.38	5.514	44.70	246.51	7.11	39.20	6.29	1402.29	7.73	0.298	0.350		7.7	3.8
C-9H-1W, 16-17	82.01	691.68	9.246	24.34	225.07	3.24	29.93	7.52	1182.53	10.93	0.272	0.329		6.9	4.3
C-9H-1W,72-73	82.57	695.04	9.246	27.84	257.40	6.47	59.85	4.30	813.92	7.53	0.415	0.426		11.2	0.8
C-9H-1W,132-133	83.14	698.46	9.246	73.66	681.02	12.08	111.70	6.10	588.77	5.44	0.426	0.439	*	11.6	0.9
C-9H-2W,36-37	83.71	701.88	9.246	56.26	520.16	7.59	70.19	7.41	394.16	3.64	0.480	0.491	*	13.2	0.7
C-9H-2W, 96-97	84.29	705.15	9.840	65.49	644.41	11.68	114.97	5.61	499.49	4.91	0.307	0.346		8.0	2.9
C-9H-3W,45-46	85.34	721.04	3.666	21.70	79.55	1.32	4.82	16.50	118.66	0.43	0.293	0.359		7.5	4.9
C-9H-3W,100-101	85.86	727.83	4.249	39.24	166.70	4.53	19.23	8.67	152.97	0.65	0.304	0.396		7.9	6.6
C-9H-4W, 4-5	86.40	734.87	4.255						575.59	2.45	0.232	0.351		5.7	8.8
C-9H-4W,45-46	86.84	740.61	4.253	43.47	184.84	3.49	14.85	12.45	278.27	1.18	0.417	0.481		11.3	4.3
C-9H-4W,68-69	87.04	743.22	4.251	98.10	417.01	13.53	57.51	7.25	349.41	1.49	0.438	0.458	*	11.9	1.4
C-9H-4W,92-93	87.28	746.35	4.254	143.19	609.08	19.10	81.23	7.50	230.36	0.98	0.352	0.433		9.3	5.6
C-9H-4W, 116-117	87.52	749.48	4.254	31.77	135.13	0.48	2.03	66.66	91.69	0.39	0.185	0.338		4.3	11.5
C-9H-5W,32-33	88.18	754.16	7.824	58.70	459.23	1.97	15.42	29.78	124.03	0.97	0.378	0.425		10.1	3.3
B-10H-1W,12-13	88.90	758.99	8.270	25.09	207.52	1.06	8.79	23.61	114.95	0.95	0.555	0.555		15.5	0.0
C-9H-6W,28-29	89.62	763.82	8.270	25.76	212.99	2.09	17.28	12.33	161.56	1.34	0.474	0.492	*	13.0	1.2
B-10H-2W, 4-5	90.33	768.58	8.275	45.29	374.79	4.51	37.32	10.04	428.38	3.54	0.448	0.456	*	12.2	0.5
B-10H-2W,74-75	91.03	773.27	8.280	34.21	283.27	5.91	48.96	5.79	217.17	1.80	0.263	0.347		6.6	6.2
B-10H-2W,144-145	91.73	777.98	8.254	104.25	860.42	17.54	144.76	5.94	572.73	4.73					
B-10H-3W,64-65	92.43	782.36	8.856	279.47	2474.97	54.81	485.38	5.10	736.98	6.53	0.341	0.387		9.0	3.3
C-10H-2W,62-63	93.15	789.18	5.857	35.04	205.19	0.76	4.46	46.00		0.00					
C-10H-2W,97-98	93.50	796.08	2.814	52.30	147.16	1.13	3.19	46.08	124.10	0.35	0.096	0.346		1.6	18.6

ODP 983 ODP Sample Label	Depth (Mcd)	Age (ka)	Bulk MAR (g/cm^2/kyr)	P410 (AU/g)	AR P410 (AU/cm^2/kyr)	P665 (AU/g)	AR P665 (AU/cm^2/kyr)	S/I	K37 (ng/g)	MAR K37 (µg/cm^2/kyr)	U^K_{37}	U^K_{37}' (CIMS *)	SST (°C)	C37:4 (%K37)
C-10H-2W-137-138	93.90	799.73	6.080						128.20	0.78	0.105	0.324	1.9	16.5
C-10H-3W,17-18	94.20	801.80	8.040	54.88	441.23	3.90	31.39	14.06	130.30	1.05	0.323	0.371	8.4	3.5
C-10H-3W, 52-53	94.55	804.21	8.057						397.64	3.20	0.174	0.321	3.9	11.1
C-10H-3W,112-113	95.15	808.36	8.030	22.11	177.55	1.34	10.76	16.50	93.91	0.75	0.367	0.395 *	9.8	2.0
C-10H-4W, 34-35	95.90	813.53	8.040	34.04	273.70	5.20	41.82	6.55	387.88	3.12	0.312	0.360	8.1	3.6
C-10H-4W,107-108	96.60	818.36	8.040	10.73	86.26	0.87	6.97	12.38	348.45	2.80	0.308	0.357	8.0	3.6
C-10H-5W,42-43	97.45	824.22	8.047	97.21	782.22	12.37	99.53	7.86	285.71	2.30	0.336	0.495	8.8	10.6
C-10H-5W,117-118	98.20	829.40	8.040	18.51	148.80	1.17	9.37	15.88	0.00	0.00				
C-10H-6W, 52-53	99.05	835.26	8.057						236.07	1.90	0.063	0.310	0.6	18.8
C-10H-6W,130-131	99.85	840.78	8.040	110.29	886.72	18.67	150.09	5.91	505.73	4.07	0.350	0.414	9.3	4.5
B-11H-2W, 20-21	100.65	846.31	8.057						267.14	2.14	0.235	0.354	5.8	8.8
B-11H-2W,107-108	101.49	851.97	8.235	107.33	883.80	19.94	164.20	5.38	708.90	5.84	0.321	0.375	8.4	4.0
B-11H-3W, 43-44	102.35	859.04	6.747						608.48	4.11	0.398	0.398	10.7	0.0
B-11H-3W,113-114	103.05	867.60	4.537	24.83	112.63	1.09	4.96	22.73	68.03	0.31	0.344	0.364	9.1	1.4
B-11H-3W 143-144	103.35	873.29	2.923							0.00				
C-11H-2W,34-35	103.59	877.85	2.922	23.71	69.30	0.48	1.41	49.02	33.44	0.10	0.279	0.465	7.1	12.7
C-11H-2W,64-65	103.89	882.70	3.435	16.01	54.98	0.25	0.85	64.73		0.00				
B-11H-4W,75-76	104.19	887.54	3.435	10.03	34.45	0.29	0.98	35.05	39.22	0.13	0.237	0.314	5.8	5.9
C-11H-2W, 120-121	104.44	891.58	3.433	22.93	78.71	1.32	4.54	17.33	211.54	0.73	0.261	0.340	6.6	5.9
B-11H-3W,02-03	104.74	894.92	4.983	104.73	521.83	14.57	72.59	7.19	330.99	1.65				
C-11H-3W,65-66	105.38	898.86	9.003	104.00	936.31	13.40	120.67	7.76	563.99	5.08	0.237	0.337	5.8	7.5
C-11H-3W,135-136	106.08	902.56	10.517	125.40	1318.83	8.58	90.18	14.62	184.54	1.94	0.325	0.356	8.5	2.3
C-11H-4W, 50-51	106.74	909.27	5.453	103.71	565.57	6.04	32.94	17.17	156.22	0.85	0.345	0.379	9.1	2.4
C-11H-4W,110-111	107.34	917.01	4.300	22.61	97.21	0.58	2.49	38.97	64.34	0.28	0.301	0.387	7.8	6.2
C-11H-5W, 20-21	107.94	921.84	6.891	58.23	401.31	7.06	48.65	8.25	466.47	3.21	0.300	0.317 *	7.8	1.3
C-11H-5W,84-85	108.59	927.07	6.895	24.92	171.80	1.40	9.64	17.82	195.09	1.35	0.229	0.334	5.6	7.8
C-11H-5W,144-145	109.19	931.90	6.891	7.65	52.70	0.87	6.02	8.75	201.86	1.39	0.318	0.358 *	8.3	2.9
B-12H-1W,30-31	109.79	936.73	6.891	83.84	577.80	13.52	93.17	6.20	495.92	3.42	0.232	0.343	5.7	8.2
B-12H-1W, 90-91	110.39	941.56	6.891	16.38	112.86	2.98	20.54	5.49	503.28	3.47	0.325	0.394	8.5	4.9
B-12H-2W,0-1	110.99	946.62	6.578	135.06	888.44	18.68	122.86	7.23	1513.36	9.96	0.344	0.408	9.1	4.5

ODP 983	**Depth**	**Age**	**Bulk MAR**	**P410**	**AR P410**	**P665**	**AR P665**	**S/I**	**K37**	**MAR K37**	**U^{K}_{37}**	**U^{K}_{37}'**		**SST**	**C37:4**
ODP Sample Label	(Mcd)	(ka)	(g/cm^2/kyr)	(AU/g)	(AU/cm^2/kyr)	(AU/g)	(AU/cm^2/kyr)		(ng/g)	(μg/cm^2/kyr)		(CIMS *)		(°C)	(%K37)
B-12H-2W,60-61	111.59	950.29	9.070	25.61	232.28	2.27	20.62	11.27	941.67	8.54	0.356	0.416		9.5	4.2
B-12H-2W,124-125	112.24	954.00	9.720	151.81	1475.55	18.42	179.04	8.24	489.18	4.75	0.319	0.409		8.3	6.4
C-12H-1W,72-73	112.95	963.64	4.086	247.83	1012.60	12.01	49.08	20.63	428.76	1.75	0.315	0.382	*	8.2	4.8
C-12H-2W,17-18	113.90	967.43	13.906	92.43	1285.36	9.44	131.24	9.79	730.75	10.16	0.151	0.364		3.3	15.6
C-12H-2W, 107-108	114.80	971.01	13.946						875.24	12.21	0.258	0.371		6.5	8.2
C-12H-3W,52-53	115.75	974.80	5.972	26.67	370.88	2.43	33.75	10.99	392.75	5.46	0.341	0.383		9.0	3.1
C-12H-3W, 142-143	116.65	983.16	9.676						929.62	5.55	0.014	0.334		-0.9	24.0
C-12H-4W,62-63	117.35	988.11	6.556	35.40	277.68	3.01	23.63	11.75	197.33	1.55	0.162	0.354		3.6	14.2
C-12H-4W, 137-138	118.10	990.86	9.673	26.59	402.25	2.24	33.94	11.85	566.64	8.57	0.164	0.347		3.6	13.6
C-12H-5W,57-58	118.80	993.43	10.017	35.06	529.72	4.70	70.95	7.47	697.18	10.53	0.313	0.404		8.2	6.4
C-12H-5W,127-128	119.50	996.00	7.419	27.89	421.47	0.74	11.13	37.88	201.05	3.04	0.323	0.412		8.4	6.3
C-12H-6W,52-53	120.25	1005.00	7.758	59.76	276.26	4.70	21.74	12.70	237.96	1.10	0.393	0.428	*	10.6	2.5
C-12H-6W,122-123	120.95	1010.30	12.808	20.13	147.46	0.90	6.63	22.25	284.84	2.09	0.286	0.389		7.3	7.4
B-13H-2W,50-51	121.71	1014.50	5.392	21.20	212.82	1.42	14.25	14.94	597.95	6.00	0.272	0.374		6.9	7.4
B-13H-2W, 124-125	122.46	1018.80	7.044						156.28	1.51	0.268	0.369	*	6.8	7.4
B-13H-3W,50-51	123.21	1025.20	6.501	24.04	156.30	1.24	8.07	19.37	308.76	2.01	0.306	0.347		7.9	3.1
C-13H-2W,22-23	123.96	1033.00	5.334	23.96	127.83	0.40	2.12	60.19	245.21	1.31	0.296	0.371		7.6	5.5
C-13H-2W,102-103	124.76	1045.00	3.698	387.06	1431.49	12.31	45.54	31.44	548.36	2.03	0.269	0.402		6.8	9.5
C-13H-3W, 37-38	125.61	1051.50	7.255	122.88	891.41	9.79	71.03	12.55	482.20	3.50	0.385	0.433	*	10.3	3.3
C-13H-3W,117-118	126.41	1056.40	9.057	95.05	860.92	8.92	80.78	10.66	398.37	3.61	0.428	0.453	*	11.6	1.7
C-13H-4W,52-53	127.26	1058.38	23.815	63.04	1501.24	6.44	153.30	9.79	306.86	7.31	0.353	0.405	*	9.4	3.7
C-13H-4W,137-138	128.11	1060.50	22.243	18.91	420.52	1.06	23.66	17.77	320.39	7.13	0.344	0.376	*	9.1	2.3
A-13H-4W, 92-93	128.93	1062.40	23.942	95.67	2290.55	16.46	394.17	5.81	1122.57	26.88	0.228	0.351		5.6	9.1
A-13H-5W,80-81	130.33	1065.44	25.548	131.89	3369.58	19.33	493.83	6.82	747.65	19.10	0.344	0.435		9.1	6.4
B-14H-2W,24-25	132.13	1073.40	12.545	27.52	345.23	2.91	36.46	9.47	751.40	9.43	0.367	0.394	*	9.8	1.9
B-14H-2W, 134-140	133.23	1080.25	8.909	46.25	412.04	4.95	44.07	9.35	455.82	4.06	0.534	0.541	*	14.8	0.5
C-14H-2W,10-11	133.95	1084.70	8.976	112.33	1008.22	19.23	172.57	5.84	303.03	2.72	0.451	0.467	*	12.3	1.1
C-14H-2W,80-81	134.65	1089.00	9.031	24.68	222.90	0.86	7.74	28.79	221.52	2.00	0.430	0.447	*	11.7	1.2
C-14H-3W, 2-3	135.35	1093.40	8.826	96.22	849.25	7.52	66.40	12.79	369.28	3.26	0.324	0.419		8.5	6.8
C-14H-3W,70-71	136.05	1097.60	9.246	64.95	600.52	1.34	12.43	48.30	141.10	1.30	0.266	0.364		6.7	7.2

ODP 983	**Depth**	**Age**	**Bulk MAR**	**P410**	**AR P410**	**P665**	**AR P665**	**S/I**	**K37**	**MAR K37**	**U^{K}_{37}**	**$U^{K}_{37}{}'$**		**SST**	**C37:4**
ODP Sample Label	(Mcd)	(ka)	(g/cm^2/kyr)	(AU/g)	(AU/cm^2/kyr)	(AU/g)	(AU/cm^2/kyr)		(ng/g)	(μg/cm^2/kyr)		(CIMS *)		(°C)	(%K37)
C-14H-3W, 134-135	136.70	1103.10	6.556	74.75	490.07	3.93	25.79	19.00	716.77	4.70	0.167	0.290	*	3.7	9.5
C-14H-4W,54-55	137.40	1109.20	6.366	20.45	130.18	0.42	2.70	48.14	407.98	2.60	0.329	0.400		8.6	5.1
C-14H-4W, 120-121	138.05	1114.70	6.556						691.55	4.53	0.334	0.349	*	8.8	1.2
C-14H-5W,34-35	138.70	1120.30	9.673	128.72	828.83	5.13	33.05	25.08	95.90	0.62	0.368	0.368		9.8	0.0
C-14H-5W,104-105	139.40	1125.16	10.017	28.27	226.08	0.51	4.05	55.77	42.07	0.34	0.268	0.294	*	6.8	2.0
C-14H-6W,21-22	140.05	1134.40	7.419	92.14	359.42	8.48	33.09	10.86	244.10	0.95	0.330	0.357		8.7	2.1
C-14H-6W, 90-91	140.75	1143.60	7.758	61.22	258.39	6.43	27.13	9.52	292.18	1.23	0.239	0.248		5.9	0.7
B-15H-1W,70-71	141.37	1147.10	12.808	13.52	132.89	0.52	5.14	25.84	32.08	0.32	0.317	0.317		8.3	0.0
B-15H-1W,140-141	142.07	1151.25	5.392	7.47	69.86	0.15	1.36	51.24	169.53	1.59	0.316	0.351	*	8.3	2.6
C-15H-1W,0-1	142.74	1154.80	7.044	50.10	524.52	3.33	34.84	15.05	475.42	4.98	0.513	0.522	*	14.2	0.6
B-15H-2W, 124-125	143.42	1158.70	9.673						574.87	5.56	0.284	0.365		7.3	5.9
C-15H-1W,134-135	144.09	1162.50	9.781	8.89	86.94	0.42	4.15	20.93	199.74	1.95	0.418	0.418		11.3	0.0
C-15H-2W,50-51	144.74	1166.10	10.017						372.00	3.73	0.350	0.367		9.3	1.2
C-15H-2W,114-115	145.39	1169.80	9.746	19.16	186.72	0.93	9.04	20.65	285.14	2.78	0.444	0.457		12.1	0.9
C-15H-3W, 44-45	146.17	1174.19	9.857	59.71	588.56	4.86	47.89	12.29	340.33	3.35	0.405	0.418		10.9	0.9
C-15H-3W,120-121	146.95	1178.75	9.489	26.19	248.54	1.12	10.60	23.45	217.35	2.06	0.444	0.470		12.1	1.8
C-15H-4W,48-49	147.73	1183.05	10.063	27.14	273.16	2.05	20.63	13.24	266.14	2.68	0.406	0.462		11.0	3.8
C-15H-4W,128-129	148.51	1187.44	9.850	54.51	536.90	4.69	46.18	11.63	277.41	2.73	0.451	0.497		12.3	3.0
C-15H-5W, 56-57	149.29	1191.85	9.825	48.35	475.06	2.77	27.20	17.47	262.58	2.58	0.452	0.452		12.4	0.0
C-15H-5W,132-133	150.06	1196.01	10.263	133.45	1369.53	8.12	83.32	16.44	102.20	1.05	0.365	0.365		9.7	0.0
C-15H-6W,60-61	150.84	1201.47	7.927	182.75	1448.72	10.89	86.35	16.78	183.39	1.45	0.274	0.410		7.0	9.7
C-15H-6W,140-141	151.62	1206.88	8.003	91.70	733.86	4.54	36.34	20.19	90.95	0.73	0.250	0.349		6.2	7.3
C-15H-CCW, 4-5	152.40	1212.31	7.962	103.02	820.17	6.19	49.29	16.64	294.95	2.35	0.511	0.511	*	14.1	0.0
C-16H-1W,52-53	153.18	1217.77	7.925	42.22	334.63	1.36	10.81	30.95	153.60	1.22	0.299	0.309		7.7	0.8
C-16H-1W,132-133	153.96	1223.23	7.925	10.01	79.33	0.32	2.53	31.35	407.14	3.23	0.402	0.418	*	10.9	1.1
C-16H-2W,60-61	154.74	1228.61	8.049	28.94	232.93	2.35	18.88	12.34	349.03	2.81	0.424	0.440	*	11.5	1.1
C-16H-2W, 136-137	155.52	1234.31	7.585	65.19	494.47	8.59	65.14	7.59	679.26	5.15	0.401	0.401		10.8	0.0
C-16H-3W,72-73	156.38	1238.53	11.300	163.68	1849.49	21.24	239.96	7.71	902.10	10.19	0.375	0.406		10.0	2.2
C-16H-4W,4-5	157.19	1242.45	11.473	30.77	353.05	0.41	4.67	75.59	150.31	1.72	0.209	0.306		5.0	7.5
C-16H-4W,88-89	158.02	1252.94	4.389	28.00	122.90	1.37	6.00	20.47	71.34	0.31	0.222	0.359		5.4	10.1

ODP 983 ODP Sample Label	**Depth** (Mcd)	**Age** (ka)	**Bulk MAR** ($g/cm^2/kyr$)	**P410** (AU/g)	**AR P410** ($AU/cm^2/kyr$)	**P665** (AU/g)	**AR P665** ($AU/cm^2/kyr$)	**S/I**	**K37** (ng/g)	**MAR K37** ($\mu g/cm^2/kyr$)	U^K_{37}	U^K_{37}' (CIMS *)		**SST** (°C)	**C37:4** (%K37)
C-16H-5W, 20-21	158.86	1259.22	7.419						539.09	4.00	0.286	0.361		7.3	5.5
C-16H-5W,104-105	159.69	1265.45	7.390	40.71	300.81	2.55	18.82	15.98	223.48	1.65	0.218	0.312		5.3	7.2
C-16H-6W, 40-41	160.53	1271.46	7.758						741.81	5.76	0.186	0.326		4.3	10.5
C-16H-6W,124-125	161.37	1277.97	7.158	89.20	638.51	4.84	34.62	18.44	285.50	2.04	0.395	0.448		10.6	3.7
C-16H-7W,56-57	162.20	1284.27	7.306	151.00	1103.27	9.25	67.60	16.32		0.00					
C-17H-1W,12-13	163.04	1290.65	7.306	135.42	989.40	4.76	34.81	28.43	213.51	1.56	0.319	0.354		8.3	2.6
C-17H-1W, 96-97	163.87	1296.98	7.277	195.88	1425.44	5.83	42.40	33.62	297.41	2.16	0.274	0.283		7.0	0.7
C-17H-2W,28-29	164.71	1303.50	7.144	12.25	87.53	0.43	3.07	28.55	128.10	0.92	0.403	0.403	*	10.9	0.0
C-17H-2W,112-113	165.54	1309.83	7.280	54.13	394.03	7.79	56.69	6.95	326.06	2.37	0.436	0.436	*	11.9	0.0
B-17H-3W,44-45	166.38	1315.95	7.608	32.68	248.67	3.62	27.58	9.02	260.61	1.98	0.483	0.508		13.3	1.7
C-17H-3W,128-129	167.22	1320.76	9.693	45.28	438.86	1.50	14.55	30.15	268.29	2.60	0.476	0.502		13.1	1.7
C-17H-4W,64-65	168.05	1325.60	9.509	549.05	5220.98	17.91	170.33	30.65	73.53	0.70	0.213	0.446		5.1	16.1
C-17H-4W,144-145	168.89	1330.53	9.459	45.30	428.48	1.77	16.73	25.61	167.85	1.59	0.432	0.432	*	11.8	0.0
C-17H-5W,80-81	169.72	1335.04	10.202	49.97	509.76	2.61	26.58	19.18	40.10	0.41	0.238	0.238		5.9	0.0
C-17H-6W, 12-13	170.56	1339.24	11.095	48.15	534.24	3.65	40.47	13.20	585.49	6.50	0.233	0.337		5.7	7.8
C-17H-6W,96-97	171.39	1343.54	10.708	23.14	247.84	1.97	21.05	11.78	358.48	3.84	0.420	0.420	*	11.4	0.0
C-17H-7W,32-33	172.23	1346.90	13.869	41.39	573.99	4.53	62.76	9.15	468.60	6.50	0.388	0.391	*	10.4	0.2
C-18H-1W,40-41	173.06	1350.18	14.038	100.96	1417.26	5.36	75.22	18.84	247.41	3.47	0.482	0.482	*	13.3	0.0
C-18H-1W,124-125	173.90	1353.56	13.775	25.94	357.29	2.12	29.19	12.24	290.61	4.00	0.538	0.538		15.0	0.0
C-18H-2W,56-57	174.74	1357.31	12.453	125.64	1564.63	4.86	60.56	25.84	269.37	3.35	0.432	0.477		11.8	3.0
C-18H-2W, 140-141	175.57	1360.90	12.808						288.80	3.70	0.436	0.442	*	11.9	0.4
C-18H-3W,76-77	176.41	1364.54	12.802	57.43	735.19	2.84	36.41	20.19	114.84	1.47	0.339	0.367		8.9	2.0
C-18H-4W, 8-9	177.24	1368.65	11.203	41.00	459.28	1.07	12.03	38.18	212.25	2.38	0.383	0.383		10.3	0.0
C-18H-4W,92-93	178.08	1373.70	9.228	91.29	842.43	3.41	31.46	26.78	78.73	0.73	0.340	0.435		9.0	6.6
C-18H-5W, 24-25	178.91	1382.24	5.392						293.42	1.58	0.272	0.272	*	6.9	0.0
C-18H-5W,108-109	179.75	1396.12	3.357	21.99	73.84	0.96	3.23	22.88	144.21	0.48	0.304	0.377		7.9	5.3
C-18H-6W, 40-41	180.58	1402.66	7.044						511.35	3.60	0.324	0.324		8.5	0.0
C-18H-6W,124-125	181.42	1406.22	13.078	40.59	530.83	1.66	21.65	24.52	300.72	3.93	0.382	0.413		10.2	2.2
C-18H-7W, 60-61	182.26	1409.68	13.488	64.48	869.74	2.31	31.10	27.96	206.91	2.79	0.336	0.337	*	8.8	0.1
A-18H-6W,48-49	183.09	1413.17	13.187	256.30	3379.84	7.89	103.99	32.50	116.19	1.53	0.272	0.342		6.9	5.2

ODP 983	**Depth**	**Age**	**Bulk MAR**	**P410**	**AR P410**	**P665**	**AR P665**	**S/I**	**K37**	**MAR K37**	**U^{K}_{37}**	**U^{K}_{37}'**		**SST**	**C37:4**
ODP Sample Label	(Mcd)	(ka)	(g/cm^2/kyr)	(AU/g)	(AU/cm^2/kyr)	(AU/g)	(AU/cm^2/kyr)		(ng/g)	(μg/cm^2/kyr)		(CIMS *)		(°C)	(%K37)
C-19H-1W,48-49	183.93	1416.75	13.017	83.90	1092.16	4.33	56.37	19.38	220.86	2.87	0.340	0.345	*	9.0	0.4
C-19H-1W,132-133	184.76	1420.97	10.898	146.69	1598.63	9.35	101.90	15.69	169.33	1.85	0.288	0.438		7.4	10.5
C-19H-2W, 68-69	185.60	1425.25	10.892	51.04	555.96	2.92	31.77	17.50	215.97	2.35	0.285	0.285	*	7.3	0.0
C-19H-3W,0-1	186.43	1429.40	11.095	47.16	523.23	2.92	32.44	16.13	166.94	1.85	0.388	0.388	*	10.4	0.0
C-19H-3W,84-85	187.27	1433.78	10.649	26.61	283.37	2.16	22.96	12.34	398.53	4.24	0.390	0.390	*	10.5	0.0
C-19H-4W,16-17	188.11	1436.72	15.829	80.44	1273.22	13.13	207.84	6.13	447.85	7.09	0.370	0.385		9.9	1.1
C-19H-4W, 100-101	188.94	1440.09	13.661	7.43	101.49	0.33	4.54	22.36	340.12	4.65	0.488	0.488	*	13.5	0.0
C-19H-5W,36-37	189.78	1443.08	15.571	26.33	409.92	1.70	26.51	15.47	555.48	8.65	0.386	0.386		10.4	0.0
C-19H-5W, 116-117	190.61	1446.33	14.197	54.10	768.01	4.71	66.92	11.48	550.14	7.81	0.400	0.400	*	10.8	0.0
C-19H-6W,52-53	191.45	1449.24	15.999	103.42	1654.52	9.63	154.04	10.74	660.01	10.56	0.322	0.352		8.4	2.2
C-19H-6W,136-137	192.28	1453.45	10.935	17.17	187.76	0.37	4.03	46.61		0.00					
C-19H-7W,68-69	193.12	1457.71	10.927	75.87	829.04	4.36	47.62	17.41	0.00	0.00	0.371	0.371		9.9	0.0
B-20H-1W, 88-89	193.95	1462.51	9.612	146.99	1412.79	13.16	126.46	11.17	428.41	4.12	0.232	0.273	*	5.7	3.2
C-20H-1W,104-105	194.79	1467.37	9.586	98.11	940.44	6.05	57.98	16.22	87.55	0.84	0.239	0.288		5.9	3.8
C-20H-2W,40-41	195.63	1472.08	9.887	18.40	181.94	1.18	11.68	15.57	156.80	1.55	0.376	0.390	*	10.0	1.1
C-20H-2W,120-121	196.46	1476.61	10.157	43.18	438.57	3.47	35.23	12.45	556.05	5.65	0.489	0.489	*	13.5	0.0
C-20H-3W, 56-57	197.30	1481.27	10.000	10.19	101.89	0.56	5.58	18.25	345.66	3.46	0.389	0.389		10.5	0.0
C-20H-3W,140-141	198.13	1485.52	10.843	46.68	506.13	3.60	39.06	12.96	639.25	6.93	0.363	0.375		9.7	0.9
C-20H-4W,72-73	198.97	1491.44	7.872	57.55	453.01	2.69	21.14	21.43	94.13	0.74	0.502	0.502		13.9	0.0
C-20H-5W,4-5	199.80	1498.08	6.935	101.70	705.22	4.48	31.04	22.72	96.93	0.67	0.337	0.442		8.9	7.3
C-20H-5W, 88-89	200.64	1504.80	6.934	263.08	1824.32	22.30	154.63	11.80	157.29	1.09	0.344	0.344		9.1	0.0

A2: Results from ODP 1087 Site A. ODP labelling is Core-Section, depth interval (cm). All other terms defined in Chapters 1 and 2.

ODP 1087A	**Depth**	**Age**	**Bulk MAR**	**P410**	**AR P410**	**P665**	**AR P665**	**S/I**	**K37**	**MAR K37**	**U^K_{37}**	**U^K_{37}'**	**SST**	**C37:4**	**Particle size**
ODP Sample Label	(Mbsf)	(ka)	(g/cm^2/kyr)	(AU/g)	(AU/cm^2/kyr)	(AU/g)	(AU/cm^2/kyr)		(ng/g)	(μg/cm^2/kyr)			(°C)	(%K37)	(Mean <30μm)
2H-4W, 36-37	13.06	497.63	2.702	304.52	822.84	43.99	118.88	6.92	5375.13	14.52	0.608	0.608	17.1	0.0	
2H-4W, 51-52	13.21	502.81	2.702	143.36	387.38	19.53	52.79	7.34	3568.35	9.64	0.599	0.619	17.4	1.3	
2H-4W, 66-67	13.36	508.74	2.364	157.52	372.41	29.67	70.15	5.31	4665.51	11.03	0.575	0.575	16.1	0.0	
2H-4W, 81-82	13.51	514.30	2.522	209.74	528.92	38.96	98.24	5.38	3504.69	8.84	0.515	0.555	15.5	2.6	
2H-4W, 96-97	13.66	519.85	2.522	159.97	403.41	22.15	55.87	7.22	4239.20	10.69	0.567	0.588	16.5	1.3	
2H-4W, 111-112	13.81	525.41	2.695	5.96	16.07	0.00	0.00		3583.20	9.66	0.625	0.625	17.6	0.0	
2H-4W, 126-127	13.96	535.33	1.509	256.61	387.29	39.20	59.16	6.55	6370.35	9.61	0.577	0.577	16.2	0.0	
2H-4W, 141-142	14.11	549.06	1.090	189.93	206.98	29.35	31.98	6.47	4289.60	4.67	0.605	0.605	17.0	0.0	
2H-5W, 04-05	14.24	561.37	1.090	309.12	336.87	50.88	55.44	6.08	7249.68	7.90	0.578	0.578	16.2	0.0	
2H-5W, 15-16	14.36	571.55	1.090	152.64	166.35	20.21	22.02	7.55	4814.19	5.25	0.580	0.598	16.8	1.1	
2H-5W, 26-27	14.47	581.72	1.090	230.58	251.28	40.10	43.70	5.75							
2H-5W, 37-38	14.58	591.89	1.090	158.33	172.55	25.79	28.10	6.14	3048.56	3.32	0.576	0.576	16.1	0.0	
2H-5W, 48-49	14.69	602.07	1.090	210.35	229.23	32.79	35.74	6.41	6215.98	6.77	0.559	0.571	16.0	0.7	
2H-5W, 60-61	14.80	612.24	1.090	209.54	228.36	32.63	35.56	6.42	4059.26	4.42	0.558	0.563	15.7	0.3	
2H-5W, 71-72	14.91	618.25	1.846	153.47	283.29	24.87	45.91	6.17	5104.38	9.42	0.539	0.539	15.0	0.0	
2H-5W, 82-83	15.02	622.80	2.435	152.56	371.44	26.27	63.97	5.81	3030.69	7.38	0.602	0.602	16.9	0.0	
2H-5W, 91-92	15.12	626.38	2.578	350.95	904.68	55.51	143.10	6.32							
2H-5W, 101-102	15.22	629.96	2.721	228.99	623.06	39.22	106.73	5.84	4276.42	11.64	0.474	0.518	14.4	2.9	
2H-5W, 111-112	15.31	633.22	2.993	491.63	1471.45	78.61	235.27	6.25	15508.10	46.42	0.421	0.469	12.9	3.3	
2H-5W, 121-122	15.41	636.48	2.993	455.83	1364.28	76.40	228.67	5.97	6308.98	18.88	0.415	0.461	12.6	3.1	
2H-5W, 130-131	15.51	638.11	5.986	309.69	1853.82	48.95	293.01	6.33	5032.80	30.13	0.541	0.561	15.7	1.3	
2H-5W, 140-141	15.61	642.91	2.035	123.03	250.32	15.55	31.64	7.91	1871.86	3.81	0.611	0.611	17.2	0.0	
2H-6W, 00-01	15.70	646.08	3.070	249.11	764.70	32.04	98.35	7.78	6551.15	20.11	0.590	0.590	16.6	0.0	
2H-6W, 10-11	15.80	649.26	3.070	130.98	402.06	21.33	65.47	6.14	4503.22	13.82	0.637	0.637	18.0	0.0	
2H-6W, 20-21	15.90	652.44	3.070	159.26	488.90	26.74	82.08	5.96	4144.87	12.72	0.545	0.545	15.2	0.0	
2H-6W, 29-30	16.00	655.62	3.070	136.78	419.89	21.67	66.52	6.31	3188.44	9.79	0.639	0.639	18.0	0.0	
2H-6W, 39-40	16.09	658.80	3.070	224.16	688.11	35.14	107.88	6.38	5605.36	17.21	0.631	0.631	17.8	0.0	
2H-6W, 49-50	16.19	661.98	3.070	104.61	321.14	12.31	37.78	8.50	4978.25	15.28	0.625	0.651	18.4	1.6	

ODP 1087A	**Depth**	**Age**	**Bulk MAR**	**P410**	**AR P410**	**P665**	**AR P665**	**S/I**	**K37**	**MAR K37**	**U^{K}_{37}**	**U^{K}_{37}'**	**SST**	**C37:4**	**Particle size**
ODP Sample Label	(Mbsf)	(ka)	(g/cm^2/kyr)	(AU/g)	(AU/cm^2/kyr)	(AU/g)	(AU/cm^2/kyr)		(ng/g)	(μg/cm^2/kyr)			(°C)	(%K37)	(Mean <30μm)
2H-6W, 59-60	16.29	665.16	3.070	139.93	429.54	24.88	76.39	5.62	6878.69	21.12	0.617	0.617	17.4	0.0	
2H-6W, 68-69	16.39	668.34	3.070	57.57	176.74	8.88	27.25	6.49	3209.13	9.85	0.703	0.703	20.0	0.0	
2H-6W, 88-89	16.58	674.64	3.070	108.75	333.83	14.96	45.91	7.27	5366.33	16.47	0.574	0.574	16.0	0.0	
2H-6W, 110-111	16.80	681.89	3.156	5.93	18.73	0.00	0.00		5963.82	18.82	0.621	0.621	17.5	0.0	
2H-6W, 132-133	17.03	689.15	3.156	269.76	851.27	42.36	133.69	6.37	11780.22	37.17	0.567	0.595	16.7	1.8	
2H-7W, 04-05	17.25	696.40	3.156	251.55	793.78	36.97	116.68	6.80	6071.02	19.16	0.573	0.573	16.0	0.0	
2H-7W, 27-28	17.47	703.66	3.156	274.91	867.52	42.78	134.99	6.43	5574.11	17.59	0.635	0.635	17.9	0.0	
2H-7W, 49-50	17.69	710.92	3.156						4136.94	13.05	0.564	0.615	17.3	3.2	
3H-1W, 21-22	17.92	740.27	0.631	526.24	331.89	72.32	45.61	7.28	12318.12	7.77	0.575	0.589	16.5	0.9	
3H-1W, 43-44	18.14	748.72	2.190	379.02	830.13	57.62	126.21	6.58	15943.13	34.92	0.563	0.575	16.1	0.8	
3H-1W, 66-67	18.36	755.10	2.901	227.84	660.87	27.85	80.79	8.18	7595.28	22.03	0.527	0.556	15.5	1.9	
3H-1W, 88-89	18.58	758.17	6.031	311.88	1880.91	46.48	280.31	6.71	6229.31	37.57	0.522	0.539	15.0	1.1	
3H-1W, 110-111	18.81	761.24	7.148	225.89	1614.57	24.55	175.50	9.20	13124.81	93.81	0.456	0.500	13.8	2.9	8.4
3H-1W, 132-133	19.03	764.30	7.148	382.39	2733.14	56.27	402.21	6.80	13100.20	93.63	0.585	0.593	16.6	0.5	
3H-2W, 05-06	19.25	767.37	7.148	1051.81	7517.86	183.72	1313.17	5.72	13928.83	99.56	0.472	0.499	13.8	1.8	
3H-2W, 27-28	19.47	770.44	7.148	654.32	4676.77	92.20	658.98	7.10	9665.51	69.08	0.562	0.582	16.3	1.2	
3H-2W, 49-50	19.70	773.50	7.148	353.89	2529.45	55.72	398.24	6.35	9299.65	66.47	0.557	0.582	16.3	1.5	
3H-2W, 71-72	19.92	776.46	7.405	332.94	2465.48	58.13	430.45	5.73	6067.04	44.93	0.584	0.623	17.6	2.4	
3H-2W, 94-95	20.14	779.64	5.961	328.98	1960.94	48.34	288.14	6.81	4673.64	27.86	0.575	0.598	16.8	1.4	
3H-2W, 116-117	20.36	782.66	6.245	191.40	1195.25	30.90	192.96	6.19	7619.41	47.58	0.595	0.629	17.7	2.1	
3H-2W, 138-139	20.59	785.77	6.093	189.37	1153.81	25.94	158.04	7.30	4351.95	26.52	0.628	0.628	17.7	0.0	
3H-3W, 10-11	20.81	788.73	6.390	150.76	963.42	30.52	195.02	4.94	1878.36	12.00	0.643	0.643	18.1	0.0	
3H-3W, 33-34	21.03	791.90	5.961	426.36	2541.36	81.53	485.94	5.23	2861.97	17.06	0.641	0.641	18.1	0.0	
3H-3W, 55-56	21.25	795.18	5.762	460.13	2651.29	76.71	442.01	6.00	3773.41	21.74	0.458	0.478	13.2	1.3	1.6
3H-3W, 77-78	21.48	798.59	5.558	421.77	2344.05	64.90	360.68	6.50	4129.42	22.95	0.523	0.547	15.2	1.5	
3H-3W, 99-100	21.70	801.99	5.937	313.43	1860.79	43.52	258.37	7.20	6199.76	36.81	0.561	0.601	16.9	2.6	
3H-3W, 122-123	21.92	805.39	5.937	428.26	2542.55	60.87	361.40	7.04	9980.96	59.26	0.518	0.537	14.9	1.2	
3H-4W, 16-17	22.37	810.59	7.776	444.30	3454.80	76.05	591.37	5.84	5913.43	45.98	0.549	0.577	16.2	1.8	
3H-4W, 38-39	22.59	813.95	6.004	395.40	2374.12	61.23	367.63	6.46	4777.74	28.69	0.535	0.548	15.3	0.8	
3H-4W, 61-62	22.81	817.47	5.743	487.46	2799.64	78.07	448.36	6.24	8921.63	51.24	0.526	0.551	15.4	1.6	

ODP 1087A	**Depth**	**Age**	**Bulk MAR**	**P410**	**AR P410**	**P665**	**AR P665**	**S/I**	**K37**	**MAR K37**	**U^{K}_{37}**	**U^{K}_{37}'**	**SST**	**C37:4**	**Particle size**
ODP Sample Label	(Mbsf)	(ka)	(g/cm^2/kyr)	(AU/g)	(AU/cm^2/kyr)	(AU/g)	(AU/cm^2/kyr)		(ng/g)	(μg/cm^2/kyr)			(°C)	(%K37)	(Mean <30μm)
3H-4W, 83-84	23.03	820.84	6.004	368.59	2213.15	63.68	382.36	5.79	5910.48	35.49	0.514	0.526	14.6	0.8	
3H-4W, 105-106	23.26	824.20	5.819	443.66	2581.78	65.00	378.25	6.83	10917.55	63.53	0.574	0.574	16.1	0.0	
3H-4W, 127-128	23.48	827.56	5.819	371.95	2164.44	67.80	394.56	5.49	4380.11	25.49	0.584	0.587	16.5	0.2	
3H-5W, 00-01	23.70	831.08	5.566	553.33	3079.96	76.94	428.29	7.19	11062.56	61.58	0.483	0.509	14.1	1.7	
3H-5W, 22-23	23.92	834.45	5.819	481.94	2804.54	76.48	445.06	6.30	11013.66	64.09	0.620	0.629	17.7	0.6	
3H-5W, 44-45	24.15	837.81	5.819	790.09	4597.72	105.96	616.63	7.46	10152.75	59.08	0.515	0.560	15.6	2.9	
3H-5W, 66-67	24.37	841.29	5.621	419.79	2359.85	68.80	386.76	6.10	6104.15	34.31	0.567	0.593	16.6	1.6	
3H-5W, 89-90	24.59	844.70	6.061	598.40	3626.99	96.38	584.15	6.21	7712.01	46.74	0.691	0.691	19.6	0.0	
3H-5W, 111-112	24.81	848.10	6.061	731.19	4431.83	103.42	626.82	7.07	8549.72	51.82	0.615	0.641	18.1	1.6	
3H-5W, 133-134	25.04	851.50	6.061	414.35	2511.46	63.69	386.01	6.51	6820.41	41.34	0.616	0.616	17.3	0.0	
3H-6W, 05-06	25.26	854.91	6.061	336.68	2040.67	55.16	334.33	6.10	9654.11	58.52	0.600	0.602	16.9	0.1	
3H-6W, 28-29	25.48	858.31	6.061	383.29	2323.18	57.63	349.29	6.65	6716.70	40.71	0.621	0.632	17.8	0.7	
3H-6W, 50-51	25.70	861.71	6.061	104.09	630.89	16.73	101.38	6.22	2434.00	14.75	0.659	0.659	18.6	0.0	
3H-6W, 72-73	25.93	865.12	6.061	233.10	1412.87	39.26	237.96	5.94	4601.12	27.89	0.648	0.648	18.3	0.0	
3H-6W, 84-95	26.15	868.52	6.061	335.89	2035.89	58.51	354.64	5.74	4501.79	27.29	0.542	0.566	15.8	1.5	
3H-6W, 117-118	26.37	873.51	4.186	193.53	810.17	35.67	149.33	5.43	4230.63	17.71	0.541	0.574	16.1	2.1	
3H-6W, 131-132	26.51	879.35	2.280	8.82	20.10	0.00	0.00		6692.54	15.26	0.597	0.597	16.7	0.0	
3H-6W, 145-146	26.65	885.33	2.225	388.17	863.58	59.84	133.13	6.49	8896.50	19.79	0.555	0.573	16.0	1.2	
3H-7W, 09-10	26.79	891.23	2.252	357.54	805.21	62.66	141.12	5.71	5215.63	11.75	0.597	0.597	16.8	0.0	
3H-7W, 23-24	26.94	897.14	2.252	249.78	562.52	43.22	97.34	5.78	6073.75	13.68	0.546	0.546	15.2	0.0	7.3
3H-7W, 37-38	27.08	903.04	2.252	276.74	623.25	47.40	106.75	5.84	3482.64	7.84	0.553	0.561	15.7	0.5	
3H-7W, 51-52	27.22	908.95	2.437	139.07	338.85	19.39	47.24	7.17	4020.21	9.80	0.576	0.593	16.6	1.1	
4H-1W, 16-17	27.36	944.88	0.401	534.49	214.09	77.90	31.20	6.86	9791.66	3.92	0.535	0.566	15.8	2.0	
4H-1W, 30-31	27.50	948.67	3.796	130.84	496.73	20.49	77.78	6.39	10749.06	40.81	0.567	0.593	16.6	1.6	
4H-1W, 44-45	27.64	952.58	3.678	236.29	869.09	43.72	160.81	5.40	6051.47	22.26	0.636	0.651	18.4	0.9	
4H-1W, 58-59	27.79	956.43	3.736	149.58	558.88	23.10	86.33	6.47	6384.25	23.85	0.623	0.646	18.2	1.4	
4H-1W, 72-73	27.93	960.28	3.736	225.14	841.19	30.37	113.47	7.41	7904.92	29.54	0.524	0.560	15.6	2.3	
4H-1W, 86-87	28.07	964.14	3.736	625.93	2338.72	87.02	325.15	7.19	15187.15	56.74	0.491	0.534	14.8	2.8	
4H-1W, 100-101	28.21	975.84	3.489	777.52	2713.12	106.29	370.88	7.32	14294.45	49.88	0.477	0.541	15.1	4.1	
4H-1W, 115-116	28.35	972.13	3.267	676.46	2210.13	75.60	246.99	8.95	17106.08	55.89	0.475	0.534	14.8	3.9	6.9

ODP 1087A ODP Sample Label	**Depth** (Mbsf)	**Age** (ka)	**Bulk MAR** ($g/cm^2/kyr$)	**P410** (AU/g)	**AR P410** ($AU/cm^2/kyr$)	**P665** (AU/g)	**AR P665** ($AU/cm^2/kyr$)	**S/I**	**K37** (ng/g)	**MAR K37** ($\mu g/cm^2/kyr$)	U^{K}_{37}	U^{K}_{37}'	**SST** (°C)	**C37:4** (%K37)	**Particle size** (Mean <30μm)
4H-1W, 129-130	28.49	976.14	3.359	45.91	154.23	0.00	0.00		19430.22	65.27	0.533	0.570	15.9	2.3	
4H-1W, 143-144	28.63	980.16	3.359	485.31	1630.33	64.20	215.68	7.56	9612.92	32.29	0.499	0.574	16.1	4.7	
4H-2W, 07-08	28.78	984.17	3.359	543.42	1825.53	85.23	286.30	6.38	8826.72	29.65	0.536	0.595	16.7	3.7	
4H-2W, 21-22	28.92	988.18	3.359	486.84	1635.46	72.04	242.00	6.76	9703.79	32.60	0.501	0.566	15.8	4.2	
4H-2W, 35-36	29.06	992.20	3.359	256.19	860.62	44.97	151.06	5.70	5192.33	17.44	0.594	0.611	17.2	1.0	
4H-2W, 50-51	29.20	996.21	3.365	310.73	1045.61	45.34	152.56	6.85	9060.75	30.49	0.511	0.546	15.2	2.2	
4H-2W, 64-65	29.34	1000.23	3.354	466.29	1563.75	60.55	203.05	7.70	8149.39	27.33	0.601	0.628	17.7	1.6	
4H-2W, 78-79	29.48	1004.24	3.359	410.54	1379.15	64.43	216.45	6.37	9447.36	31.74	0.503	0.555	15.5	3.4	
4H-2W, 92-93	29.62	1008.44	3.210	244.44	784.59	36.19	116.17	6.75	11972.95	38.43	0.554	0.580	16.2	1.6	
4H-2W, 106-107	29.77	1012.69	3.073	836.99	2572.36	109.99	338.05	7.61	12240.63	37.62	0.569	0.588	16.5	1.2	
4H-2W, 120-121	29.91	1016.93	3.073	538.32	1654.45	78.31	240.66	6.87	7918.44	24.34	0.521	0.550	15.3	1.9	
4H-2W, 135-136	30.05	1021.18	3.073	335.84	1032.14	52.09	160.08	6.45	13448.52	41.33	0.589	0.607	17.1	1.1	
4H-2W, 149-150	30.19	1025.42	3.073	272.05	836.09	46.70	143.51	5.83	4625.64	14.22	0.590	0.611	17.2	1.3	
4H-3W, 13-14	30.33	1029.67	3.073	333.20	1024.03	49.63	152.53	6.71	9049.52	27.81	0.652	0.652	18.4	0.0	
4H-3W, 27-28	30.47	1033.91	3.073	291.18	894.89	45.59	140.11	6.39	5585.24	17.17	0.609	0.609	17.1	0.0	
4H-3W, 41-42	30.62	1038.16	3.073	689.43	2118.86	101.60	312.26	6.79	11191.56	34.40	0.487	0.528	14.7	2.7	
4H-3W, 55-56	30.76	1042.40	3.073	646.91	1988.17	93.94	288.72	6.89	8191.68	25.18	0.496	0.542	15.1	3.0	
4H-3W, 69-70	30.90	1046.87	2.977	400.96	1193.49	64.27	191.29	6.24							
4H-3W, 83-84	31.04	1051.46	2.880	299.70	863.05	42.61	122.70	7.03	6319.01	18.20	0.582	0.601	16.9	1.2	
4H-3W, 98-99	31.18	1056.06	2.838	566.68	1608.43	76.66	217.58	7.39	10570.99	30.00	0.525	0.566	15.8	2.6	
4H-3W, 112-123	31.32	1060.66	2.792	454.58	1269.25	71.22	198.86	6.38	7096.48	19.81	0.572	0.606	17.0	2.1	
4H-3W, 126-127	31.46	1065.25	2.792	478.95	1337.30	73.18	204.34	6.54	8691.06	24.27	0.562	0.588	16.5	1.6	
4H-4W, 04-05	31.75	1074.45	2.792	367.17	1025.18	37.73	105.34	9.73	8465.96	23.64	0.566	0.586	16.4	1.3	
4H-4W, 18-19	31.89	1079.04	2.792	288.05	804.27	40.13	112.04	7.18	4465.11	12.47	0.618	0.626	17.6	0.5	
4H-4W, 33-34	32.03	1083.64	2.792	198.03	552.92	26.51	74.03	7.47	7147.17	19.96	0.630	0.648	18.3	1.1	
4H-4W, 47-48	32.17	1088.23	2.792	214.44	598.74	33.34	93.08	6.43	4824.06	13.47	0.643	0.669	18.9	1.6	
4H-4W, 61-62	32.31	1092.83	2.792	263.14	734.73	41.24	115.15	6.38	6308.26	17.61	0.581	0.605	17.0	1.5	
4H-4W, 75-76	32.45	1096.42	3.574	477.13	1705.14	61.14	218.51	7.80	9201.41	32.88	0.499	0.575	16.1	4.8	
4H-4W, 89-90	32.60	1100.67	3.020	741.59	2239.78	103.10	311.39	7.19	12633.14	38.16	0.547	0.585	16.4	2.4	
4H-4W, 103-104	32.74	1104.38	3.660	651.96	2386.18	88.66	324.51	7.35	6353.13	23.25	0.437	0.466	12.8	2.0	7.0

ODP 1087A ODP Sample Label	**Depth** (Mbsf)	**Age** (ka)	**Bulk MAR** (g/cm^2/kyr)	**P410** (AU/g)	**AR P410** (AU/cm^2/kyr)	**P665** (AU/g)	**AR P665** (AU/cm^2/kyr)	**S/I**	**K37** (ng/g)	**MAR K37** (μg/cm^2/kyr)	**U^K_{37}**	**U^K_{37}'**	**SST** (°C)	**C37:4** (%K37)	**Particle size** (Mean <30μm)
4H-4W, 117-118	32.88	1108.09	3.660	681.13	2492.93	97.84	358.11	6.96	13731.55	50.26	0.513	0.582	16.3	4.4	
4H-4W, 132-133	33.02	1111.81	3.660	528.63	1934.78	81.05	296.63	6.52	7241.36	26.50	0.519	0.566	15.8	3.0	
4H-4W, 146-147	33.16	1115.52	3.660	859.66	3146.34	117.19	428.91	7.34	11416.59	41.78	0.525	0.563	15.7	2.4	
4H-5W, 10-11	33.30	1119.23	3.660	673.01	2463.23	120.45	440.85	5.59	6202.66	22.70	0.527	0.564	15.8	2.4	
4H-5W, 24-25	33.45	1122.94	3.660	681.33	2493.67	99.10	362.70	6.88	10768.50	39.41	0.522	0.553	15.4	2.0	
4H-5W, 38-39	33.59	1126.65	3.660	700.19	2562.69	117.56	430.28	5.96	8844.55	32.37	0.516	0.537	14.9	1.4	
4H-5W, 52-53	33.73	1133.15	2.091	823.62	1722.22	118.85	248.53	6.93	12299.15	25.72	0.465	0.528	14.7	4.2	6.5
4H-5W, 67-68	33.87	1139.93	2.002	6.71	13.43	0.00	0.00		11106.64	22.24	0.652	0.672	19.0	1.2	
4H-5W, 81-82	34.01	1146.72	2.002	466.58	934.22	63.44	127.02	7.35	8758.15	17.54	0.529	0.589	16.5	3.8	6.5
4H-5W, 95-96	34.15	1153.50	2.002	252.17	504.91	39.78	79.66	6.34	4521.80	9.05	0.612	0.624	17.6	0.7	
4H-5W, 109-110	34.29	1160.29	2.000	192.39	384.83	21.17	42.33	9.09	6938.77	13.88	0.677	0.677	19.2	0.0	
4H-5W, 123-124	34.44	1165.71	2.502	96.98	242.63	15.42	38.57	6.29	3930.54	9.83	0.694	0.694	19.7	0.0	
4H-5W, 137-128	34.58	1170.45	2.864	120.19	344.23	14.76	42.29	8.14	4301.03	12.32	0.685	0.685	19.4	0.0	
4H-6W, 01-02	34.72	1175.28	2.807	157.11	440.97	24.87	69.80	6.32	2301.71	6.46	0.662	0.662	18.7	0.0	
4H-6W, 16-17	34.86	1180.12	2.807	247.64	695.08	32.58	91.44	7.60	6238.59	17.51	0.669	0.669	18.9	0.0	
4H-6W, 30-31	35.00	1184.95	2.807	5.87	16.49	0.00	0.00		4086.28	11.47	0.677	0.677	19.2	0.0	
4H-6W, 44-45	35.14	1189.79	2.807	125.27	351.62	15.47	43.42	8.10	5374.64	15.09	0.685	0.685	19.4	0.0	
4H-6W, 58-59	35.28	1194.62	2.807	172.81	485.03	18.14	50.90	9.53	3545.18	9.95	0.662	0.688	19.5	1.5	
4H-6W, 72-73	35.43	1199.45	2.807	211.90	594.78	25.63	71.95	8.27	3442.51	9.66	0.656	0.656	18.5	0.0	
4H-6W, 86-87	35.57	1204.29	2.807	357.80	1004.27	63.74	178.92	5.61	6437.32	18.07	0.606	0.622	17.5	1.0	
4H-6W, 101-102m	35.71	1211.71	1.843	629.85	1160.84	91.15	168.00	6.91	10854.03	20.00	0.553	0.603	16.9	3.1	7.9
4H-6W, 115-116	35.85	1218.58	1.989	330.00	656.31	49.69	98.82	6.64	5499.83	10.94	0.639	0.639	18.0	0.0	
4H-7W, 07-08	36.28	1240.55	1.866	280.05	522.62	41.36	77.18	6.77	9546.99	17.82	0.649	0.668	18.9	1.2	
4H-7W, 21-22	36.42	1247.91	1.858	238.34	442.76	30.28	56.25	7.87	5053.47	9.39	0.529	0.569	15.9	2.6	
4H-7W, 35-36	36.56	1255.27	1.858	340.05	631.71	46.45	86.28	7.32	6455.46	11.99	0.531	0.566	15.8	2.2	
5H-1W, 00-01	36.70	1316.72	0.222	276.60	61.53	41.62	9.26	6.65	5103.80	1.14	0.580	0.584	16.4	0.3	
5H-1W, 14-15	36.84	1320.34	3.773	210.77	795.22	33.92	127.98	6.21	5897.47	22.25	0.646	0.646	18.2	0.0	
5H-1W, 28-29	36.98	1323.80	3.952	180.44	713.06	26.41	104.36	6.83	5036.93	19.91	0.628	0.650	18.4	1.3	
5H-1W, 42-43	37.12	1327.26	3.952	162.97	644.04	19.31	76.30	8.44	5295.17	20.93	0.690	0.690	19.6	0.0	
5H-1W, 56-57	37.27	1330.72	3.952	121.28	479.27	13.79	54.50	8.79	3478.98	13.75	0.705	0.705	20.0	0.0	

ODP 1087A	**Depth**	**Age**	**Bulk MAR**	**P410**	**AR P410**	**P665**	**AR P665**	**S/I**	**K37**	**MAR K37**	**U^K_{37}**	**U^K_{37}'**	**SST**	**C37:4**	**Particle size**
ODP Sample Label	(Mbsf)	(ka)	(g/cm^2/kyr)	(AU/g)	(AU/cm^2/kyr)	(AU/g)	(AU/cm^2/kyr)		(ng/g)	(μg/cm^2/kyr)			(°C)	(%K37)	(Mean <30μm)
5H-1W, 70-71	37.41	1334.18	3.952	172.14	680.28	21.85	86.36	7.88	4320.07	17.07	0.656	0.656	18.5	0.0	
5H-1W, 84-85	37.55	1338.46	3.190	120.29	383.70	26.31	83.91	4.57	1966.90	6.27	0.658	0.658	18.6	0.0	
5H-1W, 99-100	37.69	1342.71	3.220	167.09	538.04	26.26	84.55	6.36	3910.78	12.59	0.676	0.676	19.1	0.0	
5H-1W, 131-132	37.83	1346.90	3.257	236.75	771.19	37.27	121.42	6.35	4572.93	14.90	0.568	0.584	16.4	1.0	
5H-1W, 127-128	37.97	1350.93	3.394	261.20	886.53	39.34	133.51	6.64	6992.14	23.73	0.546	0.576	16.1	2.0	
5H-1W, 141-142	38.11	1354.96	3.394	8.10	27.48	0.00	0.00		10613.26	36.02	0.604	0.644	18.2	2.4	
5H-2W, 05-06	38.26	1358.99	3.394	297.22	1008.79	46.42	157.56	6.40	9722.01	33.00	0.512	0.537	14.9	1.6	
5H-2W, 20-21	38.40	1363.11	3.394	403.06	1368.01	60.54	205.47	6.66	11521.22	39.10	0.589	0.600	16.8	0.7	
5H-2W, 34-35	38.55	1367.24	3.394	417.71	1417.75	65.22	221.38	6.40	13344.51	45.29	0.589	0.610	17.1	1.3	
5H-2W, 49-50	38.69	1371.37	3.394	180.05	611.09	25.89	87.87	6.95	3443.30	11.69	0.588	0.588	16.5	0.0	
5H-2W, 63-64	38.84	1375.49	3.394	232.39	788.74	34.23	116.18	6.79	6839.72	23.21	0.579	0.579	16.2	0.0	
5H-2W, 78-79	38.98	1379.62	3.394	263.51	894.38	34.85	118.30	7.56	7799.39	26.47	0.606	0.638	18.0	2.0	
5H-2W, 92-93	39.13	1383.75	3.394	364.62	1237.53	53.12	180.28	6.86	5910.92	20.06	0.586	0.586	16.4	0.0	
5H-2W, 107-108	39.27	1386.97	4.725	0.00	0.00	0.00	0.00		4372.36	20.66	0.669	0.685	19.4	1.0	
5H-2W, 121-122	39.42	1389.14	7.016	200.38	1405.90	24.38	171.02	8.22	6672.57	46.82	0.610	0.610	17.2	0.0	
5H-2W, 136-137	39.56	1391.95	5.409	184.11	995.85	25.07	135.59	7.34	5088.25	27.52	0.636	0.643	18.2	0.4	
5H-3W, 00-01	39.71	1394.77	5.409	404.02	2185.38	50.47	273.01	8.00	6729.05	36.40	0.568	0.600	16.8	2.0	
5H-3W, 15-16	39.85	1397.58	5.409	155.64	841.89	26.99	145.99	5.77	6220.37	33.65	0.713	0.713	20.3	0.0	
5H-3W, 29-30	40.00	1400.40	5.409	141.70	766.48	17.63	95.35	8.04	5486.35	29.68	0.634	0.634	17.9	0.0	
5H-3W, 44-45	40.14	1403.21	5.409	77.12	417.16	12.48	67.51	6.18	3294.54	17.82	0.666	0.666	18.9	0.0	
5H-3W, 58-59	40.29	1406.03	5.409	245.43	1327.54	37.83	204.63	6.49	14061.76	76.06	0.578	0.596	16.7	1.1	
5H-3W, 73-74	40.43	1408.84	5.409	252.86	1367.75	42.35	229.05	5.97	6629.43	35.86	0.648	0.648	18.3	0.0	
5H-3W, 87-88	40.58	1411.66	5.409	412.67	2232.17	66.97	362.23	6.16	10615.20	57.42	0.624	0.624	17.6	0.0	
5H-3W, 102-103	40.72	1414.47	5.110	346.58	1771.14	52.22	266.88	6.64	5361.62	27.40	0.656	0.656	18.5	0.0	
5H-3W, 116-117	40.87	1417.29	5.110	265.86	1358.62	40.68	207.87	6.54	6972.64	35.63	0.675	0.675	19.1	0.0	
5H-3W, 131-132	41.01	1421.72	3.247	358.24	1163.17	51.02	165.67	7.02	9850.55	31.98	0.628	0.640	18.1	0.7	
5H-4W, 10-11	41.30	1429.56	3.666	518.03	1899.14	73.12	268.06	7.08	14581.42	53.46	0.633	0.633	17.8	0.0	
5H-4W, 24-25	41.45	1433.49	3.666	446.85	1638.18	83.78	307.14	5.33	5376.60	19.71	0.684	0.684	19.4	0.0	
5H-4W, 39-40	41.59	1437.41	3.666	320.52	1175.05	55.55	203.65	5.77	5588.08	20.49	0.590	0.638	18.0	2.9	
5H-4W, 53-54	41.74	1441.33	3.666	294.01	1077.88	41.32	151.47	7.12	8087.46	29.65	0.659	0.659	18.6	0.0	

ODP 1087A ODP Sample Label	**Depth** (Mbsf)	**Age** (ka)	**Bulk MAR** (g/cm^2/kyr)	**P410** (AU/g)	**AR P410** (AU/cm^2/kyr)	**P665** (AU/g)	**AR P665** (AU/cm^2/kyr)	**S/I**	**K37** (ng/g)	**MAR K37** (μg/cm^2/kyr)	**U^K_{37}**	**U^K_{37}'**	**SST** (°C)	**C37:4** (%K37)	**Particle size** (Mean <30μm)
5H-4W, 68-69	41.88	1445.26	3.666	194.46	712.90	21.59	79.16	9.01	3772.17	13.83	0.668	0.668	18.9	0.0	
5H-4W, 82-83	42.03	1449.18	3.666	149.17	546.85	19.48	71.40	7.66	6122.63	22.45	0.698	0.698	19.8	0.0	
5H-4W, 97-98	42.17	1453.10	3.666	185.04	678.38	30.81	112.96	6.01	5366.60	19.67	0.691	0.691	19.6	0.0	
5H-4W, 111-112	42.32	1457.03	3.629	261.09	947.52	43.23	156.89	6.04	7509.77	27.25	0.699	0.699	19.9	0.0	
5H-4W, 126-127	42.46	1460.95	3.629	443.14	1608.22	73.70	267.45	6.01	10631.47	38.58	0.623	0.641	18.1	1.1	
5H-4W, 140-141	42.61	1465.24	3.320	199.49	662.26	28.67	95.17	6.96	10009.50	33.23	0.537	0.570	15.9	2.1	
5H-5W, 05-06	42.75	1469.72	3.189	267.08	851.72	36.48	116.35	7.32							
5H-5W, 19-20	42.90	1474.17	3.189	187.77	600.34	25.57	81.76	7.34	8952.49	28.55	0.593	0.593	16.6	0.0	
5H-5W, 34-35	43.04	1478.62	3.197	246.59	788.39	37.61	120.24	6.56	6357.00	20.32	0.626	0.652	18.4	1.6	
5H-5W, 48-49	43.19	1483.08	3.197	246.87	789.30	40.01	127.91	6.17	10658.85	34.08	0.618	0.618	17.4	0.0	
5H-5W, 63-64	43.33	1487.53	3.197	134.46	429.90	22.23	71.07	6.05	7861.82	25.14	0.625	0.635	17.9	0.6	
5H-5W, 77-78	43.48	1491.98	3.197	233.70	822.53	40.04	140.94	5.84	6851.97	21.91	0.602	0.602	16.9	0.0	
5H-5W, 92-93	43.62	1496.44	3.520	206.88	728.11	30.98	109.02	6.68	6562.66	23.10	0.699	0.699	19.8	0.0	
5H-5W, 106-107	43.77	1500.89	3.520	255.81	900.32	34.15	120.18	7.49	7564.29	26.62	0.634	0.634	17.9	0.0	
5H-5W, 121-122	43.91	1505.35	3.520	314.50	1203.38	40.47	154.87	7.77	8878.49	31.25	0.615	0.624	17.6	0.5	
5H-5W, 135-136	44.06	1509.44	3.826	452.64	1918.42	55.84	236.65	8.11	11510.94	44.05	0.529	0.579	16.2	3.1	
5H-6W, 00-01	44.20	1513.14	4.238	7.18	28.71	0.00	0.00		7467.71	31.65	0.641	0.660	18.7	1.1	
5H-6W, 14-15	44.35	1517.11	3.902	387.01	1510.03	46.75	182.39	8.28	10899.58	42.53	0.616	0.616	17.3	0.0	

A3: Biomarker indices from ODP 1087 Site A (Chapter 4). ODP labelling is Core-Section, depth interval (cm). All other terms defined in Chapters 2 and 4.

ODP 1087A	**Depth**	**Age**	**K37**	U^{K}_{37}	U^{K}_{37}'	**SST**	U^{K}_{38}	U^{K}_{38} Me	$U^{K}_{38\,Et}$	U^{K}_{37}' /$U^{K}_{38\,Et}$	**K38**	**K38 Et**	**K37 / K38**	**K37/K38 Et**
ODP Sample Label	(Mbsf)	(ka)	(ng/g)			(°C)					(ng/g)	(ng/g)		
2H-4W, 36-37	13.06	497.63	5375.13	0.608	0.608	17.1	0.646	0.461	0.713	0.853	4913.20	3603.93	1.094	1.491
2H-4W, 51-52	13.21	502.81	3568.35	0.599	0.619	17.4	0.661	0.478	0.728	0.850	2856.89	2088.42	1.249	1.709
2H-4W, 66-67	13.36	508.74	4665.51	0.575	0.575	16.1	0.630	0.436	0.703	0.817	4072.33	2959.52	1.146	1.576
2H-4W, 81-82	13.51	514.30	3504.69	0.515	0.555	15.5	0.617	0.399	0.694	0.800	2620.44	1938.94	1.337	1.808
2H-4W, 96-97	13.66	519.85	4239.20	0.567	0.588	16.5	0.630	0.434	0.707	0.831	3580.76	2568.80	1.184	1.650
2H-4W, 111-112	13.81	525.41	3583.20	0.625	0.625	17.6	0.643	0.451	0.709	0.881	2769.11	2062.32	1.294	1.737
2H-4W, 126-127	13.96	535.33	6370.35	0.577	0.577	16.2	0.591	0.416	0.662	0.872	5241.80	3717.83	1.215	1.713
2H-4W, 141-142	14.11	549.06	4289.60	0.605	0.605	17.0	0.639	0.465	0.708	0.854	3313.48	2370.48	1.295	1.810
2H-5W, 04-05	14.24	561.37	7249.68	0.578	0.578	16.2	0.593	0.421	0.661	0.874	5693.09	4082.53	1.273	1.776
2H-5W, 15-16	14.36	571.55	4814.19	0.580	0.598	16.8	0.648	0.453	0.713	0.839	3739.66	2799.34	1.287	1.720
2H-5W, 37-38	14.58	591.89	3048.56	0.576	0.576	16.1	0.636	0.433	0.710	0.812	2375.34	1742.16	1.283	1.750
2H-5W, 48-49	14.69	602.07	6215.98	0.559	0.571	16.0	0.645	0.438	0.713	0.801	5293.97	3998.64	1.174	1.555
2H-5W, 60-61	14.80	612.24	4059.26	0.558	0.563	15.7	0.628	0.405	0.707	0.797	3309.74	2443.26	1.226	1.661
2H-5W, 71-72	14.91	618.25	5104.38	0.539	0.539	15.0	0.609	0.416	0.679	0.795	4369.83	3199.35	1.168	1.595
2H-5W, 82-83	15.02	622.80	3030.69	0.602	0.602	16.9	0.670	0.460	0.742	0.811	2391.21	1785.56	1.267	1.697
2H-5W, 101-102	15.22	629.96	4276.42	0.474	0.518	14.4	0.625	0.364	0.717	0.723	2931.53	2166.40	1.459	1.974
2H-5W, 111-112	15.31	633.22	15508.10	0.421	0.469	12.9	0.579	0.310	0.673	0.697	11690.77	8675.10	1.327	1.788
2H-5W, 121-122	15.41	636.48	6308.98	0.415	0.461	12.6	0.578	0.312	0.675	0.683	4436.45	3247.84	1.422	1.943
2H-5W, 130-131	15.51	638.11	5032.80	0.541	0.561	15.7	0.639	0.435	0.723	0.776	3683.99	2608.29	1.366	1.930
2H-5W, 140-141	15.61	642.91	1871.86	0.611	0.611	17.2	0.675	0.485	0.751	0.814	1493.53	1067.54	1.253	1.753
2H-6W, 00-01	15.70	646.08	6551.15	0.590	0.590	16.6	0.652	0.400	0.741	0.797	5688.44	4207.96	1.152	1.557
2H-6W, 10-11	15.80	649.26	4503.22	0.637	0.637	18.0	0.692	0.482	0.767	0.831	3483.61	2572.07	1.293	1.751
2H-6W, 20-21	15.90	652.44	4144.87	0.545	0.545	15.2	0.582	0.391	0.657	0.830	3056.02	2200.31	1.356	1.884
2H-6W, 29-30	16.00	655.62	3188.44	0.639	0.639	18.0	0.666	0.466	0.738	0.867	2423.71	1784.37	1.316	1.787
2H-6W, 39-40	16.09	658.80	5605.36	0.631	0.631	17.8	0.656	0.488	0.723	0.873	4749.96	3391.48	1.180	1.653
2H-6W, 49-50	16.19	661.98	4978.25	0.625	0.651	18.4	0.687	0.519	0.755	0.863	3726.77	2654.24	1.336	1.876
2H-6W, 59-60	16.29	665.16	6878.69	0.617	0.617	17.4	0.647	0.460	0.714	0.864	6035.17	4449.65	1.140	1.546
2H-6W, 68-69	16.39	668.34	3209.13	0.703	0.703	20.0	0.723	0.588	0.771	0.912	2507.26	1841.85	1.280	1.742

ODP 1087A ODP Sample Label	**Depth** (Mbsf)	**Age** (ka)	**K37** (ng/g)	U^K_{37}	U^K_{37}'	**SST** (°C)	U^K_{38}	U^K_{38} Me	$U^K_{38\,Et}$	$U^K_{37}'/U^K_{38\,Et}$	**K38** (ng/g)	**K38 Et** (ng/g)	**K37 / K38**	**K37/K38 Et**
2H-6W, 88-89	16.58	674.64	5366.33	0.574	0.574	16.0	0.611	0.422	0.689	0.833	4388.19	3106.88	1.223	1.727
2H-6W, 110-111	16.80	681.89	5963.82	0.621	0.621	17.5	0.649	0.439	0.724	0.858	4453.60	3277.50	1.339	1.820
2H-6W, 132-133	17.03	689.15	11780.22	0.567	0.595	16.7	0.626	0.429	0.704	0.846	9844.42	7046.78	1.197	1.672
2H-7W, 04-05	17.25	696.40	6071.02	0.573	0.573	16.0	0.611	0.450	0.675	0.849	4690.01	3365.54	1.294	1.804
2H-7W, 27-28	17.47	703.66	5574.11	0.635	0.635	17.9	0.647	0.498	0.709	0.895	4823.10	3410.79	1.156	1.634
2H-7W, 49-50	17.69	710.92	4136.94	0.564	0.615	17.3	0.659	0.481	0.731	0.841	3001.16	2129.37	1.378	1.943
3H-1W, 21-22	17.92	740.27	12318.12	0.575	0.589	16.5	0.629	0.437	0.696	0.846	9353.18	6930.50	1.330	1.799
3H-1W, 43-44	18.14	748.72	15943.13	0.563	0.575	16.1	0.594	0.409	0.666	0.863	12214.44	8794.82	1.314	1.825
3H-1W, 66-67	18.36	755.10	7595.28	0.527	0.556	15.5	0.572	0.373	0.643	0.865	5663.87	4168.10	1.341	1.822
3H-1W, 88-89	18.58	758.17	6229.31	0.522	0.539	15.0	0.576	0.412	0.642	0.839	4204.64	3002.63	1.482	2.075
3H-1W, 110-111	18.81	761.24	13124.81	0.456	0.500	13.8	0.547	0.369	0.613	0.816	9285.77	6795.11	1.413	1.932
3H-1W, 132-133	19.03	764.30	13100.20	0.585	0.593	16.6	0.625	0.403	0.692	0.857	9820.25	7548.20	1.334	1.736
3H-2W, 05-06	19.25	767.37	13928.83	0.472	0.499	13.8	0.534	0.331	0.600	0.831	10706.70	8076.91	1.301	1.725
3H-2W, 27-28	19.47	770.44	9665.51	0.562	0.582	16.3	0.592	0.432	0.657	0.886	7254.60	5161.52	1.332	1.873
3H-2W, 49-50	19.70	773.50	9299.65	0.557	0.582	16.3	0.582	0.433	0.645	0.902	7464.98	5243.49	1.246	1.774
3H-2W, 71-72	19.92	776.46	6067.04	0.584	0.623	17.6	0.596	0.446	0.657	0.949	4312.27	3070.04	1.407	1.976
3H-2W, 94-95	20.14	779.64	4673.64	0.575	0.598	16.8	0.581	0.461	0.637	0.938	3726.42	2535.75	1.254	1.843
3H-2W, 116-117	20.36	782.66	7619.41	0.595	0.629	17.7	0.644	0.492	0.706	0.890	5558.58	3953.94	1.371	1.927
3H-2W, 138-139	20.59	785.77	4351.95	0.628	0.628	17.7	0.629	0.503	0.679	0.925	3747.12	2686.41	1.161	1.620
3H-3W, 10-11	20.81	788.73	1878.36	0.643	0.643	18.1	0.615	0.483	0.671	0.957	1492.57	1049.22	1.258	1.790
3H-3W, 33-34	21.03	791.90	2861.97	0.641	0.641	18.1	0.621	0.479	0.680	0.943	2673.12	1890.52	1.071	1.514
3H-3W, 55-56	21.25	795.18	3773.41	0.458	0.478	13.2	0.477	0.340	0.540	0.886	2924.41	2004.85	1.290	1.882
3H-3W, 77-78	21.48	798.59	4129.42	0.523	0.547	15.2	0.521	0.379	0.583	0.939	3216.29	2238.73	1.284	1.845
3H-3W, 99-100	21.70	801.99	6199.76	0.561	0.601	16.9	0.613	0.451	0.676	0.890	3110.31	2243.39	1.993	2.764
3H-3W, 122-123	21.92	805.39	9980.96	0.518	0.537	14.9	0.533	0.415	0.582	0.922	8585.28	6036.45	1.163	1.653
3H-4W, 16-17	22.37	810.59	5913.43	0.549	0.577	16.2	0.567	0.415	0.639	0.903	5054.40	3425.83	1.170	1.726
3H-4W, 38-39	22.59	813.95	4777.74	0.535	0.548	15.3	0.526	0.409	0.578	0.948	3587.50	2480.77	1.332	1.926
3H-4W, 61-62	22.81	817.47	8921.63	0.526	0.551	15.4	0.530	0.415	0.581	0.949	7402.34	5134.33	1.205	1.738
3H-4W, 83-84	23.03	820.84	5910.48	0.514	0.526	14.6	0.514	0.376	0.577	0.912	4459.07	3069.79	1.325	1.925
3H-4W, 105-106	23.26	824.20	10917.55	0.574	0.574	16.1	0.560	0.442	0.612	0.939	9096.09	6302.61	1.200	1.732

ODP 1087A ODP Sample Label	**Depth** (Mbsf)	**Age** (ka)	**K37** (ng/g)	U^{K}_{37}	U^{K}_{37}'	**SST** (°C)	U^{K}_{38}	U^{K}_{38} Me	$U^{K}_{38\,Et}$	$U^{K}_{37}'/U^{K}_{38\,Et}$	**K38** (ng/g)	**K38 Et** (ng/g)	**K37 / K38**	**K37/K38 Et**
3H-4W, 127-128	23.48	827.56	4380.11	0.584	0.587	16.5	0.570	0.443	0.624	0.942	3269.71	2300.14	1.340	1.904
3H-5W, 00-01	23.70	831.08	11062.56	0.483	0.509	14.1	0.496	0.364	0.553	0.920	9450.79	6590.06	1.171	1.679
3H-5W, 22-23	23.92	834.45	11013.66	0.620	0.629	17.7	0.611	0.481	0.665	0.946	8441.60	5975.93	1.305	1.843
3H-5W, 44-45	24.15	837.81	10152.75	0.515	0.560	15.6	0.533	0.374	0.606	0.925	7983.61	5458.77	1.272	1.860
3H-5W, 66-67	24.37	841.29	6104.15	0.567	0.593	16.6	0.593	0.460	0.651	0.911	4454.73	3093.57	1.370	1.973
3H-5W, 89-90	24.59	844.70	7712.01	0.691	0.691	19.6	0.676	0.579	0.716	0.966	6367.25	4483.26	1.211	1.720
3H-5W, 111-112	24.81	848.10	8549.72	0.615	0.641	18.1	0.632	0.495	0.690	0.928	6235.56	4378.59	1.371	1.953
3H-5W, 133-134	25.04	851.50	6820.41	0.616	0.616	17.3	0.630	0.500	0.679	0.907	5332.34	3870.45	1.279	1.762
3H-6W, 05-06	25.26	854.91	9654.11	0.600	0.602	16.9	0.604	0.463	0.664	0.907	7527.84	5281.99	1.285	1.829
3H-6W, 28-29	25.48	858.31	6716.70	0.621	0.632	17.8	0.633	0.522	0.679	0.931	5430.45	3834.86	1.237	1.751
3H-6W, 50-51	25.70	861.71	2434.00	0.659	0.659	18.6	0.649	0.526	0.701	0.941	2057.30	1445.08	1.183	1.684
3H-6W, 72-73	25.93	865.12	4601.12	0.648	0.648	18.3	0.647	0.530	0.698	0.929	3860.39	2695.98	1.192	1.707
3H-6W, 84-95	26.15	868.52	4501.79	0.542	0.566	15.8	0.561	0.419	0.624	0.906	3496.30	2413.53	1.288	1.865
3H-6W, 117-118	26.37	873.51	4230.63	0.541	0.574	16.1	0.572	0.424	0.643	0.892	3472.06	2349.23	1.218	1.801
3H-6W, 131-132	26.51	879.35	6692.54	0.597	0.597	16.7	0.585	0.435	0.650	0.917	5037.07	3510.53	1.329	1.906
3H-6W, 145-146	26.65	885.33	8896.50	0.555	0.573	16.0	0.563	0.429	0.622	0.921	6906.13	4798.54	1.288	1.854
3H-7W, 09-10	26.79	891.23	5215.63	0.597	0.597	16.8	0.602	0.453	0.663	0.900	3717.23	2628.36	1.403	1.984
3H-7W, 23-24	26.94	897.14	6073.75	0.546	0.546	15.2	0.560	0.444	0.611	0.894	4680.96	3245.97	1.298	1.871
3H-7W, 37-38	27.08	903.04	3482.64	0.553	0.561	15.7	0.562	0.395	0.628	0.893	2469.72	1762.93	1.410	1.975
3H-7W, 51-52	27.22	908.95	4020.21	0.576	0.593	16.6	0.599	0.475	0.653	0.909	3182.01	2210.81	1.263	1.818
4H-1W, 16-17	27.36	944.88	9791.66	0.535	0.566	15.8	0.575	0.421	0.632	0.895	6544.05	4761.74	1.496	2.056
4H-1W, 30-31	27.50	948.67	10749.06	0.567	0.593	16.6	0.592	0.477	0.638	0.929	8458.75	6057.07	1.271	1.775
4H-1W, 44-45	27.64	952.58	6051.47	0.636	0.651	18.4	0.656	0.534	0.703	0.926	4394.28	3178.24	1.377	1.904
4H-1W, 58-59	27.79	956.43	6384.25	0.623	0.646	18.2	0.656	0.537	0.703	0.918	5064.33	3608.94	1.261	1.769
4H-1W, 72-73	27.93	960.28	7904.92	0.524	0.560	15.6	0.565	0.427	0.628	0.891	5810.16	3987.36	1.361	1.982
4H-1W, 86-87	28.07	964.14	15187.15	0.491	0.534	14.8	0.539	0.416	0.595	0.897	12006.27	8229.99	1.265	1.845
4H-1W, 100-101	28.21	975.84	14294.45	0.477	0.541	15.1	0.554	0.409	0.618	0.876	9931.09	6919.06	1.439	2.066
4H-1W, 115-116	28.35	972.13	17106.08	0.475	0.534	14.8	0.545	0.417	0.607	0.880	12378.67	8323.65	1.382	2.055
4H-1W, 129-130	28.49	976.14	19430.22	0.533	0.570	15.9	0.599	0.473	0.654	0.871	12294.95	8556.16	1.580	2.271
4H-1W, 143-144	28.63	980.16	9612.92	0.499	0.574	16.1	0.594	0.449	0.649	0.885	6632.79	4837.11	1.449	1.987

ODP 1087A ODP Sample Label	**Depth** (Mbsf)	**Age** (ka)	**K37** (ng/g)	U^{K}_{37}	U^{K}_{37}'	**SST** (°C)	U^{K}_{38}	U^{K}_{38} Me	$U^{K}_{38\,Et}$	$U^{K}_{37}' / U^{K}_{38\,Et}$	**K38** (ng/g)	**K38 Et** (ng/g)	**K37 / K38**	**K37/K38 Et**
4H-2W, 07-08	28.78	984.17	8826.72	0.536	0.595	16.7	0.618	0.491	0.678	0.878	5516.50	3740.84	1.600	2.360
4H-2W, 21-22	28.92	988.18	9703.79	0.501	0.566	15.8	0.574	0.452	0.633	0.895	7242.57	4903.03	1.340	1.979
4H-2W, 35-36	29.06	992.20	5192.33	0.594	0.611	17.2	0.628	0.502	0.687	0.889	3658.95	2498.57	1.419	2.078
4H-2W, 50-51	29.20	996.21	9060.75	0.511	0.546	15.2	0.549	0.423	0.610	0.895	6955.07	4691.04	1.303	1.931
4H-2W, 64-65	29.34	1000.23	8149.39	0.601	0.628	17.7	0.640	0.488	0.705	0.890	5933.73	4163.21	1.373	1.957
4H-2W, 78-79	29.48	1004.24	9447.36	0.503	0.555	15.5	0.566	0.428	0.627	0.886	6523.27	4524.66	1.448	2.088
4H-2W, 92-93	29.62	1008.44	11972.95	0.554	0.580	16.2	0.589	0.461	0.647	0.896	8551.98	5863.29	1.400	2.042
4H-2W, 106-107	29.77	1012.69	12240.63	0.569	0.588	16.5	0.601	0.469	0.662	0.888	9286.46	6361.92	1.318	1.924
4H-2W, 120-121	29.91	1016.93	7918.44	0.521	0.550	15.3	0.557	0.407	0.627	0.878	5407.26	3694.18	1.464	2.143
4H-2W, 135-136	30.05	1021.18	13448.52	0.589	0.607	17.1	0.605	0.475	0.662	0.918	11248.57	7851.02	1.196	1.713
4H-2W, 149-150	30.19	1025.42	4625.64	0.590	0.611	17.2	0.597	0.475	0.652	0.938	3192.29	2201.06	1.449	2.102
4H-3W, 13-14	30.33	1029.67	9049.52	0.652	0.652	18.4	0.655	0.517	0.713	0.915	7351.56	5191.62	1.231	1.743
4H-3W, 27-28	30.47	1033.91	5585.24	0.609	0.609	17.1	0.607	0.485	0.658	0.926	3946.09	2779.86	1.415	2.009
4H-3W, 41-42	30.62	1038.16	11191.56	0.487	0.528	14.7	0.537	0.405	0.597	0.885	8536.55	5876.90	1.311	1.904
4H-3W, 55-56	30.76	1042.40	8191.68	0.496	0.542	15.1	0.548	0.404	0.618	0.877	5632.74	3776.03	1.454	2.169
4H-3W, 83-84	31.04	1051.46	6319.01	0.582	0.601	16.9	0.596	0.439	0.669	0.899	4673.55	3201.70	1.352	1.974
4H-3W, 98-99	31.18	1056.06	10570.99	0.525	0.566	15.8	0.574	0.452	0.637	0.888	7938.58	5226.93	1.332	2.022
4H-3W, 112-123	31.32	1060.66	7096.48	0.572	0.606	17.0	0.617	0.487	0.673	0.901	4766.61	3325.33	1.489	2.134
4H-3W, 126-127	31.46	1065.25	8691.06	0.562	0.588	16.5	0.596	0.457	0.656	0.897	6830.42	4775.90	1.272	1.820
4H-4W, 04-05	31.75	1074.45	8465.96	0.566	0.586	16.4	0.597	0.471	0.650	0.901	6344.54	4468.26	1.334	1.895
4H-4W, 18-19	31.89	1079.04	4465.11	0.618	0.626	17.6	0.633	0.488	0.692	0.905	3058.99	2173.65	1.460	2.054
4H-4W, 33-34	32.03	1083.64	7147.17	0.630	0.648	18.3	0.637	0.518	0.686	0.944	5600.65	3964.00	1.276	1.803
4H-4W, 47-48	32.17	1088.23	4824.06	0.643	0.669	18.9	0.664	0.522	0.719	0.931	3568.25	2576.45	1.352	1.872
4H-4W, 61-62	32.31	1092.83	6308.26	0.581	0.605	17.0	0.603	0.460	0.669	0.904	4623.71	3166.70	1.364	1.992
4H-4W, 75-76	32.45	1096.42	9201.41	0.499	0.575	16.1	0.584	0.451	0.647	0.889	6374.52	4333.21	1.443	2.123
4H-4W, 89-90	32.60	1100.67	12633.14	0.547	0.585	16.4	0.595	0.450	0.661	0.884	9601.53	6561.21	1.316	1.925
4H-4W, 103-104	32.74	1104.38	6353.13	0.437	0.466	12.8	0.471	0.328	0.542	0.860	4504.49	3008.33	1.410	2.112
4H-4W, 117-118	32.88	1108.09	13731.55	0.513	0.582	16.3	0.585	0.444	0.637	0.914	11040.35	8037.90	1.244	1.708
4H-4W, 132-133	33.02	1111.81	7241.36	0.519	0.566	15.8	0.563	0.416	0.627	0.902	5297.09	3694.24	1.367	1.960
4H-4W, 146-147	33.16	1115.52	11416.59	0.525	0.563	15.7	0.568	0.449	0.624	0.901	9210.98	6265.10	1.239	1.822

ODP 1087A	**Depth**	**Age**	**K37**	U^{K}_{37}	U^{K}_{37}'	**SST**	U^{K}_{38}	U^{K}_{38} Me	$U^{K}_{38\,Et}$	$U^{K}_{37}'/U^{K}_{38\,Et}$	**K38**	**K38 Et**	**K37 / K38**	**K37/K38 Et**
ODP Sample Label	(Mbsf)	(ka)	(ng/g)			(°C)					(ng/g)	(ng/g)		
4H-5W, 10-11	33.30	1119.23	6202.66	0.527	0.564	15.8	0.573	0.445	0.635	0.889	4298.77	2896.81	1.443	2.141
4H-5W, 24-25	33.45	1122.94	10768.50	0.522	0.553	15.4	0.566	0.431	0.637	0.868	8443.02	5548.75	1.275	1.941
4H-5W, 38-39	33.59	1126.65	8844.55	0.516	0.537	14.9	0.560	0.428	0.624	0.861	6297.79	4246.93	1.404	2.083
4H-5W, 52-53	33.73	1133.15	12299.15	0.465	0.528	14.7	0.542	0.368	0.629	0.840	8910.71	5933.47	1.380	2.073
4H-5W, 67-68	33.87	1139.93	11106.64	0.652	0.672	19.0	0.694	0.590	0.737	0.911	7925.06	5587.34	1.401	1.988
4H-5W, 95-96	34.15	1153.50	4521.80	0.612	0.624	17.6	0.624	0.488	0.682	0.915	3193.22	2240.76	1.416	2.018
4H-5W, 109-110	34.29	1160.29	6938.77	0.677	0.677	19.2	0.697	0.578	0.747	0.906	5185.54	3650.81	1.338	1.901
4H-5W, 123-124	34.44	1165.71	3930.54	0.694	0.694	19.7	0.699	0.559	0.753	0.923	2767.22	2005.46	1.420	1.960
4H-5W, 137-128	34.58	1170.45	4301.03	0.685	0.685	19.4	0.699	0.586	0.744	0.922	3447.43	2470.58	1.248	1.741
4H-6W, 01-02	34.72	1175.28	2301.71	0.662	0.662	18.7	0.689	0.562	0.742	0.892	1726.38	1252.59	1.333	1.838
4H-6W, 16-17	34.86	1180.12	6238.59	0.669	0.669	18.9	0.665	0.535	0.717	0.933	4886.56	3498.21	1.277	1.783
4H-6W, 30-31	35.00	1184.95	4086.28	0.677	0.677	19.2	0.680	0.571	0.727	0.931	2956.03	2072.08	1.382	1.972
4H-6W, 44-45	35.14	1189.79	5374.64	0.685	0.685	19.4	0.683	0.563	0.730	0.938	4367.98	3128.90	1.230	1.718
4H-6W, 58-59	35.28	1194.62	3545.18	0.662	0.688	19.5	0.700	0.558	0.752	0.915	2599.75	1912.13	1.364	1.854
4H-6W, 72-73	35.43	1199.45	3442.51	0.656	0.656	18.5	0.661	0.508	0.723	0.908	2726.29	1939.09	1.263	1.775
4H-6W, 86-87	35.57	1204.29	6437.32	0.606	0.622	17.5	0.641	0.497	0.703	0.885	4823.69	3378.92	1.335	1.905
4H-6W, 101-102m	35.71	1211.71	10854.03	0.553	0.603	16.9	0.611	0.426	0.690	0.873	8790.92	6148.42	1.235	1.765
4H-6W, 115-116	35.85	1218.58	5499.83	0.639	0.639	18.0	0.651	0.508	0.712	0.898	4058.05	2843.16	1.355	1.934
4H-7W, 07-08	36.28	1240.55	9546.99	0.649	0.668	18.9	0.680	0.531	0.736	0.909	7171.37	5212.44	1.331	1.832
4H-7W, 21-22	36.42	1247.91	5053.47	0.529	0.569	15.9	0.576	0.426	0.644	0.884	3813.84	2620.19	1.325	1.929
4H-7W, 35-36	36.56	1255.27	6455.46	0.531	0.566	15.8	0.582	0.434	0.651	0.870	4790.43	3262.38	1.348	1.979
5H-1W, 00-01	36.70	1316.72	5103.80	0.580	0.584	16.4	0.583	0.431	0.650	0.898	3847.89	2666.04	1.326	1.914
5H-1W, 14-15	36.84	1320.34	5897.47	0.646	0.646	18.2	0.681	0.550	0.733	0.880	4617.46	3305.37	1.277	1.784
5H-1W, 28-29	36.98	1323.80	5036.93	0.628	0.650	18.4	0.685	0.555	0.738	0.881	3661.06	2590.57	1.376	1.944
5H-1W, 42-43	37.12	1327.26	5295.17	0.690	0.690	19.6	0.703	0.590	0.746	0.925	4255.77	3064.54	1.244	1.728
5H-1W, 56-57	37.27	1330.72	3478.98	0.705	0.705	20.0	0.709	0.571	0.758	0.930	2621.94	1933.04	1.327	1.800
5H-1W, 70-71	37.41	1334.18	4320.07	0.656	0.656	18.5	0.646	0.493	0.708	0.926	3399.89	2413.94	1.271	1.790
5H-1W, 84-85	37.55	1338.46	1966.90	0.658	0.658	18.6	0.648	0.460	0.717	0.918	1521.29	1110.63	1.293	1.771
5H-1W, 99-100	37.69	1342.71	3910.78	0.676	0.676	19.1	0.661	0.542	0.711	0.950	3451.87	2426.03	1.133	1.612
5H-1W, 131-132	37.83	1346.90	4572.93	0.568	0.584	16.4	0.587	0.445	0.653	0.895	3485.61	2389.30	1.312	1.914

ODP 1087A ODP Sample Label	**Depth** (Mbsf)	**Age** (ka)	**K37** (ng/g)	U^{K}_{37}	U^{K}_{37}'	**SST** (°C)	U^{K}_{38}	U^{K}_{38} Me	$U^{K}_{38\ Et}$	$U^{K}_{37}'/U^{K}_{38\ Et}$	**K38** (ng/g)	**K38 Et** (ng/g)	**K37 / K38**	**K37/K38 Et**
5H-1W, 127-128	37.97	1350.93	6992.14	0.546	0.576	16.1	0.580	0.464	0.635	0.908	5617.36	3826.46	1.245	1.827
5H-1W, 141-142	38.11	1354.96	10613.26	0.604	0.644	18.2	0.657	0.529	0.709	0.908	7752.34	5497.10	1.369	1.931
5H-2W, 05-06	38.26	1358.99	9722.01	0.512	0.537	14.9	0.531	0.412	0.587	0.913	7522.88	5127.60	1.292	1.896
5H-2W, 20-21	38.40	1363.11	11521.22	0.589	0.600	16.8	0.615	0.476	0.673	0.891	8044.44	5667.92	1.432	2.033
5H-2W, 34-35	38.55	1367.24	13344.51	0.589	0.610	17.1	0.615	0.479	0.670	0.910	10713.90	7646.90	1.246	1.745
5H-2W, 49-50	38.69	1371.37	3443.30	0.588	0.588	16.5	0.591	0.431	0.658	0.894	2639.65	1855.87	1.304	1.855
5H-2W, 63-64	38.84	1375.49	6839.72	0.579	0.579	16.2	0.581	0.452	0.636	0.910	5485.88	3827.43	1.247	1.787
5H-2W, 78-79	38.98	1379.62	7799.39	0.606	0.638	18.0	0.647	0.497	0.707	0.903	5754.55	4118.33	1.355	1.894
5H-2W, 92-93	39.13	1383.75	5910.92	0.586	0.586	16.4	0.568	0.424	0.629	0.932	4854.71	3419.25	1.218	1.729
5H-2W, 107-108	39.27	1386.97	4372.36	0.669	0.685	19.4	0.686	0.550	0.739	0.926	3378.19	2417.12	1.294	1.809
5H-2W, 121-122	39.42	1389.14	6672.57	0.610	0.610	17.2	0.624	0.511	0.672	0.909	5431.04	3804.22	1.229	1.754
5H-2W, 136-137	39.56	1391.95	5088.25	0.636	0.643	18.2	0.617	0.477	0.678	0.949	3958.91	2771.72	1.285	1.836
5H-3W, 00-01	39.71	1394.77	6729.05	0.568	0.600	16.8	0.599	0.459	0.656	0.914	5354.58	3814.70	1.257	1.764
5H-3W, 15-16	39.85	1397.58	6220.37	0.713	0.713	20.3	0.715	0.599	0.759	0.939	4916.61	3555.94	1.265	1.749
5H-3W, 29-30	40.00	1400.40	5486.35	0.634	0.634	17.9	0.639	0.492	0.697	0.909	4454.17	3205.33	1.232	1.712
5H-3W, 44-45	40.14	1403.21	3294.54	0.666	0.666	18.9	0.697	0.552	0.751	0.888	2357.57	1715.52	1.397	1.920
5H-3W, 58-59	40.29	1406.03	14061.76	0.578	0.596	16.7	0.583	0.460	0.637	0.935	12106.03	8416.03	1.162	1.671
5H-3W, 73-74	40.43	1408.84	6629.43	0.648	0.648	18.3	0.648	0.515	0.700	0.925	4900.79	3517.17	1.353	1.885
5H-3W, 102-103	40.72	1414.47	5361.62	0.656	0.656	18.5	0.651	0.521	0.705	0.930	3817.90	2710.03	1.404	1.978
5H-3W, 116-117	40.87	1417.29	6972.64	0.675	0.675	19.1	0.681	0.526	0.749	0.901	5354.26	3727.30	1.302	1.871
5H-3W, 131-132	41.01	1421.72	9850.55	0.628	0.640	18.1	0.655	0.517	0.713	0.898	7487.20	5278.16	1.316	1.866
5H-4W, 10-11	41.30	1429.56	14581.42	0.633	0.633	17.8	0.641	0.512	0.698	0.906	11881.22	8214.87	1.227	1.775
5H-4W, 24-25	41.45	1433.49	5376.60	0.684	0.684	19.4	0.665	0.554	0.716	0.955	4309.05	2936.98	1.248	1.831
5H-4W, 39-40	41.59	1437.41	5588.08	0.590	0.638	18.0	0.645	0.456	0.731	0.872	4105.29	2820.98	1.361	1.981
5H-4W, 53-54	41.74	1441.33	8087.46	0.659	0.659	18.6	0.652	0.526	0.702	0.939	6994.05	4992.66	1.156	1.620
5H-4W, 68-69	41.88	1445.26	3772.17	0.668	0.668	18.9	0.681	0.554	0.735	0.909	2925.13	2058.09	1.290	1.833
5H-4W, 82-83	42.03	1449.18	6122.63	0.698	0.698	19.8	0.710	0.587	0.755	0.925	5228.81	3825.52	1.171	1.600
5H-4W, 97-98	42.17	1453.10	5366.60	0.691	0.691	19.6	0.676	0.549	0.728	0.950	4574.67	3243.67	1.173	1.654
5H-4W, 111-112	42.32	1457.03	7509.77	0.699	0.699	19.9	0.694	0.574	0.744	0.941	6606.52	4692.31	1.137	1.600
5H-4W, 126-127	42.46	1460.95	10631.47	0.623	0.641	18.1	0.663	0.514	0.723	0.887	7636.13	5441.25	1.392	1.954

ODP 1087A ODP Sample Label	**Depth** (Mbsf)	**Age** (ka)	**K37** (ng/g)	**U^K_{37}**	**U^K_{37}'**	**SST** (°C)	U^K_{38}	U^K_{38} Me	$U^K_{38\ Et}$	U^K_{37}' /$U^K_{38\ Et}$	**K38** (ng/g)	**K38 Et** (ng/g)	**K37 / K38**	**K37/K38 Et**
5H-4W, 140-141	42.61	1465.24	10009.50	0.537	0.570	15.9	0.571	0.413	0.639	0.893	8097.94	5672.79	1.236	1.764
5H-5W, 19-20	42.90	1474.17	8952.49	0.593	0.593	16.6	0.601	0.488	0.651	0.911	7449.41	5176.99	1.202	1.729
5H-5W, 34-35	43.04	1478.62	6357.00	0.626	0.652	18.4	0.642	0.510	0.694	0.940	4753.89	3412.04	1.337	1.863
5H-5W, 48-49	43.19	1483.08	10658.85	0.618	0.618	17.4	0.620	0.512	0.663	0.931	9126.14	6514.52	1.168	1.636
5H-5W, 63-64	43.33	1487.53	7861.82	0.625	0.635	17.9	0.637	0.504	0.691	0.919	5881.84	4181.11	1.337	1.880
5H-5W, 77-78	43.48	1491.98	6851.97	0.602	0.602	16.9	0.605	0.453	0.668	0.902	5592.17	3946.25	1.225	1.736
5H-5W, 92-93	43.62	1496.44	6562.66	0.699	0.699	19.8	0.695	0.582	0.742	0.941	5251.75	3710.87	1.250	1.768
5H-5W, 106-107	43.77	1500.89	7564.29	0.634	0.634	17.9	0.632	0.467	0.699	0.908	6270.10	4448.82	1.206	1.700
5H-5W, 121-122	43.91	1505.35	8878.49	0.615	0.624	17.6	0.624	0.490	0.681	0.915	7196.36	5022.21	1.234	1.768
5H-5W, 135-136	44.06	1509.44	11510.94	0.529	0.579	16.2	0.591	0.435	0.652	0.887	9018.28	6473.52	1.276	1.778
5H-6W, 00-01	44.20	1513.14	7467.71	0.641	0.660	18.7	0.658	0.517	0.719	0.918	5689.92	3979.92	1.312	1.876
5H-6W, 14-15	44.35	1517.11	10899.58	0.616	0.616	17.3	0.622	0.490	0.680	0.907	8411.00	5834.73	1.296	1.868

A4: Coccolith results from ODP 1087 Site A (Chapter 4). ODP labelling is Core-Section, depth interval (cm). All other terms defined in Chapters 2 and 4.

ODP 1087A	**Depth**	**Age**	**Coccolith species (percentage of total counted)**								**Coccolith abundance**	**Bulk MAR**	**Coccolith AR**
ODP Sample Label	(Mbsf)	(ka)	Small placoliths	Small Gephyrocapsa	G.oceanica	G.carribbeanica	P.lacunosa	Medium Reticulofenestra	Others	Number counted	(n°x10^8/g)	(g/cm^2/kyr)	(n°x10^8/cm^2/kyr)
2H 4W, 5	12.63	486.10	2.96	19.41	21.04	55.46	0.65	0.00	0.49	613	140.60	2.70	379.9
2H 5W, 80	14.88	621.96	3.56	30.00	19.78	41.56	2.00	0.00	3.11	450	110.57	1.85	204.1
2H 6W, 145	17.03	693.20	4.58	49.58	22.92	0.00	17.08	0.00	5.83	240	54.27	3.16	171.3
3H 2W, 5	19.23	767.23	2.23	53.64	31.17	6.68	4.05	0.00	2.23	494	117.61	7.15	840.6
3H 3W, 75	21.43	798.20	8.38	79.82	5.29	5.94	0.57	0.00	0.00	1229	308.57	5.56	1715.0
3H 4W, 145	23.43	830.32	10.36	81.51	5.12	0.67	1.11	0.00	1.22	898	197.47	5.82	1149.1
3H 5W, 70	24.18	841.79	13.21	76.60	4.91	2.14	1.26	0.00	1.89	795	175.18	5.62	984.8
3H 6W, 145	26.43	851.19	45.82	41.49	10.06	0.00	1.70	0.00	0.93	646	140.75	6.06	853.1
4H 1W, 140	28.60	979.18	27.18	62.36	6.27	0.38	1.90	1.33	0.57	526	118.99	3.36	399.7
4H 2W, 70	29.40	1001.90	23.70	64.31	5.64	0.43	3.47	1.30	1.16	692	148.85	3.35	499.2
4H 3W, 130	31.48	1066.42	18.05	74.21	4.01	0.00	1.15	1.43	1.15	698	155.57	2.79	434.4
4H 5W, 60	33.68	1136.59	33.34	56.97	0.61	0.00	3.33	4.85	0.91	330	80.18	2.09	167.7
4H 7W, 60	36.38	1248.93	46.68	38.67	2.21	0.28	6.63	1.66	3.87	362	85.94	1.86	159.6
5H 2W, 60	38.80	1374.46	46.63	46.33	0.60	1.65	3.60	0.30	0.90	667	147.89	3.39	501.9
5H 3W, 138	41.08	1423.58	40.95	41.27	7.94	3.49	3.81	0.95	1.59	315	70.27	3.67	257.6
5H 5W, 60	43.20	1486.57	35.20	39.25	9.30	11.21	1.87	0.31	3.12	321	74.21	3.20	237.3
5H 6W, 140	45.50	1552.11	48.59	28.87	3.52	13.03	2.11	0.70	3.17	284	42.01	5.39	226.5
6H 1W, 140	47.60	1600.00	36.32	37.81	8.21	12.69	2.24	0.50	2.24	402	90.52	5.39	488.0
6H 3W, 70	49.90	1650.00	39.65	30.61	6.71	11.66	4.08	2.92	4.37	343	80.08	5.39	431.7
6H 4W, 140	52.00	1700.00	41.92	31.74	6.59	2.69	6.59	5.09	5.39	334	75.92	6.05	459.4
6H 5W, 70	52.80	1750.00	32.97	43.60	12.26	4.90	2.45	1.09	2.72	367	80.40	6.05	486.5

A5: Results from ODP 849. ODP labelling is Site-Core-Section, depth interval (cm). All other terms defined in Chapters 1 and 2.

ODP 849 ODP Sample Label	**Depth** (Rmcd)	**Age** (ka)	**Bulk MAR** ($g/cm^2/kyr$)	**P410** (AU/g)	**AR P410** ($AU/cm^2/kyr$)	**P665** (AU/g)	**AR P665** ($AU/cm^2/kyr$)	**S/I**	**K37** (ng/g)	**MAR K37** ($\mu g/cm^2/kyr$)	U^{K}_{37}'	**SST** (°C)	**Particle size** (Mean <30μm)
C-2H-2W, 38-40	15.39	500.10	1.518	1.03	1.56	0.07	0.11	14.77	46.63	70.78	0.859	24.689	
C-2H-2W, 50-51	15.51	505.08	1.518	4.46	6.77	0.44	0.67	10.14	69.75	105.89	0.881	25.356	
C-2H-2W, 62-63	15.62	509.70	1.499	57.93	86.85	0.91	1.37	63.45	163.16	244.61	0.857	24.634	
C-2H-2W, 74-75	15.74	514.64	1.530	14.11	21.58	1.50	2.30	9.40	112.27	171.72	0.854	24.542	
C-2H-2W, 88-89	15.88	519.78	1.716	8.35	14.33	0.46	0.78	18.26	71.29	122.32	0.887	25.537	
C-2H-2W, 104-105	16.04	524.85	1.990	10.90	21.68	1.39	2.76	7.85	29.18	58.07	0.877	25.243	
C-2H-2W, 122-123	16.22	529.94	2.228	6.90	15.38	0.49	1.09	14.17	41.45	92.36	0.839	24.089	
C-2H-2W, 138-139	16.38	534.67	2.129	6.01	12.79	0.49	1.04	12.34	43.40	92.41	0.846	24.302	
C-2H-3W, 2-3	16.52	539.76	1.733	19.74	34.21	0.88	1.53	22.41	126.65	219.43	0.836	23.993	
C-2H-3W, 14-15	16.64	544.86	1.483	8.58	12.72	0.85	1.26	10.07	113.77	168.68	0.843	24.217	
C-2H-3W, 24-26	16.74	549.66	1.312	17.20	22.57	3.46	4.54	4.97	220.73	289.64	0.836	24.002	
C-2H-3W, 34-35	16.84	554.63	1.267	8.19	10.37	0.52	0.66	15.73	153.60	194.57	0.860	24.714	
C-2H-3W, 44-45	16.94	559.67	1.251	8.72	10.91	0.59	0.74	14.69	27.33	34.19	0.838	24.069	
C-2H-3W, 55-56	17.05	564.81	1.350	4.86	6.57	0.35	0.47	13.82	58.85	79.42	0.877	25.228	
C-2H-3W, 67-68	17.17	570.01	1.452	28.55	41.47	0.68	0.98	42.18	166.81	242.29	0.865	24.882	
C-2H-3W, 80-81	17.30	574.94	1.662	6.34	10.53	0.55	0.92	11.42	48.90	81.28	0.916	26.426	
C-2H-3W, 94-95	17.44	579.98	1.748	7.41	12.95	0.45	0.78	16.52	55.13	96.34	0.918	26.499	
C-2H-3W, 124-125	17.74	589.85	1.916	30.96	59.32	3.78	7.24	8.19	157.19	301.13	0.867	24.938	
C-2H-3W, 140-141	17.90	594.95	1.976	7.10	14.04	0.64	1.26	11.15	98.90	195.48	0.891	25.657	
C-2H-4W, 21-22	18.21	604.80	1.983	7.47	14.81	0.50	0.98	15.08	100.01	198.32	0.887	25.544	
C-2H-4W, 36-37	18.36	609.92	1.845	8.70	16.06	0.40	0.74	21.83	159.31	293.98	0.905	26.087	
C-2H-4W, 48-49	18.48	614.66	1.595	4.40	7.01	0.35	0.55	12.70	28.91	46.11	0.874	25.150	
C-2H-4W, 60-61	18.60	619.89	1.446	7.66	11.08	0.26	0.38	29.37	36.49	52.76	0.867	24.941	
C-2H-4W, 70-71	18.70	624.79	1.286	5.05	6.49	0.70	0.90	7.20	46.37	59.62	0.863	24.822	
C-2H-4W, 80-81	18.80	629.85	1.244	13.39	16.66	2.04	2.54	6.57	0.00	0.00			
C-2H-4W, 90-91	18.90	634.90	1.249	2.83	3.53	0.27	0.34	10.53	104.96	131.06	0.850	24.423	
D-2H-2W, 4-5	19.04	637.40	3.528						130.33	459.80	0.845	24.267	12.9
D-2H-2W, 12-13	19.11	644.52	1.375	5.31	7.31	0.65	0.89	8.18	66.56	41.23	0.844	24.228	

ODP 849	Depth	Age	Bulk MAR	P410	AR P410	P665	AR P665	S/I	K37	MAR K37	U^{K}_{37}'	SST	Particle size
ODP Sample Label	(Rmcd)	(ka)	($g/cm^2/kyr$)	(AU/g)	($AU/cm^2/kyr$)	(AU/g)	($AU/cm^2/kyr$)		(ng/g)	($\mu g/cm^2/kyr$)		(°C)	(Mean <30μm)
D-2H-2W, 23-25	19.24	649.67	1.592	1.96	3.12	0.27	0.43	7.22	90.63	144.27	0.838	24.049	
D-2H-2W, 36-37	19.39	655.12	1.732	2.92	5.06	0.27	0.46	10.90	59.79	103.58	0.842	24.174	
D-2H-2W, 52-53	19.53	659.86	1.863	7.02	13.07	0.38	0.72	18.26	72.44	134.93	0.859	24.701	
D-2H-2W, 68-69	19.69	665.13	1.913	11.98	22.91	1.45	2.78	8.25	181.71	347.56	0.818	23.467	
D-2H-2W, 85-86	19.84	669.96	1.957	4.25	8.32	0.80	1.56	5.32	108.64	212.56	0.834	23.930	
D-2H-2W, 100-101	19.99	674.63	2.021	7.84	15.85	1.79	3.62	4.38	81.87	165.47	0.858	24.668	
D-2H-2W, 116-117	20.17	679.93	2.140	5.28	11.30	0.60	1.28	8.82	236.62	506.31	0.870	25.025	
D-2H-2W, 135-136	20.37	685.56	2.238	22.81	51.06	3.14	7.02	7.27	307.84	688.96	0.901	25.959	
D-2H-3W, 3-4	20.54	690.39	2.217	8.30	18.41	0.80	1.78	10.33	272.30	603.79	0.873	25.108	
D-2H-3W, 23-24	20.67	694.34	2.073	9.58	19.87	1.66	3.44	5.77	91.05	188.78	0.882	25.389	
D-2H-3W, 43-44	20.82	699.35	1.885	15.13	28.51	2.61	4.91	5.80	269.68	508.24	0.897	25.854	
D-2H-3W, 61-62	20.95	704.43	1.615	14.69	23.72	1.68	2.72	8.73	104.77	169.22	0.885	25.476	
D-2H-3W, 87-88	21.17	714.59	1.364	23.12	31.54	3.43	4.67	6.75	220.55	300.85	0.845	24.274	
D-2H-3W, 99-100	21.27	719.78	1.213	33.58	40.73	4.14	5.02	8.12	555.84	674.17	0.829	23.781	11.8
D-2H-3W, 111-112	21.36	724.66	1.163	11.53	13.40	1.22	1.42	9.46	250.18	290.87	0.851	24.468	
D-2H-3W, 119-120	21.45	729.73	1.119	15.81	17.68	1.43	1.60	11.06	116.73	130.59	0.836	24.002	
D-2H-3W, 130-131	21.54	734.99	1.077	10.06	10.83	0.98	1.06	10.26	74.24	79.95	0.917	26.466	
D-2H-3W, 140-141	21.63	740.36	1.056	11.90	12.57	0.44	0.47	26.77	132.48	139.88	0.896	25.830	
D-2H-4W, 0-1	21.69	744.04	1.029	10.45	10.74	0.92	0.94	11.38	47.07	48.42			
D-2H-4W, 9-11	21.78	749.54	1.031	7.17	7.39	0.48	0.49	15.07	325.49	335.45	0.856	24.610	
D-2H-4W, 19-20	21.87	754.93	1.051	7.26	7.63	1.07	1.12	6.81	95.69	100.60	0.869	24.998	
D-2H-4W, 28-29	21.95	759.58	1.084	28.63	31.02	4.70	5.09	6.09	321.05	347.90	0.799	22.885	
D-2H-4W, 38-39	22.05	764.98	1.168	9.62	11.23	0.79	0.92	12.24	71.28	83.25	0.871	25.074	
D-2H-4W, 48-49	22.15	769.63	1.352	5.75	7.78	0.45	0.61	12.68	463.74	627.06	0.835	23.974	
D-2H-4W, 60-61	22.28	774.90	1.555	3.29	5.12	0.32	0.49	10.36	58.86	91.54	0.884	25.453	
D-2H-4W, 73-74	22.43	779.76	1.946	2.58	5.01	0.15	0.29	17.27	54.71	106.44	0.898	25.886	
D-2H-4W, 91-92	22.62	784.84	2.356	1.93	4.55	0.09	0.21	21.89	37.03	87.25	0.898	25.887	
D-2H-4W, 110-111	22.81	789.90	2.364	4.53	10.70	0.29	0.70	15.38					
D-2H-4W, 125-126	22.93	794.80	1.960	8.18	12.62	1.07	1.66	7.63	91.02	178.42	0.831	23.848	12.3
D-2H-4W, 136-138	23.03	799.36	1.383	2.12	2.94	0.12	0.16	18.27	107.40	148.54	0.861	24.753	

ODP 849 ODP Sample Label	**Depth** (Rmcd)	**Age** (ka)	**Bulk MAR** (g/cm^2/kyr)	**P410** (AU/g)	**AR P410** (AU/cm^2/kyr)	**P665** (AU/g)	**AR P665** (AU/cm^2/kyr)	**S/I**	**K37** (ng/g)	**MAR K37** (μg/cm^2/kyr)	U^{K}_{37}'	**SST** (°C)	**Particle size** (Mean <30μm)
D-2H-4W, 146-147	23.12	804.62	1.077	4.66	5.02	0.48	0.52	9.74	148.18	159.58	0.835	23.977	
D-2H-5W, 5-6	23.21	810.00	1.054	7.07	7.45	0.52	0.54	13.71	139.31	146.77	0.864	24.835	
D-2H-5W, 10-11	23.26	813.20	0.985	6.92	6.81	0.82	0.81	8.43	114.27	112.56	0.869	24.985	
D-2H-5W, 18-19	23.36	819.55	0.992	6.58	6.53	0.60	0.59	11.00	165.95	164.66	0.859	24.697	
D-2H-5W, 25-26	23.46	825.30	1.096	4.35	4.77	0.39	0.42	11.24	52.03	57.05	0.909	26.201	
D-2H-5W, 34-35	23.59	831.84	1.252	3.10	3.89	0.21	0.26	14.79	96.06	120.28	0.905	26.094	
D-2H-5W, 41-42	23.66	834.48	1.668	5.92	9.87	0.52	0.86	11.44	115.70	192.96	0.898	25.889	
D-2H-5W, 52-53	23.84	839.84	2.116	5.77	12.20	0.25	0.52	23.43	214.22	453.34	0.861	24.767	
D-2H-5W, 73-74	24.07	844.99	2.811	4.09	11.49	0.40	1.13	10.20	136.02	382.37	0.849	24.401	
D-2H-5W, 95-96	24.29	849.81	2.880	2.53	7.28	0.51	1.47	4.96	62.67	180.51	0.899	25.907	
D-2H-5W, 113-114	24.47	854.85	2.250	2.86	6.43	0.18	0.40	16.17	45.02	101.30	0.905	26.103	
D-2H-5W, 126-127	24.61	859.64	1.839	11.22	20.64	0.88	1.63	12.69	138.41	254.60	0.908	26.180	
D-2H-5W, 136-137	24.72	864.48	1.432	25.85	37.02	2.68	3.84	9.65	125.07	179.07	0.842	24.168	
D-2H-5W, 146-147	24.84	869.88	1.400	26.87	37.62	4.45	6.23	6.04	296.18	414.65	0.799	22.867	12.7
D-2H-6W, 05-06	24.94	874.58	1.340	15.53	20.82	1.42	1.90	10.97	173.58	232.67	0.832	23.891	13.0
D-2H-6W, 16-17	25.06	879.92	1.416	7.60	10.76	0.56	0.79	13.67	128.54	181.98	0.813	23.308	
D-2H-6W, 27-28	25.17	884.54	1.500	10.69	16.04	1.27	1.90	8.42	129.66	194.49	0.790	22.598	
D-2H-6W, 41-42	25.31	889.60	1.745	22.59	39.42	4.33	7.56	5.21	280.46	489.35	0.788	22.548	12.7
B-3H-4W, 89-91	25.64	899.80	2.037	2.99	6.08	0.26	0.52	11.69	58.28	118.73	0.861	24.752	13.6
B-3H-4W, 126-127	26.01	909.90	2.309	68.85	158.95	5.98	13.81	11.51	351.12	810.61	0.834	23.945	
B-3H-5W, 9-10	26.34	919.94	2.070	31.33	64.86	3.53	7.32	8.87	286.20	592.46	0.828	23.765	
B-3H-5W, 57-58	26.82	939.75	1.527	9.58	14.62	0.24	0.37	39.65	108.69	165.91	0.898	25.893	
C-3H-1W, 53-54	26.93	944.98	1.326	3.05	4.04	0.30	0.40	10.07	35.39	46.94	0.899	25.922	
C-3H-1W, 63-65	27.03	949.58	1.369	1.93	2.65	0.23	0.32	8.31	35.51	48.60	0.872	25.096	
C-3H-1W, 75-76	27.15	954.64	1.492	9.77	14.59	1.23	1.83	7.97	40.38	60.27	0.918	26.475	
C-3H-1W, 88-89	27.28	959.86	1.570	24.49	38.44	4.51	7.08	5.43	309.72	486.27	0.892	25.694	
C-3H-1W, 103-104	27.43	964.76	1.928	13.35	25.74	2.30	4.44	5.80	157.17	303.00	0.852	24.470	
C-3H-1W, 121-122	27.61	969.79	2.255	15.00	33.83	2.33	5.26	6.44	268.14	604.75	0.865	24.874	
C-3H-1W, 140-141	27.80	974.72	2.428	11.04	26.81	1.23	2.99	8.96	116.64	283.20	0.863	24.821	
C-3H-2W, 7-8	27.97	979.77	2.120	29.23	61.97	4.99	10.57	5.86	448.03	949.79	0.838	24.067	12.2

ODP 849	**Depth**	**Age**	**Bulk MAR**	**P410**	**AR P410**	**P665**	**AR P665**	**S/I**	**K37**	**MAR K37**	**U^{K}_{37}'**	**SST**	**Particle size**
ODP Sample Label	(Rmcd)	(ka)	(g/cm^2/kyr)	(AU/g)	(AU/cm^2/kyr)	(AU/g)	(AU/cm^2/kyr)		(ng/g)	(µg/cm^2/kyr)		(°C)	(Mean <30µm)
C-3H-2W, 20-21	28.10	984.80	1.629	7.58	12.35	1.06	1.73	7.12	114.16	185.95	0.841	24.151	
C-3H-2W, 31-32	28.20	989.30	1.400	3.66	5.12	0.38	0.53	9.73	132.50	185.50	0.863	24.833	
C-3H-2W, 40-41	28.30	994.30	1.260	2.88	3.63	0.25	0.32	11.31	41.49	52.28	0.892	25.711	
C-3H-2W, 50-52	28.41	1000.09	1.197	6.49	7.77	1.00	1.20	6.49	70.36	84.24	0.881	25.369	
C-3H-2W, 59-60	28.50	1004.75	1.216	5.20	6.32	0.52	0.63	10.04	68.04	82.75	0.866	24.914	
C-3H-2W, 70-71	28.60	1009.68	1.277	4.08	5.21	0.41	0.53	9.89	128.81	164.47	0.868	24.972	
C-3H-2W, 85-86	28.74	1015.85	1.430	3.58	5.12	0.32	0.45	11.32	96.50	138.03	0.875	25.192	
C-3H-2W, 95-96	28.84	1019.88	1.565	7.30	11.42	0.55	0.86	13.33	108.93	170.50	0.844	24.241	
C-3H-2W, 107-108	28.97	1024.79	1.665	5.03	8.38	0.65	1.08	7.73	90.22	150.24	0.886	25.515	
C-3H-2W, 120-121	29.10	1029.95	1.588	4.75	7.54	0.58	0.92	8.19	81.82	129.94	0.906	26.124	
C-3H-2W, 133-134	29.22	1034.99	1.499	5.38	8.07	0.48	0.72	11.15	92.20	138.21	0.886	25.519	
C-3H-2W, 146-147	29.36	1041.36	1.385	12.10	16.77	1.77	2.45	6.85	310.94	430.76	0.866	24.895	
C-3H-3W, 03-04	29.43	1044.50	1.405	5.55	7.80	1.00	1.40	5.58	164.07	230.45	0.875	25.187	
D-3H-3W, 7-9	29.54	1049.43	1.406	13.17	18.52	2.38	3.34	5.54	65.94	92.68	0.890	25.642	
D-3H-3W, 15-16	29.67	1054.63	1.576	23.60	37.19	2.36	3.72	10.00	283.20	446.18	0.853	24.517	11.7
D-3H-3W, 29-30	29.82	1060.13	1.718	11.49	19.74	0.90	1.54	12.78	298.97	513.52	0.860	24.716	
D-3H-3W, 45-46	29.98	1064.98	2.078	6.80	14.14	0.82	1.70	8.30	95.34	198.15	0.878	25.270	
D-3H-3W, 75-76	30.30	1074.90	2.032	13.94	28.33	1.97	4.00	7.08	79.25	161.06	0.918	26.472	
D-3H-3W, 106-107	30.55	1084.75	1.599	25.33	40.49	3.80	6.08	6.66	215.69	344.88	0.871	25.069	
D-3H-3W, 117-118	30.66	1089.90	1.346	8.06	10.85	0.43	0.58	18.58	163.94	220.61	0.892	25.710	
D-3H-3W, 125-126	30.76	1094.90	1.260	2.99	3.77	0.49	0.62	6.05	229.55	289.23	0.866	24.900	
D-3H-3W, 133-135	30.87	1100.05	1.345	5.80	7.80	0.77	1.04	7.52	170.69	229.51	0.872	25.080	
D-3H-3W, 142-143	30.99	1105.38	1.420	5.27	7.48	0.55	0.79	9.52	41.19	58.48	0.894	25.758	
D-3H-4W, 2-3	31.10	1109.66	1.620	4.16	6.73	0.34	0.55	12.22	51.40	83.27	0.884	25.462	
D-3H-4W, 16-17	31.24	1114.72	1.742	6.50	11.33	0.48	0.83	13.64	35.81	62.38	0.918	26.485	
D-3H-4W, 32-33	31.42	1120.28	2.039	11.77	23.98	1.69	3.45	6.96	47.11	96.03	0.887	25.534	
D-3H-4W, 46-47	31.56	1124.80	1.953	14.54	28.38	1.80	3.51	8.09	269.93	527.04	0.863	24.804	11.7
D-3H-4W, 58-59	31.69	1129.70	1.671	11.48	19.19	1.32	2.21	8.70	200.12	334.49	0.872	25.088	
D-3H-4W, 70-71	31.81	1134.79	1.485	6.05	8.99	0.31	0.45	19.78	68.18	101.25	0.904	26.070	
D-3H-4W, 79-80	31.91	1139.60	1.310	15.48	20.28	0.97	1.27	15.92	197.15	258.27	0.875	25.187	

ODP 849 ODP Sample Label	**Depth** (Rmcd)	**Age** (ka)	**Bulk MAR** ($g/cm^2/kyr$)	**P410** (AU/g)	**AR P410** ($AU/cm^2/kyr$)	**P665** (AU/g)	**AR P665** ($AU/cm^2/kyr$)	**S/I**	**K37** (ng/g)	**MAR K37** ($\mu g/cm^2/kyr$)	U^{K}_{37}'	**SST** (°C)	**Particle size** (Mean <30μm)
D-3H-4W, 94-95	32.10	1149.81	1.172	7.96	9.33	1.23	1.44	6.47	64.59	75.72	0.903	26.025	
D-3H-4W, 100-101	32.16	1153.23	1.104	12.29	13.57	1.79	1.97	6.87	97.04	107.18	0.891	25.658	
D-3H-4W, 110-111	32.28	1160.14	1.095	11.62	12.72	0.85	0.93	13.62	117.15	128.24	0.897	25.852	
D-3H-4W, 142-143	32.48	1171.50	1.109	11.72	13.00	1.67	1.86	7.00	196.38	217.82	0.855	24.572	
D-3H-4W, 149-150	32.55	1175.35	1.145	9.42	10.79	1.29	1.48	7.30	43.08	49.35	0.936	27.037	
D-3H-5W, 17-18	32.63	1179.60	1.186	9.05	10.73	0.94	1.11	9.64	91.69	108.73	0.927	26.752	
D-3H-5W, 32-33	32.74	1184.96	1.293	13.72	17.74	1.42	1.84	9.63	42.64	55.13	0.938	27.094	
D-3H-5W, 41-42	32.83	1189.02	1.398	6.50	9.08	0.36	0.51	17.90	73.67	102.99	0.945	27.296	
D-3H-5W, 50-51	32.94	1193.45	1.561	5.13	8.01	0.33	0.52	15.43	89.39	139.55	0.905	26.080	
D-3H-5W, 61-62	33.12	1199.94	1.748	3.61	6.31	0.30	0.52	12.15	60.11	105.04	0.907	26.146	
D-3H-5W, 65-66	33.27	1204.74	1.970	2.97	5.85	0.30	0.60	9.78	100.17	197.36	0.886	25.508	
D-3H-5W, 77-78	33.45	1209.88	2.208	2.71	5.97	0.37	0.81	7.39	96.84	213.86	0.895	25.782	
D-3H-5W, 104-105	33.65	1214.85	2.533	6.64	16.82	0.47	1.18	14.24	151.77	384.39	0.879	25.301	11.4
D-3H-5W, 136-137	33.88	1220.02	2.803	12.89	36.12	0.82	2.30	15.73	136.80	383.41	0.909	26.220	
D-3H-6W, 03-4	34.12	1225.18	2.930	12.57	36.83	0.96	2.81	13.12	44.21	129.54	0.952	27.527	
D-3H-6W, 11-12	34.20	1227.00	2.774	6.98	19.36	0.58	1.61	11.99	63.25	175.49	0.945	27.317	
D-3H-6W, 21-22	34.42	1232.37	2.581	5.37	13.87	0.38	0.98	14.18	106.61	275.22	0.908	26.189	
D-3H-6W, 32-33	34.75	1241.73	2.221	15.32	34.04	3.30	7.32	4.65	66.75	148.27	0.899	25.922	
D-3H-6W, 46-47	34.85	1244.75	2.083	7.00	14.58	0.50	1.05	13.90	44.18	92.01	0.891	25.678	
D-3H-6W, 87-89	35.02	1250.01	2.036	9.29	18.92	0.99	2.02	9.36	121.63	247.66	0.888	25.567	
D-3H-6W, 109-110	35.16	1254.24	2.084	13.28	27.68	1.08	2.25	12.30	203.38	423.82	0.868	24.972	10.8
D-3H-6W, 121-122	35.32	1258.80	2.210	1.94	4.28	0.18	0.40	10.63	141.50	312.66	0.880	25.329	
D-3H-6W, 134-135	35.58	1265.42	2.476	6.84	16.93	0.55	1.35	12.53	118.04	292.26	0.864	24.838	
D-3H-7W, 7-8	35.79	1269.89	2.962	12.28	36.37	0.95	2.81	12.93	109.36	323.94	0.907	26.142	
D-3H-7W, 38-39	36.03	1274.89	3.022	5.78	17.47	0.43	1.30	13.41	77.78	235.03	0.900	25.950	
D-3H-7W, 66-67	36.35	1283.00	2.486	12.14	30.18	1.61	3.99	7.56	117.81	292.86	0.896	25.832	
D-3H-7W, 70-71	36.29	1284.00	6.930						124.77	864.66	0.907	26.163	
D-3H-7W, 80-81	36.56	1290.09	1.035	12.01	22.42	1.27	2.36	9.48	161.58	167.18	0.878	25.264	
C-4H-1W, 05-06	36.73	1296.42	1.692	16.45	27.83	1.83	3.10	8.98	131.90	223.22	0.876	25.222	
C-4H-1W, 13-15	36.82	1299.85	1.651	20.03	33.08	3.75	6.19	5.35	238.26	393.39	0.875	25.187	

ODP 849	**Depth**	**Age**	**Bulk MAR**	**P410**	**AR P410**	**P665**	**AR P665**	**S/I**	**K37**	**MAR K37**	**U^{K}_{37}'**	**SST**	**Particle size**
ODP Sample Label	(Rmcd)	(ka)	(g/cm^2/kyr)	(AU/g)	(AU/cm^2/kyr)	(AU/g)	(AU/cm^2/kyr)		(ng/g)	(μg/cm^2/kyr)		(°C)	(Mean <30μm)
C-4H-1W, 25-26	36.95	1304.80	1.655	7.49	12.39	0.75	1.24	10.00	82.88	137.17	0.880	25.319	
C-4H-1W, 37-38	37.09	1309.81	1.762	14.19	25.01	0.90	1.59	15.76	130.23	229.49	0.895	25.786	
C-4H-1W, 51-52	37.25	1315.08	1.913	4.47	8.56	0.36	0.69	12.35	55.70	106.53	0.915	26.390	
C-4H-1W, 69-70	37.41	1319.70	2.179	7.76	16.91	0.45	0.98	17.26	105.01	228.79	0.893	25.739	
C-4H-2W, 26-27	37.61	1324.84	2.455	8.26	20.29	0.83	2.03	9.99	84.50	207.41	0.919	26.502	
C-4H-2W, 59-60	37.83	1330.01	2.681	26.42	70.83	1.77	4.75	14.93	230.00	616.60	0.873	25.127	
C-4H-2W, 76-77	38.04	1335.00	2.649	7.77	20.59	0.75	1.98	10.42	161.61	428.05	0.884	25.452	
C-4H-2W, 87-88	38.23	1339.86	2.465	34.83	85.86	3.69	9.09	9.44	580.65	1431.60	0.857	24.646	
C-4H-2W, 100-101	38.40	1344.78	2.173	18.03	39.18	3.03	6.59	5.95	184.20	400.25	0.859	24.702	
C-4H-2W, 116-118	38.56	1349.82	2.002	2.90	5.81	0.21	0.42	13.80	70.27	140.65	0.924	26.678	
C-4H-2W, 133-134	38.71	1354.84	1.882	3.16	5.96	0.45	0.85	7.04	21.62	40.70	0.949	27.429	
C-4H-3W, 1-2	38.85	1359.53	1.883	11.53	21.70	0.98	1.85	11.71	89.96	169.36	0.924	26.678	
C-4H-3W, 20-21	39.02	1364.86	2.008	10.92	21.92	1.25	2.51	8.73	103.87	208.60	0.920	26.547	
D-4H-1W, 25-26	39.07	1366.24	2.274	6.92	15.75	0.97	2.20	7.15	134.63	306.21	0.925	26.709	
D-4H-1W, 46-47	39.28	1371.78	2.389	3.94	9.40	0.57	1.37	6.86	136.84	326.97	0.882	25.400	
D-4H-1W, 52-53	39.45	1377.00	2.054	8.46	17.37	0.92	1.88	9.24	189.81	389.78	0.886	25.502	
D-4H-1W, 59-60	39.71	1387.20	1.605	4.43	7.10	0.61	0.98	7.25	82.76	132.81	0.908	26.182	
D-4H-1W, 66-67	39.78	1389.95	1.605	6.74	10.82	0.76	1.21	8.93	100.17	160.76	0.872	25.083	
D-4H-1W, 74-75	39.88	1394.74	1.315	2.03	2.67	0.11	0.14	19.28	40.87	53.73	0.928	26.798	
D-4H-1W, 87-89	39.96	1398.85	1.227	2.92	3.58	0.53	0.65	5.53	60.41	74.11	0.935	26.986	
D-4H-1W, 104-105	40.10	1406.55	1.145	8.13	9.31	0.60	0.69	13.48	74.91	85.80	0.927	26.747	
D-4H-1W, 109-110	40.15	1409.53	1.059	6.34	6.72	0.33	0.35	19.10	87.13	92.25	0.922	26.608	
D-4H-1W, 119-120	40.24	1414.88	1.059	6.00	6.35	0.65	0.69	9.24	120.05	127.11	0.906	26.109	
D-4H-1W, 124-125	40.32	1419.64	1.059	7.11	7.53	0.92	0.97	7.77	109.13	115.55	0.888	25.586	
D-4H-1W, 131-132	40.43	1425.65	1.154	6.00	6.93	1.10	1.27	5.44	103.14	119.03	0.897	25.855	
D-4H-1W, 139-140	40.51	1429.79	1.216	4.59	5.59	0.62	0.75	7.46	91.15	110.83	0.918	26.478	
D-4H-1W, 148-149	40.62	1434.95	1.343	6.84	9.18	1.04	1.40	6.55	45.31	60.85	0.915	26.405	
D-4H-2W, 14-15	40.75	1439.83	1.680	5.36	9.01	0.39	0.65	13.87	43.96	73.85	0.931	26.884	
D-4H-2W, 29-30	40.89	1444.99	1.709	3.73	6.37	0.50	0.85	7.46	51.99	88.87	0.924	26.663	
D-4H-2W, 38-40	40.99	1448.86	1.626	4.18	6.80	0.44	0.72	9.46	35.30	57.41	0.936	27.031	

ODP 849	**Depth**	**Age**	**Bulk MAR**	**P410**	**AR P410**	**P665**	**AR P665**	**S/I**	**K37**	**MAR K37**	**$U^{K}_{37}{}'$**	**SST**	**Particle size**
ODP Sample Label	(Rmcd)	(ka)	(g/cm^2/kyr)	(AU/g)	(AU/cm^2/kyr)	(AU/g)	(AU/cm^2/kyr)		(ng/g)	(μg/cm^2/kyr)		(°C)	(Mean <30μm)
D-4H-2W, 45-46	41.11	1454.58	1.321	7.22	9.54	0.73	0.97	9.86	41.69	55.06	0.874	25.151	
D-4H-2W, 58-59	41.28	1464.78	1.050	7.23	7.60	0.56	0.59	12.81	282.09	296.28	0.896	25.804	
D-4H-2W, 61-62	41.31	1466.91	0.887	5.79	5.14	0.38	0.33	15.35	96.61	85.72	0.889	25.607	
D-4H-2W, 67-68	41.35	1469.75	0.887	9.24	8.20	0.79	0.70	11.69	167.44	148.57	0.908	26.190	
D-4H-2W, 80-81	41.44	1476.32	0.863	6.65	5.74	0.56	0.48	11.91	81.38	70.23	0.864	24.844	
D-4H-2W, 102-103	41.49	1480.10	0.834	5.25	4.38	0.52	0.44	9.99	57.76	48.20	0.930	26.849	
D-4H-2W, 113-114	41.54	1483.87	0.834	6.78	5.66	0.96	0.80	7.08	28.29	23.61	0.938	27.079	
D-4H-2W, 123-125	41.64	1490.20	0.996	5.60	5.58	0.61	0.60	9.24	77.30	77.00	0.939	27.129	
D-4H-2W, 133-134	41.72	1494.84	1.086	6.47	7.03	0.48	0.52	13.44	45.62	49.56	0.895	25.802	
D-4H-2W, 142-143	41.91	1502.90	1.485	9.61	14.28	0.59	0.87	16.36	72.19	107.21	0.879	25.312	

A6: Results from ODP 806 Site B. ODP labelling is Core-Section, depth interval (cm). All other terms defined in Chapters 1 and 2. The samples from ODP 805 Site C used to bridge a coring gap are also shown (as discussed in Chapters 1 and 2), with labelling Site-Core-Section, depth interval (cm). U^K_{37}' and SST values are shown only for those samples where the C37:3 alkenone could be detected.

ODP 806B ODP Sample Label	**Depth** (Mbsf)	**Age** (ka)	**Bulk MAR** (g/cm^2/kyr)	**P410** (AU/g)	**AR P410** (AU/cm^2/kyr)	**P665** (AU/g)	**AR P665** (AU/cm^2/kyr)	**S/I**	**K37** (ng/g)	**MAR K37** (μg/cm^2/kyr)	U^K_{37}' (CIMS *)	**SST** (°C)
2H-3W, 84-85	10.348	500	2.057	16.843	34.64684	2.40787	4.952994137	6.9951	262.00	0.54	*	
2H-3W, 96-97	10.469	505	2.057	38.971	80.1640567	5.53216	11.37966082	7.0445	112.37	0.23		
2H-3W, 108-109	10.589	510	2.04	24.868	50.7314	1.66083	3.3881	14.973	145.31	0.30		
2H-3W, 121-122	10.711	515	2.0252	16.462	33.3393422	2.78453	5.639230939	5.912	161.32	0.33	0.994	28.79
2H-3W, 133-134	10.834	520	2.0418	17.749	36.2393849	1.40285	2.864334171	12.652	157.90	0.32		
2H-3W, 146-147	10.963	525	2.1414	15.199	32.5478452	1.79313	3.839813568	8.4764	74.90	0.16	*	
2H-4W, 9-10	11.092	530	2.1414	13.904	29.7736279	0.69486	1.487971144	20.01	68.90	0.15		
2H-4W, 23-24	11.228	535	2.2576	33.825	76.3624335	4.45026	10.04691099	7.6006	86.44	0.20	0.985	28.53
2H-4W, 36-37	11.368	540	2.296	33.973	78.0030779	2.40713	5.526772803	14.114	151.68	0.35		
2H-4W, 50-51	11.509	545	2.3124	12.069	27.9073646	1.36571	3.158077714	8.8368	69.40	0.16	0.983	28.45
2H-4W, 65-66	11.651	550	2.3288	62.852	146.368961	10.2617	23.89736933	6.1249	181.47	0.42	0.993	28.76
2H-4W, 79-80	11.789	555	2.2632	31.951	72.3119427	3.41537	7.729662305	9.3551	235.10	0.53	0.986	28.55
2H-4W, 92-93	11.92	560	2.1484	22.391	48.1050871	1.01508	2.18078794	22.059	251.99	0.54		
2H-4W, 104-105	12.048	565	2.0992	22.514	47.2617184	2.53475	5.320945174	8.8822	161.06	0.34		
2H-4W, 117-118	12.172	570	2.1328	38.14	81.3447062	2.87856	6.139391625	13.25	60.70	0.13	0.994 *	28.78
2H-4W, 129-130	12.292	575	2.064	14.797	30.5400519	1.81494	3.746025974	8.1527	53.66	0.11		
2H-4W, 140-141	12.405	580	1.9436	33.088	64.3093736	2.49839	4.855870209	13.244	194.94	0.38		
2H-5W, 01-02	12.518	585	1.9436	44.278	86.0586625	5.87659	11.42173241	7.5346	267.76	0.52	0.982 *	28.41
2H-5W, 13-14	12.633	590	1.978	32.308	63.9044892	2.72056	5.38127529	11.875	375.03	0.74		
2H-5W, 25-26	12.751	595	2.0296	30.757	62.4237592	3.9993	8.116972714	7.6905	88.86	0.18	0.994	28.77
2H-5W, 37-38	12.872	600	2.0812	25.044	52.1219197	1.64083	3.414902333	15.263	119.43	0.25	0.993 *	28.77
2H-5W, 49-50	12.996	605	2.1328	29.853	63.6702361	3.97858	8.485525512	7.5034	130.87	0.28		
2H-5W, 61-62	13.117	610	2.0812	25.774	53.6411957	1.51083	3.144346333	17.06	87.29	0.18		
2H-5W, 76-77	13.264	615	2.5284	13.743	34.7490104	1.42826	3.611214783	9.6225	75.30	0.19	0.992 *	28.72
2H-5W, 86-87	13.363	620	1.7028	19.768	33.6609618	1.23283	2.099264322	16.035	97.94	0.17		
2H-5W, 98-99	13.488	625	2.15	5.266	11.3219359	0.42108	0.905315692	12.506	15.28	0.03	0.993 *	28.77

ODP 806B	**Depth**	**Age**	**Bulk MAR**	**P410**	**AR P410**	**P665**	**AR P665**	**S/I**	**K37**	**MAR K37**	**U^{K}_{37}'**		**SST**
ODP Sample Label	(Mbsf)	(ka)	(g/cm^2/kyr)	(AU/g)	(AU/cm^2/kyr)	(AU/g)	(AU/cm^2/kyr)		(ng/g)	(μg/cm^2/kyr)	(CIMS *)		(°C)
2H-5W, 111-112	13.613	630	1.975	46.425	91.6888956	5.20874	10.28725728	8.9129	171.42	0.34	0.987	*	28.58
2H-5W, 123-124	13.737	635	1.9592	6.5181	12.770273	0.59331	1.162422284	10.986	79.50	0.16			
2H-5W, 135-136	13.858	640	1.9118	29.284	55.9843522	1.3408	2.563333831	21.84	91.16	0.17	0.980	*	28.38
2H-5W, 147-148	13.979	645	1.9118	43.308	82.7954093	5.56602	10.6411219	7.7807	202.07	0.39	0.992		28.71
2H-6W, 9-10	14.099	650	1.896	60.772	115.223662	3.56136	6.752338308	17.064	432.53	0.82			
2H-6W, 21-22	14.218	655	1.8802	29.686	55.8153088	4.32162	8.125507561	6.8691	153.09	0.29	0.988		28.61
2H-6W, 33-34	14.335	660	1.9422	25.936	50.3725755	8.71917	16.9343655	2.9746	141.74	0.28			
2H-6W, 45-46	14.45	665	1.909	31.939	60.9721626	3.63592	6.940975728	8.7844	127.98	0.24			
2H-6W, 56-57	14.564	670	1.8924	66.153	125.188818	2.60479	4.92929604	25.397	218.18	0.41	0.996	*	28.85
2H-6W, 67-68	14.672	675	1.7928	18.541	33.240688	2.99502	5.369468478	6.1907	118.21	0.21			
2H-6W, 77-78	14.779	680	1.7762	80.111	142.293356	2.62604	4.664366003	30.506	146.64	0.26	0.995	*	28.81
2H-6W, 88-89	14.884	685	1.743	22.875	39.8717913	3.41437	5.951252294	6.6997	145.86	0.25	0.993		28.76
2H-6W, 98-99	14.987	690	1.7098	23.291	39.8226668	0.93667	1.601512667	24.866	131.54	0.22	0.997	*	28.89
2H-6W, 103-104	15.037	692.5	1.66	16.98	28.187355	1.93117	3.20574238	8.7928	74.43	0.12			
2H-6W, 108-109	15.087	695	1.66	7.6184	12.6465789	0.6038	1.002309942	12.617	57.33	0.10	0.997	*	28.89
2H-6W, 118-119	15.187	700	1.7	32.891	55.91534	1.07048	1.819817579	30.726	130.79	0.22		*	
2H-6W, 128-129	15.284	705	1.649	17.266	28.4717248	2.03976	3.363556575	8.4648	82.89	0.14	0.997	*	28.88
2H-6W, 138-139	15.381	710	1.649	55.655	91.775095	2.09333	3.451906667	26.587	61.94	0.10			
2H-6W, 147-148	15.475	715	1.598	9.3058	14.870685	0.94343	1.507593272	9.8639	86.48	0.14			
2H-7W, 7-8	15.571	720	1.632	82.832	135.181106	4.52482	7.384510638	18.306	357.50	0.58			
2H-7W, 16-17	15.667	725	1.632	61.199	99.8769147	7.71274	12.58719454	7.9348	222.55	0.36	0.992		28.73
2H-7W, 26-27	15.76	730	1.581	45.293	71.6084422	5.72194	9.04639196	7.9157	392.85	0.62	0.983	*	28.45
2H-7W, 35-36	15.857	735	1.649	36.865	60.7902902	3.48132	5.740699713	10.589	84.16	0.14	0.995	*	28.82
2H-7W, 45-46	15.953	740	1.632	84.52	137.936478	1.95937	3.197691542	43.136	215.37	0.35			
2H-7W, 54-55	16.047	745	1.598	81.312	129.935928	6.64583	10.62004167	12.235	201.02	0.32			
2H-7W, 64-65	16.14	750	1.581	72.268	114.254917	2.53	3.99993	28.564					
805C-2H-4W, 54-55	12.846	755		7.5498		0.666		11.336	26.84				
805C-2H-4W, 60-61	12.908	760	1.0292	12.35	12.71062	0.46917	0.482866333	26.323	25.21	0.03	0.987	*	28.58
805C-2H-4W, 70-71	13.006	765	1.6268	13.265	21.5797046	1.54448	2.512566548	8.5887	71.14	0.12	0.985		28.50
805C-2H-4W, 79-80	13.092	770	1.4276	14.821	21.159152	1.00553	1.435493523	14.74	108.98	0.16	0.976		28.25

ODP 806B	**Depth**	**Age**	**Bulk MAR**	**P410**	**AR P410**	**P665**	**AR P665**	**S/I**	**K37**	**MAR K37**	**U^{K}_{37}'**		**SST**
ODP Sample Label	(Mbsf)	(ka)	($g/cm^2/kyr$)	(AU/g)	($AU/cm^2/kyr$)	(AU/g)	($AU/cm^2/kyr$)		(ng/g)	($\mu g/cm^2/kyr$)	(CIMS *)		(°C)
805C-2H-4W, 87-88	13.178	775	1.4276	21.809	31.1339917	2.96366	4.230925	7.3587	60.49	0.09	0.991	*	28.70
805C-2H-4W, 96-97	13.262	780	1.3944	16.217	22.6122922	0.9085	1.266807843	17.85	176.75	0.25			
805C-2H-4W, 104-105	13.344	785	1.3612	11.465	15.6056985	1.00686	1.370533122	11.387	85.74	0.12			
3H-1W, 12-13	16.12	790		41.293		3.37789		12.224	277.48		0.987		28.59
3H-1W, 23-24	16.232	795	1.904	12.058	22.9585195	0.81437	1.550556322	14.807	45.16	0.09	0.997	*	28.88
3H-1W, 34-35	16.34	800	1.836	56.749	104.190716	4.85904	8.92119403	11.679	124.98	0.23			
3H-1W, 46-47	16.46	805	2.04	26.577	54.2170139	3.57292	7.28875	7.4385	141.27	0.29	0.972		28.13
3H-1W, 57-58	16.57	810	1.87	37.031	69.2480556	1.67974	3.141111111	22.046	224.19	0.42			
3H-1W, 67-68	16.667	815	1.649	17.673	29.1422671	2.0328	3.352083668	8.6938	156.28	0.26	0.993		28.76
3H-1W, 77-78	16.776	820	1.853	34.377	63.7011003	1.67164	3.097552239	20.565	150.93	0.28			
3H-1W, 87-88	16.873	825	1.649	10.07	16.6057193	0.68421	1.128263158	14.718	140.26	0.23			
3H-1W, 96-97	16.967	830	1.598	16.247	25.9622261	0.88449	1.413412541	18.368	195.87	0.31			
3H-1W, 105-106	17.058	835	1.547	11.655	18.0309234	0.97267	1.50471865	11.983	24.00	0.04	0.992	*	28.72
3H-1W, 115-116	17.15	840	1.656	20.325	33.6582687	1.32007	2.186029851	15.397	116.00	0.19			
3H-1W, 124-125	17.245	845	1.71	19.233	32.8880172	2.27529	3.890741379	8.4529	127.55	0.22	0.994		28.80
3H-1W, 133-134	17.337	850	1.656	40.537	67.1294851	0.91089	1.508435644	44.503	136.44	0.23			
3H-1W, 142-143	17.422	855	1.53	20.906	31.9868987	1.74402	2.66835443	11.988	81.72	0.13			
3H-2W, 1-2	17.514	860	1.656	29.017	48.0513267	1.66914	2.76409901	17.384	143.25	0.24	0.993		28.77
3H-2W, 10-11	17.6	865	1.548	22.017	34.0824164	2.53015	3.916668942	8.7019	76.02	0.12			
3H-2W, 19-20	17.692	870	1.656	11.306	18.72246	1.00833	1.6698	11.212	89.31	0.15	0.997	*	28.87
3H-2W, 36-37	17.869	880	1.4691	34.197	50.2393219	3.53483	5.193012687	9.6744	279.67	0.41	0.987	*	28.58
3H-2W, 45-46	17.955	885	1.4276	36.068	51.490982	4.10197	5.855971027	8.7929	129.95	0.19	0.979		28.34
3H-2W, 54-55	18.046	890	1.5106	49.098	74.1679423	5.0675	7.6549655	9.6889					
3H-2W, 64-65	18.141	895	1.577	23.63	37.2646382	2.39702	3.780098916	9.8581	105.86	0.16	0.983		28.45
3H-2W, 73-74	18.237	900	1.5936	46.58	74.2306654	3.95122	6.296663415	11.789	345.79	0.55	0.981		28.40
3H-2W, 83-84	18.332	905	1.577	16.883	26.6251129	1.12515	1.77436569	15.005	71.46	0.11	0.982		28.44
3H-2W, 92-93	18.428	910	1.6704	64.486	107.717136	3.3925	5.666832	19.008	166.88	0.28	0.988		28.60
3H-2W, 102-103	18.523	915	1.653	19.199	31.7354209	1.65819	2.740991525	11.578	79.98	0.13	0.989	*	28.63
3H-2W, 111-112	18.618	920	1.653	50.762	83.909035	2.41667	3.99475	21.005	264.82	0.44			
3H-2W, 121-122	18.714	925	1.6704	38.448	64.2238244	4.74492	7.925912195	8.103	185.90	0.31	0.991		28.70

ODP 806B ODP Sample Label	**Depth** (Mbsf)	**Age** (ka)	**Bulk MAR** ($g/cm^2/kyr$)	**P410** (AU/g)	**AR P410** ($AU/cm^2/kyr$)	**P665** (AU/g)	**AR P665** ($AU/cm^2/kyr$)	**S/I**	**K37** (ng/g)	**MAR K37** ($\mu g/cm^2/kyr$)	**U^{K}_{37}'** (CIMS *)		**SST** (°C)
3H-2W, 130-131	18.809	930	1.653	50.636	83.7012861	4.03483	6.669567164	12.55	396.29	0.66	0.989	*	28.65
3H-3W, 1-2	19.013	940	1.7748	25.668	45.554679	1.39833	2.481762	18.356	292.06	0.52	0.993		28.75
3H-3W, 13-14	19.135	945	2.1228	25.313	53.7335324	3.32622	7.060891103	7.61	115.67	0.25	0.992		28.74
3H-3W, 25-26	19.258	950	2.1402	19.631	42.014291	1.77197	3.792377612	11.079	183.22	0.39	0.996		28.84
3H-3W, 38-39	19.38	955	2.2204	17.843	39.6181415	1.74236	3.868731878	10.241	170.70	0.38	0.997		28.89
3H-3W, 62-63	19.625	965	2.2295	19.515	43.5097114	2.34341	5.224641465	8.3278	83.49	0.19			
3H-3W, 74-75	19.747	970	2.2204	15.711	34.8848271	0.8258	1.83359665	19.025	83.40	0.19	0.994	*	28.79
3H-3W, 98-99	19.986	980	2.1749	57.312	124.648068	5.5049	11.97261127	10.411	788.50	1.71	0.985		28.51
3H-3W, 110-111	20.102	985	2.088	37.055	77.3711278	5.89787	12.31475188	6.2828	172.18	0.36	0.993		28.76
3H-3W, 133-134	20.336	995	2.106	21.191	44.6276791	1.85561	3.907925134	11.42	199.34	0.42	0.996	*	28.86
3H-3W, 145-146	20.452	1000	2.088	35.869	74.8944478	2.22637	4.648656716	16.111	85.72	0.18			
3H-4W, 06-07	20.569	1005	2.106	56.978	119.996547	5.70084	12.00596763	9.9947	165.73	0.35	0.989		28.64
3H-4W, 18-19	20.686	1010	2.106	83.763	176.40558	2.6125	5.501925	32.063	254.07	0.54	0.996		28.86
3H-4W, 30-31	20.803	1015	2.106	32.504	68.4538986	5.03568	10.60514366	6.4548	136.72	0.29	0.997		28.88
3H-4W, 42-43	20.921	1020	2.0296	55.247	112.129451	3.46064	7.023707873	15.964	89.01	0.18			
3H-4W, 54-55	21.04	1025	2.0468	10.388	21.261135	1.19792	2.451895833	8.6713	66.79	0.14	0.995		28.82
3H-4W, 65-66	21.158	1030	2.0296	34.223	69.4596773	3.02	6.129392	11.332	233.78	0.47	0.989		28.63
3H-4W, 77-78	21.277	1035	2.0468	28.565	58.4670323	4.15522	8.504907868	6.8745	267.61	0.55	0.983		28.47
3H-4W, 89-90	21.395	1040	2.0296	23.337	47.3640987	1.34167	2.723046667	17.394	132.62	0.27	0.994	*	28.79
3H-4W, 101-102	21.514	1045	2.0468	20.568	42.0976973	2.34403	4.797763739	8.7744	86.90	0.18			
3H-4W, 113-114	21.632	1050	1.9824	13.831	27.4181939	0.50337	0.997874747	27.477	35.58	0.07	0.991	*	28.71
3H-5W, 11-12	22.112	1070	2.016	33.965	68.4741386	3.77475	7.60990099	8.998	356.58	0.72			
3H-5W, 23-24	22.232	1075	2.016	29.496	59.4632889	4.51173	9.095644444	6.5376	189.57	0.38	0.976		28.25
3H-5W, 35-36	22.352	1080	2.136	49.081	104.83666	7.3225	15.64086	6.7027	376.38	0.80			
3H-5W, 47-48	22.472	1085	2.136	37.228	79.5196865	5.2931	11.30606897	7.0334	221.24	0.47	0.980		28.37
3H-5W, 59-60	22.592	1090	2.136	20.278	43.3139783	1.64946	3.52323913	12.294	101.12	0.22			
3H-5W, 68-69	22.682	1095	1.602	18.641	29.8624667	1.66759	2.671483333	11.178	32.35	0.05	0.997	*	28.88
3H-5W, 77-78	22.773	1100	1.6198	14.303	23.1679276	0.52217	0.845806897	27.392	43.62	0.07		*	
3H-5W, 86-87	22.863	1105	1.602	16.982	27.2054656	1.9771	3.167312977	8.5894	67.61	0.11			
3H-5W, 95-96	22.954	1110	1.6198	47.338	76.678673	4.07873	6.606721943	11.606	173.47	0.28	0.992	*	28.71

ODP 806B	**Depth**	**Age**	**Bulk MAR**	**P410**	**AR P410**	**P665**	**AR P665**	**S/I**	**K37**	**MAR K37**	**U^{K}_{37}'**		**SST**
ODP Sample Label	(Mbsf)	(ka)	(g/cm^2/kyr)	(AU/g)	(AU/cm^2/kyr)	(AU/g)	(AU/cm^2/kyr)		(ng/g)	(µg/cm^2/kyr)	(CIMS *)		(°C)
3H-5W, 104-105	23.044	1115	1.602	29.958	47.9934778	4.47213	7.164348123	6.6989	84.45	0.14	0.992		28.73
3H-5W, 113-114	23.135	1120	1.6198	11.626	18.8318211	0.89024	1.442017073	13.059	100.87	0.16	0.994	*	28.78
3H-5W, 122-123	23.225	1125	1.602	29.779	47.7063576	3.42605	5.488529801	8.692	115.10	0.18			
3H-5W, 131-132	23.316	1130	1.6198	24.607	39.858	2.34644	3.800766667	10.487	244.75	0.40	0.986	*	28.55
3H-5W, 140-141	23.406	1135	1.602	32.503	52.0699907	4.25234	6.812242991	7.6436	87.47	0.14	0.999		28.93
3H-5W, 149-150	23.497	1140	1.6198	27.224	44.0976586	3.32841	5.391354023	8.1793					
3H-6W, 07-08	23.575	1145	1.3884	25.297	35.1219429	2.76099	3.833357143	9.1622	58.85	0.09			
3H-6W, 15-16	23.652	1150	1.3706	20.173	27.6493915	0.67974	0.931649673	29.678	142.12	0.19			
3H-6W, 23-24	23.73	1155	1.3884	16.852	23.3975654	1.56714	2.175814134	10.753	84.04	0.12			
3H-6W, 30-31	23.808	1160	1.3884	27.195	37.7569595	2.76458	3.8383475	9.8403	430.56	0.60	0.985		28.53
3H-6W, 38-39	23.885	1165	1.3244	28.899	38.2741089	2.97143	3.93536	9.7257	367.70	0.49	0.987		28.58
3H-6W, 46-47	23.963	1170	1.3416	30.606	41.061192	3.14345	4.217251741	9.7365	138.59	0.19	0.994	*	28.80
3H-6W, 54-55	24.041	1175	1.3416	16.94	22.7270659	2.57563	3.455460116	6.5771	112.95	0.15	0.997		28.89
3H-6W, 61-62	24.118	1180	1.3244	22.065	29.2222801	1.41993	1.880561438	15.539	249.01	0.33			
3H-6W, 69-70	24.196	1185	1.3416	10.957	14.7001424	1.20898	1.621965325	9.0632	125.85	0.17	0.995		28.80
3H-6W, 77-78	24.273	1190	1.3244	20.05	26.5545528	1.65662	2.194022781	12.103	239.18	0.32			
3H-6W, 85-86	24.351	1195	1.3416	55.606	74.601013	11.5702	15.52263755	4.8059	226.64	0.30	0.992		28.72
3H-6W, 92-93	24.429	1200	1.3416	16.755	22.4788898	0.4935	0.662074146	33.952	63.81	0.09	0.999	*	28.93
3H-6W, 102-103	24.524	1205	1.634	21.034	34.3701512	1.88058	3.07287457	11.185	74.64	0.12			
3H-6W, 131-132	24.811	1220	1.6837333	22.019	37.0736178	1.27236	2.142311111	17.305	165.30	0.28	0.998	*	28.92
3H-6W, 140-141	24.906	1225	1.672	16.367	27.3648354	1.58575	2.65138036	10.321	31.69	0.05		*	
3H-7W, 0-1	25.001	1230	1.672	52.87	88.3991067	4.94581	8.269399015	10.69	163.03	0.27			
3H-7W, 09-10	25.097	1235	1.6896	24.072	40.6712284	3.26359	5.514167376	7.3758	97.92	0.17			
3H-7W, 19-20	25.192	1240	1.672	29.516	49.3502112	1.89026	3.160521452	15.615	259.01	0.43	0.998	*	28.90
3H-7W, 28-29	25.287	1245	1.672	23.19	38.7734684	3.26934	5.46633474	7.0931	291.15	0.49	0.992		28.72
3H-7W, 38-39	25.383	1250	1.6704	22.579	37.715278	2.60479	4.351037398	8.6681	159.18	0.27	0.994		28.77
3H-7W, 47-48	25.478	1255	1.653	14.497	23.9627944	1.29043	2.133087278	11.234	196.72	0.33	0.994		28.77
4H-1W, 7-8	25.574	1260	1.6704	13.599	22.7157861	1.2896	2.154154455	10.545	145.46	0.24			
4H-1W, 16-17	25.669	1265	1.653	11.547	19.087313	1.25382	2.07255916	9.2095	125.15	0.21			
4H-1W, 26-27	25.764	1270	1.653	13.614	22.5037814	1.57286	2.599944724	8.6555	195.36	0.32			

ODP 806B ODP Sample Label	**Depth** (Mbsf)	**Age** (ka)	**Bulk MAR** (g/cm^2/kyr)	**P410** (AU/g)	**AR P410** (AU/cm^2/kyr)	**P665** (AU/g)	**AR P665** (AU/cm^2/kyr)	**S/I**	**K37** (ng/g)	**MAR K37** (μg/cm^2/kyr)	**U$^K_{37}$'** (CIMS *)		**SST** (°C)
4H-1W, 38-39	25.88	1275	2.0184	20.607	41.5938994	2.35276	4.74881227	8.7588	184.36	0.37			
4H-1W, 45-46	25.955	1280	1.305	20.239	26.4116418	2.84577	3.713731343	7.1119	264.20	0.34			
4H-1W, 57-58	26.071	1285	2.0184	18.663	37.6692234	2.44745	4.939927928	7.6255	97.13	0.20			
4H-1W, 66-67	26.168	1290	1.6878	23.928	40.3849528	0.57165	0.96483271	41.857	73.40	0.12		*	
4H-1W, 76-77	26.264	1295	1.6704	36.3	60.635071	4.96169	8.288012903	7.316	289.84	0.48	0.979		28.34
4H-1W, 86-87	26.361	1300	1.6878	31.241	52.7285204	2.1879	3.692734395	14.279	370.02	0.62	0.990		28.68
4H-1W, 95-96	26.457	1305	1.6704	37.272	62.2589816	3.64278	6.084892833	10.232	110.94	0.19	0.986		28.55
4H-1W, 105-106	26.554	1310	1.6878	28.847	48.6884571	2.81363	4.748842857	10.253	271.75	0.46			
4H-1W, 115-116	26.651	1315	1.6878	59.049	99.6625317	7.32114	12.35661707	8.0655	226.77	0.38	0.992		28.71
4H-1W, 124-125	26.747	1320	1.6704	13.328	22.263606	2.00168	3.34359799	6.6586	64.54	0.11			
4H-1W, 134-135	26.844	1325	1.6878	3.1079	5.24559702	0.07678	0.129596206	40.476	53.13	0.09		*	
4H-1W, 144-145	26.94	1330	1.6704	16.142	26.9632478	0.98507	1.645468657	16.386	50.96	0.09	0.998	*	28.92
4H-2W, 03-04	27.037	1335	1.6878	27.622	46.6197996	3.19415	5.391089825	8.6476	114.49	0.19	0.987		28.57
4H-2W, 13-14	27.133	1340	1.6704	21.828	36.4621307	1.61304	2.694415842	13.532	215.22	0.36			
4H-2W, 22-23	27.22	1345	1.5138	19.925	30.1621415	1.81795	2.752010769	10.96	84.08	0.13	0.978		28.30
4H-2W, 42-43	27.423	1355	1.6849	34.247	57.7026247	4.19753	7.072419753	8.1588	337.73	0.57	0.992		28.72
4H-2W, 61-62	27.616	1365	1.6019	11.799	18.90083	1.57486	2.522760629	7.4921	207.08	0.33			
4H-2W, 71-72	27.713	1370	1.6102	10.158	16.3568809	0.9531	1.534679732	10.658	121.60	0.20			
4H-2W, 80-81	27.809	1375	1.5936	22.895	36.4860669	2.95268	4.70539306	7.7541	74.41	0.12			
4H-2W, 91-92	27.914	1380	1.743	18.87	32.8897772	1.76155	3.070383663	10.712	169.01	0.29	0.995		28.81
4H-2W, 101-102	28.019	1385	1.743	13.548	23.6137478	1.51542	2.64138209	8.9399	206.54	0.36	0.992		28.72
4H-2W, 112-113	28.124	1390	1.911	47.27	90.3325916	2.5363	4.846876238	18.637	472.51	0.90			
4H-2W, 122-123	28.229	1395	1.911	43.939	83.9667607	6.27658	11.99455368	7.0004	315.54	0.60	0.987		28.58
4H-2W, 133-134	28.334	1400	1.911	18.112	34.611395	1.98	3.78378	9.1473	371.84	0.71	0.991		28.68
4H-2W, 143-144	28.439	1405	1.911	18.766	35.8625115	2.81178	5.373308314	6.6742	112.74	0.22			
4H-3W, 4-5	28.544	1410	1.911	9.5508	18.2516425	0.46083	0.8806525	20.725	33.44	0.06		*	
4H-3W, 15-16	28.65	1415	1.9292	5.3825	10.3838778	0.56624	1.092388889	9.5057	63.71	0.12	0.995	*	28.81
4H-3W, 25-26	28.755	1420	1.911	29.928	57.1925012	2.21138	4.22595122	13.839	158.83	0.30	0.998	*	28.91
4H-3W, 36-37	28.869	1425	2.0748	36.951	76.6655357	4.95081	10.27193568	7.4636	196.07	0.35			
4H-3W, 48-49	28.984	1430	1.817	21.006	38.1685585	1.99491	3.624753181	10.53	303.26	0.55			

ODP 806B ODP Sample Label	**Depth** (Mbsf)	**Age** (ka)	**Bulk MAR** (g/cm^2/kyr)	**P410** (AU/g)	**AR P410** (AU/cm^2/kyr)	**P665** (AU/g)	**AR P665** (AU/cm^2/kyr)	**S/I**	**K37** (ng/g)	**MAR K37** (µg/cm^2/kyr)	**U^{K}_{37}'** (CIMS *)	**SST** (°C)
4H-3W, 59-60	29.098	1435	1.8012	21.927	39.4951261	2.38023	4.287263051	9.2122	194.03	0.35	0.982	28.41
4H-3W, 71-72	29.212	1440	1.8012	34.226	61.6484245	3.55637	6.405738235	9.6239	395.55	0.71	0.987	28.57
4H-3W, 82-83	29.327	1445	1.817	27.812	50.5341881	3.4835	6.329516502	7.9839	148.83	0.27		
4H-3W, 91-92	29.441	1450	1.8012	18.947	34.126736	1.30167	2.344562	14.556	119.32	0.21	0.998 *	28.92
4H-3W, 105-106	29.555	1455	1.8012	8.5303	15.3647818	1.54902	2.790094118	5.5069	63.78	0.11	*	
4H-3W, 117-118	29.67	1460	2.047	16.648	34.0776277	0.39055	0.799450249	42.626	124.24	0.25		
4H-3W, 127-128	29.779	1465	1.9402	16.272	31.5711109	2.59318	5.03127979	6.275	148.16	0.29	0.989	28.62
4H-3W, 138-139	29.889	1470	1.958	14.588	28.5639567	1.80417	3.532558333	8.0859	213.71	0.42	0.995	28.83
4H-3W, 148-149	29.998	1475	1.9402	24.03	46.6232618	2.82203	5.475310169	8.5152	269.09	0.52		
4H-4W, 10-11	30.108	1480	1.958	39.152	76.6591095	2.77861	5.440512438	14.09	378.41	0.74	0.994	28.79
4H-4W, 21-22	30.217	1485	1.9402	24.023	46.6102573	2.50586	4.861864324	9.5869	137.64	0.27	0.995	28.81
4H-4W, 32-33	30.326	1490	1.9402	19.381	37.6026928	1.61833	3.139890333	11.976	104.97	0.20		
4H-4W, 43-44	30.435	1495	1.9184	24.814	47.6023322	4.04614	7.762113748	6.1327	41.45	0.08		
4H-4W, 54-55	30.545	1500	1.936	18.138	35.1147591	1.01485	1.964752475	17.872	111.09	0.22		